Development of bifunctional, carbon-supported nanocatalysts for wastewater treatment

Bence Solymosi

Submitted in accordance with the requirements for the degree of
Doctor of Philosophy

The University of Leeds

School of Chemistry

April 2025

I confirm that the work submitted is my own, and that appropriate credit has been given, where reference has been made to the work of others.

Acknowledgements

I am very grateful for having had the opportunity to study at the University of Leeds, these 6.5 years have been the most formative part of my professional and personal life, so far. First, I'd like to thank the EPSRC, the University of Leeds and the School of Chemistry for the fully funded studentship I was offered.

I will forever be grateful to Charlotte Willans and Tom Chamberlain for taking me on as an Erasmus+ trainee in 2019, without which I would have never had the chance to study in Leeds. Thanks to the Willans Group who have been very welcoming and helpful in my Erasmus+ project and some parts of my PhD, and getting settled in Leeds. I am also grateful to Tom and Charlotte for offering to take me on as a PhD student after my traineeship.

I consider myself very lucky for having had Tom Chamberlain and Robert Menzel as my supervisors during my PhD. I am very grateful for the professional opportunities and endless mentorship I have received, and I am very thankful for having been able to form my project according to my interests.

I would like to thank Chris Pask for the XRD training and help in interpreting the data he has given me, and Alex Kulak for the many SEM images, and Raman and BET measurements he has done for me. Similarly I gratefully acknowledge the great quality TEM images Zabeada Aslam has captured. I am grateful to my Transfer Viva (Chris Pask) and APR assessors (mainly Richard Bourne) who have helped improve the project with their valuable suggestions. I am very grateful to Andrew Britton and Beth Wilneff for the XPS measurements they have done and the help they have given me in interpreting the data. I also acknowledge support from the Henry Royce Institute (EPSRC grants: EP/P022464/1, EP/R00661X/1), which funded the VXSF Facilities (https://engineering.leeds.ac.uk/vxsf) within the Bragg Centre for Materials Research at Leeds'.

I would like to thank Caillean Convery, a PGR of the Mamlouk Group at Newcastle University for recording RRDE voltammograms for me.

I am very happy to have met the people in 2.07 and the iPRD (Xiangyi, Alex, Anthony, Sean, Rachel, Tom M., Sarah, Zara, Han, Jerry, Odhran, Tom P., Tom D., Pia, Holly, Brendan, and Ricardo). It's been great walking all over the North with you!

Finally, I am eternally grateful for the endless love and support my parents and my brothers have given me. I truly wouldn't be where I am without you.

Abstract

Globally 1 in 3 people do not have access to safe drinking water.[1] Households, industry, and agriculture often introduce persistent organic pollutants into their waste streams, and by extension into surface waters, ground water and eventually drinking water supplies.[2] An increasing number of these pollutants are being linked to potentially serious negative health effects.[3-4] The ideal solution to this problem would be to prevent these compounds from reaching surface waters, but failing that, there is a pressing need for sustainable, highly active tertiary water treatment solutions.

The most common experimental tertiary water treatment methods use coagulation-flocculation, adsorption on activated carbon materials, ozonation, advanced oxidation processes (AOPs), and various bioremediation processes.[5] Some of these methods do not actually destroy pollutants, just transfer or concentrate them into another phase, which often ends up being incinerated, while others suffer from high costs and/or slow detoxification.

This thesis discusses the development of carbon-supported bifunctional catalysts that are capable of both generating H_2O_2 and decomposing it into reactive oxygen species, which can then be used to efficiently degrade aqueous organics.

The first chapter of this thesis explores the emergent synergism between a macroscale carbon, graphitic nanofibres (GNFs), and a Fenton-like catalyst (MnO_2). Extensive characterisation is used to uncover the structure-performance relationships governing the activity of this composite catalyst. A novel metric is also suggested for the field of organics removal, which separates out the different contributions to overall organics removal. This research has shown that the most active MnO_2-GNF composite facilitates more than three times as much truly catalytic dye degradation than unsupported MnO_2. The ability of the composite to dissipate heat has been identified as a crucial factor in this increased catalytic activity.

The second chapter explores the chemical modification of two macroscale carbon materials, GNF and carbon beads (CB), via acid oxidation, and the effect of this modification on sorption characteristics. Observations show that GNF was mostly unchanged by acid oxidation, but CB went through significant changes. In this case, overall surface area decreased moderately but the ratio of micropore area to overall surface area increased, while the concentration of acidic surface functional groups doubled. This led to a strong suppression in the mostly irreversible adsorption of the studied organics.

These acid oxidised carbon materials (oGNF and oCB) are then used as catalyst supports in Chapter 3. In this chapter the synthesis and thorough characterisation of Co, Mn spinels is discussed, along with the catalytic performance of composites made of the most active spinel, and GNF, oGNF, CB and oCB. It was found that the formation of composites only led to an enhanced catalytic performance in the case of Co_2MnO_4-oCB, compared to the unsupported catalyst. Results also show that oCB composites facilitate a much higher truly catalytic activity, partly because of the prevention of adsorption.

Finally, in Chapter 4 the electrocatalytic activity of the previously synthesised composites are investigated in O_2 reduction. The electrochemical activity of GNF and oGNF supported Co, Mn spinels has been investigated with multiple electroanalytical methods. Results showed negligible O_2 reduction activity in the case of all studied materials.

This research highlights the suitability of macroscale carbon materials as catalyst supports in Fenton-like chemistry, while also emphasises the need for a nuanced approach to catalytic activity in the field, as not all organics removal modes are equally desirable. Additionally, the results discussed here show that the acid oxidation of macroscale carbon supports is a viable way of enhancing the catalytic activity of composites made with such materials.

Table of Contents

List of Figures

List of Abbreviations

AOP – Advanced oxidation process

BET – Braun-Emmett-Teller

BJH – Barrett-Joyner-Halenda

CB – Carbon beads

CV – Cyclic voltammetry

DMPO - 5,5-Dimethyl-1-pyrroline N-oxide

FWHM – Full width at half maximum

GNF – Graphitic nanofibres

oCB – Oxidised carbon beads

oGNF – Oxidised graphitic nanofibres

ORR – Oxygen reduction reaction

PBSAC – Polymer based spherical activated carbon

ROS – Reactive oxygen species

RRDE – Rotating ring disk electrode

SEM – Scanning electron microscopy

TEM – Transmission electron microscopy

TGA – Thermogravimetric analysis

XPS – X-ray photoelectron spectroscopy

XRD – X-ray diffraction

Chapter 1 – Introduction and theoretical context

1.1 Project Aims

This project aims to create a catalytic system capable of removing harmful anthropogenic organic compounds from surface waters in a more sustainable way than currently available solutions are capable of. The project aims to achieve this by not only using an environmentally friendly oxidant, but also by generating it on demand, *in situ*. Accordingly, the two main pillars of this work are the electrochemical production of H_2O_2, and its activation in organics removal reactions. The former is based on the two electron reduction of oxygen facilitated by a catalyst, while the latter makes use of Fenton-like chemistry. This project aims to strike a balance between industrial relevance and catalytic performance, accordingly cost and scalability were important factors in choosing what materials are used.

In this introduction a brief overview is given of the most important theoretical foundations of the project via a survey of the literature. More detailed and focused introductions will be given at the beginning of each chapter.

1.2 Theoretical Basis and Context

1.3 Advanced Oxidation Processes (AOPs)

AOPs are water treatment processes that are most commonly used as tertiary treatment methods on waters having a chemical oxygen demand of less than about 5 g/l. [6] AOPs often incorporate adsorption and bioremediation in addition to chemical degradation, but these will not be discussed here. Chemical degradation methods typically use *in situ* generated highly reactive and non-selective oxidizing radical species to remove organic or less frequently inorganic pollutants from water. Removal of organics is achieved via gradual decomposition into smaller and more highly substituted oxidation products. The process ultimately results in small, stable inorganic molecules and ions like water, carbon dioxide, nitrates, sulphates etc., which is referred to as full mineralisation. [7]

There are many types of AOPs, but only the type used in this work will be discussed in detail. AOPs can be grouped together based on the oxidant, the activation method used and based on whether the catalyst and the reactants are in the same phase or not (homogeneous or heterogeneous). The oxidant is most commonly H_2O_2, O_3 or peroxymonosulfate and while these are considered strong oxidants, various methods are used to generate much more powerful reactive oxygen species (ROS) from these molecules, like hydroxyl radicals ($OH^{\cdot}$),

superoxide radical anions ($O_2^{\cdot-}$), or singlet oxygen ($^1O_2$). This generation of radicals is generally referred to as activating the oxidant. The most common methods of activation are photolysis, sonolysis, or thermally activated catalysis[1]. [2-3] In this work thermally activated catalytic decomposition of H_2O_2 is used as the source of ROS.

1.4 Fenton Chemistry

The basis of Fenton chemistry[2] was discovered and developed by Henry John Horstman Fenton in the period between the 1870s and 1890s. [10] Based on his work, aqueous mixtures of H_2O_2 and an Fe(II) salt came to be known as Fenton's reagent, and by extension this chemistry is referred to as Fenton chemistry. Other similar systems that use Fe-free transition metal or metal oxide catalysts are referred to as Fenton-like chemistry.

$$k_1 = 4.00 \cdot 10^7 e^{-\frac{8500}{RT}} Ms^{-1} \quad (1)$$

$$k_1 = 1.78 \cdot 10^9 e^{-\frac{10100}{RT}} Ms^{-1} \quad (2)$$

The next major contribution towards a deeper understanding of Fenton chemistry was made by Fritz Haber and Joseph Joshua Weiss. In their 1934 publication Haber and Weiss have hypothesised that the decomposition of H_2O_2 catalysed by aqueous Fe(II) salts proceeds through the generation of $OH^{\cdot}$ and $O_2^{\cdot-}$, and its kinetics can be described by equation (1). [11] J. H. Baxendale *et al.* also corroborated Haber and Weiss' kinetics findings in an article published in 1946, reporting that the rate of the reaction between aqueous Fe(II)/Fe(III) and H_2O_2 can be described kinetically by equation (2). [12] These results place the rate of generating ROS in Fenton chemistry at $1.3 \cdot 10^6$ and $3.0 \cdot 10^7$ M/s according to (1) and (2) respectively.

The first experiments intended to probe the rate constant between these radicals and larger organic molecules in water, were conducted in the 1970s. Buxton[3] *et al.* compiled a large range of such rate constants, and published these in 1988. [13] Rate constants between radicals were found to be in the range of 10^9-10^{10} $M^{-1}s^{-1}$, while the reactions between radicals and small inorganic molecules generally have rate constants of 10^7-10^9 $M^{-1}s^{-2}$. Reactions between $OH^{\cdot}$ and

[1] Thermal activation is used to refer to reactions in which the reactants overcome the activation energy barrier simply due to the kinetic energy provided by ambient temperature.

[2] A large part of research into Fenton chemistry was done by British researchers, and in particular researchers associated with the British Dyestuffs Corporation (which had manufacturing sites in Huddersfield and Manchester), the University of Manchester and the University of Leeds.

[3] George V. Buxton was an accomplished radiation chemist at the Cookridge Radiation Research Centre of the University of Leeds.

large organic molecules like Methylene Blue, Rhodamine B, or Coumarin have rate constants of 10^9-10^{10} $M^{-1}s^{-2}$, while smaller molecules like ethanol, hexane, or propionic acid show rate constants of 10^8-10^9 $M^{-1}s^{-2}$. Based on the above it is safe to say that any reaction involving ROS happens very rapidly, and the rate determining step is likely to be the generation of these radicals.

Instrumental evidence of $OH^{\cdot}$ and $O_2^{\cdot-}$ became possible to generate with high confidence from the late 1970s when a combination of selective spin traps, most importantly 5,5-Dimethyl-1-pyrroline N-oxide (DMPO), and high resolution EPR spectroscopy became available. [9-10] The research into ROS up to this point was mostly focused on cell biology involving oxidative stress or cancer. The first EPR studies specifically aimed at industrially relevant Fenton chemistry were also published around this time as illustrated by a selected article from Croft *et al.*. [16] The first publication about using a catalytic water treatment system based on Fenton chemistry on a laboratory and pilot scale was published in 1988, and the field can be considered to have started in the late 1980s. [12–15]

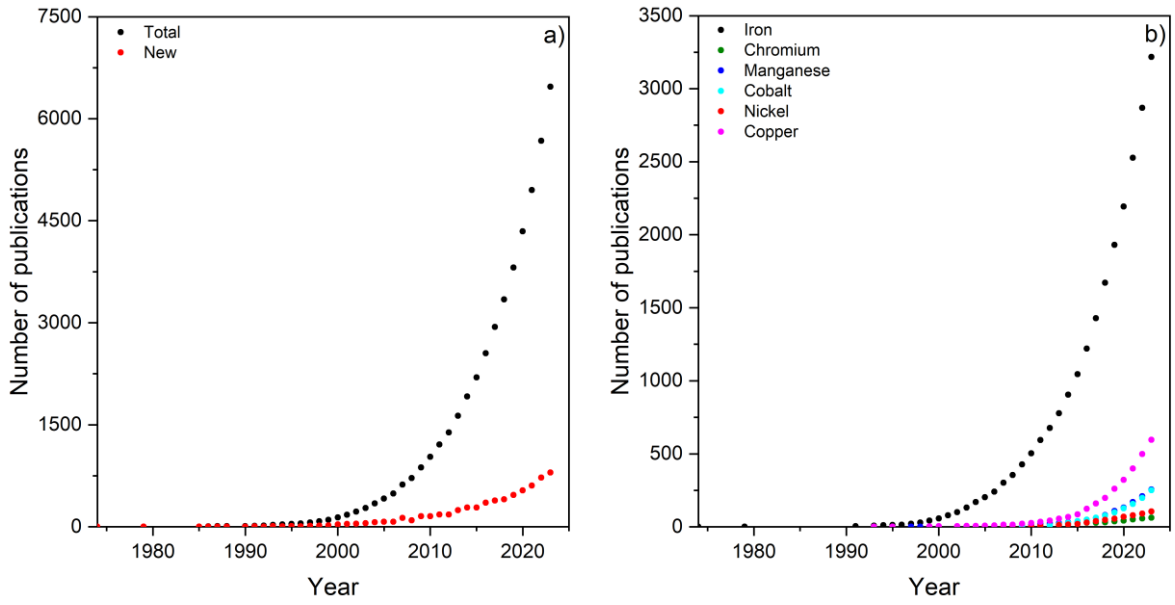

Figure 1 – Graphs showing results of a survey of relevant literature; a: Graph showing the number of publications containing the keywords 'Fenton' and 'degradation' versus year of publication. b: Graph showing the number of publications containing an element's name in addition to 'Fenton' and 'degradation';
Data is based on a survey of literature using Scopus (accessed 2025.02.24.).

In the last three decades research into Fenton chemistry in the field of water treatment has gone through an exponential growth, as Figure 1 illustrates. The number of new publications indexed by Scopus containing the keywords 'Fenton' and 'degradation' went from

1 in 1974 to 798 in 2023, with the total number of publications being almost 6500 by 2023[4][5]. Further differentiating this analysis based on what element a reported catalyst is made of, shows that while Fe is still the dominant choice, other transition metals of the 3d row are garnering more and more research interest, as well, especially Cu, Mn and Co.

The first research article about the application of ROS for water treatment purposes was published in 1987 by Glaze *et al.*. [21] In this paper the authors coined the term 'advanced oxidation process', and defined it as water treatment methods that generate $OH^{\cdot}$ radicals in sufficiently large concentrations to affect water purity. The authors mentioned AOP systems using O_3/H_2O_2, O_3/UV, H_2O_2/UV, and O_3 and H_2O_2 activated by a metal or metal oxide. Using O_3 and H_2O_2 has become the most common choice because of the environmental friendliness, high oxidation potential and capability of generating $OH^{\cdot}$ radicals in aqueous media these oxidants have.

An important milestone in the research and development of AOPs using Fe-based catalysts is the comprehensive, highly-cited 2006 review article by Pignatello *et al.*. [22] According to Pignatello Fenton-based AOPs compare favourably to other AOPs that also rely on the generation of $OH^{\cdot}$ radicals. The authors note that the reagents are readily available and are relatively easy to store and handle. AOPs based on Fenton chemistry have a number of limiting factors, some of which are specific to Fenton chemistry while others are specific to AOPs in general. The former category includes the significant number of non-productive reactions, the requirement for sufficiently low pH (generally 3-5), the potential interference by compounds capable of chelating Fe ions, and the fact that normal operation produces a toxic sludge, that also depletes the catalyst. The latter category includes interference by non-target radical scavengers like bicarbonate and halide ions, the inability of $OH^{\cdot}$ radicals to attack certain compounds (e.g. perchlorinated aromatics), and the potential need for pre-treatment for biological wastewater. The authors noted that the fundamental reactions of systems based on Fenton chemistry are fairly well understood, but the whole system itself is very complex, and difficult to fully understand. The most important reactions happening in homogeneous Fenton chemistry are listed below (equations (3) to (10)). In general, this mechanism involves aqueous

[4] Some additional search terms were used to exclude publications from non-chemistry related journals. Additionally, only publications about thermally activated redox catalysis were included (ergo photocatalysis, electrocatalysis, etc. were excluded).

[5] In all literature surveys of this thesis only Scopus will be used, since it has been shown that 99.11% of all published articles overlap between Scopus and Web of Science, and Scopus offers a better search interface. [242]

Fe ions cycling between +2 and +3 oxidation states, while $OH^{\cdot}$, $O_2^{\cdot-}$, and other species are being generated as a result of reactions between the catalyst and H_2O_2. It's important to note that the radicals can recombine to form H_2O_2, H_2O and O_2, and this mechanism also leads to a gradual increase in pH.

$$Fe^{2+} + H_2O_2 \rightarrow Fe^{3+} + OH^- + OH^{\cdot} \quad (3)$$

$$Fe^{3+} + H_2O_2 \rightarrow Fe^{2+} + HO_2^{\cdot} + H^+ \quad (4)$$

$$OH^{\cdot} + H_2O_2 \rightarrow HO_2^{\cdot} + H_2O \quad (5)$$

$$OH^{\cdot} + Fe^{2+} \rightarrow Fe^{3+} + OH^- \quad (6)$$

$$Fe^{3+} + HO_2^{\cdot} \rightarrow Fe^{2+} + O_2H^+ \quad (7)$$

$$Fe^{2+} + HO_2^{\cdot} + H^+ \rightarrow Fe^{3+} + H_2O_2 \quad (8)$$

$$HO_2^{\cdot} + HO_2^{\cdot} \rightarrow H_2O_2 + O_2 \quad (9)$$

$$HO_2^{\cdot} + H_2O_2 \rightarrow OH^{\cdot} + H_2O + O_2 \quad (10)$$

As shown above, these radicals are extremely reactive and only minimally selective which leads to a complex network of parallel and consecutive reactions. This makes kinetic and mechanistic predictions extremely challenging, and it also serves as a barrier for applying Fenton-based AOPs to waste streams of changing compositions. Pignatello *et al.* noted that some of the main challenges where improvements are necessary for Fenton-based AOPs to be competitive in water treatment are mechanistic clarifications including participating catalyst species, potential side reactions with scavengers and intended degradation products, immobilization of the catalyst, and thus limiting leaching, eliminating the need for low pH, and elucidating the role of surface and solution phase catalysts.

A more recent highly-cited review article by Bokare *et al.* published in 2014 has summarised the state of the art for Fe-free, Fenton-like AOP systems. [23] The authors describe Fe-free catalysts based on Al, Ce, Cr, Co, Cu, Mn and Ru. This is an extensive review, but for this thesis only the section detailing Mn and Co-based catalysts are relevant, so only these will be discussed. A basic requirement for any Fenton-like catalyst system is the availability of easily accessible oxidation states for the metal ions to cycle through. Each Fe-free catalyst system has its advantages and disadvantages which need to be carefully weighed when selecting a metal for experimental study.

According to Bokare *et al.* Mn-based systems have the advantage of a wide scale of oxidation states ranging from 0 to 7, of which +2 to +4 are the most common, most easily accessible and thus most catalytically relevant. Mn(II) and Mn(III) are both theoretically water soluble although $Mn_{(aq)}^{2+}$ requires pH<4 and reducing conditions to be stable in solution, while Mn(III) is only stable in solution while complexed. Mn-based Fenton-like catalysts show good stability in the pH range 3.5 to 7.0; dissolution is practically absent above pH=5.5. This significantly reduces the likelihood that a Mn-based Fenton-like catalyst would leach Mn ions during its operation. In a Fenton-like system Mn ions cycle between the oxidation states +2 and +4 through a +3 state. While all possible oxide polymorphs of Mn have been found to be excellent catalysts of H_2O_2 activation, the exact mechanisms depend on a large number of factors, including composition, presence or absence of a catalyst support, reactant concentrations etc. Mn is also a naturally abundant element, so any potential catalyst would benefit from the low cost associated with this.

According to Bokare *et al.* Co based materials have also been widely studied as Fenton-like AOP catalysts, although mostly with peroxymonosulfate as the oxidant. According to publications reviewed by Bokare et al. Co-based materials have shown excellent reactivity and recyclability in Fenton-like AOP systems; they even exhibited comparable and in some cases enhanced reactivity in alkaline media, which is a rare property for Fenton-like catalysts. Unfortunately, this excellent catalytic activity is somewhat overshadowed by a high stoichiometric requirement of H_2O_2, and excessive metal leaching from immobilized catalysts in some cases. The latter of which is the largest drawback of Co-based systems as Co compounds exhibit significant environmental toxicity.

The past decades also saw intense research into elucidating the exact mechanism of Fenton chemistry. He *et al.* published one of the most highly cited review articles about the decomposition mechanism of H_2O_2 facilitated by Fe containing materials in which they propose an interfacial decomposition mechanism. [24] They propose equations (11)-(20) as the most important non-substrate-specific steps. The authors found that H_2O_2 binds to the surface of the catalyst via a hydroxide containing terminal Fe(III) ion of the lattice. This step produces a hydroperoxyl ($OOH^{\cdot}$) radical and reduces the affected Fe ion. The Fe(II) ion then gets reoxidised by a solvated H_2O_2 molecule, which also produces a $OH^{\cdot}$ radical. These are the main radical producing steps, but due to the extremely high reactivity of radicals there are several additional reactions taking place. Overall, this mechanism produces $OH^{\cdot}$ and $OOH^{\cdot}$ radicals and O_2 via the

cycling of Fe ions between +3 and +2 oxidation states. It is worth noting that this mechanism also leads to a gradual increase in pH. This general mechanism is expected to hold true for all Fenton chemistry catalysts, as the below reactions are not specific to Fe(III) and Fe(II) ions, but rather to a lower and a higher oxidation state metal ion in an oxide or oxyhydroxide lattice.

$$\equiv \mathrm{Fe^{III}} - \mathrm{OH} + \mathrm{H_2O_2} \rightleftharpoons (\mathrm{H_2O_2})_s \quad (11)$$

$$(\mathrm{H_2O_2})_s \rightleftharpoons (\equiv \mathrm{Fe^{II}} \cdot \mathrm{OOH}) + \mathrm{H_2O} \quad (12)$$

$$(\equiv \mathrm{Fe^{II}} \cdot \mathrm{OOH}) \rightarrow \equiv \mathrm{Fe^{II}} + \mathrm{OOH^{\cdot}} \quad (13)$$

$$\equiv \mathrm{Fe^{II}} + \mathrm{H_2O_2} \rightarrow \equiv \mathrm{Fe^{III}} - \mathrm{OH} + \mathrm{OH^{\cdot}} \quad (14)$$

$$\equiv \mathrm{Fe^{III}} - \mathrm{OH} + \mathrm{OOH^{\cdot}}/\mathrm{O_2^{\cdot -}} \rightarrow \equiv \mathrm{Fe^{II}} + \mathrm{H_2O}/\mathrm{OH^-} + \mathrm{O_2} \quad (15)$$

$$\mathrm{OH^{\cdot}} + \equiv \mathrm{Fe^{II}} \rightarrow \equiv \mathrm{Fe^{III}} - \mathrm{OH} \quad (16)$$

$$\mathrm{OH^{\cdot}} + (\mathrm{H_2O_2})_s \rightarrow \equiv \mathrm{Fe^{III}} - \mathrm{OH} + \mathrm{OOH^{\cdot}} + \mathrm{H_2O} \quad (17)$$

$$(\mathrm{H_2O_2})_s + \mathrm{OOH^{\cdot}}/\mathrm{O_2^{\cdot -}} \rightarrow \equiv \mathrm{Fe^{III}} - \mathrm{OH} + \mathrm{H_2O}/\mathrm{OH^-} + \mathrm{OH^{\cdot}} + \mathrm{O_2} \quad (18)$$

$$\mathrm{OOH^{\cdot}} + \mathrm{OOH^{\cdot}} \rightarrow (\mathrm{H_2O_2})_s + \mathrm{O_2} \quad (19)$$

$$\mathrm{OH^{\cdot}} + \mathrm{OOH^{\cdot}}/\mathrm{O_2^{\cdot -}} \rightarrow \mathrm{H_2O} + \mathrm{O_2} \quad (20)$$

$\equiv \mathrm{Fe}$: terminal Fe ion in a crystal lattice; $(\mathrm{H_2O_2})_s$: surface bound molecule;
$(\equiv \mathrm{Fe^{2+}} \cdot \mathrm{OOH})$: adduct of lattice Fe ion and hydroperoxyl radical

The most common substrate-specific reactions are additions of radicals and H abstractions, but the exact degradation pathway is going to be dependent on the model pollutant used in any experiment.

Overall two mechanisms have been identified through which Fenton and Fenton-like chemistry can proceed, homogeneous and heterogeneous (see equations (3) to (10) and (11) to (20), respectively). In reality there will always be a dominant pathway but both will be present since even in the case of heterogeneous catalysts there will be some amount of leached metal ions, which will facilitate the homogeneous reaction pathway. He *et al.* termed this heterogeneous catalysis induced homogeneous catalysis.

1.5 Carbonaceous Catalyst Supports

The industrialisation of heterogeneous catalysis started in the 19th century with processes like catalytic hydrogenation, the contact process for H_2SO_4 production, or later on

the Haber-Bosch process, and steam reforming of hydrocarbons. The first industrial heterogeneous catalysts were often single phase materials, either metals like Pt, or minerals like V oxides. With later discoveries, like Langmuir's theory of reactions through surface bound species, and Taylor's discovery of active sites, it became apparent that the most active part of a catalyst is its outermost atomic layer or layers. [20-21] A good example of how supported catalysts were developed can be seen in the history of the Sabatier process. [27] The first experimental catalysts used finely dispersed Ni, but this deactivated very quickly, and was pyrophoric, so it had to be prepared immediately before an experiment, which was not suitable for industrial usage. [28] This catalyst has become the target of intense research interest, which lead to a synthetic method for Ni/diatomite catalysts, and later a fully synthetic Ni/SiO_2 catalyst. [29–32] This almost century-long process showed how significant an impact a catalyst support can have on the overall performance of a catalyst, from smaller catalyst particles and by extension larger overall catalytically active surfaces to the emergent interface between catalyst and support, which can further enhance activity.

The most common choice for industrial catalyst supports have been aluminium oxides and silicates, since these are naturally abundant, cheap materials. But as the study of carbon materials advanced it was realized that they have a much larger degree of customizability, more elaborate surface morphologies and as a consequence the potential for much larger surface areas. In a 1998 review by Rodríguez-Reinoso *et al.*, the authors remark that although carbon science has been an established field for about two decades, the use of carbon as industrial catalyst supports and catalysts is still lacking, and their full potential has not been realised. [33] The authors also mention that the property that makes carbon supports more promising than oxidic supporting materials is that not only the surface topology, but also the surface chemistry can be tailored to fit the needs of the catalyst in question. The most important property of carbon materials that make them ideal supports is that the number and characteristics of their functional groups are widely customizable. Oxygen and nitrogen groups are the most important since these are the most common, but sulphur and halogenide groups are also present in some materials. From the viewpoint of this thesis, the most important properties of these materials are that the graphitic layers can facilitate the adsorption of organics, mainly through interaction between π-orbitals, while the terminal functional groups can anchor metal ions, and thus act as nucleation and crystal growth sites.

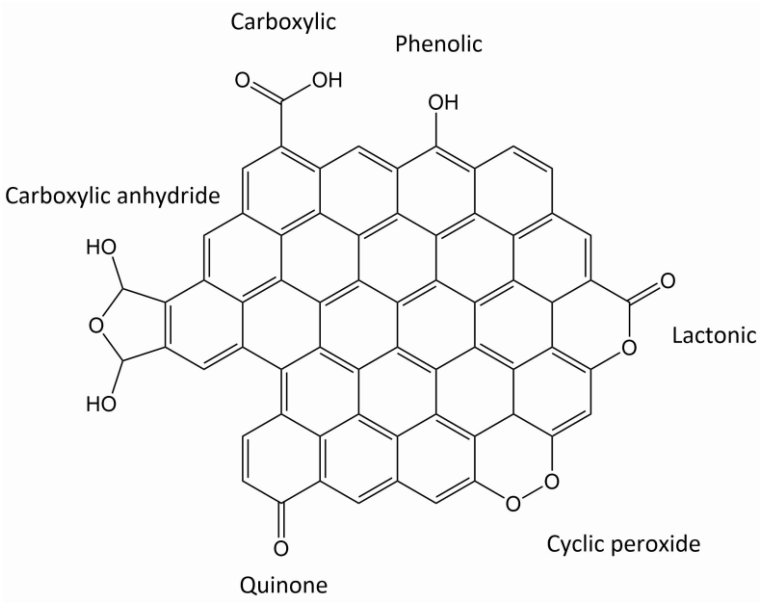

Figure 2 – Illustration of the most common terminal oxygen functional groups in carbon materials on a theoretical graphene nanoflake.

In the 2000s and 2010s carbon science have gone through an exponential growth, which translated into a huge increase in research interest surrounding carbon nanomaterials. For the first time companies around the world have been able to produce graphene-based materials, among them graphitic nanofibres (GNFs).

1.6 Oxygen Reduction Reaction (ORR)

The oxygen reduction reaction (ORR) is a very important process, both in biological, and technological systems, but owing to its radical intermediates, mechanistic studies were only possible after the discovery of electron spin resonance spectroscopy in 1944-45 by Yevgeny Zavoisky. [34] In the following decades intense research interest surrounded this topic, although the motivation was mainly to gain a deeper understanding of the cellular respiration step of photosynthesis. At this time the state of the art for studying ORR was to use Pt and Pd catalysts. By using such systems researchers established important kinetic and thermodynamic parameters, dependences on conditions, and some mechanistic understanding of the process. Damjanovic *et al.* established that ORR can generally proceed through two mechanisms on Pt catalysts: one leading to H_2O_2 and one to H_2O, but the intermediates and thus the exact mechanisms, were not fully elucidated. [30-31] Toda *et al.* published an article in 1999, which was the first to identify the correct mechanisms and intermediates of ORR on Pt. This also unlocked research into promoting one mechanism over the other. [37]

While noble metals have been found to be excellent catalysts of the ORR, this thesis aims to use non-noble metal catalysts. It was only during the 1970s that research into non-noble

metal oxide catalysts started in the context of oxygen reduction. The first significant articles of inorganic catalysts were published by King and Tseung, in which they studied the electrocatalytic activity of Co_2NiO_4 in oxygen reduction. [33-34] At this time this field was mostly interested in creating better cathode materials to be used in batteries, so even though the electrochemical reaction of interest was oxygen reduction, the preferred mechanism was the 4 e^- pathway. During the 2000s the interest in carbon supported non-noble metal and metal oxide ORR catalysts has been significantly increasing. [40] This especially increased after the rediscovery and full characterization of graphene, and the subsequent emergence of nanocarbon materials like nanotubes, nanofibers etc.

1.7 Summary

In summary, the work presented in this thesis is underpinned by the theoretical basis set out in the introduction above. More focused individual introductions will be given before the discussions of results in each chapter. The first chapter will examine the catalytic activity of Mn oxide – carbon nanofibre composites in Fenton-like chemistry, probing whether there is an emergent synergism between the support and the catalyst. This chapter also showcases the use of a metric that could improve the comparability between published results. The second chapter discusses the acid oxidation of macroscale carbon materials, with a thorough characterisation of the effect of such a treatment on surface morphology and chemistry. The resulting materials adsorption performance is also evaluated. The third chapter discusses the evaluation of carbon supported mixed metal oxide catalysts in Fenton-like chemistry. It starts off by describing the synthesis of mixed metal spinels, but also probes the suitability of the normal and acid oxidised carbon materials of the second chapter as catalyst supports. Finally, the catalytic activity of the resulting composite catalysts is evaluated. The fourth and final chapter discusses the electrocatalytic reduction of oxygen with the aim of promoting the production of H_2O_2 as the product of the process. Some carbon supported mixed metal oxide composites are evaluated as catalysts of this electrochemical process. To conclude, a summary is given of the results discussed in this chapter along with recommendations for future work in this project.

Chapter 2 - General experimental details

2.1 Chemicals

The water used in experiments of all chapters was produced internally. First, tap water is fed into an Elga Purelab Option-R15 which produces type II+ water, referred to as deionised water from this point onwards. [41] This water has a resistivity of 15 MΩ·cm. Feeding this deionised water through an Elga Purelab Flex purifier, type I water is obtained, which is referred to as ultrapure water from here on out. This ultrapure water has a resistivity of 18.2 MΩ·cm, and TOC content of 1 ppb.

The acetone used in all work presented in this thesis was purchased from Sigma-Aldrich, and it was of analytical purity.

2.2 Characterisation of Materials

2.2.1 X-ray Diffraction (XRD)

XRD analysis of Chapters 2-4 were done using a Bruker D2 Phaser instrument, the X-rays were generated from a Cu anode at 30.0 kV 10.0 mA using the Cu $K_{\alpha 1}$ emission. The XRD analysis of Chapter 4 was done using a Malvern Panalytical Aeris instrument, similarly using a Cu $K_{\alpha 1}$ analysing beam.

The crystallite size, defined as the lower limit of coherently diffracting crystalline domains, was estimated using the Scherrer-equation (see equation (21)). [42] The value of K was 0.9 as is customary when the FWHM of peaks is used as β instead of the integral breadth. [43]

$$\tau = \frac{K \cdot \lambda}{\beta \cdot \cos(\theta)} \tag{21}$$

where τ: lower limit for coherently diffracting crystalline domains, K: Scherrer-constant, λ: X-ray wavelength, β: FWHM of XRD peak, θ: Bragg angle.

The extent of instrumental line broadening was identified by recording XRD pattern of a corundum probe, illustrated by Figure 3 and Figure 5. The corundum probe's diffraction pattern is made up of doublet signals of 2:1 ratios, where the separation between the doublet peaks increases with 2θ. No additional data processing was done to remove the $K_{\alpha 2}$ peaks in the remainder of this thesis.

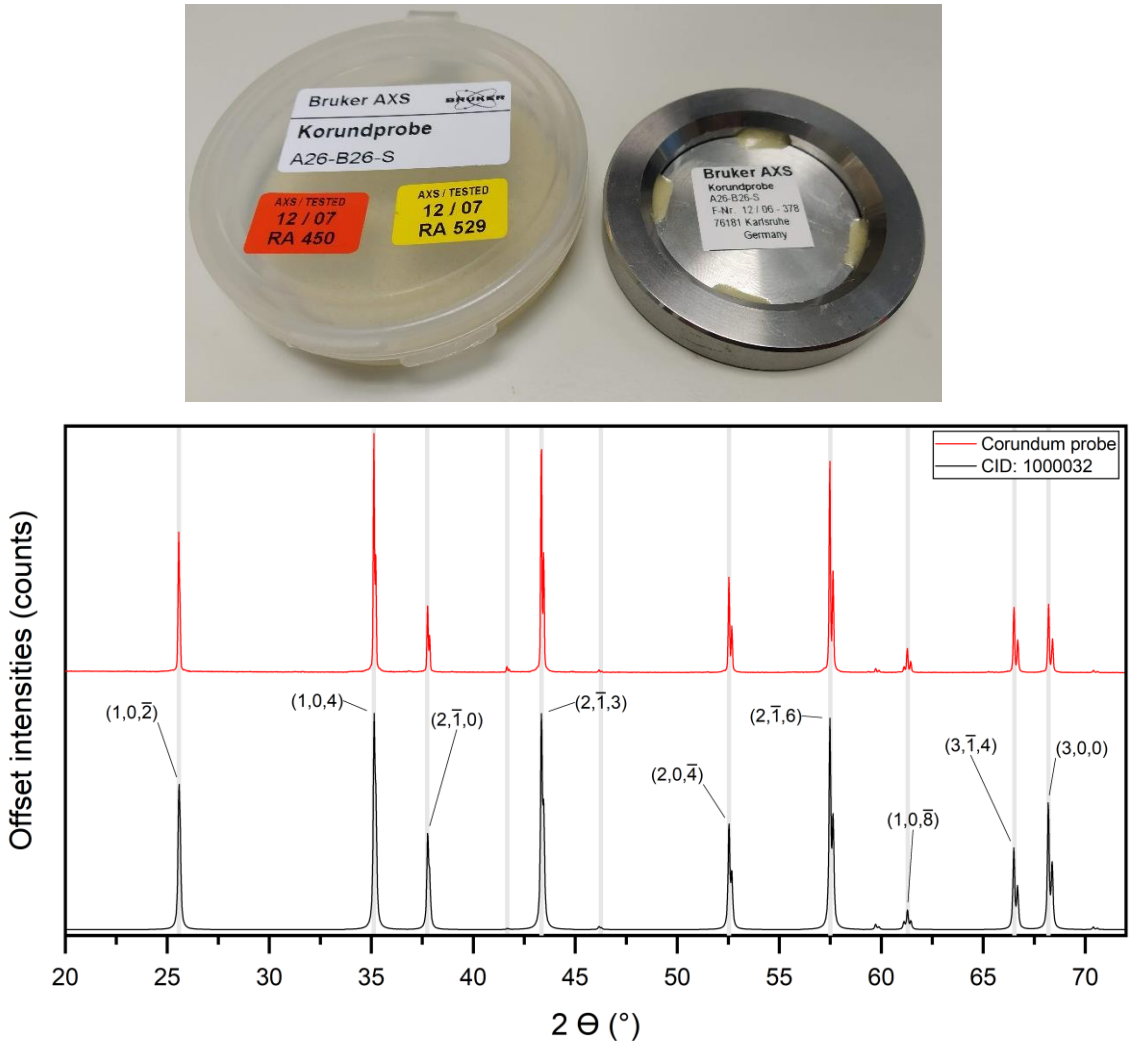

Figure 3 – Top: Image of corundum probe used in the identification of instrumental line broadening. Bottom: XRD pattern of corundum probe (red trace) against a simulated diffraction pattern (black trace) of the same materials. The simulated pattern was generated with both the Cu Kα1 and Cu Kα2 sources.

The line broadening of the corundum probe was determined at peaks originating from Cu $K_{\alpha 1}$ in the 2θ range of 30-60 °, since this range fits the diffraction patterns discussed in this thesis. The determined FWHM values are shown by Figure 4. The FWHM values in this range were averaged, which gives 0.07341.

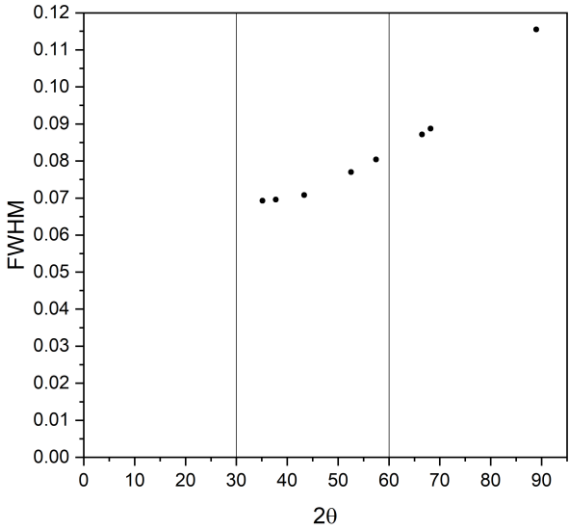

Figure 4 – FWHM values of corundum probe XRD peaks

This was taken to be the instrumental broadening in all measurements. For any sample this should be taken into consideration according to (22). [44]

$$\beta_{\text{total}}^2 = \beta_{\text{sample}}^2 + \beta_{\text{instrument}}^2 \tag{22}$$

To provide an example on how the instrumental broadening is taken into consideration, the diffraction pattern of a GNF sample is used (see Figure 5). In this case total line broadening was measured as 1.915, which means broadening due to the imperfections of the sample is 1.914. In any calculation including instrumental line broadening it is taken into consideration as described above.

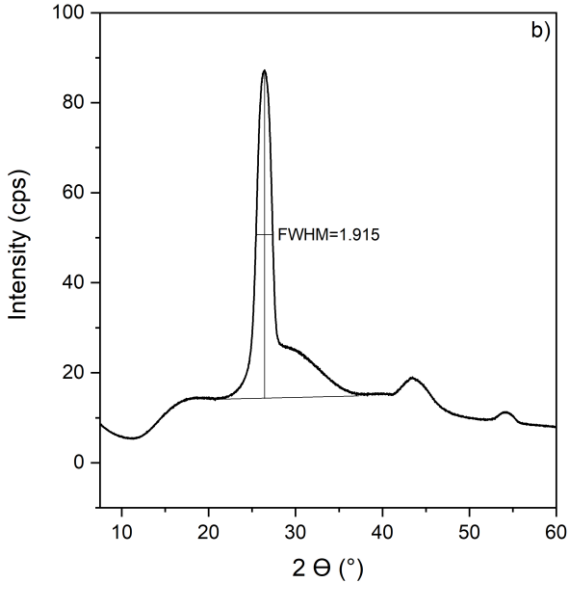

Figure 5 –XRD pattern of GNF including FWHM of the (002) peak.

Finally, an example is given as to how the Williamson-Hall method is used in this work to separate overall line broadening into size and strain contributions using the diffraction pattern of the corundum probe. [45] The line broadening originating from the sample is caused by size and strain effects of the crystallites, the former is inversely proportional to broadening, while the latter is linearly proportional to it as described by equations (23) and (24).

$$\beta_L = \frac{K \cdot \lambda}{L \cdot \cos\theta} \tag{23}$$

K=constant, λ=X-ray wavelength, L:mean linear dimension of particle, θ:Bragg-angle

$$\beta_\varepsilon = C \cdot \varepsilon \cdot \tan\theta \tag{24}$$

C=constant, ε:lattice strain, θ:Bragg-angle

If one considers the different broadening contributions to be simply additive, which is a common approach, (equation (25)), the above equations can be reorganised into an expression resembling the equation of a line (equation (26)).

$$\beta_{sample} = \beta_L + \beta_\varepsilon = C \cdot \varepsilon \cdot \sin\theta + \frac{K \cdot \lambda}{L} \tag{25}$$

$$\beta_{sample} \cdot \cos\theta = C \cdot \varepsilon \cdot \sin\theta + \frac{K \cdot \lambda}{L} \tag{26}$$

Figure 6 shows the so called Williamson-Hall plot gained by plotting $\beta_{sample} \cdot \cos\theta$ versus $\sin\theta$, the slope is equal to $C \cdot \varepsilon$, while the intercept to $\frac{K \cdot \lambda}{L}$. Both the slope and the intercept are very small meaning that crystallites are quite large, and the lattice strain negligible. The former observation is also supported by considering that the estimated crystallite size according to the Scherrer-method is 200 ± 40 nm in this case, which is a large value.

Neither the Scherrer nor the Williamson-Hall method will be used to gain definite values of crystallite sizes and lattice strains, but rather it will be used to compare similar materials.

2.2.2 Scanning Electron Microscopy (SEM)

SEM images were produced by Dr. Alexander Kulak, a Research Officer of the School of Chemistry, University of Leeds, using an FEI Quanta 650 instrument. This instrument is capable of recording energy dispersive X-ray (EDX) spectra with an Oxford Instruments INCA 350 detector, and images with an Everhart–Thornley detector (ETD) for secondary electrons (SE) and a concentric backscatter (CBS) detector for backscattered electrons. EDX spectra was used

for elemental analysis, SE images were used to study topography and morphology, while CBS images were used to highlight areas of different atomic numbers. All images in this thesis are SE images unless otherwise noted. Samples were mounted on high purity carbon tabs without any specific preparation. The tabs were then stuck to steel sample holder pins.

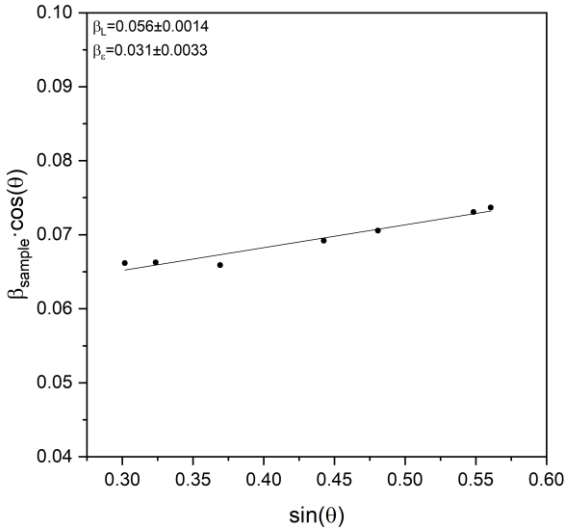

Figure 6 – Williamson-Hall plot for the corundum probe used in determining instrumental line broadening

2.2.3 Transmission Electron Microscopy (TEM)

TEM images were recorded using a FEI Titan3 Themis 300 instrument by Dr. Zabeada Aslam, a Research Officer of Leeds Electron Microscopy and Spectroscopy Centre (LEMaS), and images were analysed by the author. Samples were made into a very dilute slurry by first dispersing 2 mg of each in 5 mL IPA, homogenising by sonication, and then 100-fold dilution. The resulting liquid was dropcast onto lacey carbon covered sample holder chips.

2.2.4 N_2 Sorption Experiments

N_2 sorption experiments were done using a Micromeritics ASAP 2020 instrument operated by Dr. Alexander Kulak. Prior to the experiments the samples were dried at 120 °C for 2 hours under a flow of nitrogen. Surface areas and sorption isotherms were generated using BET theory. The macro-, and mesopore size distribution was analysed by applying the BJH method, while the contributions of micropores to the overall surface area was identified by applying the deBoer t-plot method. All dataanalysis was done with the instrument's software by the author. Samples were analysed as they were, without any specific preparation. Roughly 100 mg of each sample was loaded into the analysis vessel.

2.2.5 Thermogravimetric Analysis (TGA)

TGA experiments were done using a Waters SDT 650 instrument. First, all samples were heated to 120 °C over the course of 20 minutes. This temperature was held for 10 minutes to make sure all surface adsorbed water is removed. The samples were then heated to 900 °C at a rate of about 10 °C/min. The final temperature was held for another 10 minutes. Samples were analysed without any specific preparation. Roughly 5-10 mg of each sample was used in a measurement. All data was recorded and analysed by the author.

2.2.6 Raman Spectroscopy

Raman spectra were recorded by Dr. Alexander Kulak using a Horiba LabRAM HR Evolution Raman microscope with a 50 W 532 nm laser, passing through an edge filter. A hole size of 50 µm and laser powers of 1-10% were used. Samples were analysed without any specific preparation; a few mg was placed on a glass slide for analysis.

2.2.7 X-ray Photoelectron Spectroscopy (XPS)

XPS measurements were done using a UHV-XPS SPECS FLEXPES system which contains an Al K_α X-ray source of 1486.7 eV wavelength at a generating power of 400 W and a voltage of 15 kV. The pressure inside the analysis chamber was 10^{-9} mbar. The analysis spot size was 3.5 mm by 1 mm oval in all cases. The instrument is equipped with a SPECS Phoibos 150 hemispherical analyser with a 1D delay line detector. Slits were always fully open and all measurements were done in medium area mode. Survey spectra were done with a step size of 1 eV and a pass energy of 50 eV, while high resolution spectra were collected at 0.1 eV resolution with a 30 eV pass energy. All measurements were done with at least some charge neutralisation using a low energy electron flood gun. Samples were used without any further preparation. Experiments were carried out by the XPS Research Officer of the Bragg Centre for Materials Research at Leeds, Dr. Andrew Britton.

We acknowledge support from the Henry Royce Institute (EPSRC grants: EP/P022464/1, EP/R00661X/1), which funded the VXSF Facilities (https://engineering.leeds.ac.uk/vxsf) within the Bragg Centre for Materials Research at Leeds'.

The analysis of the results was done using CasaXPS. Deconvolution of XPS signals were done by adopting the exact peak parameters of other researchers. For example, the deconvolution of high resolution Mn 2p spectra were done by adopting the spectral fitting parameters of Biesinger *et al.*. [46] These authors have published detailed peak shapes, and

peak components of many binary oxides of transition metals, which can be used to differentiate between oxidation states. For example, when deconvoluting a high resolution Mn 2p spectrum it can be assumed that the oxidation states present are +2, +3 and +4 and so peak fittings of MnO, MnOOH and MnO_2 can be used to estimate the amount of each oxidation state in the sample.

The calibration of binding energies was done using published values of adventitious carbon C 1s peak shifts for certain types of materials, like metal oxides [47]. In the case of homologous materials, like an untreated carbon material and its acid oxidised version, the same exact peak parameters were used in order to enable comparison.

2.3 Assessment of Catalytic Activity

2.3.1 Kinetics

The catalytic performance of the prepared materials in Fenton-like chemistry was assessed through studying the kinetics and quantified removals of a model pollutant in batch reactions. In order to study kinetics, the rate of overall dye removal was used. To do this, the concentration of the dye was plotted against time. Any fittings of c(dye) vs time graphs are solely to aid the understanding of the reader, these graphs were not used in kinetic analysis. The rates of reactions were generated by plotting ln(c (dye)) vs time, where the slope of the resulting line is equal to the k value of the reaction.

2.3.2 Truly Catalytic Degradation

As the later chapters will discuss, the field of Fenton chemistry lacks a quantified metric that allows for easy comparison between different catalysts. To address this, the metrics of truly catalytic degradation and catalytic efficiency are proposed here. In order to define this metric, the assumption is made that the concentration of dyes in a degradation reaction mixture can only decrease through two modes: adsorption on the catalyst and degradation by ROS. Accordingly, the overall dye removal is separated into adsorption and truly catalytic dye removal contributions facilitated by a certain mass of the catalyst. These are calculated as set out by (27). This metric quantifies how much dye is actually degraded by a certain amount of the catalyst.

2.3.3 Catalytic Efficiency

The term catalytic efficiency has been defined to quantify the economy of H_2O_2 consumption needed to achieve any given truly catalytic dye removal. H_2O_2 consumption has been defined as the difference in H_2O_2 concentration between the starting point and end point of a degradation reaction, minus the amount of H_2O_2 decomposed without a catalyst present, divided by the amount of MnO_2 present in the catalyst (see (28)). The previously defined truly catalytic degradation is then divided by the H_2O_2 consumption. This metric quantifies the percentage of H_2O_2 consumption that is used to achieve a certain amount of truly catalytic degradation.

$$\begin{aligned}\text{Truly catalytic degradation (nmol/mg)} &= \text{Overall dye removal (nmol/mg)} - \\ \text{Adsorption capacity (nmol/mg)} &= \\ &\left(\frac{(c(\text{dye})_{t=0} - c(\text{dye})_{t=60}) \cdot V(\text{reaction mixture})}{m(\text{Composite catalyst})}\right)_{\text{Overall dye removal}} \\ &- \left(\frac{(c(\text{dye})_{t=0} - c(\text{dye})_{t=60}) \cdot V(\text{reaction mixture})}{m(\text{Composite catalyst})}\right)_{\text{adsorption}}\end{aligned} \tag{27}$$

$$\begin{aligned}H_2O_2\ \text{consumption}(\text{nmol/mg}) &= \left(\frac{c(H_2O_2)_{t=0} - c(H_2O_2)_{t=60}}{m(MnO_2\ \text{in composite})}\right)_{\text{dye degradation}} \\ &- \left(\frac{c(H_2O_2)_{t=0} - c(H_2O_2)_{t=60}}{m(MnO_2\ \text{in composite})}\right)_{\text{control without catalyst}}\end{aligned} \tag{28}$$

$$\begin{aligned}\text{Catalytic efficiency} &= \frac{\text{Truly catalytic degradation}}{\text{Hydrogen peroxide consumption}} \cdot 100 = \\ &\frac{\left(\frac{c(\text{dye})_{t=0} - c(\text{dye})_{t=60}}{m(MnO_2\ \text{in composite})}\right)_{\text{dye degradation}} - \left(\frac{c(\text{dye})_{t=0} - c(\text{dye})_{t=60}}{m(MnO_2\ \text{in composite})}\right)_{\text{adsorption}}}{\left(\frac{c(H_2O_2)_{t=0} - c(H_2O_2)_{t=60}}{m(MnO_2\ \text{in composite})}\right)_{\text{dye degradation}}} \cdot 100\end{aligned} \tag{29}$$

Chapter 3- Investigating the emergent synergism between a catalyst and its support in Fenton-like organics removal

3.1 Introduction

The work presented in this chapter is part of the wider field of AOPs using noble metal-free Fenton chemistry, so first an overview of the relevant literature is given. A broader introduction to Fenton chemistry has been given in the introduction chapter, but here a more technical introduction is given, specifically for the materials used. The most important criterion in choosing a Fenton catalyst is that the metal centre should be able to rapidly cycle between oxidation states. This can be done if the metal ion has a large number of unpaired valence electrons. It is also an important consideration that the metal ion should form stable compounds with the chosen chalcogenide, most commonly oxygen, at multiple oxidation states. These requirements identify the middle elements of the 3d row of the periodic table as ideal Fenton catalysts, especially Cr, Mn, Fe, Co, and Ni. In this chapter, the catalytically active component is not required to be novel as the focus is on the emergent synergism between the catalyst and the support. Therefore, MnO_2 was chosen, as it is cheap and its behaviour in Fenton-like chemistry is extensively researched, and well understood. A commercial, macroscale carbon support was used to form novel composite catalysts, with which the author aimed to make this work relevant for real life applications.

This chapter aims to contribute to the field of Fe-free, metal oxide catalysed Fenton-like chemistry by reporting the catalytic activity of a novel composite, probing the emergent synergism between the carbon support and the catalyst, and also by demonstrating a universal metric for the field.

3.2 Literature Review

3.2.1 Catalyst Synthesis

Many different crystal lattice types have been researched for transition metal oxides to be used in AOPs, including binary oxides, bimetallic oxides in spinel or perovskite lattices, or clays like layered double hydroxides.[48] For this chapter binary oxides of Mn are the most relevant, so only these will be discussed.

3.2.2 Synthesis and Physico-chemical Properties of MnO_2 Materials

When it comes to binary oxides, manganese has three main oxidation states, +2, +3, and +4. The +2 oxidation state is the most stable - it is the only one stable in solution as a hydrated ion - while the +3 and +4 oxidation states are only stable in complexes.[49] MnO_2 contains Mn(III) and Mn(IV) ions, the latter generally being dominant. The Mn ions are surrounded by the oxide ions in an octahedral geometry in MnO_2.

MnO_2 has four main polymorphs, α, β, γ, and δ, where the main difference is how the $[MnO_6]$ octahedra are connected.[50] The most relevant polymorph for this work is α-MnO_2, which is often also called hollandite-type MnO_2 after the natural mineral analogue. These materials have a general composition of $A^{+/2+}[M^{2+/3+}_xM^{4+}_{8-x}]O_{16}$, where x is generally below 3.[51] Hollandite-type Mn oxides can be further differentiated based on the counterion they contain, like Cryptomelane for $K(Mn^{3+}Mn^{4+}_7)O_{16}$, Hollandite $Ba(Mn^{3+}_2Mn^{4+}_6)O_{16}$, or Coronadite $Pb(Mn^{3+}_2Mn^{4+}_6)O_{16}$.[5–7]

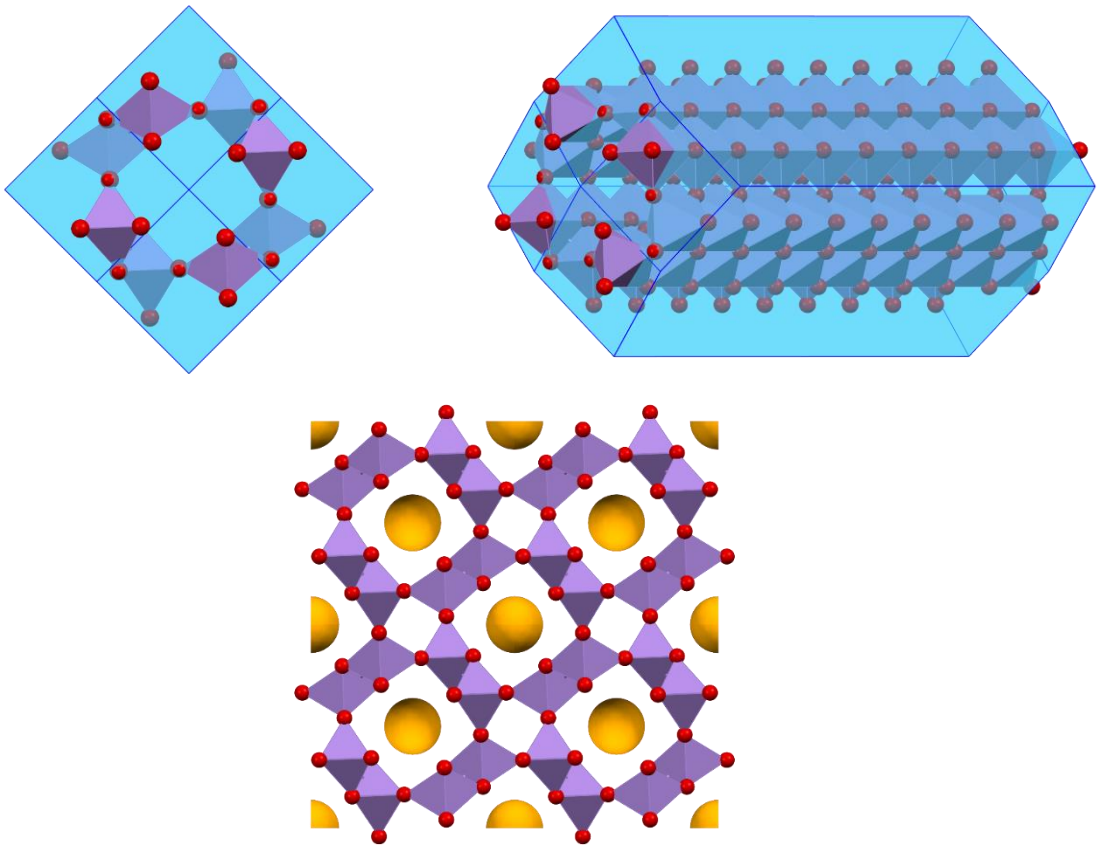

Figure 7 – Illustration of α-MnO_2 (CID:1514116) particle simulated using CCDC Mercury; **Top left:** view along c axis showing 2 × 2 tunnel structure; **Top right:** Rotated view of $[MnO_6]$ octahedra along a 2 x 2 tunnel; **Bottom:** Illustration of 2 x 2 tunnels occupied by counterions (orange).

Hollandite-type Mn oxides contain $[MnO_6]$ units in an edge-, or vertex-sharing configuration, which leads to the formation of 2 x 2 tunnels in the material, as illustrated by

Figure 7. Larger structures in hollandite-type Mn oxides are then made up of stacks of these 2 x 2 tunnels, which inevitably leads to 1 x 1 tunnels, as well. The 2 x 2 tunnels are roughly 460 pm wide, which is large enough to accommodate hydrated ions of up to about 140 pm in diameter, while the 1 x 1 tunnels are empty.[55]

Cryptomelanes have been extensively researched in the field of battery cathodes and supercapacitors, and although the present application is different, these articles can be used to illustrate the state of the art for the synthesis and physico-chemical properties of these materials.

The precipitation of MnO_2 is thermodynamically favoured, it is by far the most stable oxide in acidic media, and the most stable by a slight margin in alkaline media.[49] Most syntheses are thus using acidic conditions. The most common syntheses involve the oxidation of Mn(II), the synproportionation of Mn(II) and Mn(VII) and the disproportionation of Mn(VII), either at atmospheric pressure, or hydrothermally.[56–58] The most commonly used characterisation methods are XRD, Raman spectroscopy, electron microscopy, BET, TGA and XPS.

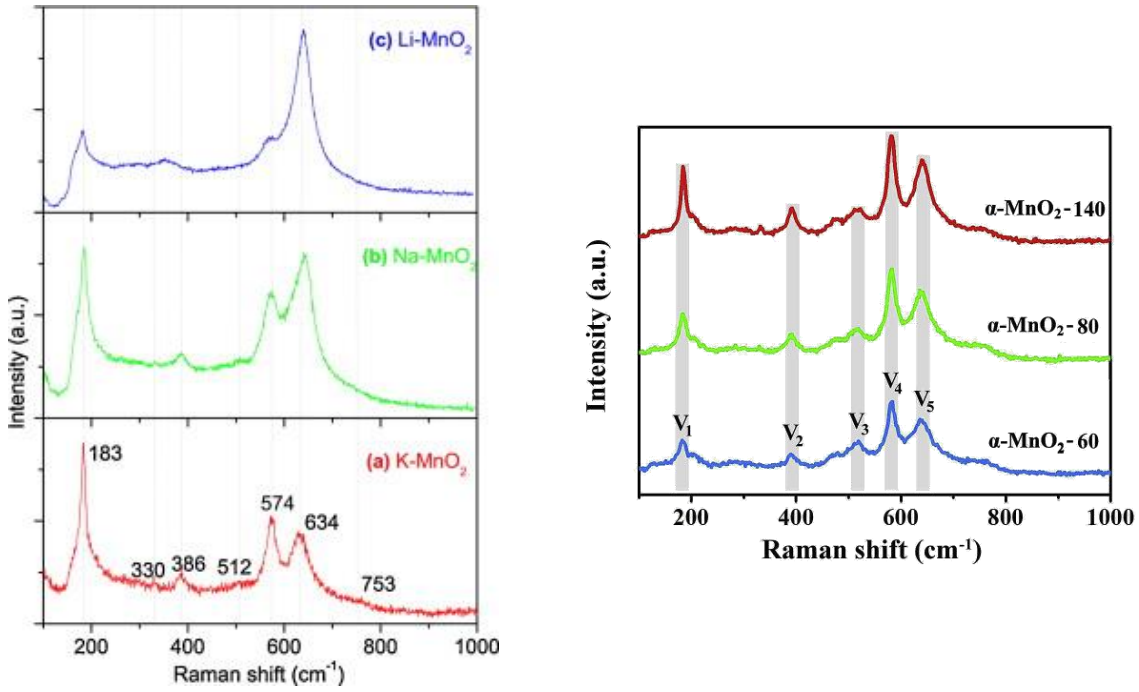

Figure 8 – Raman spectra of Cryptomelanes showing the influence of counterion (**left**), and temperature of hydrothermal treatment (**right**). Sources: Left: [57]; Right: [59]

Cryptomelanes tend to precipitate as 20-40 nm wide, roughly 500-2000 nm long needles, and these can then form larger urchin-like structures that have diameters in the few microns range.[50] In rare cases flat nanoflakes can also form.[60] These materials generally produce

sharp XRD peaks, due to large particle sizes and high crystallinity. The crystallinity of prepared materials can generally be increased by increasing the synthetic temperature or changing the ratio of reactants.[59]

The Raman spectra of Cryptomelanes can be used to confirm the identity of the counterion, and the Raman signal intensity is also very sensitive to crystallinity. The main Raman signals are illustrated by Figure 8; the most important are the peaks at about 580 and 635 cm^{-1}. The presence of these peaks has been associated with a well-developed tetragonal α-MnO_2 structure with a 2 x 2 tunnel, while the ratio of them can be used to identify the counterion. Researchers of the field have found that the surface area of MnO_2 materials is generally in the range of 20 to 200 m^2/g, but can be as large as 300 m^2/g, with the exact value being strongly dependent on crystallinity and the tunnel structure.[60][14-15] Cryptomelanes containing 2 x 2 tunnels tend to have surface areas of 70-90 m^2/g.[16–18] Thermogravimetric analysis of Cryptomelanes show extensive dehydration below about 400 °C, where water is initially removed from the surface, and then from the tunnels.[56][19-20] Further weight loss steps are due to thermal reduction to Mn_2O_3 and then to Mn_3O_4, with the former not always being clearly visible. Santos *et al.* also confirmed these thermal reduction steps via temperature-programmed desorption experiments where they often recorded multiple weight loss steps for the reduction to Mn_2O_3, as well.[58]

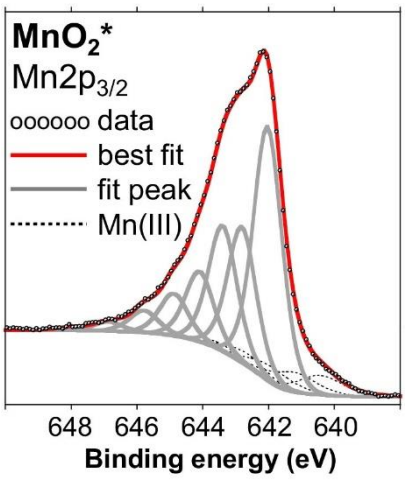

Source: [68]

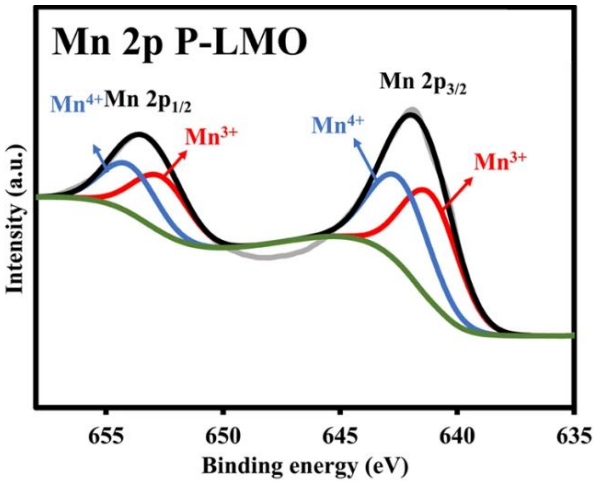

Source: [69]

Figure 9 – Deconvolutions of XPS spectra; **Left:** Correct deconvolution by Ilton *et al.*; **Right:** Incorrect deconvolution by Tomon *et al.*.

Studies of Cryptomelanes commonly use XPS in the characterisation of MnO_2 samples. The main XPS regions of interest are Mn 2p and O 1s; the former often being challenging to deconvolute due to the co-occurrence of multiple oxidation states. In addition to this, it can be

hard to find high quality publications with properly deconvoluted XPS data, including peak fitting parameters. Many researchers just fit a certain number of peaks under the envelope curve of XPS data, the number being equal to the number of expected oxidation states in the sample. In reality, multiplet splitting leads to several different energy levels for each oxidation state. Figure 9 shows an example of a correctly deconvoluted high resolution Mn 2p3/2 peak, and an incorrectly deconvoluted one.

When it comes to the analysis of high resolution O 1s spectra it is generally agreed by the field that the lowest binding energy, and usually dominant component of the peak is associated with lattice oxide ions, and is usually positioned at around 527 eV. It is also well understood that if there is a third peak at around 531 eV, this is due to the presence of hydroxide ions. There is less agreement about the assignment of the peak component between these two. In this work the deconvolution of high resolution O 1s spectra is based on the work of Biesinger *et al.*, who assign the middle peak to oxygen ions chemisorbed onto defective oxygen sites.[46] As such the middle peak is going to be treated as a proxy for oxygen vacancies.

There are other widely used practices that are heavily criticised, like using the C 1s peak of adventitious carbon to calibrate binding energies, since this can undergo a shift of 1-2 eV based on the sample type, and surface charging can increase it even further.[70] In this work the problem of binding energy calibration was solved by using publications from the journal Surface Science Spectra. Publications here contain very specific technical and spectral details of pure samples, including a recommended shift of binding energies, like it can be seen in the work of Militello and Gaarenstroom.[71] Nonetheless, in XPS data analysis, one should consider not just peak positions, but their shapes, and the magnitude of multiplet splittings. The analysis of XPS data should be done in light of the findings of other characterisation methods, as well. Fortunately MnO_2 is a widely studied material and so it is possible to find highly cited publications with peak fitting parameters, like those of Nesbitt and Baranjee, Ilton *et al.*, and Stranick.[68][26-27] In addition to this, the author has to mention that the XPS sections of this whole work would have been significantly more difficult, and lower quality had it not been for the work of B. Vincent Cris and Mark Biesinger, who created xpslibrary.com and xpsfitting.com, respectively.[28-29]

3.2.3 Composites

The most commonly used supports in materials science research are carbon materials, biochars, silica, and zeolites.[76] Only carbon materials are relevant for this work, so the others will not be discussed.

In the last decade or so, graphene-based materials have been the most popular choice of carbonaceous catalyst supports for MnO_2, especially nanotubes, nanofibers, graphene and its derivatives. As noted above, Cryptomelane forms relatively thin, long needles on its own, but this can be influenced with the use of carbon supports. Zhao *et al.* have prepared MnO_2 nanosheets made up of nanoneedles, which formed spikes on the surface of the support in the presence of N-doped CNTs (see Figure 10, left side).[77]

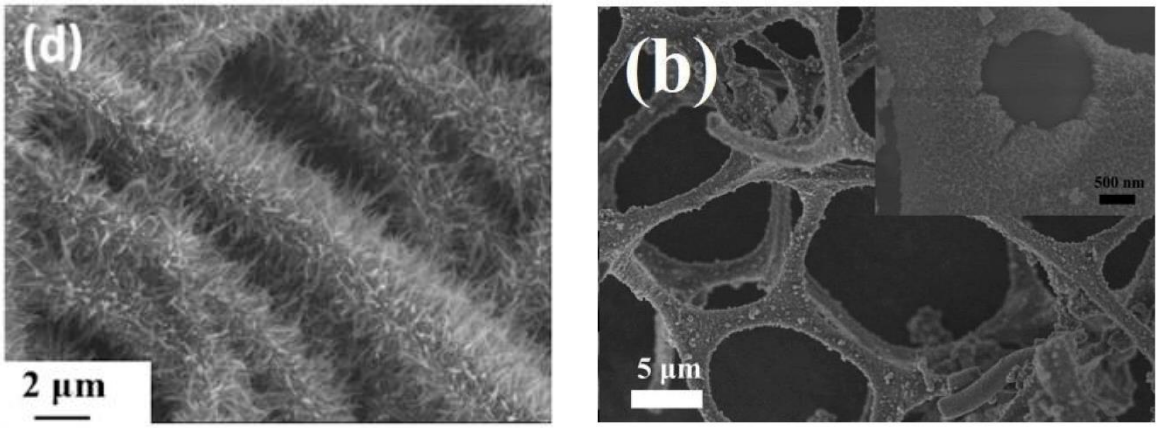

Source: [77] Source:[78]

Figure 10 – Electron micrographs showing typical morphologies of MnO_2-carbon nanofibre composites.

Similarly Ye *et al.* produced graphene supported MnO_2 which showcase a more even coverage of the metal oxide on the carbon fibres (see Figure 10, right side).[78] These morphologies represent the extremes in the literature, namely spikes versus an even nanosheet coating of MnO_2.

3.2.4 Dye Degradation

The research of MnO_2 as a functional material is a very active field with applications ranging from Fenton-like chemistry to supercapacitors.[33–35] Only Fenton-like chemistry is relevant for this work, so only this will be discussed.

The main reaction parameters that define a Fenton-like reaction is the choice of catalyst, oxidant and activation method. For this work, the most relevant of these are MnO_2 as catalyst, H_2O_2 as oxidant, and thermal activation[6].

The most common aim in the use of Fenton-like chemistry is to use the generated ROS to degrade organic pollutants in water. These radicals are extremely reactive towards organics, and generally don't introduce secondary pollution[7] into the reaction medium, so these are ideal oxidants. Accordingly, the most important characteristic of a Fenton-like catalyst is how quickly it can facilitate the removal of certain organics. Different organic compounds are degraded through different reaction pathways, but overall reaction mechanisms are similar in the case of the same oxidant and activation method.

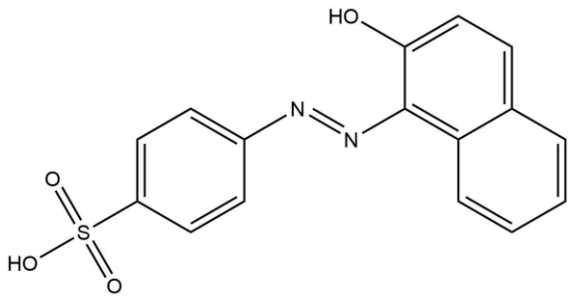

Figure 11 – Molecular structure of acid orange 7.

The assessment of catalytic activity in Fenton-like chemistry is most often done by monitoring the disappearance of a model pollutant. The model pollutant is most commonly a dye, since this way it is very simple to monitor its concentration via UV-Vis spectrometry. A survey of the literature indexed by Scopus shows that there are more than 60000 articles with the keywords 'dye degradation' (Scopus accessed on 2025.03.21.). The main classes of dyes are azo, anthraquinone and phthalocyanine.[82] When these are combined with the keywords 'dye degradation' there are 15000, 650, and 270 articles indexed by Scopus for azo, anthraquinone and phthalocyanine dyes respectively, which means azo dyes are by far the most researched. Since this work does not aim to elucidate new degradation mechanisms, the chosen model pollutant is acid orange 7 (AO7); its molecular structure is illustrated by Figure 11. There are more than 1000 articles published with the key words 'acid orange 7 degradation'. Such

[6] Thermal activation is used to refer to processes where the reactants overcome the activation energy barrier simply by possessing some kinetic energy due to the ambient temperature. Reactions were always done at room temperature.

[7] Secondary pollution refers to aqueous species generated as a result of normal operation of the catalyst. These can include metal ions originating from the catalyst, or degradation by-products originating from the oxidant.

published results were used to aid experimental design of this work. Since AO7 is so commonly used, its degradation pathway in Fenton chemistry is well-known. Zheng *et al.* have found that the first step in the degradation of AO7 is the cleavage of the azo-bond, which leads to the loss of colour.[83] It is important to keep in mind that while the loss of colour is what's monitored via UV-Vis, the overall degradation mechanism is far more complicated, and full removal of colour is not the same as full mineralisation of organics. Nonetheless, most researchers only use UV-Vis monitoring, as it is extremely easy to do, and it is a good proxy for catalytic performance. The most common approach to kinetic evaluation of dye degradation reactions is to assume that the disappearance of the dye follows pseudo-first order kinetics, for which the H_2O_2, and by extension the ROS have to be in large excess compared to the dye.[84] A more complete evaluation of dye degradation would involve using chromatography or total organic and inorganic carbon content measurements, where the former also allows researchers to probe the degradation mechanism.

One significant problem is that many researchers only use kinetic curves at different pH values, temperatures, concentrations etc. in characterising the performance of catalysts. Further, articles often omit crucial details that would allow comparison, like the composition of hybrid catalyst, or reaction parameters; often the only published metric of dye degradation is percentage removal. For any article to be a suitable comparison, the catalytic metal oxide, and the oxidant has to be the same, while it is crucial to know the catalyst loading, pH, and the catalyst concentration, dye concentration, and oxidant concentration used in the dye degradation. So while kinetics is an important aspect of catalytic performance, it would also be really important to quantify organics removal in some way to make results comparable. Nonetheless, considering the k values facilitated by different MnO_2 catalysts can be used to give a rough basis of comparison. Kim *et al.* have found that an α-MnO_2 catalyst of 48 ± 3 m^2/g surface area facilitates a rate of reaction of 0.030 ± 0.002 min^{-1}, when used at a concentration of 0.1 mg/mL, with 1.45 M H_2O_2 in the removal of 0.16 mM methylene blue.[85] Additional comparisons are made throughout this chapter for individual physico-chemical properties.

In summary, the field of Fenton chemistry still relies heavily on Fe-based catalysts which have significant drawbacks. This work focuses on Fe-free Fenton-like chemistry, specifically using MnO_2 as the catalyst, and H_2O_2 as the oxidant. This field has received considerable research attention since the discovery of Fenton chemistry in the 1870s, but major issues still remain that prevent wide-scale industrial application. One of the main issues is that there is no

single metric that researchers use to quantify organics removal, and so comparison between research outputs is challenging or even impossible. Additionally, not all aspects of Fenton-like chemistry are well understood, especially when it comes to emergent interactions between the catalyst and support in composite catalysts.

3.3 Experimental Details

3.3.1 Chemicals

$KMnO_4$ (>99% purity) was purchased from Sigma Aldrich, while concentrated H_2SO_4 (≥95%; analytical grade) was purchased from Fisher Scientific.

The carbon nanofibres used in these experiments were purchased from Applied Sciences Inc. (Cedarville, OH, United States). This line of products are collectively called Pyrograf III; there are multiple grades but the present work used PR-19-XT-HHT type.

Acid orange 7 (AO7, ≥85%) was purchased from Aldrich. The H_2O_2 solution (30% w/v) was purchased from Fischer Scientific, and it was stored in a refrigerator. $TiOSO_4$ solution (15% solution in dilute H_2SO_4) was purchased from Sigma Aldrich.

3.3.2 Methods

3.3.2.1 MnO_2 Synthesis

The synthesis of MnO_2 was done by adapting a procedure originally reported by Korošec *et al.*.[67] The first step of this procedure involves the preparation of an aqueous solution of $KMnO_4$ (3.2 mmol, 505.7 mg) in ultrapure water (36 mL), and the subsequent slow addition of H_2SO_4 (1.6 mL, 98%); this corresponds to a pH of 2.97. In the next step the solution is homogenised, and is then hydrothermally treated at 90 °C for 10 h. The resulting slurry was then separated from the supernatant via vacuum filtration, and washed with ultrapure water (3 x 50 mL), and then with acetone (3 x 50 mL). The wet solids were then dried in a vacuum oven overnight at 70 °C, 0.1 bar. The dried solids were gently ground using a mortar and pestle. This synthetic method produces a fine, dark brown powder (Yield: 268 ± 4.9 mg, 96 ± 1.8%). The synthetic method was optimised for the production of neat metal oxide and then used as is for the production of composites.

3.3.2.2 Composite Synthesis

Composites were made in two different ways: a) *ex situ* composites, where the neat metal oxide was co-sonicated with certain amounts of GNF, and b) *in situ* composites, where certain amounts of GNF were added to the synthetic mixture before the hydrothermal treatment.

Ex situ composites were made by mixing previously made MnO_2 with GNF in five different ratios, as laid out by Table 1. For example the catalyst of 84.6% loading was made by measuring out MnO_2 (25.0 mg), GNF (4.6 mg), mixing them in a sample vial, and then sonicating the closed sample vial in an ultrasound bath for 30 min.

Table 1 - Amounts of MnO_2 and GNF used in the preparation of *ex situ* composites

m(MnO_2) (mg)	**m(GNF) (mg)**	**Nominal loading of MnO_2 on GNF (%)**
25.0	455.0	5.2
	182.0	12.1
	45.4	35.5
	13.5	65.0
	4.6	84.6

In situ composites were made by adding different amounts of GNF to the synthetic mixture of MnO_2 in five different nominal loadings (see Table 2). These ratios were chosen to cover the whole range of loadings at reasonable intervals.

First a trial run of the synthesis was performed to see if ethanol can be used in this reaction mixture to aid the dispersion of the otherwise very hydrophobic GNFs. In this experiment a reaction mixture of $KMnO_4$ (505.7 mg), H_2SO_4 (1.6 mL cc.) and ultrapure water (36 mL) was prepared. After homogenisation 2 mL ethanol and 250 mg GNF was added. After this the mixture was homogenised again, sealed into a hydrothermal reactor and was heated to 90 °C for 10 h. The experiment was unsuccessful so ethanol or any other organic solvent was not used in further syntheses.

In the subsequent synthetic reactions the amount of $KMnO_4$, water and H_2SO_4 was always the same, since the most important internal factors determining the morphology and crystallographic form of the product are pH and how oxidising the reaction mixture is.[86] For example, the composite of 84.6% nominal loading was made by using 505.7 mg $KMnO_4$ and

50.6 mg GNF. The theoretical maximum yield of MnO_2 would be 278 mg, and assuming that all of the MnO_2 and GNF will be collected, this corresponds to a loading of 84.6%. Yields were above 85% in all cases.

Table 2 – Amounts of $KMnO_4$ and GNF used in the preparation of *in situ* composites

m($KMnO_4$) (mg)	**m(GNF) (mg)**	**Nominal loading of MnO_2 on GNF (%)**
505.7	5057.0	5.2
	2023.0	12.1
	505.7	35.5
	151.7	65.0
	50.6	84.6

Table 3 – Recorded yields of MnO_2-GNF composite syntheses

Catalyst loading (%)	**Yield (%)**	**Catalyst loading (%)**	**Yield (%)**
5.18	84.7	45.6	92.1
11.8	86.5	64.2	94.3
34.9	90.1	83.7	98.3

3.3.2.3 Dye Degradation Experiments

Dye degradation experiments were done by preparing a solution of AO7 (1.59 mL, 1.5 mM), H_2O_2 (7.5 mL, 30% m/V) and ultrapure water (32.5 mL). This mixture was prepared in a roundbottom flask, submerged in 18 °C water; both being simultaneously stirred at 600 rpm. After an initial homogenisation, a sample (800 µL) was taken and analysed via UV-Vis spectroscopy to determine the starting dye concentration. The catalyst was then added and further samples of the same volume as above were regularly taken. Right after the samples were taken, they were passed through a syringe filter with a 0.2 µm pore size hydrophilic PTFE filter and analysed via UV-Vis spectroscopy at 485 nm. Dye concentrations were calculated using a previously recorded calibration curve, shown by Supplementary figure 1. Catalyst concentrations were between 0.3 and 0.6 mg/mL.

3.3.2.4 Determination of H_2O_2 Concentration

Before using the $TiOSO_4$ solution, its concentration was determined via a novel method. A certain mass of the solution was put into a pre-weighed crucible with a lid, which was then heated up to 800 °C for 4 h. At this temperature $TiOSO_4$ turns into TiO_2 completely.[87] The mass of the crucible was measured again, and from this the amount of TiO_2 contained in it can be calculated, which in turn can be used to calculate the concentration of the original solution. The concentration of the $TiOSO_4$ solution was found to be 15.4 ± 0.25%.

H_2O_2 concentrations were determined via a titration method adapted from a publications by Eisenberg.[88] A sample of the reaction mixture (5 µL) is pipetted into a 10 mL volumetric

flask that already contains ultrapure water (about 2 mL), $TiOSO_4$ solution (100 µL, 15%), and H_2SO_4 (100 µL, 98%). The flask was filled to 10 mL, homogenised and a sample (800 µL) was pipetted into a quartz cuvette for UV-Vis analysis at 407.5 nm. Concentrations were calculated by using a calibration curve shown by Supplementary figure 2.

3.4 Discussion of Results

3.4.1 Metal Oxide Synthesis

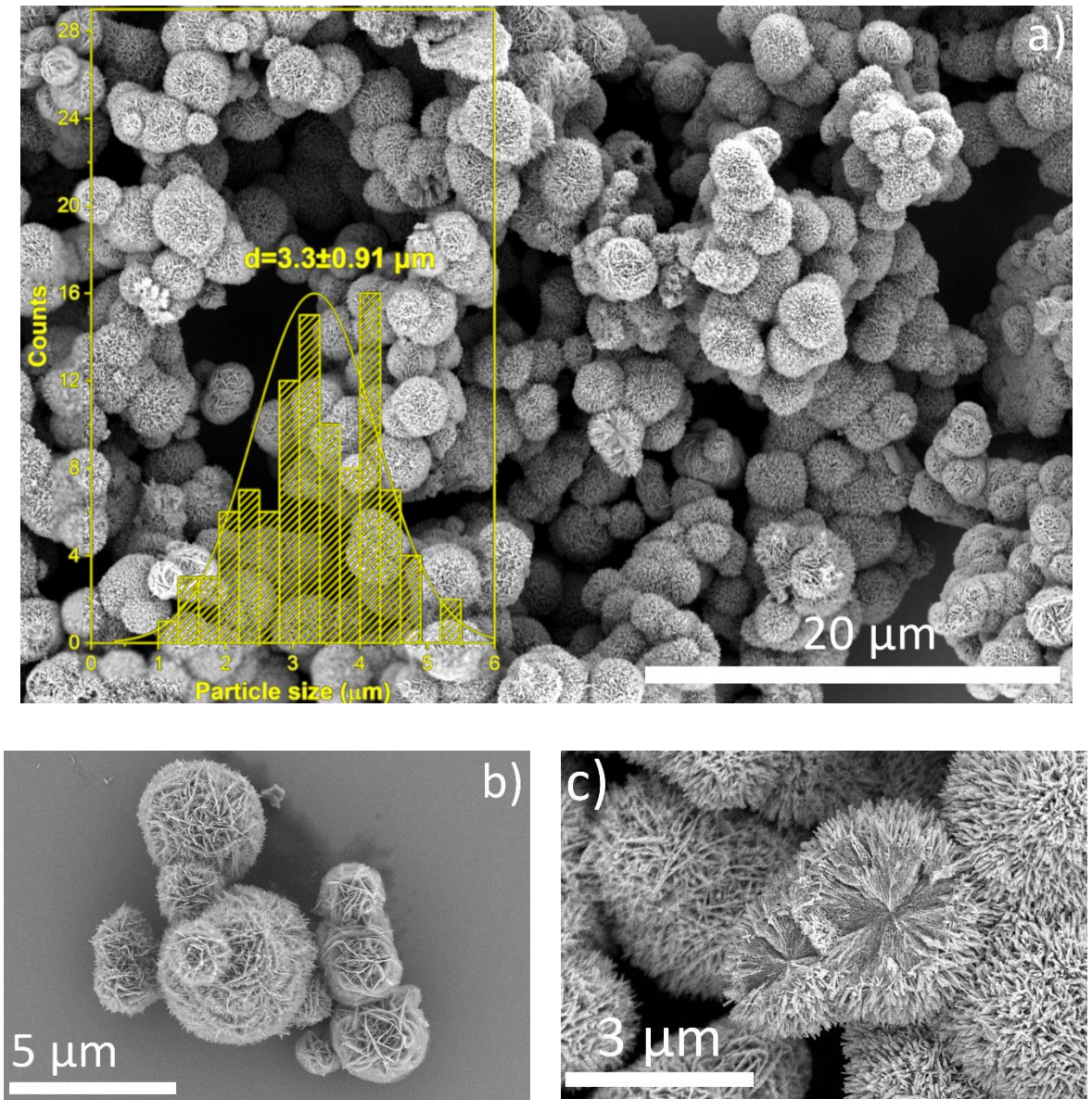

Figure 12 – SEM images of MnO_2 samples; **a:** Micrograph showing several particles and their size distribution; **b:** close-up of a few particles; **c:** close-up of internal structure of 2 particles.

The synthetic method published by Korošec *et al.* has previously been successfully used by this research group to prepare MnO_2. The authors of this synthetic procedure claim that this

method produces Cryptomelane type α-MnO_2 nanorods, with the commonly accepted molecular formula of $K(Mn^{3+},Mn^{4+})_8O_{16}$. In this material a small amount of the Mn(IV) ions is replaced by Mn(III) which leads to a negative charge balanced out by hydrated K^+ ions occupying the channels.

The hydrothermal synthesis was done in a stainless steel pressure reactor with a PTFE insert. The internal volume of the reactor is 36 mL. Due to safety concerns arising from heating a volatile liquid in an enclosed space it was only ever filled to 24.5 mL, which is 2/3 of the overall internal volume. The probable internal pressure of the reactor was estimated for risk assessment purposes before this line of work was started. It was found that the thermal decomposition of $KMnO_4$ contributes a negligible amount of O_2 gas to the vapour phase; roughly 4 mbar excess pressure. Accordingly the overall pressure was estimated as the saturated steam pressure at 90 °C, which is 700 mbar. This is well below the maximum pressure of 30 bar that the hydrothermal reactor is rated for. In many cases, the supernatant would have a very slight pinkish tint after the hydrothermal treatment which explains the less than 100% yield. This is probably due to the mild nature of the synthesis. According to SEM analysis the material is made up of large, urchin-like structures of 3.3 ± 0.9 µm diameter (see Figure 12). The nanorods on the outside of the particles are much larger and thicker than the ones on the inside. Nitrogen sorption experiments show that this material has a surface area of 76.0 ± 0.4 m^2/g, which is towards the higher end of published values for similar materials.[64][43-45]

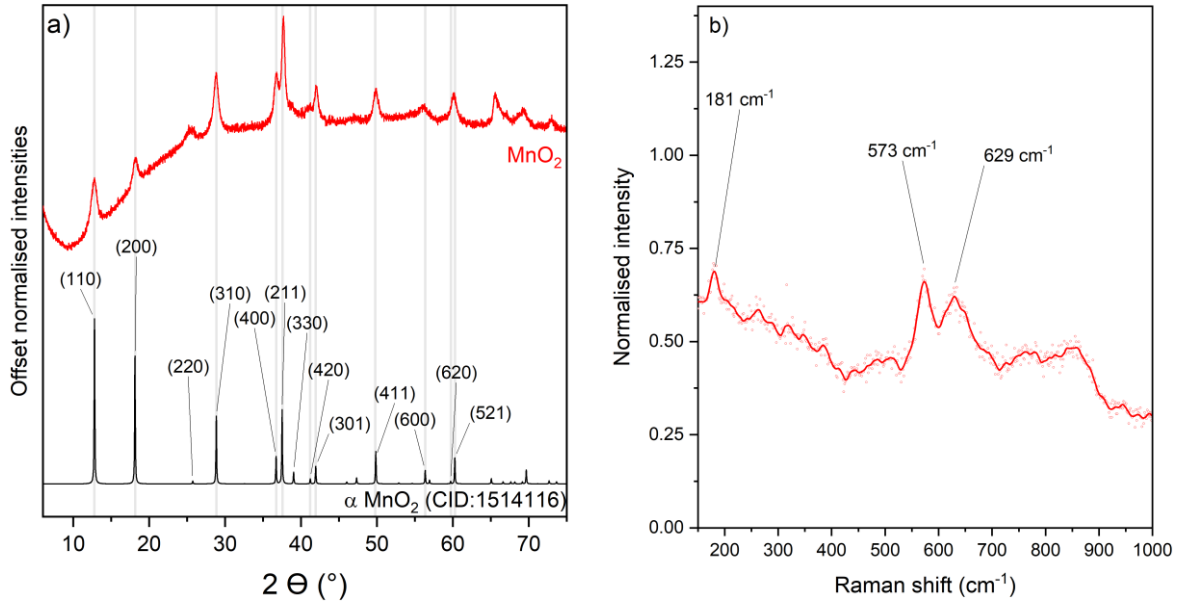

Figure 13 – **a:** XRD pattern of MnO_2 sample prepared via hydrothermal method. The black trace corresponds to a simulated reference diffractogram of an α-MnO_2, while the red trace to a MnO_2 sample; b: Raman spectrum of MnO_2 sample.

X-ray diffraction was used to identify the main phase of the produced material, by comparing it to a reference diffraction pattern for α-MnO_2 (see Figure 13a). The diffraction pattern of this sample matches the reference pattern of α-MnO_2 well. The peaks are broad and low intensity which is generally explained by either size and strain effects (i.e. small crystallite size, or high microstrain), or low crystallinity. The baseline of the recorded data is elevated due to the X-ray fluorescence of Mn ions in the sample. Two secondary analysis methods were used, the Scherrer-method and the Williamson-Hall method. The Scherrer-method is often used to estimate the size of coherently diffracting crystalline domains, which is a lower limit for particle size. This method is considered rudimentary at best, as it makes a number of assumptions, the two main ones being that particles are spherical and that peak broadening is entirely due to size effects. The Williamson-Hall method is best used with XRD data that is free of distortions, like X-ray fluorescence, and the data should be refined for best results. Considering these limitations, these secondary analysis methods provide tentative results, but this can still be useful in probing whether supporting the catalyst on GNF brings about any significant crystallographic changes. The results of secondary analysis will only be presented and discussed later in this chapter, along with the results of XRD analysis for the composites. Raman spectroscopy was also used to further characterise the sample (see Figure 13b). Without going into too much detail regarding the meaning of the peaks the MnO_2 sample was found to exhibit three main signals: 181, 573 and 629 cm^{-1}. This is in good agreement with previously published results. The low intensity of the peaks points towards low crystallinity, while the ratio of the 573 and 629 cm^{-1} peaks confirms that the counterion is potassium.[57]

Next, TGA analysis of MnO_2 was done, the results of which are shown on Figure 14. The positions and extents of observed weight loss steps are consistent with literature.[45-46] The steps below 500 °C correspond to removal of water, below 300 °C water is being removed from the external surface, while between 300 and 500 °C water is being removed from inside the 2 x 2 tunnels. The steps around 550 and 650 °C correspond to formation of Mn_2O_3, while the step at 850 °C corresponds to the formation of Mn_3O_4.[67] The formation of Mn_2O_3 oxide seems to happen in two steps, which is likely due to the involvement of different polymorphs of either MnO_2 or Mn_2O_3.[58] Overall, a very small mass loss was seen, which is typical of such metal oxides.

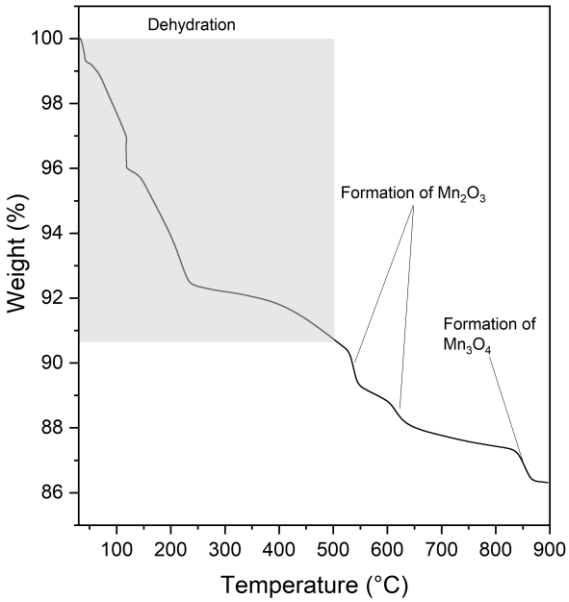

Figure 14 – TGA curve of MnO_2 sample with the identification of weight loss steps.

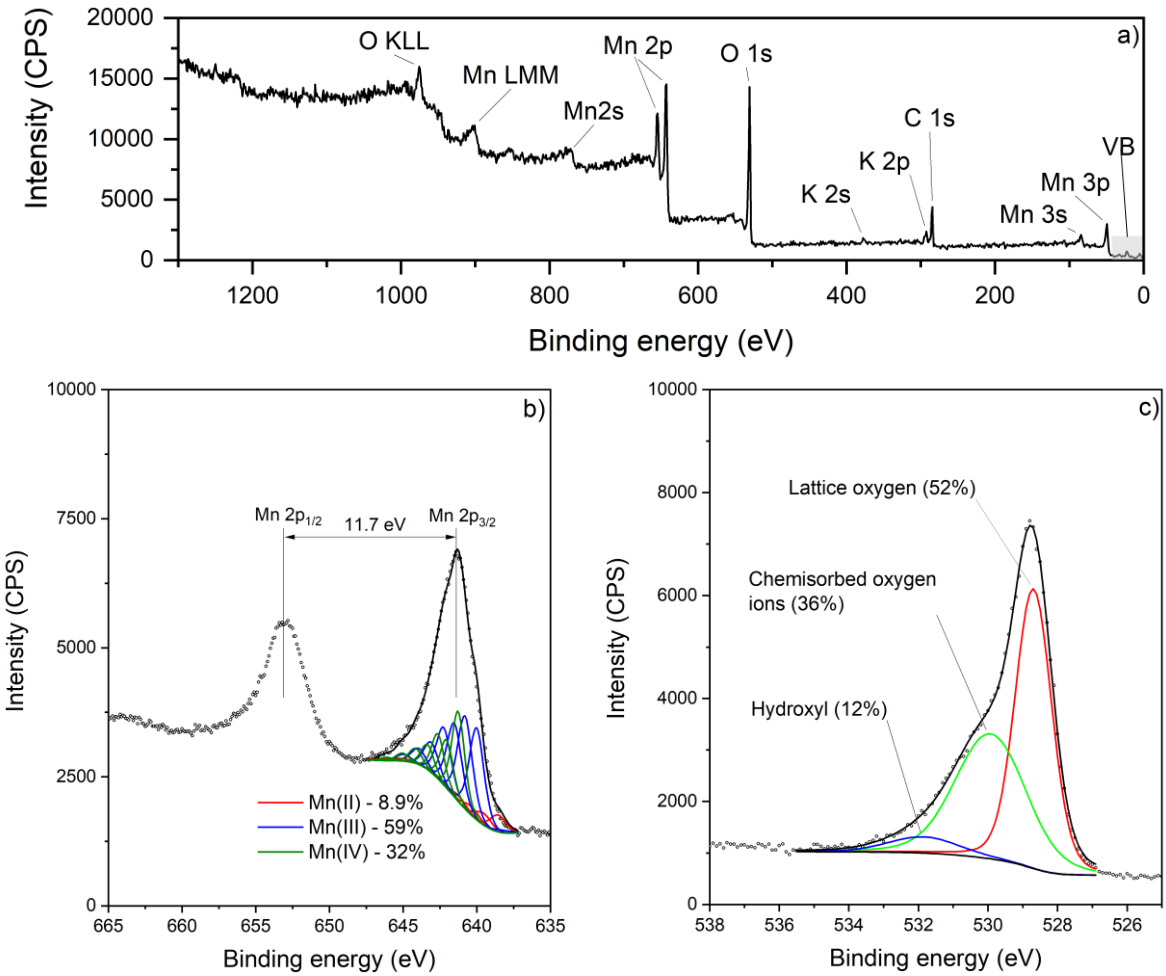

Figure 15 – XPS spectra of MnO_2 sample. **a:** Survey spectrum; **b:** High resolution spectrum of Mn2p region; **c:** High resolution spectrum of the O 1s region.

Finally, XPS was used to study the oxidation state distribution of metal and oxygen ions in the MnO_2 sample. The high resolution XPS spectrum of the Mn 2p region was deconvoluted according to Stranick, and Biesinger *et al.* (see Figure 15).[46][73] This analysis shows that the surface of the sample contains 59% Mn(III) which is significantly more than what would be expected for the bulk material. It has to be noted that the analysis depth of XPS is roughly 5-10 nm, so this analysis only describes an external layer. Further analysis of XPS data also shows that the splitting in the Mn 2p doublet is 11.7 eV, which is in accordance with values published for α-MnO_2 samples.[73][92] The presence of 9.9% potassium indicates that the sample is a Cryptomelane type α-MnO_2. This potassium content is in good agreement with values published by the original authors of the synthetic method that was adapted for this work.

The high resolution O 1s spectrum shows a large number of what is termed chemisorbed oxygen ions here. This peak has received many names in the literature, but it is generally used as a proxy for oxygen vacancies. Hou *et al.* have found that high surface Mn(III) content in MnO_2 samples can be associated to a large number of oxygen vacancies being present, which would explain the simultaneously high Mn(III) and chemisorbed oxygen ion content.[93] All of the above are consistent with published details of Cryptomelane-type α-MnO_2 materials.[49–51]

3.4.2 GNF

Samples of GNF were characterised using a variety of methods from bulk to atomic. These materials are made from natural gas, using an FeS catalyst, and the resulting nanofibres and graphitised at 3000 °C. According to the producer this material is made up of fibres of 70-200 nm diameter, and 30-100 µm length, with a surface area of 20-30 m^2/g.[97] In this chapter only analysis relevant to the present results will be discussed.

3.4.2.1 Electron Microscopy

Electron microscopy analysis shows that the material is mostly made up of long, thin fibres but also contains some undefined particles and fibres with excessive distortions (see Figure 16a,b). The latter has been deemed a side-product of synthesis, and is likely a mass of amorphous carbon. The fibres have a diameter of 148 ± 70 nm; their length could not be determined. The observed diameter is in good agreement with dimensions claimed by the producer. Figure 16c shows a TEM image of GNF, which shows that each fibre has an internal stacked cup structure, and an external sheath. Accordingly the interior of the fibres contain a

sawtooth-like surface with step edges, while the exterior is smooth. The structure of GNF will be discussed in much greater depth in Chapter 2.

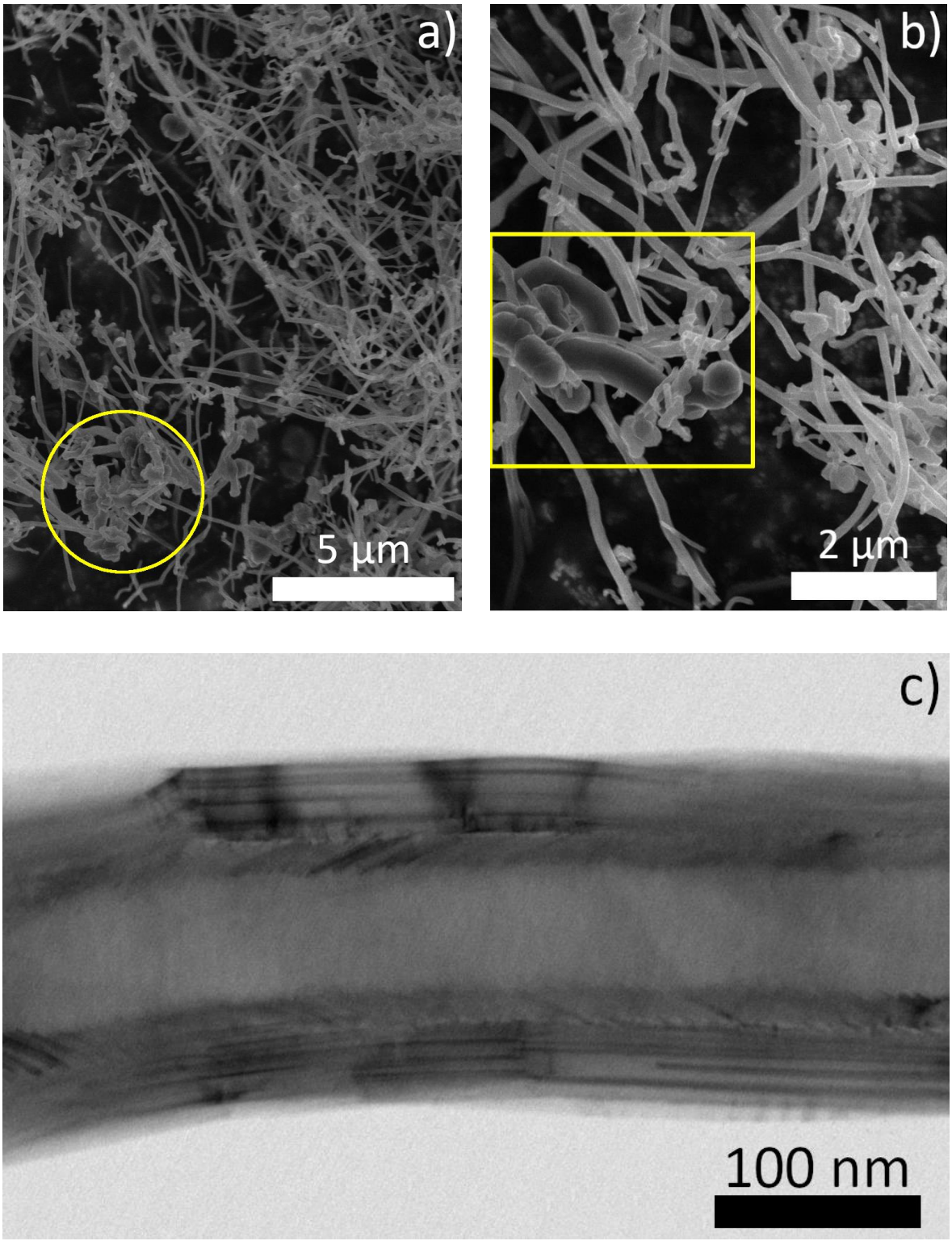

Figure 16 – Electron microscope images of GNF samples; **a,b:** SEM images of GNF, with amorphous particle highlighted; **c:** TEM image of an individual GNF particle.

3.4.2.2 Bulk Characterisation

While the characterisation of a commercial sample is not very interesting in itself, in-depth bulk analysis of GNF will be presented here, to serve as a comparison for later chapters. At first glance, XRD analysis of GNF indicates relatively high graphiticity as illustrated by Figure 17, but peaks are broader than it would be expected for a highly ordered graphitic carbon which points towards lattice distortions. The most important signal is the intense peak originating from the (002) atomic plane at 26.4 °. This peak is relatively broad for a graphitic carbon; it corresponds to apparent lattice spacings of 0.36 to 0.32 nm, with the maximum of the peak corresponding to an interatomic spacing of 0.34 nm.

There are some differences between the reference and the measured XRD pattern, which can be explained by considering the potential distortion factors that differentiate GNF from an ideal graphite sample. According to Li *et al.* the most important distortion factors in graphitic nanofibres are rotation, translation, and the curvature of the graphitic layers in the material.[98] All three of these are inherently present in GNF due to the geometry of the graphitic layers that make up a fibre.

The diffractogram shows two broad peaks, designated with one and two asterisks that are difficult to assign due to their low intensity. These could either be minor populations of graphitic layers with excessive distortions or they could also arise from the large undefined particles shown by electron micrographs. No further analysis of these secondary peaks was done, as these are unlikely to originate from the fibres that make up the bulk of the material.

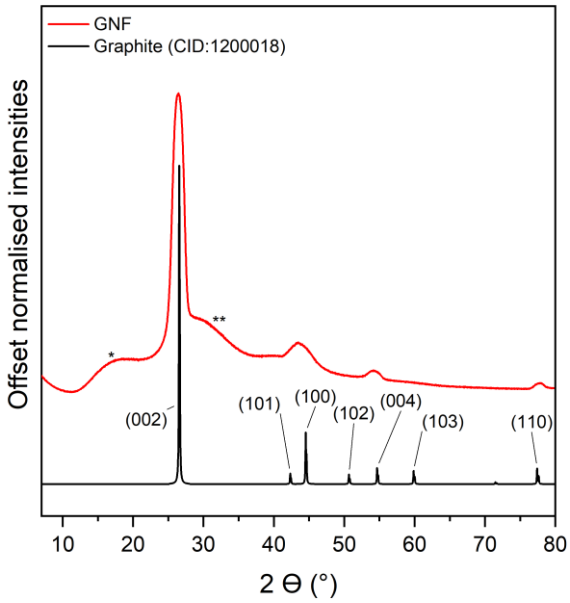

Figure 17 – XRD pattern of GNF along with a graphite reference pattern (CID:1200018).

In order to study the morphology and porosity of the fibres N_2 sorption was used, the results of which are illustrated by Figure 18. The surface area of GNF is 10.3 ± 0.1 m^2/g, and the isotherm is consistent with a non-porous material. This is in good agreement with the structure of these fibres as shown by electron microscopy. The BET surface area is lower than the 20-30 m^2/g range the producer claims, and is quite low in general for a carbon material.[99] Other researchers using the same material have reported surface areas in the 15-25 m^2/g range.[55–57]

GNF samples were also characterised by TGA (see Figure 18b). The onset temperature is in line with highly graphitic carbon materials, but otherwise the graph shows no features.[103]

3.4.3 MnO_2-GNF Composites

3.4.3.1 Bulk Characterisation

The above synthetic method was planned to be used to produce both neat MnO_2 and MnO_2-GNF composites. In order to facilitate comparability between these two types of syntheses, identical parameters were planned to be used in both.

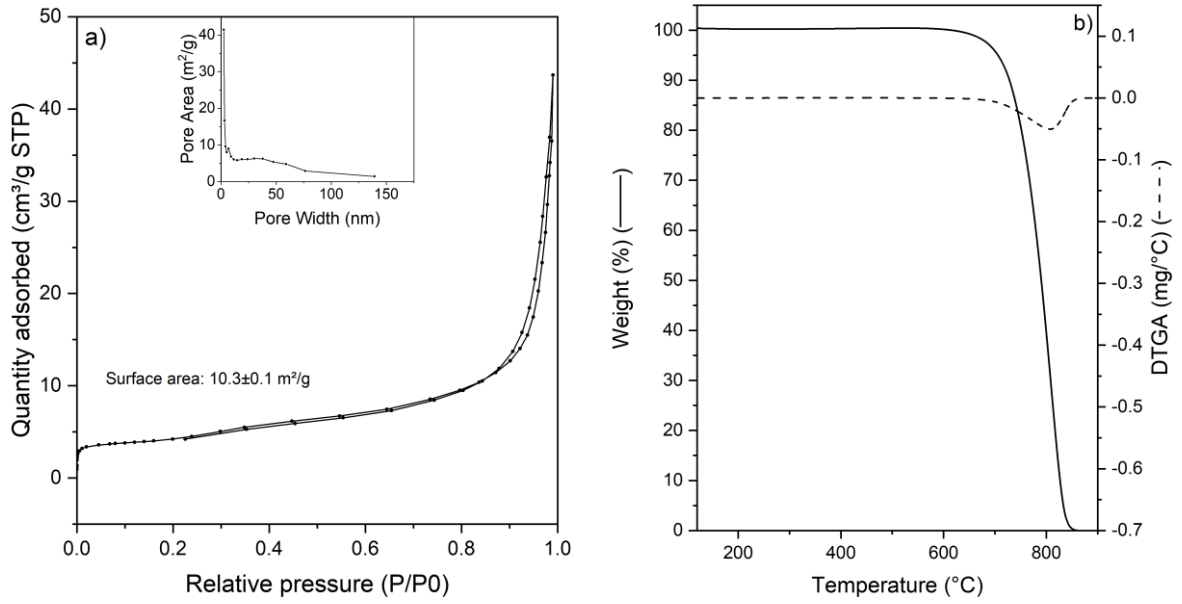

Figure 18 – **a:** Results of N_2 sorption experiments for GNF fitted with a curve via the BET model; **b:** TGA curve for GNF

The synthetic mixture was initially planned to include a small amount of ethanol in the reaction mixture in order to better disperse the otherwise very hydrophobic GNF, but the use of organic solvents proved problematic, since organic solvents react with $KMnO_4$ under these circumstances.

$$4\ KMnO_4 + 5\ CH_3CH_2OH + 6\ H_2SO_4 = 2\ K_2SO_4 + 4\ MnSO_4 + 5\ CH_3COOH + 11\ H_2O \quad (30)$$

$$2\ KMnO_4 + 3\ MnSO_4 + 2\ H_2O = 5\ MnO_2 + K_2SO_4 + 2\ H_2SO_4 \quad (31)$$

$$MnO_2 + 2\ H_2SO_4 = O_2 + 2\ MnSO_4 + 2\ H_2O \quad (32)$$

Bojler eladó!

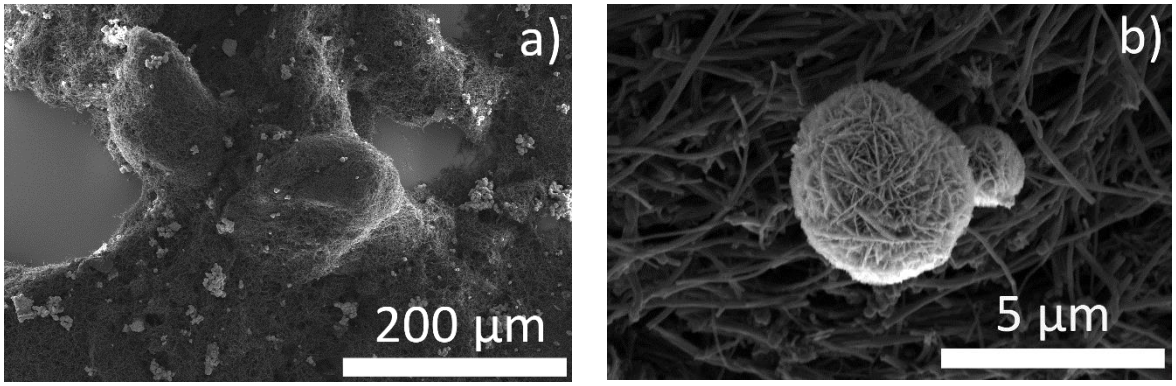

Figure 19 – SEM images of *ex situ* MnO_2-GNF composites; **a:** Overview of *ex situ* composite of 34.9% loading; **b:** Close-up of *ex situ* composite of 34.9% loading.

When ethanol was used, the reaction mixture came out completely clear after the hydrothermal step. Equations (30) - (32) describe what likely happened. Since the reaction mixture included a large excess of both sulphuric acid and ethanol, presumably all of the Mn has been transformed into $MnSO_4$. Due to this problem no organic solvent was used to disperse the GNF, and 5 min of sonication was used for the same purpose, instead. These synthetic approaches were chosen in order to isolate any potential emergent synergistic effects.

Composite samples were imaged using electron microscopy which reveals a large difference in the degree of dispersion between the two composite types. In the case of the *ex situ* composites, the support merely physically disperses the already formed, large catalyst particles (see Figure 19). In the case of the *in situ* composite, large aspect ratio nanoneedles are dispersed along the fibres. Figure 20c shows a representative *in situ* composite particle, which describes all other recorded images well. No catalyst particles were found that were definitely positioned on the inside of the fibre. The main indication of this would be catalyst particles perfectly lining up with the internal sawtooth-like surface of the fibre.

XRD analysis shows that the characteristic peaks of MnO_2 and GNF are visible in accordance with their ratio in the case of both *in situ* and *ex situ* composites (see Figure 21). Results of secondary analysis for the XRD data of both composite types can be seen on Supplementary figure 3. Results of both the Scherrer and Williamson-Hall analysis show large variations, which is due to the interference of X-ray fluorescence. Nonetheless these results

show no difference in terms of either crystallite size or microstrain between the unsupported catalyst and the composites.

The makeup of *in situ* composites was further analysed via TGA, which showed a good agreement between the expected and real composition, as illustrated by Figure 22a-b. In the case of 34.9, 64.2, and 83.7% loadings, where the average difference was 0.1%. In the case of 11.8 and 5.2% loadings the difference was 7.2 and 3.0% respectively. This is most likely due to how these were made. The synthetic mixtures of these included 5 and 2 g of GNF, which is a very large amount in terms of volume; 5 g of GNF filled up the entire reactor and soaked up all of the reaction mixture.

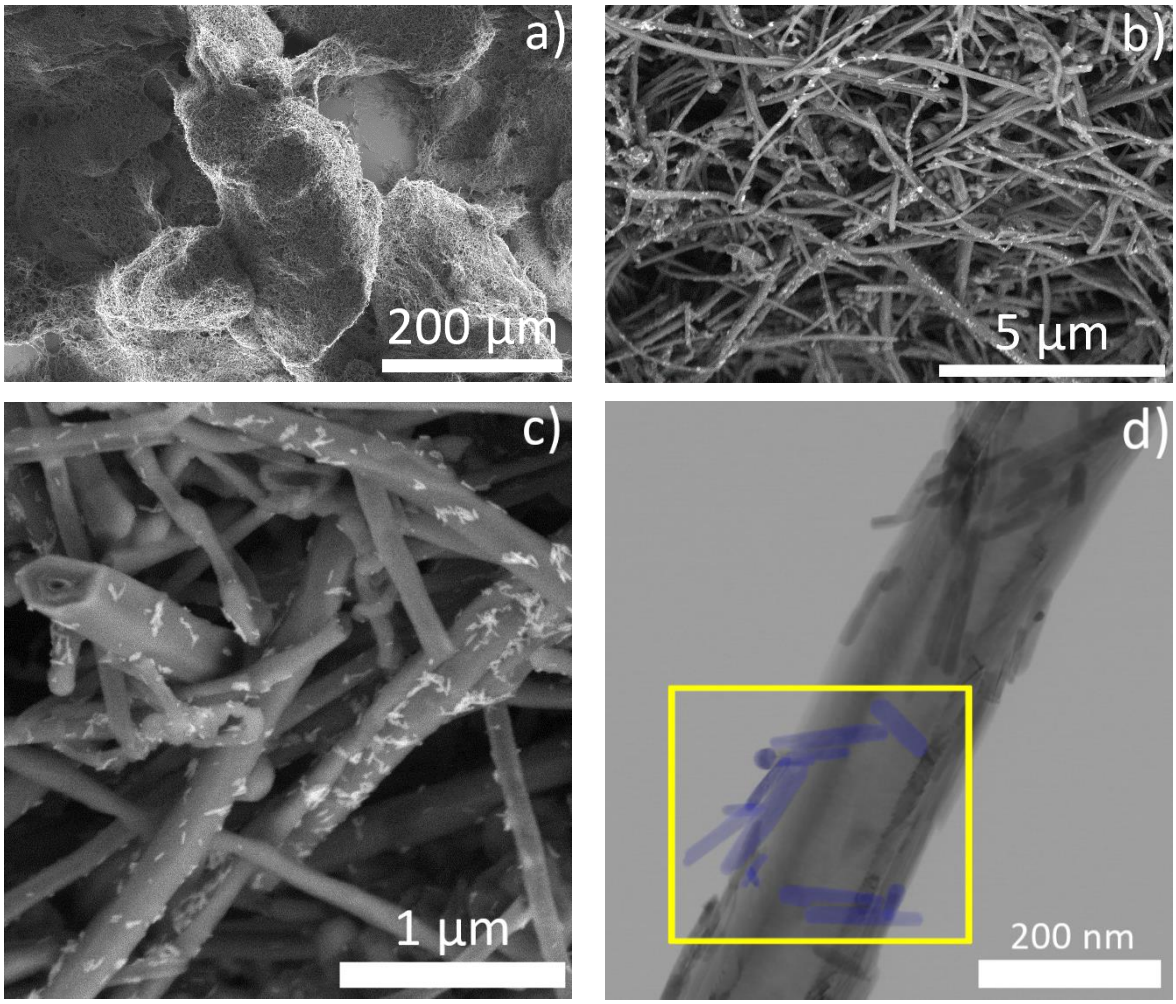

Figure 20 – Electron micrographs of *in situ* MnO_2-GNF composite of 34.9% MnO_2 loading; **a,b,c:** SEM images of large numbers of fibres showing high degree of dispersion of MnO_2; **d:** TEM image of an individual fibre with catalyst particles highlighted in a small section of the image.

Accordingly, this relatively large discrepancy between the expected and real composition is most likely due to inhomogeneous precipitation of MnO_2 particles. Normally this wouldn't be a problem as product batches are homogenised after synthesis but in this case due to the fibrous nature of GNF homogenisation was evidently not as successful.

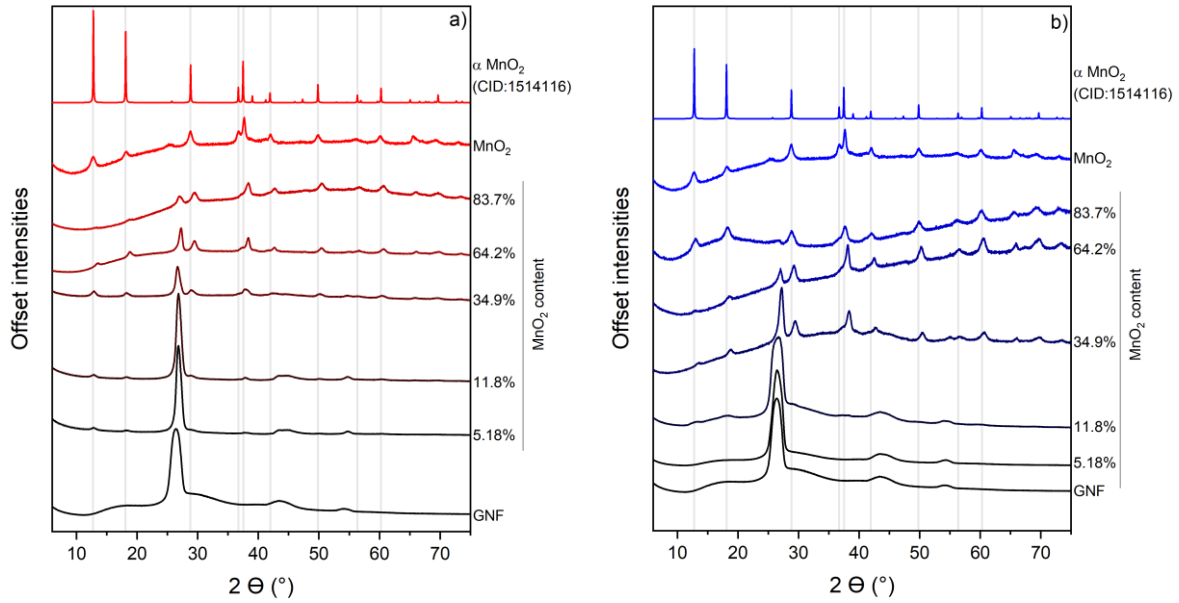

Figure 21 – XRD patterns of MnO_2 composites; **a:** *ex situ* composites; b: *in situ* composites.

Finally, the composites were characterised by N_2 sorption experiments. The measured surface areas are between that of pure MnO_2 and pure GNF. The trend is roughly linear, although some composites deviate from a purely linear trend.

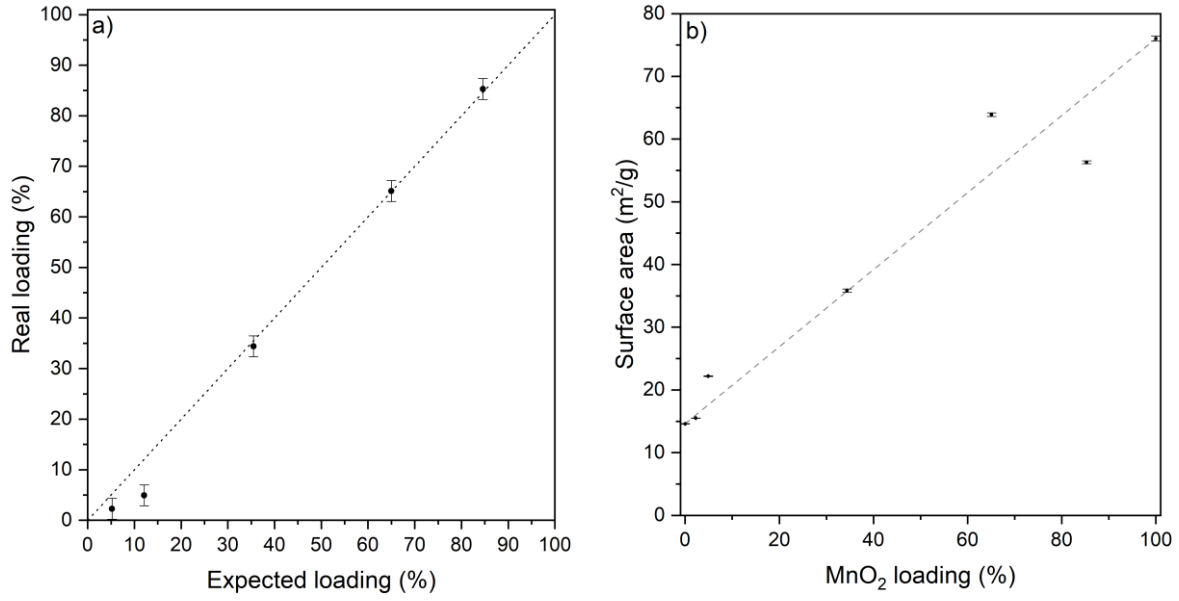

Figure 22 – Results of bulk characterisation for *in situ* MnO_2-GNF composites; **a:** Real loadings versus expected loadings for *in situ* MnO_2-GNF composites, calculated from TGA data; **b:** Surface areas measured via N_2 sorption.

3.4.3.2 XPS Analysis

Similarly to neat MnO_2, an *in situ* composite has also been analysed using XPS in order to study its chemical state (see Figure 23). The survey spectrum shows no unexpected peaks, only those associated with the components of the catalyst. As Figure 23b shows, there are some noteworthy differences between this spectrum and that of the MnO_2 sample. The Mn ions

seems to be in a generally higher oxidation state. There is a negligible amount of Mn(II), ions, slightly less Mn(III) ions and significantly more Mn(IV) ion in this case than what was seen for the unsupported MnO_2. The O 1s spectrum also shows more lattice oxygen and less hydroxyl oxygen in the case of the composite versus the unsupported catalyst. All of the above points towards the catalyst being in a more crystalline state, and of a higher overall oxidation state.

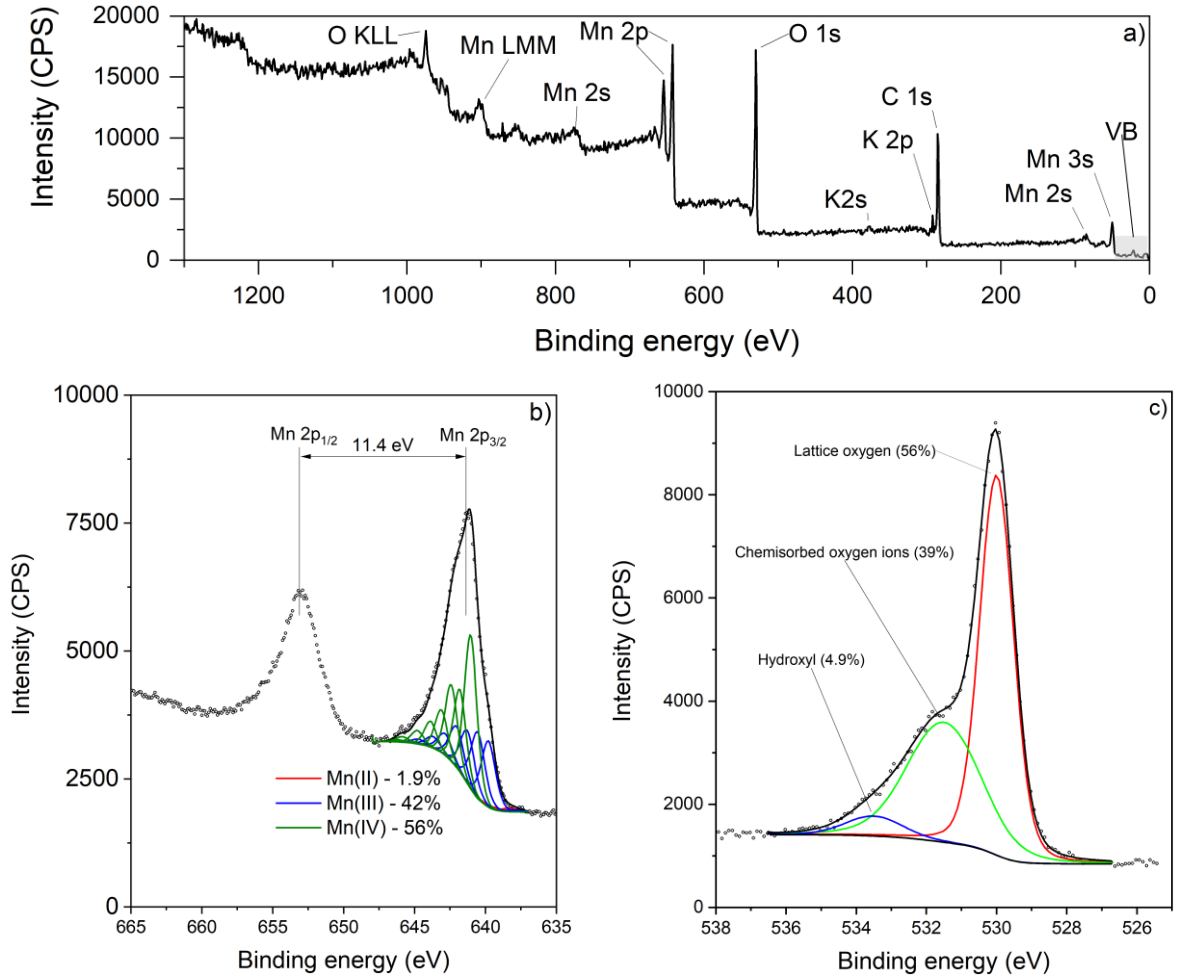

Figure 23 – XPS spectra of an *in situ* 34.9% MnO_2-GNF composite. **a:** Survey spectrum; **b:** High resolution spectrum of Mn2p region; **c:** High resolution spectrum of the O 1s region.

3.4.4 Dye Degradation Experiments

The catalytic activities of the above described composites were tested in a model organics removal reaction, where acid orange 7 (AO7) acted as a model pollutant, and H_2O_2 was used as the oxidant. The reactions were conducted in a round bottom flask, with a large cold water heat sink surrounding the reaction vessel. This was done to suppress the auto-accelerating effect of the highly exothermic catalytic decomposition of H_2O_2. A kinetic curve of a reaction without a heat sink can be seen on Supplementary figure 4.

The concentration of H_2O_2 was 1.8 M in these reaction mixtures. This is a large excess which was used in order to make sure the generation of ROS is not limited by the concentration of the oxidant throughout the reaction. Strictly speaking UV-Vis monitoring only shows the disappearance of the dye, or in other words the reaction between ROS and dye molecules. Since the oxidant is in such a large excess the discolouration of the dye can be approximated as a pseudo-first order process. A starting AO7 concentration of 0.068 mM was used to make sure the absorbance of samples were always in the dynamic range of the spectrometer used without any dilution. The amount of catalyst used was such that the reaction mixture always contained 1.0 mg/mL MnO_2 in each experiment. Prior to the dye degradation experiments it was found that when no catalyst is present, the same concentration of H_2O_2 degrades about 1.5% of the usual dye amount in 60 min, at a rate constant of about $5 \cdot 10^{-5}$ 1/min (See Supplementary figure 4c).

3.4.4.1 Comparison between Composite Types

The first parameter studied was the type of composite. For these experiments *in situ* and an *ex situ* composites of the same loading were used, along with GNF, and MnO_2 alone as controls. For the comparison of different composite types 34.9% loadings were chosen as this is a large enough ratio where bulk analysis is feasible, but not large enough for unsupported catalyst particles to be the dominant determinant of catalytic activity. Figure 24 compiles the kinetic data recorded with these materials. Relative dye concentrations were plotted against time, and a plot of ln(c) vs time was used to calculate k values.

All curves show a significant drop in the first few minutes, which is assumed to be caused by an initial imbalance between the heat generated by the reaction and the heat dissipated by the support as illustrated by Supplementary figure 5. Once these two processes reach equilibrium, the reactions follow a steady exponential curve. The results show that GNF possesses no catalytic activity, the dye removal seen here is assumed to be purely due to adsorption; MnO_2 on its own also shows low activity. The two composites on the other hand show markedly different behaviour. The *ex situ* composite roughly behaves as if its activity was a sum of that of MnO_2 and GNF, meaning that the rate of degradation is roughly the same but there is also a significant amount of adsorption happening. On the other hand, the *in situ* composite facilitates a much quicker dye removal, which corresponds to a roughly 10 times larger k value, as illustrated by Figure 24b. It is difficult to find comparable research output in order to contextualise this catalytic performance due to the number and wide range of reaction

parameters usually involved in such research but in general reported k values are in the range of $5 \cdot 10^{-3}$ min^{-1} and $200 * 10^{-3}$ min^{-1}.[59–61] This observed rate constant is in the middle range of reported values, but it has to be said that this k value was achieved with no external activation or pH adjustment both of which are common in this field.

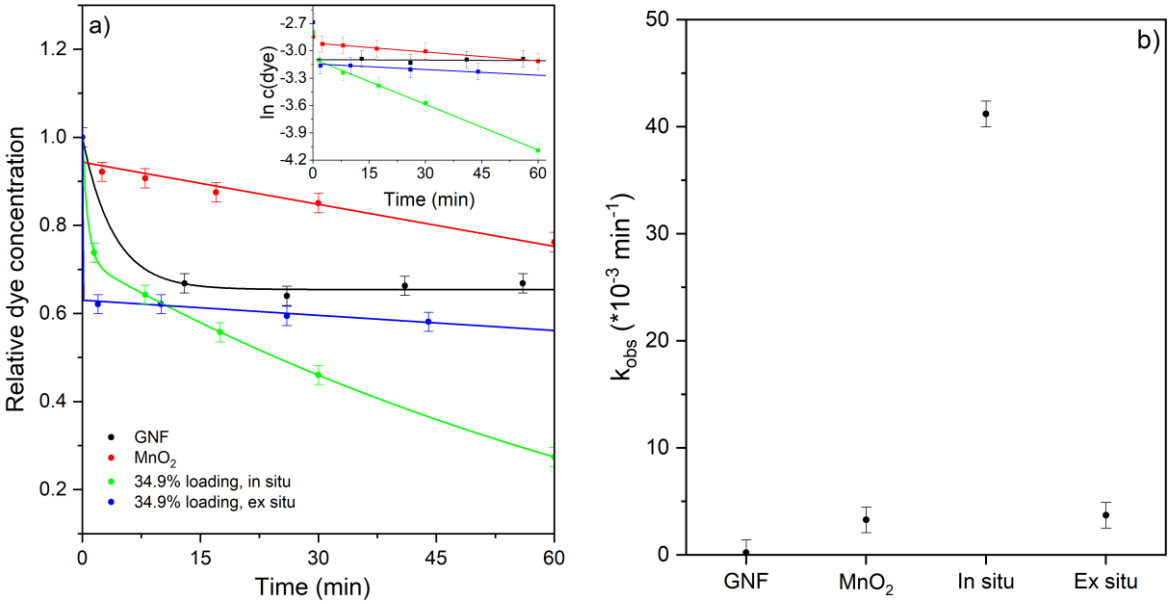

Figure 24 – **a:** Kinetic curves for GNF, MnO_2, an *in situ* and an *ex situ* composite; **b:** k values derived from the kinetic curves.
Reaction parameters: 1.0 mg/mL MnO_2 (or equivalent in the case of composites), 0.068 mM AO7, 1.8 M H_2O_2.

3.4.4.2 Comparison between Catalyst Loadings for *In Situ* Composites

After studying how the type of composite affects catalytic performance, similar experiments were done with *in situ* composites of different MnO_2 loadings on GNF where additional reaction parameters have been monitored in order to gain a deeper understanding of catalytic performance. The amount of catalyst used was reduced from 1.0 mg/mL to 0.6 mg/mL MnO_2. This was done in order to make sure all composites produce kinetic curves that provide useful information (i.e. dye removal is not too rapid). Figure 25 summarises the kinetic curves for these composites, showing that the composite of 64.2% loading facilitates a significantly higher dye removal compared to all the other loadings. The rate constant associated with this composite places it among the best catalysts studied by other researchers as noted above.

To delve deeper into the exceptional catalytic activity of 64.2% MnO_2-GNF additional reaction parameters were considered to probe the efficiency of the reaction. The additional parameters are temperature and H_2O_2 concentration versus time, both of which were studied in control experiments prior to dye degradations (see Supplementary figure 4). These control experiments led to two important findings. First, adsorption on GNF happens very quickly

under the studied conditions, which means that the initial drop in dye concentration in the kinetic curve of *in situ* composites is at least partly explained by adsorption. Second, roughly 10% of the H_2O_2 decomposes in the first few minutes of a reaction, even if there is no catalyst or GNF present, leading to a temperature increase of 3 °C.

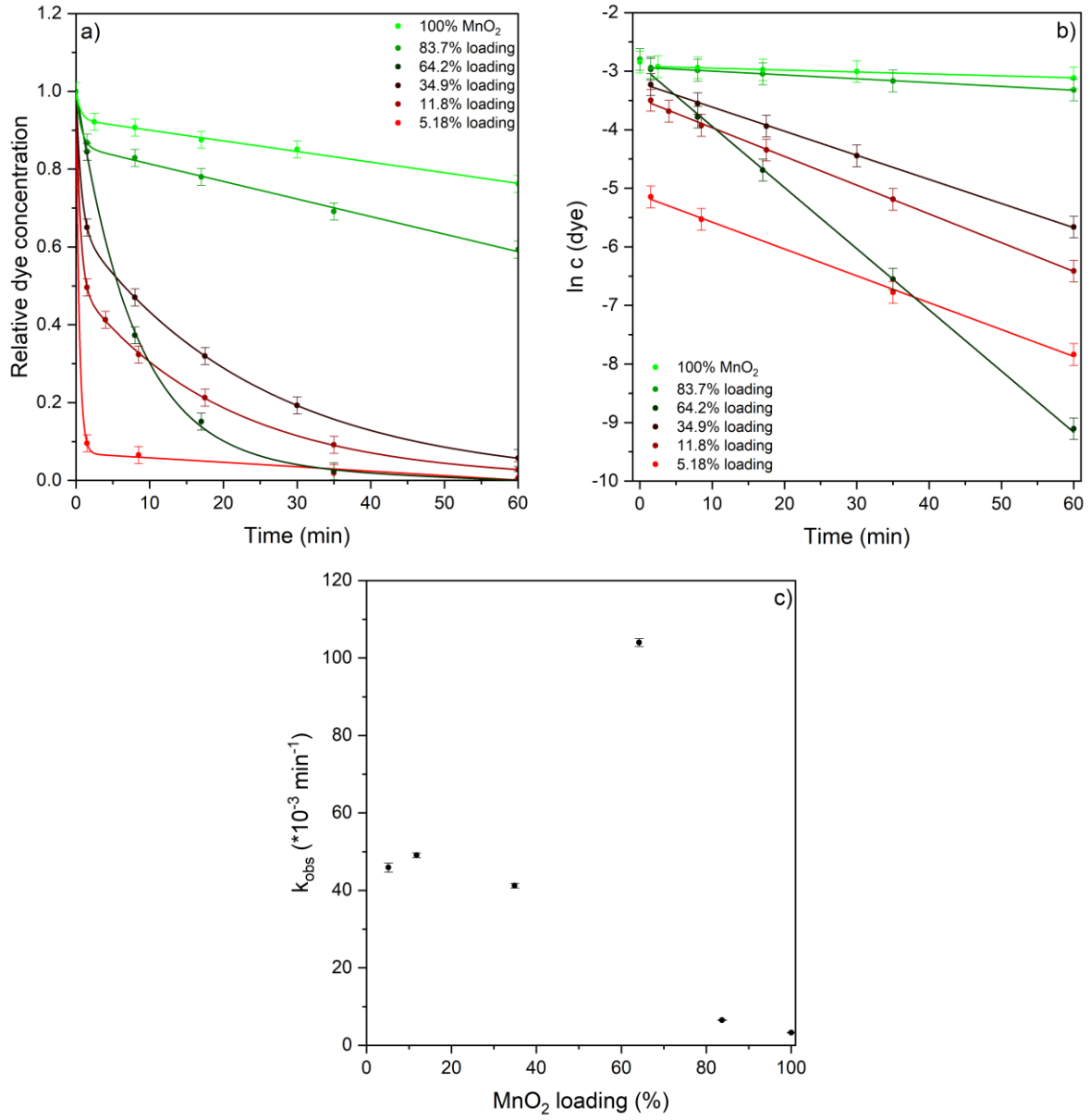

Figure 25 – Kinetic curves for *in situ* MnO_2-GNF composites; **a:** Graph showing relative dye concentration versus time for *in situ* composites; **b:** Graph showing ln c(dye) versus time for *in situ* composites; **c:** Summary of observed rate constants for *in situ* composites.
Reaction parameters: 0.6 mg/mL MnO_2 (or equivalent in the case of composites), 0.068 mM AO7, 1.8 M H_2O_2.

To explain why these composites are more active than the unsupported catalyst is it worth comparing the most active composite to pure MnO_2 (see Figure 26). In the case of unsupported MnO_2 a large temperature peak can be seen in the first 10 min, but after this the reaction slows down. This is associated with an initial accelerated decomposition of H_2O_2 without a corresponding rapid degradation of the dye. While in the case of the composite a

smaller peak and a more gradual increase is seen in temperature. Additionally, in the case of the composite, the dye and H_2O_2 concentrations decrease almost in tandem, which signifies a lesser degree of unproductive decomposition.

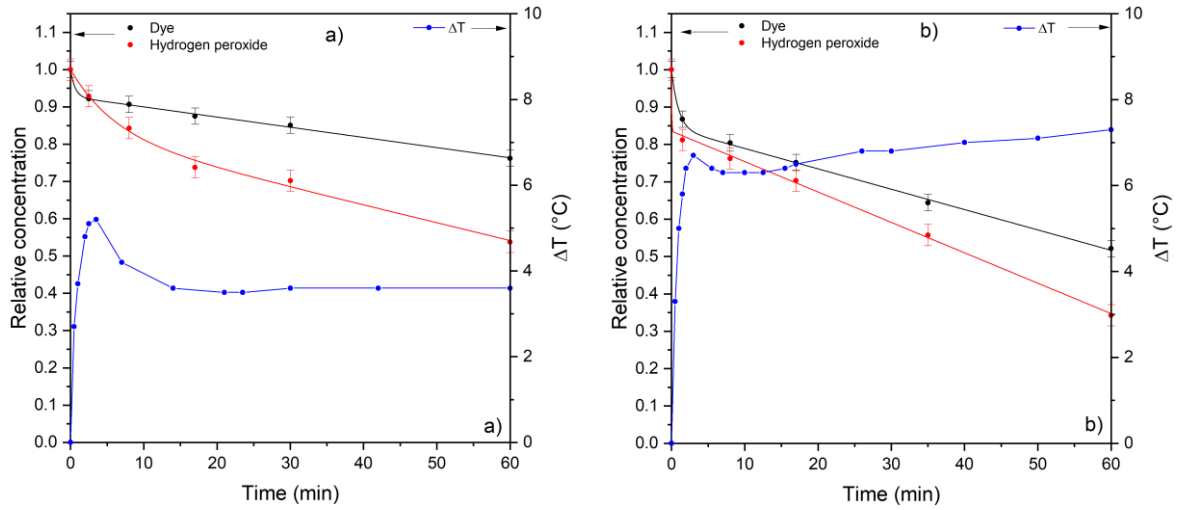

Figure 26 – Kinetic curves showing dye concentration, H_2O_2 concentration and the temperature of the reaction mixture versus time; **a:** 0.6 mg/mL MnO_2 ; **b:** 0.93 mg/mL 64.2% MnO_2-GNF (equivalent to 0.6 mg/mL MnO_2). Reaction parameters: 0.068 mM AO7, 1.8 M H_2O_2.

3.4.4.3 Truly Catalytic Degradation and Catalytic Efficiency

Finally, to quantify the dye removal activity of these materials truly catalytic dye removal and catalytic efficiency are used. In order to do the former, adsorption properties also have to be considered. Adsorption capacities have been identified for all *in situ* composites by measuring how much dye is adsorbed from a large excess over 3 days.

In all of the above experiments the overall decrease in dye concentration has been used to quantify degradation, but this is only an approximation of organics removal. In reality overall dye removal is made up of adsorption on the catalyst and truly catalytic degradation facilitated by the catalyst. Additionally, dye degradation experiments contained different amounts of composites in order to make sure the amount of MnO_2 present is always the same. These factors make direct comparison difficult based solely on the kinetic curves.

The calculated values of truly catalytic dye degradation for each composite are shown on Figure 27. These graphs confirm that the composite of 64.2% loading is the most active, facilitating roughly twice as much truly catalytic dye degradation than the two next best composites. Unfortunately, it is not feasible to provide comparison with results published by other researcher due to the novel nature of this metric.

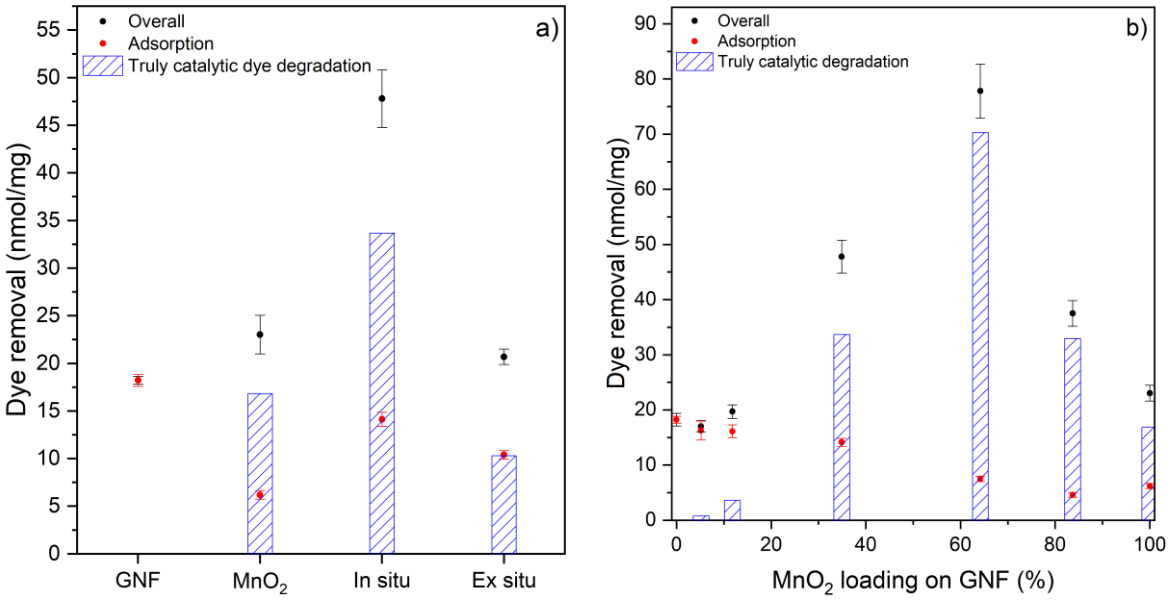

Figure 27 – **a:** Quantified dye removal contributions for all *in situ* MnO_2-GNF composites; **b:** Truly catalytic degradation contribution for all *in situ* MnO_2-GNF composites.

Catalytic efficiency describes another aspect of the performance of these materials, namely what percentage of H_2O_2 decompositions lead to the decomposition of a dye molecule, as well. This metric is calculated by dividing truly catalytic dye degradation values by H_2O_2 consumption. It should be noted that this number is expected to be relatively low for two reasons. The first being that the decrease in absorbance at 485 nm only describes the cleavage of the azo-bond in AO7, which is only the first step in a complex network of parallel and sequential reactions. For reference a theoretical full mineralisation by hydroxyl radicals alone would require 40 equivalents of these radicals for each equivalent of AO7. The second reason is that the hydroxyl radicals generated from the catalytic decomposition of H_2O_2 also participate in unproductive reactions, meaning reactions that don't lead to the degradation of aqueous organics.

This metric practically describes the economy of the reaction, which is generally overlooked in this field. It allows for an easy comparison between different catalysts regardless of the concentration of model pollutant and oxidant. This metric also confirms the composite of 64.2% loading as the most active (see Figure 28).

On a final note, truly catalytic degradation an catalytic efficiency have been defined based on UV-Vis spectrometry, as this preserves the straightforward nature of monitoring dye degradation with this method. As such these metrics can be used without the need for additional instrumentation.

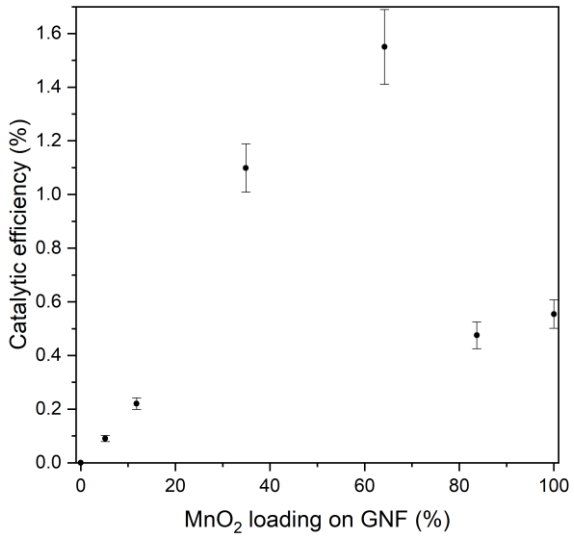

Figure 28 – Graph showing the catalytic efficiencies of all *in situ* MnO_2-GNF composites.

3.5 Conclusions and Future Prospects

Studies into the catalytic activity of macroscale carbon supported catalysts are relatively underexplored in the field of Fenton-like chemistry. This work contributes to filling this gap, by reporting on the performance of a novel MnO_2-GNF composite catalysts in Fenton-like dye degradation experiments. By extensively characterising the catalysts the relationship between structure and performance has been studied, especially the synergism that emerges in composite catalysts versus simple physical mixtures of the same components. The increased catalytic activity of these composite catalysts can be mainly attributed to a significantly higher dispersion of the catalyst, and the ability to dissipate heat generated during these experiments and by extension the avoidance of heat spikes. It was found that the most active MnO_2-GNF composite facilitated more than ten times the rate of degradation and three times as much truly catalytic degradation when compared to the unsupported catalyst. Additionally, the usage of two novel metrics are presented here, that can be used to compare different catalysts of dye degradation experiments in a more comprehensive way.

There are some studies that would improve the work presented in this chapter. XRD analysis with an instrument equipped with a Co X-ray anode would allow for the generation of higher quality X-ray diffractograms, and as such unlock the possibility of more precise secondary analysis of XRD data. Identifying the relationship between UV-Vis absorbance and TOC removal could be used to expand the scope of the above presented metrics. Further, dye degradations with selective radical quenchers could be used to elucidate the mechanism of ROS generation, since it would allow for the identification of the dominant radical. Finally, the

effect of supporting the catalyst on GNF could be further explored by measuring the amount of Mn that leaches into the reaction mixture during consecutive dye degradation experiments.

Chapter 4 - Chemical modification of macroscale carbon materials via acid oxidation and its effects on sorption characteristics

4.1 Introduction

Carbon materials are increasingly being researched to be used as catalyst supports due to the wide range of customisability in morphology and surface chemistry these materials offer, but the use of macroscale carbons in this area is still relatively underexplored. There are some unique features of macroscale carbon materials that both make them attractive as catalyst supports, but can also severely affect catalytic performance. The most important one of these is that carbon materials generally have very high surface areas of up to 3000 m^2/g, often due to extensive internal pore structures and a wide range of surface chemistries. This can lead to high dispersion, and sound anchoring of catalyst particles, but also to unwanted, irreversible adsorption of reactants. In the case of macroscale supports, this adsorption can lead to reactants occupying surfaces deep within the internal pore structure which would separate them from the catalysts and thus severely affect catalytic performance. This chapter aims to use acid oxidation of two macroscale supports in order to showcase that this treatment can suppress unwanted adsorption.

There are many molecular scale carbon materials being extensively researched like graphene and its derivatives, but for this work macroscale carbon materials were chosen. The main reason for this is that the scale-up of materials like graphene is very challenging, whereas macroscale materials can be used in packed bed reactors without further processing like pelletisation. Specifically spherical and fibrous supports have been chosen, as these are very common geometries of carbon materials, and they were expected to behave very differently in these experiments. Graphitic carbon materials are very inert, and as such require powerful oxidation methods in order to significantly change the surface morphology and chemistry. Acidic Piranha solution was chosen as the acid oxidation medium in this work, as the effects of this on macroscale carbon materials is underexplored compared to other strong oxidants. An important, but often overlooked aspect of adsorption is also reported here, which is the reversibility of the process.

Overall, this chapter aims to contribute to the field of chemical modification of macroscale carbon materials. The effects of acid oxidation were thoroughly characterised both in terms of surface morphology and chemistry, and its effects on adsorption characteristics.

4.2 Adsorbents

Industrial adsorbents are an extremely diverse group of materials, so first an outline of the literature will be provided. Only a fraction of the whole field will be further discussed, for a full review see Adsorption Processes for Water Treatment and Purification by Bonilla-Petriciolet *et al.*.[107]

When it comes to organics removal from aqueous sources, there are eight general technology groups: adsorption, AOPs, biodegradation, coagulation/flocculation, electrochemical processes, ion exchange, membrane separation, and photochemical processes. For this chapter, only adsorption is relevant, so only this will be discussed. The main advantages of adsorptive organics removal are high efficiency, simple operation, low cost, and no possibility of secondary pollution.[108] The main disadvantages on the other hand are costly regeneration, the loss of adsorbent during intended operation in some cases, problematic disposal of adsorbent residues, and that adsorption is ineffective for some organics.[108] There are many different types of adsorbent materials, but since this work used synthetic materials, only these will be discussed. The most important classes of synthetic adsorbent materials are graphene and its derivatives, metal organic frameworks (MOFs), activated carbons (ACs), clays, and zeolites.

Out of all the graphene-based materials the most relevant group for this work is carbon nanofibres (CNFs), often also called graphitic nanofibres (GNFs); this work will use the latter name. An emerging category of synthetic ACs called polymer based spherical activated carbons (PBSAC) should also be mentioned, since these are the most relevant type of ACs for this chapter. In the below subchapters PBSAC and GNFs are going to be described in more detail.

4.2.1 PBSACs

PBSACs are generally produced by generating microdroplets of a polymer, which are then cured and carbonised at high temperatures. This can be followed by two further steps of activation with either steam or carbon dioxide; these steps can be used to alter the surface chemistry of the resulting materials. The most common application of these materials is to be used as adsorbents in either air or water purification. As such the spherical shape and relatively

large diameter of these materials serves to reduce the backpressure caused in packed bed columns and other similar arrangements, compared to powders or fibres.

Most highly cited articles use materials produced by Blücher GmbH, and some of the most influential articles are also published with researchers associated with the company. The first article of the field was published in 2010 by Böhringer *et al.* where the authors discussed the production of PBSAC materials, their physico-chemical properties, like surface area, and porosity, and a few examples of these materials being used in the adsorption of aqueous organics.[109] Other important articles have been published by Tagliavini *et al.*, and Boussouga *et al.*.[4-5] The PBSACs produced by Blücher were found to be quite monodisperse with smooth surfaces, their diameters are between 200 and 500 µm. These researchers reported surface area values in the range of 1400-2200 m^2/g, with this surface area being mostly due to the presence of extensive internal pore structures in the micro- and mesopore regimes; overall pore volume was reportedly in the 0.6-1.8 cm^3/g range. Typical pore structures are illustrated by Figure 29. Macropores have been reported to be a negligible contribution to overall surface area. When studying the surface chemistry of these materials researchers found that the only heteroatom being present in any substantial amounts was oxygen, most samples having an oxygen content of 3-5% when measured with XPS.

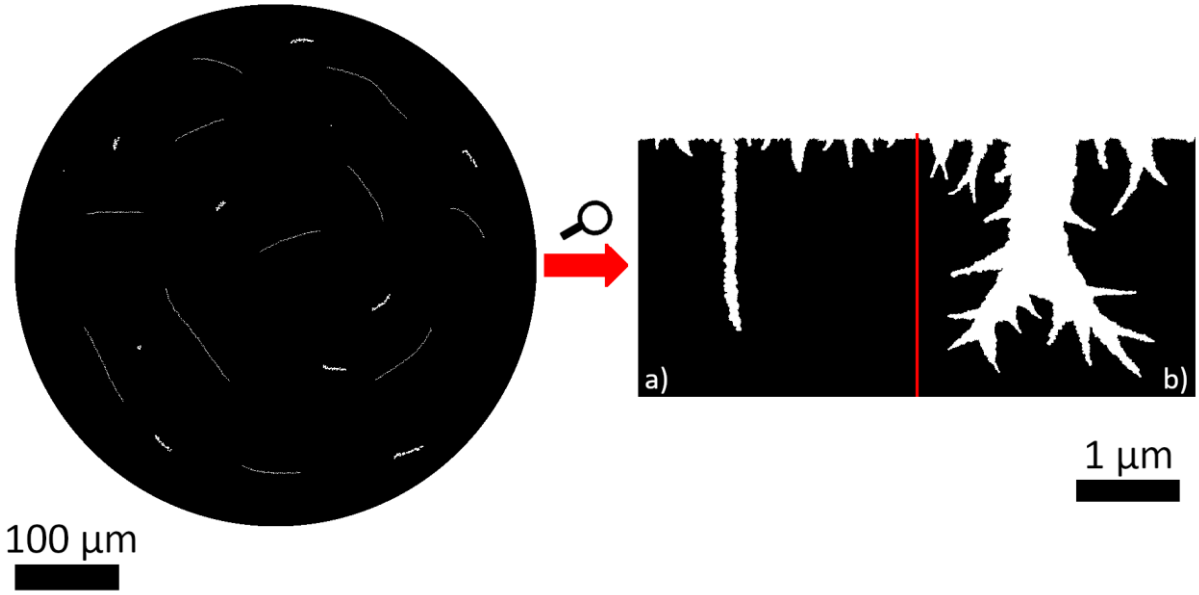

Figure 29 – Schematic illustration of internal pore structure of a PBSAC type material. The zoomed in section shows the cross section of a small surface area with mostly small, shallow pores (**a**), and deeper, more extensive pore structures (**b**).Scale bars are based on typical literature dimensions of similar materials, but are only illustrative.

This was made up of 0.5-1.5% C=O bonds and 2.5-3.5% C-O bonds. Boussouga *et al.* have proposed adsorption and transport mechanisms through which an adsorbate can occupy the surface of these materials. According to their publication adsorption mechanisms are defined by both longer range, non-specific electrostatic interactions, meaning Coulombic interactions, and shorter range, specific interactions like hydrogen bonding, van der Waals forces and interactions with a π system. They also propose that once the relatively slow surface adsorption has happened, the surface bound species can go through intraparticle diffusion, which can move molecules to more thermodynamically favourable surface sites, like micropores or capillaries.

4.2.2 GNFs

GNFs are macroscale, tubular carbon materials that are made up by the stacking of graphitic carbon layers in different configurations, ultimately leading to a large aspect ratio particle. The beginning of the graphitic nanotube and nanofibre field is difficult to pin down, as different sources claim it to be at different times.[112] The first publications on the formation of graphitic fibres from the thermal decomposition of hydrocarbon gases dates back to the late 1800s, early 1900s, but at this time the microstructure was not known at all.[7–9] After the invention of the electron microscope, significant progress was made in the 1950s in elucidating the microstructure of these nanofibres.[10–12] The exact formation mechanism of GNFs was first published by R.T.L. Baker in 1989.[119] Finally, a seminal article was published in Nature by Iijima in 1991, which most researchers regard as the foundational publication of the field of graphitic nanotubes and nanofibres.[120]

There are three general types of cylindrical GNFs, namely helical, tubular and ‘stacked cup’, based on how the graphene layers stack onto each other.[121] Out of these only stacked cup type GNFs are relevant for this work, so only these will be discussed. The first articles about stacked cup type GNFs were published in 2002 by the highly influential Marinobu Endo Research Group at Shinshu University and researchers associated with the GSI Creos Corporation.[16–18]

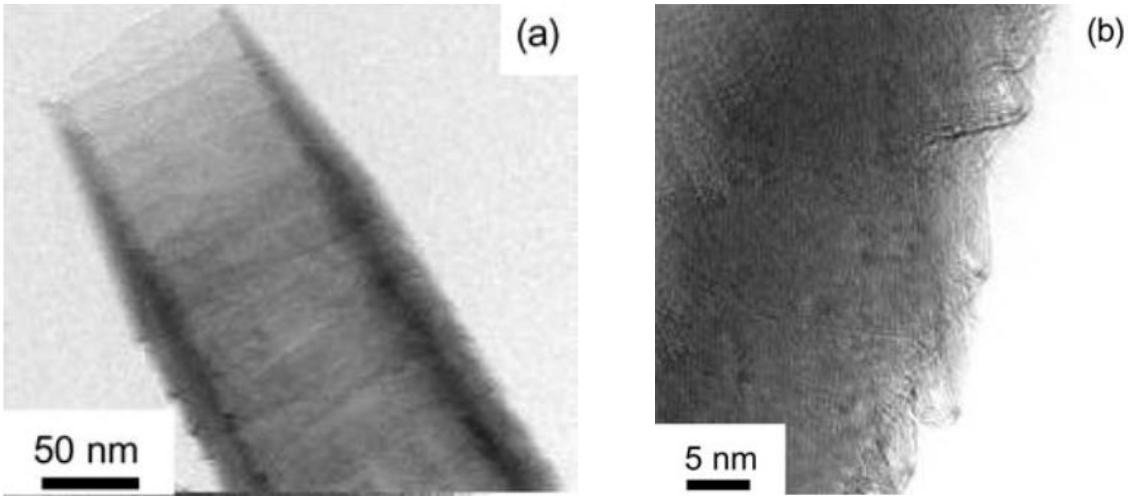

Figure 30 – TEM images showing the stacked cup structure and sawtooth external surface of GNFs.[123]

They describe fibres of 50-200 nm diameter, exhibiting a stacked cup structure, which can be understood as a series of truncated cones that form a hollow tube with sawtooth external and internal surfaces (see Figure 30). The graphitic layers making up these truncated cones are distorted, and the extent to which individual layers interact electronically depends on the cone angle, all of which leads to unique crystallographic properties. In these early publications stacked cup GNFs are made up of only these truncated cone layers, but these fibres can also have an outer sheath that is made up of cylindrical layers that are coaxial to the fibre, as illustrated by Figure 31.

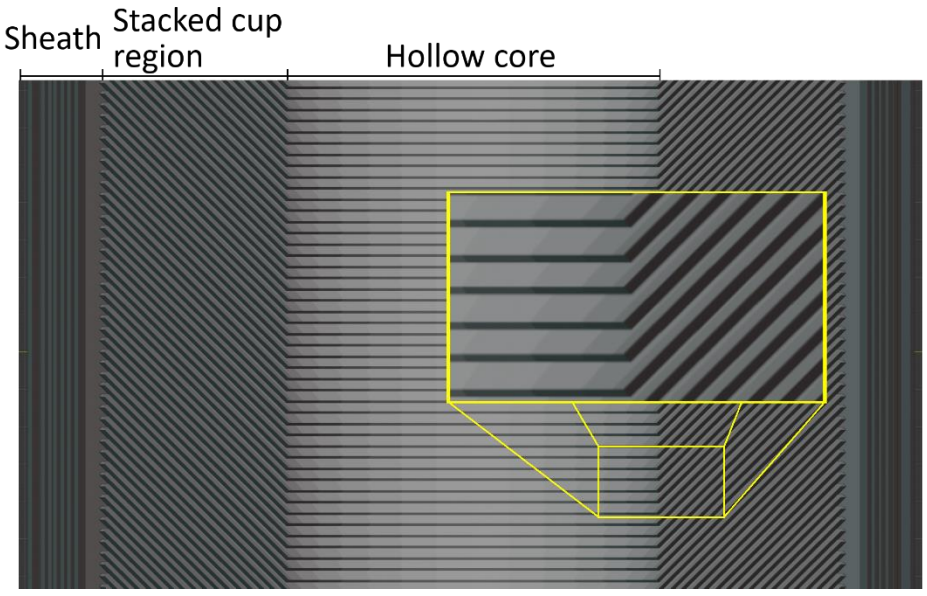

Figure 31 – Illustration of a theoretical GNF cut in half longitudinally. Image made by the author using Blender 4.1.

Kim *et al.* reported that heat treatment can form bonds between neighbouring graphitic layer ends which leads to the internal and external sawtooth-like structure transforming into a series of hairpin-like loops.

4.2.3 Factors Affecting Sorption Performance

Adsorption processes are generally studied by assuming either a pseudo-first order (PFO) or pseudo-second order (PSO) kinetic profile.[125] According to Vareda, these are empirical models that contain assumptions, hence the word pseudo in their name. The two main assumptions all adsorption models make are that the concentration of the adsorbate is constant in solution, and that adsorption process is controlled by the adsorption capacity of the adsorbent, and not the concentration of the adsorbate in solution. The physical meaning of these approaches is still a matter of debate in this field, but in terms of kinetic analysis these approaches mean that the kinetics of the adsorption is dependent on the concentration of surface sites raised to either the first or second power. These models are used to calculate the equilibrium adsorbate concentration on a material at any time during the adsorption process, which can then be compared to experimental data to probe adsorption kinetics. The most commonly used PFO model is Lagergren kinetics, while the most common PSO model is Ho and McKay's kinetics.[20-21]

Another approach to kinetically study adsorption is to create models based on the physical processes shaping the adsorption process based on empirical observations. The two most commonly used isotherms describing adsorption processes are the Langmuir and Freundlich isotherms. Any process that follow the former is said to follow Langmuir kinetics, while processes that follow the latter are said to follow Freundlich kinetics. The main difference between the Langmuir and Freundlich models is that the former assumes that surface adsorption sites are energetically homogeneous, while the latter assumes these are heterogeneous. As such, whether an adsorption process can be described well by either Langmuir, Freundlich or other kinetic model will inform researchers of the physical processes driving adsorption.[125] Ideally adsorption processes should be followed to equilibrium, or even saturation for the above models to have maximum explanatory power. The most important implication of choosing either PFO or PSO in kinetic analysis is that the linearization step will be different, which is used to derive rates of adsorption. In the case of PFO the rate of adsorption is proportional to the natural logarithm of adsorbate concentration, while in the case of PSO the rate of adsorption is proportional to reciprocal adsorbate concentration.[127]

The most important factor affecting sorption performance is the shape, surface morphology and surface chemistry of the adsorbent itself, but additional factors worth mentioning are the pH of the sorption medium, temperature and the molecular structure of the adsorbate.

Due to the way ACs are made, i.e. by using an activation step, all ACs will be made up of graphitic carbon domains, and surface functional groups. The most common method of modifying carbon materials is through the manipulation of surface chemistry by removing or introducing specific surface functional groups. The most important heteroatoms in ACs are oxygen, sulphur, and nitrogen. According to an extensive review article by Bhatnagar *et al.* there are three general approaches to modifying ACs: chemical, physical and biological.[128] For this work only chemical modifications are relevant, so the others will not be discussed. The most common liquid phase chemical modifications include acidic treatment, alkaline treatment, and impregnation. Acidic and alkaline treatment both oxidise the surface of materials, and improve hydrophilicity. Impregnation is generally used to enhance adsorption of a specific target ion or molecule, which is not relevant for this work.

Acidic treatment is generally used to introduce acidic functional groups, remove inorganic deposits and traces of metals.[129] The introduced functional groups are most commonly oxygen or sulphur groups. Similarly, alkaline treatment is used to introduce basic functional groups to the surface of materials, most commonly containing oxygen and nitrogen. For this work acidic treatments are the most relevant so only these will be further discussed.

The most common oxidants used for the introduction of acidic surface groups are H_2SO_4, HNO_3, $(NH_4)_2S_2O_8$, and H_2O_2. These have different acid strengths and oxidation potentials so their effect on the surface chemistry and the introduced functional groups will be different. Moreno-Castilla *et al.* have reported the effects of treating ACs with HNO_3, H_2O_2 or $(NH_4)_2S_2O_8$.[130] They have found that treatment with HNO_3 lead to the highest increase in total oxygen content, a roughly 16-fold increase from 0.9 to 15.6%, while H_2O_2 and $(NH_4)_2S_2O_8$ lead to increases of 8-, and 7-fold increase, from 0.9 to 7.5 and 6.5%, respectively. An interesting observation these researchers made is that the choice of oxidant changed the ratio between new surface and internal functional groups. Acid oxidation with HNO_3 lead to a slightly larger increase in internal functional groups, while the other two oxidants introduced significantly more functional groups onto the external surface. Lopez-Ramon *et al.* have done similar research in which they acid oxidised carbon materials with H_2O_2 and $(NH_4)_2S_2O_8$, and

reported the results.[131] Their research showed that acid oxidation lead to a 2-5-fold increase in acidic oxygen functional group content measured via Boehm-titration from 0.24 to 0.57 mmol/g, and 0.22 to 1.10 mmol/g in two different samples. They also reported that the pH of net zero charge seems to be inversely proportional to the amount of oxygen functional groups introduced, which means that the fewer oxygen functional groups were introduced, the stronger they were in acidity.

The most relevant aspect of the modification of surface chemistry in adsorption experiments for this work is how it affects the adsorption of large organic molecules, like dyes. This is quite a complex question, as it depends on both the graphiticity and number of functional groups of the adsorbent, but also on the molecular structure of the adsorbate. The most common pollutants of surface waters are pharmaceuticals, steroid hormones, surfactants, industrial chemicals and pesticides, which are generally all large molecules with unsaturated bonds, even rings, and polar or even ionic functional groups. This means that maximal adsorptive removal from aqueous sources would require tailoring the adsorbent to the specific application. Nonetheless, there are some general trends that should be recognised. According to the above, acidic and alkaline treatment can introduce functional groups that are either negatively or positively charged, according to their pK_a values, and the pH of the reaction medium. This can lead to electrostatic attraction or repulsion between the adsorbent and the adsorbate. On the other hand AC materials will always contain graphitic layers, which can participate in π stacking with aromatic ring containing aqueous organics. Pereira *et al.* have published an extensive article that illustrates this well.[132] They studied how acidic and alkaline treatment of ACs affect their adsorption properties towards both anionic and cationic dyes. They observed that treatment with HNO_3 leads to the introduction of the highest amount of oxygen functional groups, mainly carboxylic groups, but also carboxylic anhydride, lactone, phenol, and carbonyl groups. According to their research H_2O_2 treatment did not change the surface chemistry of the samples, while NH_3 treatment led to the removal of some oxygen functional groups and the introduction of some amine groups. In other words HNO_3 treatment made the surface of the ACs more charged at neutral pH, NH_3 treatment made the surface less charged at neutral pH, while H_2O_2 treatment did not change the surface charge. They then studied the adsorption of several dyes on these treated AC samples in neutral media, including dyes that are negatively and positively charged at the pH of the reaction mixture. They found that the adsorption of cationic dyes was enhanced by acidic oxygen functional groups, mainly

carboxylic groups, since these circumstances led to electrostatic attraction between the adsorbent and the adsorbate. The adsorption of anionic dyes was found to be hindered by the presence of acidic oxygen functional groups due to the emerging electrostatic repulsion. As such, enhancements in the adsorption of anionic dyes can be made by removing the electrostatic barrier that these functional groups would otherwise create. Lastly, it should be mentioned that temperature, dye concentration and adsorbent dose are all important factors that can affect adsorption performance, but these were not studied in this work, so these will not be discussed.

Finally, it should be noted that reusability and the ability to be regenerated are very important considerations for any AC materials intended for industrial usage. Regeneration of adsorbent ACs is quite challenging, as the aims of producing a highly efficient adsorbent and a highly regenerable adsorbent are diametrically opposed. It is common practice, that once an adsorbent is saturated, it is incinerated or put into landfill, which is not sustainable, and poses significant risks of pollution.[133] The chemical or physical regeneration of adsorbents also pose challenges, as it is difficult to strike a good balance between high removal efficiency, and the preservation of the morphology and surface chemistry of the adsorbent. The most straightforward method of regeneration is solvent extraction, which can be done with organic solvents or water. Since saturated adsorbents will contain large quantities of organics deep within their pore structures, the best solvents are those that can effectively reach these and dissolve the deposited organics. Salvador *et al.* have reported that boiling water can recover 100% of Sirius Red dye, 100% of o-chlorophenol, up to 90% of phenol and up to 30% of aniline to name only a few adsorbates.[134] The removal efficiency of hot water can be further enhanced using low concentrations of acids, bases or surfactants. While water tends not to be the best solvent of the organics that usually saturate industrial adsorbents, it is a much more environmentally friendly choice than organic solvents, and in many cases it can provide similar desorption capabilities.

In summary it can be said that there is a large overlap between industrial adsorbents and catalyst supports, even though adsorption itself can be viewed as both desirable and undesirable depending on the application and the extent of reversibility. When it comes to carbon materials being used as catalyst supports, irreversible adsorption is not desirable, but it is still worth approaching this through the widely researched field of industrial adsorbents, since the main factors controlling adsorption are the same. PBSAC type carbon materials have

high surface areas, which is largely due to their extensive internal pore structures, while GNF type carbon materials have lower surface areas, but their surface chemistry is much more narrowly defined. The adsorption properties of chemically modified PBSAC and GNF type materials is a relatively underexplored area, especially when it is done in order to enhance the catalytic activity of composites made with these. There is a wide range of reagents used in the modification of these materials, but in any case the reagent has to be a sufficiently powerful oxidiser to affect these otherwise inert materials. While Piranha solution is a staple in wet chemistry laboratories, its use in the chemical modification of macroscale carbon supports have scarcely been reported. The work presented in this chapter aims to address these gaps in the literature, with the additional aim of creating the foundation for the next chapter, in which these materials will be used as catalyst supports.

4.3 Experimental Details

4.3.1 Chemicals

Concentrated H_2SO_4 (≥95%; analytical grade) and H_2O_2 solution (30% w/v) was purchased from Fischer Scientific; the latter was stored in a refrigerator.

The carbon beads were purchased from IBU-Tec, batch number 2018.30.7037. These beads have since been discontinued, which is why there is only limited information presented here. The carbon nanofibres used in these experiments were purchased from Applied Sciences Inc. (Cedarville, OH, United States). This line of products are collectively called Pyrograf III; there are multiple grades but the present work used PR-19-XT-HHT type.

Na_2CO_3 (99.5%, analytical grade), $NaHCO_3$ (99.7%) and potassium hydrogen phthalate (0.2 M, analytical grade) were purchased from Fisher Scientific. Acid orange 7 (≥85%) was purchased from Aldrich, sulfanilic acid (99% purity) and 2-naphthol (99% purity) were both purchased from Sigma-Aldrich. The HCl (37% solution) and NaOH (analytical grade pellets) were both purchased from Fisher Scientific. DMF (≥99.5% purity) was purchased from Fisher Scientific.

4.3.2 Methods

4.3.2.1 Acid Oxidation

The carbon supports were oxidised using a 1:3 mixture of 30% w/v H_2O_2 and 98% H_2SO_4, commonly referred to as Piranha solution. Acid oxidation was done by first preparing the

solution by the slow addition of cold H_2O_2 to the acid, then 1 g of carbon material was added. The solution was stirred at 1000 rpm and left to react overnight. The acid oxidised carbon materials were filtered out, washed with ultrapure water (5 x 250 mL) and acetone (3 x 250 mL).

4.3.2.2 Size Analysis via Light Microscopy

The light microscopy images were produced using a Zeiss Axioimager Z1 microscope. The diameter distribution data of untreated carbon beads (CB) and acid oxidised carbon beads (oCB) was produced by using Fiji (also known as ImageJ 2). A Circle Hough Transform plugin was used to automate the generation of digital diameters, which were then converted into real diameters using the scale bars.

4.3.2.3 Zeta Potential

Zeta potentials were recorded using a Malvern Zetasizer Nano instrument. CB and oCB were crushed into a fine dust using a mortar and pestle. A suspension was prepared by adding 0.5 mg crushed up sample to 1.5 mL water, which was further diluted by taking 100 µL of it and adding it to 500 µL of water.

4.3.2.4 Boehm-Titration

Before the Boehm-titration itself, the exact concentrations of all solutions used were determined using acid-base titrations. First, a NaOH solution, a HCl solution, a $NaHCO_3$ solution, and a Na_2CO_3 solution were made up, each of of 0.05 M concentration. The exact concentration of the NaOH solution was measured via titration with a 0.2 M potassium hydrogen phthalate solution. Once the exact concentration of the NaOH solution was known, it was used to determine the exact concentration of the HCl solution, which in turn was used to determine the exact concentrations of the $NaHCO_3$ and the Na_2CO_3 solutions via titrations. All of these solutions were stored in plastic bottles.

The Boehm-titration itself is a double back titration, where 200 mg of the carbon material is added to 15 mL of one of the bases along with 500 µL isopropanol. The solution is left to equilibrate overnight, then 15 mL of HCl is added. The excess HCl is then titrated with $NaHCO_3$. Before the carbon materials, blank titrations were also done, which is the same procedure as above, but with no carbon materials present. Whenever NaOH was used, it was purged with N_2 before and during any usage in order to minimise the false consumption of NaOH arising from its reaction with atmospheric CO_2.

4.3.2.5 Adsorption Studies with Carbon Materials

Adsorption capacity studies were done by adding carbon materials (100 mg) to an AO7 solution (1.5 mM, 1.59 mL) for 3 days. The resulting solution was then diluted back into the dynamic range of the spectrometer and analysed.

Adsorption kinetics studies were done by preparing a solution of AO7 (1.5 mM, 1.59 mL), H_2O_2 solution (30%, 7.5 mL) and ultrapure water (32.5 mL) and adding a carbon material (50 mg). Samples of 0.8 mL were taken just before the carbon material was added and then 7.5, 15, 30, and 60 min after the carbon material was added. The first sample, i.e. the one that was taken before the carbon material was added, was put back into the reaction mixture after the analysis to reduce the skewing effect a reduction in volume would have had. The UV-Vis samples were passed through a 0.2 µm pore size hydrophilic PTFE syringe filter, and then analysed in a Thermo Fisher Nanodrop UV-Vis spectrometer. The pH was adjusted by either substituting 1 mL of the ultrapure water in the reaction mixture for 37% HCl solution, or by simply adding 0.2 g NaOH to the solution before the carbon materials. In either case the solution was stirred at 800 rpm until the solution became homogeneous.

4.3.2.6 Desorption Studies

To study the reversibility of adsorption on the beads, first 10 mg of either CB or oCB was saturated with an AO7 solution (1.5 mM, 8 mL). The beads were left in the solution for 3 days, and were then filtered out without subsequent washing with water or acetone. The beads were then put into a vial, and 2 mL of 85 °C water was added. The vial was then closed and put into an 85 °C water bath for 2 h. After this time a sample of 300 µL was taken, it was diluted with 1.2 mL water, and the resulting solution was analysed via UV-Vis. This hot water wash was done three consecutive times for three CB and and oCB batches, after which the beads were put into in 2 mL DMF at room temperature overnight, and the amount of desorption was similarly quantified.

4.4 Discussion of Results

4.4.1 Acid Oxidation

Acid oxidation of carbon materials is generally done using a strong, oxidiser like HNO_3, H_2SO_4, etc, where concentrations, contact time, temperature and other experimental parameters can be used to customise the oxidation process. In this work Piranha solution was

chosen as the oxidiser to circumvent the need for having to optimise experimental parameters. Piranha solution is an extremely strong oxidant and with the 10 hour contact time, it was expected to introduce significant changes to the otherwise very inert and stable graphitic carbon materials. Additionally, acid oxidation of carbon materials with Piranha solution is a relatively unexplored area of this field.

It should be mentioned that there are very important safety precautions that need to be taken into consideration when using Piranha solution. Preparing this solution is highly exothermic, mainly due to the heat of dissolution of H_2SO_4, but also because of the decomposition of H_2O_2. The temperature of the reaction mixture can reach temperatures of up to 175 °C during normal usage, so it is very important to prepare and use this mixture under a fume hood, and that the H_2O_2 is added slowly to the acid while the mixture is being strongly stirred. This ensures that no pockets of high H_2O_2 concentration can occur that could lead to runaway reactions.

Any traces of this mixture could significantly affect any reactions the acid oxidised materials are used in, so it is crucial to remove all traces of it. To achieve this, plenty of ultrapure water, and then acetone was used in the washing steps, both of which are miscible with H_2SO_4.[135] The use of acetone raises the possibility of the formation of explosive triacetone triperoxide (TATP) and diacetone triperoxide (DATP). To eliminate the possibility of TATP and DATP formation the acid mixture was left to react with carbon materials overnight, which was expected to lead to a near complete depletion of H_2O_2. The subsequent washing with water ensured that even if there was any H_2O_2 left in solution, it was washed away before the use of acetone. Finally Oxley *et al.* found that TATP and DATP are unlikely to form in dilute solutions of less than 3% H_2O_2. By the time acetone is used, the amount of H_2O_2 present should be well below this concentration, if at all present.[136]

The mechanism by which Piranha solution oxidises substrates is well known, as it is commonly used for cleaning laboratory glassware, silicone chips, etc. The most important reactions relating to the generation of oxidising species are shown by equations (33) to (35).

$$H_2SO_4 + H_2O_2 \rightleftharpoons H_2SO_5 + H_2O \quad (33)$$

$$H_2SO_5 \rightarrow HSO_3O^{\cdot} + OH^{\cdot} \quad (34)$$

$$H_2SO_4 + H_2O_2 = [H_3O]^+ + HSO_4^- + O^{\cdot} \quad (35)$$

As the above reactions illustrate the most important oxidising species are $HSO_3O^{\cdot}$, $OH^{\cdot}$ and $O^{\cdot}$ radicals. Accordingly, the main newly introduced functional groups in the acid oxidised

carbon materials are expected to be oxide and hydroxide groups, and to a lesser extent sulfate groups.

To understand the effects of acid oxidation, the carbon materials were characterised by various microscopy methods, and bulk and molecular level characterisation methods, as well. The results of these will be discussed in the following subsection.

4.5 Graphitic Nanofibers (GNFs)

4.5.1 Electron Microscopy

Some results of electron microscopy analysis of these fibres have been presented in the previous chapter, but additional images are presented here that are relevant to the acid oxidation (see Figure 32). Due to the nature of TEM imaging only a small number of fibres have been analysed. The diameter of GNF and oGNF are 111 ± 30 nm and 122 ± 35 nm respectively, so acid oxidation did not change the diameter. There are very few articles that can serve as good comparisons, but this finding is in accord with observations in those.[31-32] Each fibre is made up of a stacked cup internal structure and a cylindrical outer sheath with a smooth external surface. The graphitic layers in the stacked cup region are positioned at an angle of 29 ± 3 ° to the outer sheath. The internal surface of the fibres' channel contains two configurations of the innermost graphitic layers: hairpin-like structures forming step-edges and simple overlays as illustrated by Figure 32.

oGNF samples were also analysed using TEM. The only difference between the normal and acid oxidised fibres is that in the case of the latter, the hairpin-like structures of the internal step edges opened up, forming dangling graphitic layers (see Figure 33).

This is likely because these bent graphitic layers are significantly strained and so are the most reactive part of the fibre. By comparison the external surface of the fibres looks unchanged. This is due to the significantly higher stability of these stacked graphitic layers. The internal step-edges of such materials have been identified before but their cleavage as a result of acid oxidation is a novel finding.[33-34]

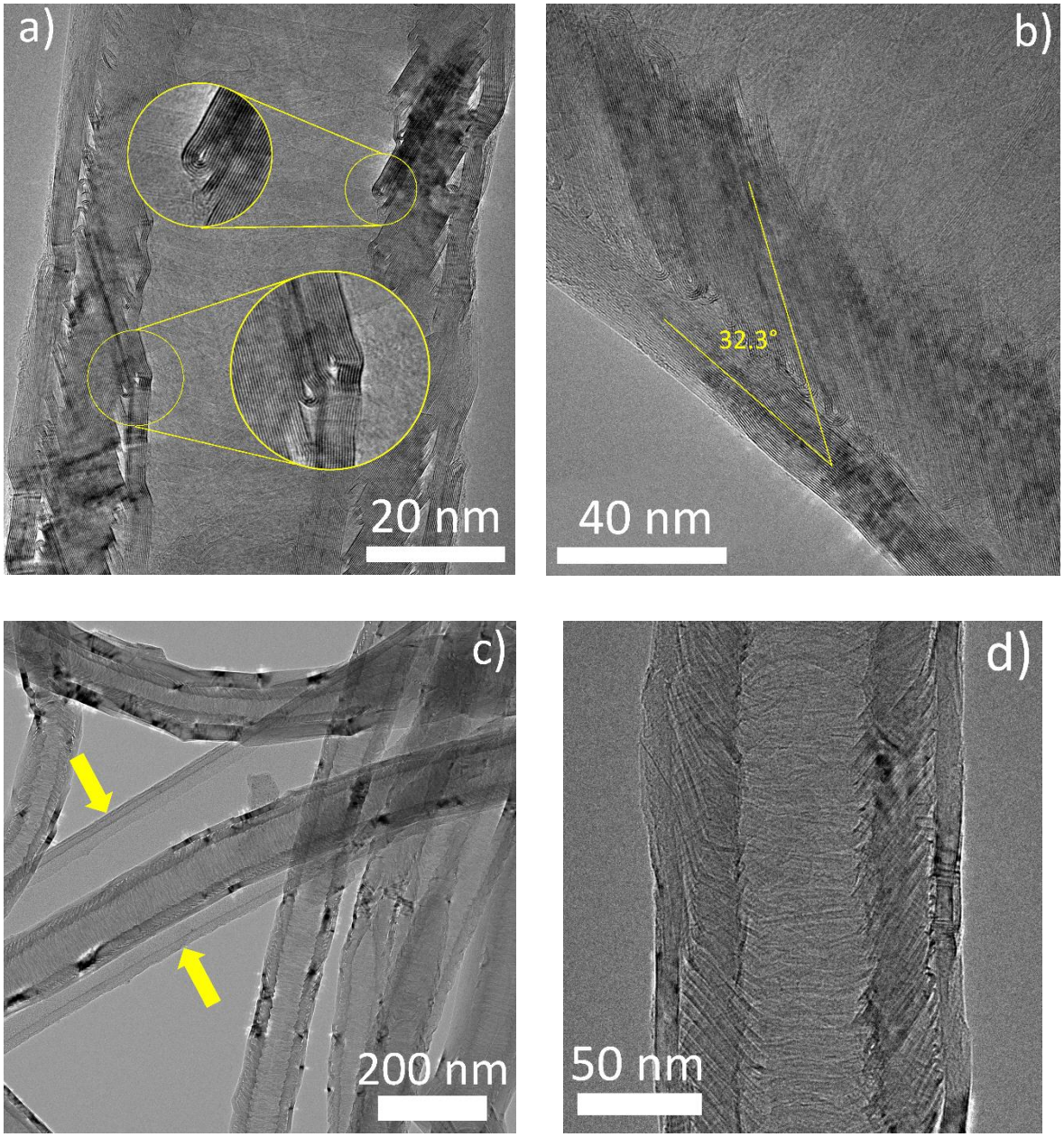

Figure 32 – TEM images showing distinctive features of a GNF fibre; **a:** Overlaying and hairpin-like internal terminal layers; **b:** Representative example of the angle between the stacked cup layers and the outer sheath layers. **c:** Overview TEM image of multiple fibres; arrows indicate the lacy carbon substrate of the sample holder chip; **d:** TEM close-up image of a single fibre showing stacked cup structure.

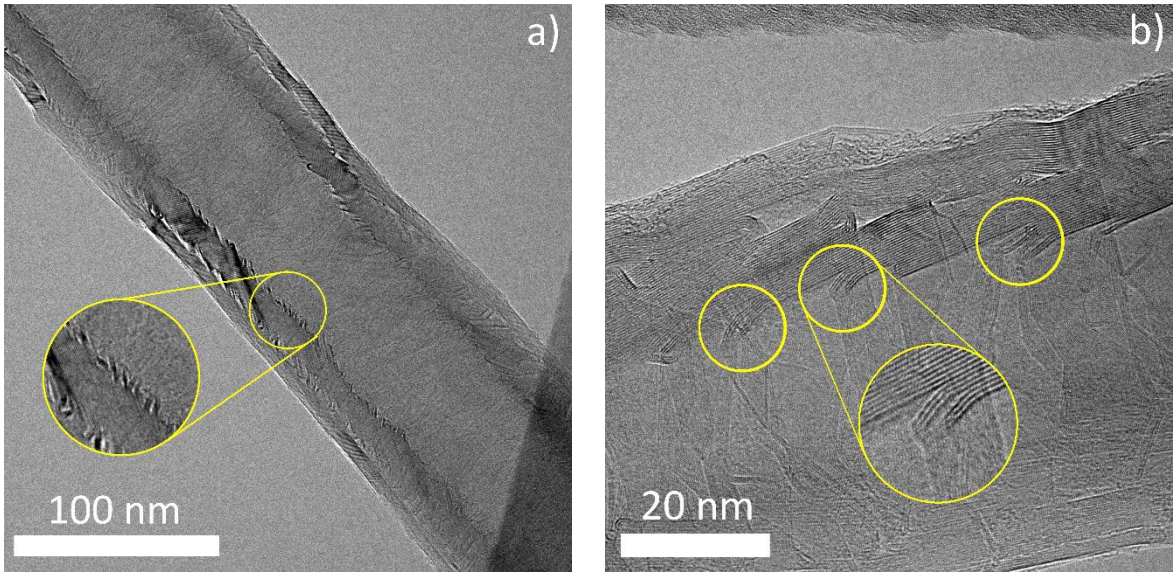

Figure 33 – TEM images of oGNF samples; **a:** Overview of a single fibre; **b:** Close-up image showing the internal step edges.

4.5.2 Bulk Characterisation

The X-ray diffractograms of GNF has been briefly described in Chapter 1, so in this chapter only its contrast with oGNF will be discussed. Both diffractograms correspond to highly graphitic carbon materials, as shown by Figure 34a. The previously unidentified broad, low intensity peaks designated with one and two asterisks in Chapter 1 have disappeared as a result of the acid oxidation, which supports the previous hypothesis that these signals originate from the undefined particulate matter seen on SEM images. These particles were likely dissolved by acid oxidation. The most important difference between the diffractograms of GNF and oGNF is that in the case of GNF the (002) peak is a single moderately sharp peak at 26.4 °, while in the case of oGNF there is also a sharp second peak at 27.1 °. This is most likely explained by the emergence of a second population of graphitic layers that have a slightly lower interlayer spacing. The likely explanation for this is the opening of the hairpin-like step-edges inside the fibres. Li *et al.* have reported that the increased curvature of graphitic layers can shift the (002) XRD peak to slightly lower 2 θ values.[98] It follows then, that the removal of distortion stemming from curvature would lead to the (002) peak shifting to slightly higher 2 θ values.

Raman analysis of GNF and oGNF shows results consistent with highly graphitic materials, containing several graphitic layers and some defects, as illustrated by Figure 34b. The most important pieces of information gained from Raman experiments are the positions, peak shapes, intensities and ratios between the areas of the G and D bands.

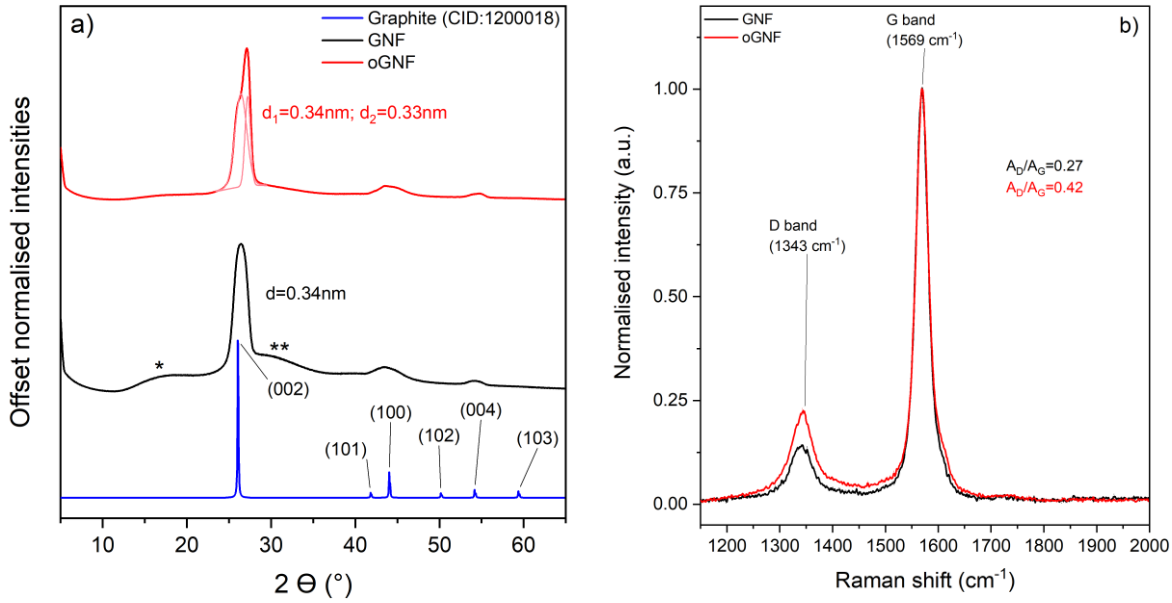

Figure 34 – **a:** X-ray diffractograms of GNF and oGNF along with a graphite reference pattern (CID:1200018); **b:** Raman spectra of GNF and oGNF.

The G band corresponds to the in-plane stretching vibration of sp^2 carbon pairs both in rings and in chains. The shape and intensity of this band is dependent on the number and lateral extent of graphene sheets, and any strain that might distort the graphitic layers.[141] The position of the G band in single layer graphene is 1585 cm^{-1}, while in single-walled carbon nanotubes it is 1584 cm^{-1}.[27-28] In both cases the increasing number of graphitic layers leads to the G band shifting to lower frequencies.[144] In the case of GNF and oGNF the G band is sharp and high intensity with no obvious shoulder and it is more intense than the D band, which means the samples are highly graphitic. The D band corresponds to the breathing vibration modes of aromatic rings adjacent to defects in the graphitic layer. The intensity of this band is generally proportional to the concentration of defects, like edges, holes, sp^3 carbon atoms, heteroatoms or grain boundaries.[145] The presence of the D band shows that there are defects present in the graphitic layers for both GNF and oGNF. The ratio between the areas of the D and G bands increased from 0.27 for GNF to 0.42 for oGNF[8]. This indicates a moderate concentration of defects in both cases, but also a small, definite increase in defect concentration as a result of the acid oxidation. There are no publications indexed by Scopus that could serve as a good comparison, meaning Raman analysis of carbon nanofibers made up of a stacked cup internal structure and a cylindrical outer sheath. The specific distortions

[8] In order to compare the defect densities of GNF and oGNF areas were used instead of peak heights as Cançado *et al.* found that for materials of low defect density, area ratio is a better descriptor.[243] The A_D:A_G ratios of GNF and oGNF correspond to I_D:I_G ratios of 0.14 and 0.22, respectively.

affecting the graphitic layers of GNF stem from its geometry, which in turn defines its Raman spectrum. The closest comparison the author found is the chemical modification of MWCNT, for which other researchers reported I_D:I_G ratios of 0.5-1.0.[41-42]

Lastly, GNF and oGNF were characterised using N_2 sorption and TGA in order to gain more information about their bulk structure, the results of which are shown on Figure 18. The N_2 sorption isotherms show that surface area is very low, practically no porosity is seen, which is in line with the structure of these materials seen in electron microscopy analysis. The BET surface areas of GNF and oGNF are 10.3 ± 0.1 m^2/g and 13.4 ± 0.1 m^2/g, respectively, which is significantly lower than the values published by the producer of GNF or other researchers using the same material.[43–46]

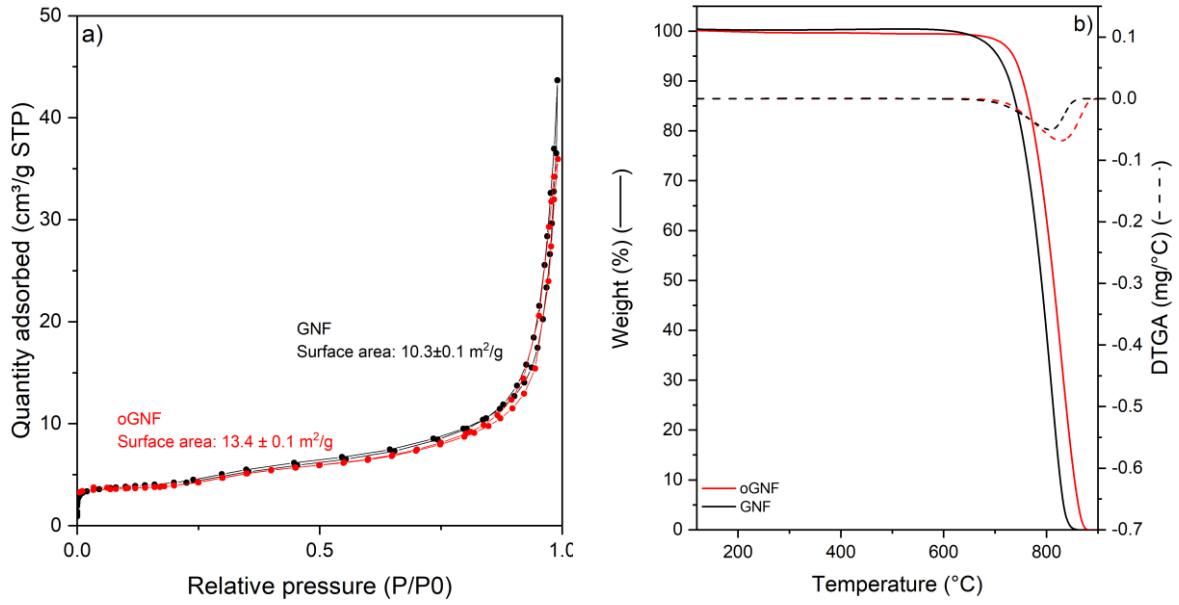

Figure 35 – **a:** Results of N_2 sorption experiments for GNF fitted with a curve via the BET model; **b:** TGA curve for GNF

Thermogravimetric analysis shows no significant difference between GNF and oGNF other than a 20 °C increase in decomposition temperature from 800°C in the case of GNF to 820°C for oGNF. In the case of carbon materials higher decomposition temperatures are usually associated with more graphitic carbons, so in this case the slight shift means that oGNF is slightly more graphitic in nature.[103] This is unlikely to originate from the fibres themselves becoming more graphitic, as the heat generated during the acid oxidation is not enough to cause this.[141] Instead it is likely to stem from the removal of the particles identified in GNF batches in Chapter 1.

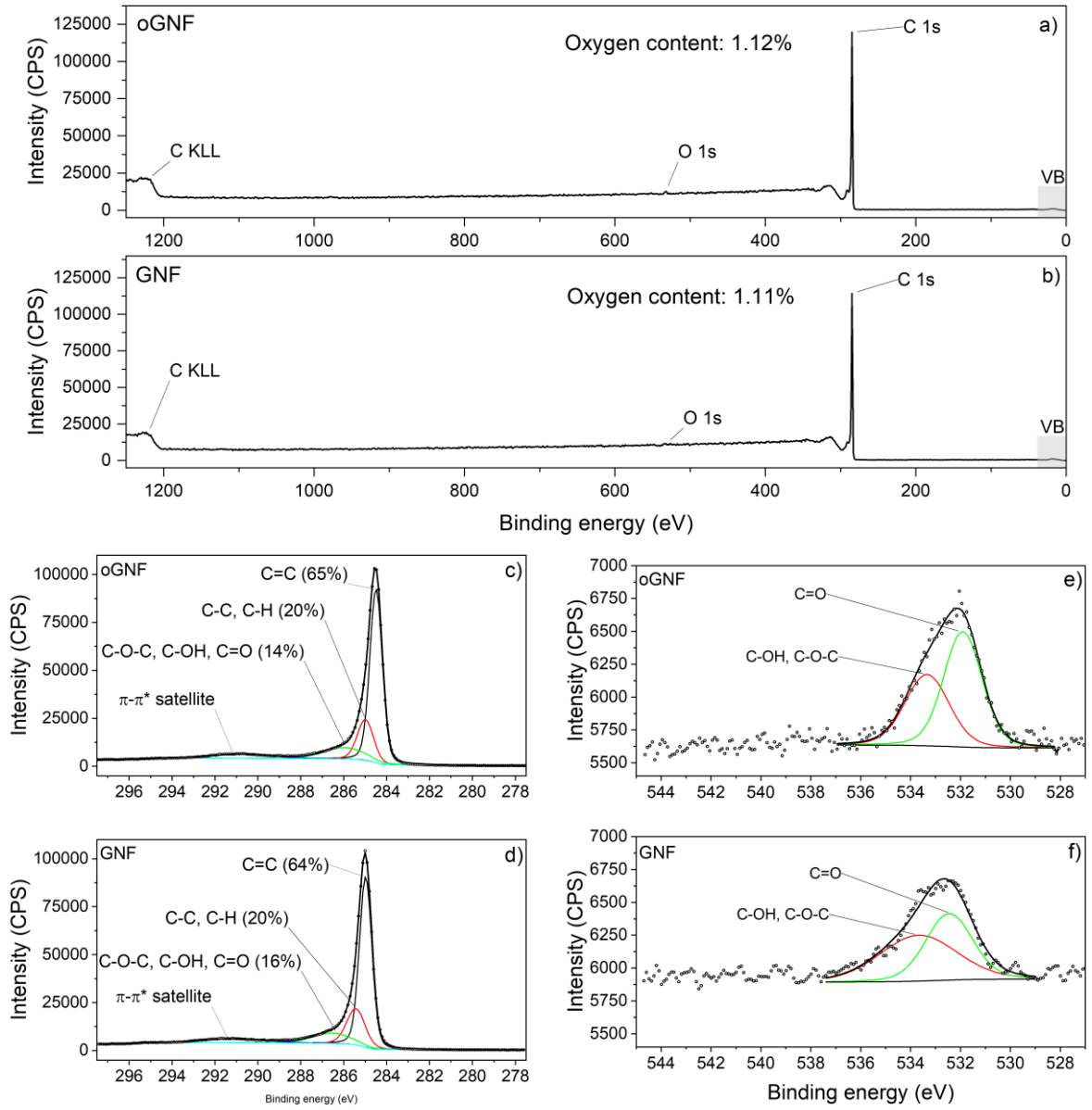

Figure 36 – Quantification of heteroatom functionalities in GNF and oGNF via XPS analysis; **a,b:** Survey spectra; **c,d:** High resolution C 1s spectra; **e,f:** High resolution O 1s spectra.

4.5.3 XPS Analysis

For the latter parts of this thesis it is crucial to have a good understanding of the surface chemistry of GNF and oGNF and so XPS and Boehm-titration were used to quantify the amount of heteroatoms in the fibres. The XPS analysis shows a very low amount of functional groups on the surface of GNF, and it seems to be almost exclusively oxygen as illustrated by Figure 36. The ratio between the O 1s and C 1s peak areas translate to a 1.11% n/n concentration of oxygen functional groups. In the case of oGNF this ratio is 1.12%, which means the acid oxidation did not introduce any detectable increase in surface oxygen functional group concentration. There was a marginal increase in oxidised sulphur species on the surface of oGNF compared to GNF, as illustrated by Supplementary figure 6. This is due to either residues

from the acid oxidation or the addition of new functional groups. The O 1s:C 1s ratios are in line with previously published oxygen contents of up to 3% for similar materials.[36–38] XPS analysis returned an O 1s signal that is too low in intensity for confident deconvolution, and as such a different method was used to differentiate the oxygen functional groups on the surface of the fibres: Boehm titration.

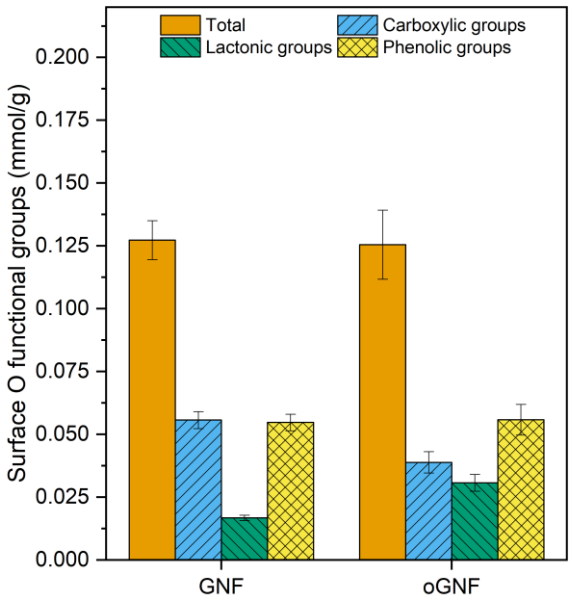

Figure 37 – Graph showing the different oxygen functional groups on GNF and oGNF as determined by Boehm titration.

4.5.4 Boehm Titration

The results of Boehm titrations are shown by Figure 37. The main difference between the different surface chemistry analysis methods used is that the X-ray of XPS interacts with only the external 5-10 nm layer of the sample, while in the case of Boehm titration the titrant interacts with all surface functional groups not just ones on the external surface. Results show very low oxygen content for both GNF and oGNF, and their values are not different. Literature survey of relevant publications show that the amount of surface oxygen functional groups identified in carbon materials via Boehm-titration is generally between 0.5 and 2.0 mmol/g [50–52]. The distribution of oxygen functional group types did change, the amount of lactonic groups increased slightly while the amount of carboxylic groups decreased slightly. The former could be explained by the removal of the particles identified in Chapter 1, while the latter is likely due to the introduction of new functional groups to the fibres. Overall. The low concentration of oxygen functional groups is in line with the results of XPS analysis.

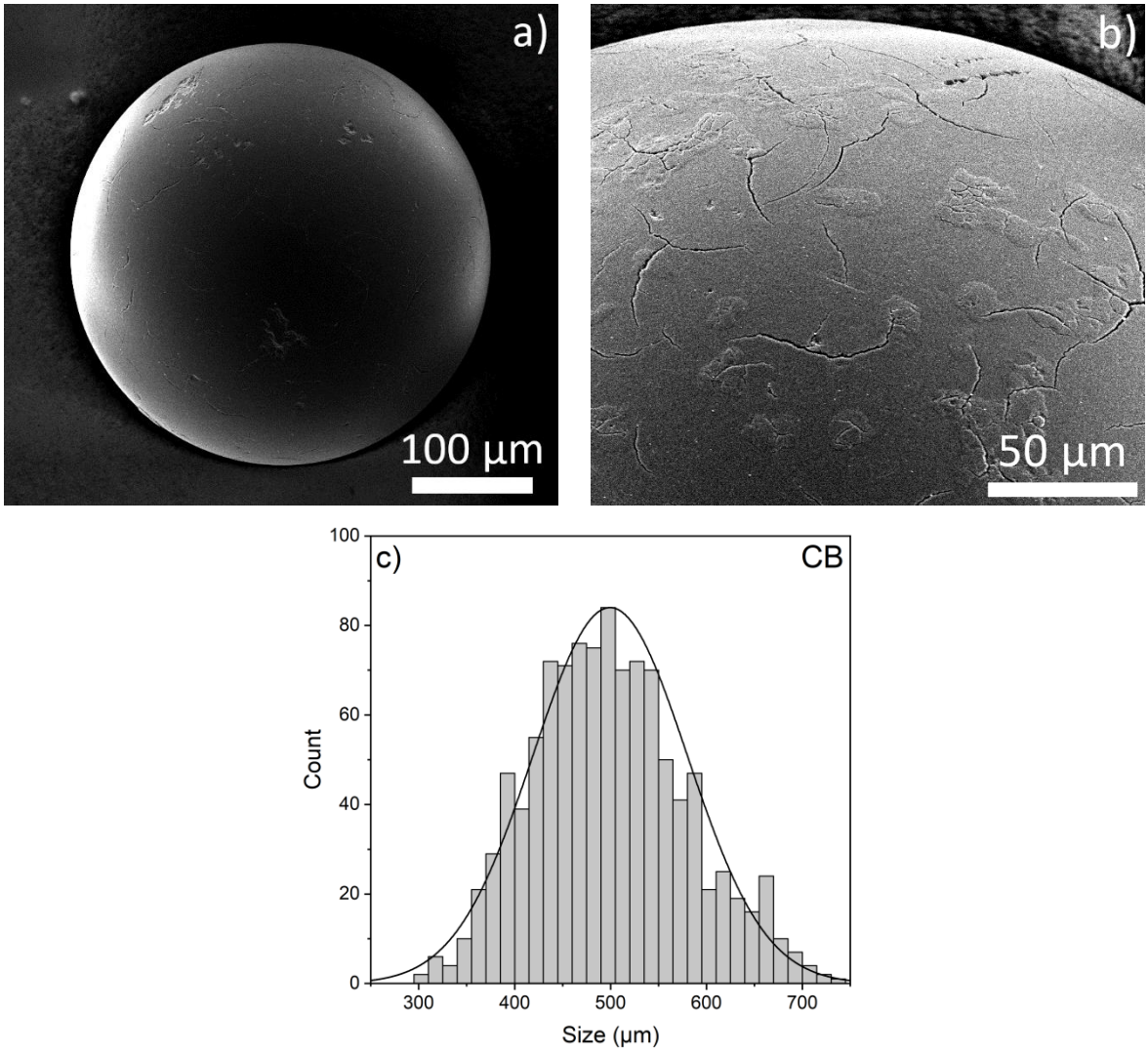

Figure 38 – Size and surface morphology analysis of CB; **a:** SEM image of a whole bead; **b:** close-up of the surface of a bead; **c:** diameter distribution of CB generated from light microscope images.

4.6 Carbon Beads (CB)

4.6.1 Light and Electron Microscopy

The carbon beads are macroscale supports and as such the distribution of their diameter was first analysed with light microscopy, while their surface morphology was analysed using SEM. The untreated beads have a mean diameter of 500 ± 80 µm based on 1070 beads. The beads are quite smooth, the main surface feature is the presence of 0.5-1.5 µm wide cracks. Some beads were cracked in half which showed that the internal structure is homogeneous as illustrated by Supplementary figure 7. EDX mapping of the cracked surface was also attempted but the surface proved to be too uneven to be properly aligned with the detector, and as such results were not reliable.

The acid oxidised beads on the other hand look significantly different. The mean diameter in this case is 380 ± 60 µm based on 1275 beads. The range of diameters decreased, especially towards the higher end which points towards the larger beads being more affected by the acid oxidation than the smaller ones. The size distribution of oCB also show significantly more particles of less than 200 µm diameter (see Supplementary figure 10).

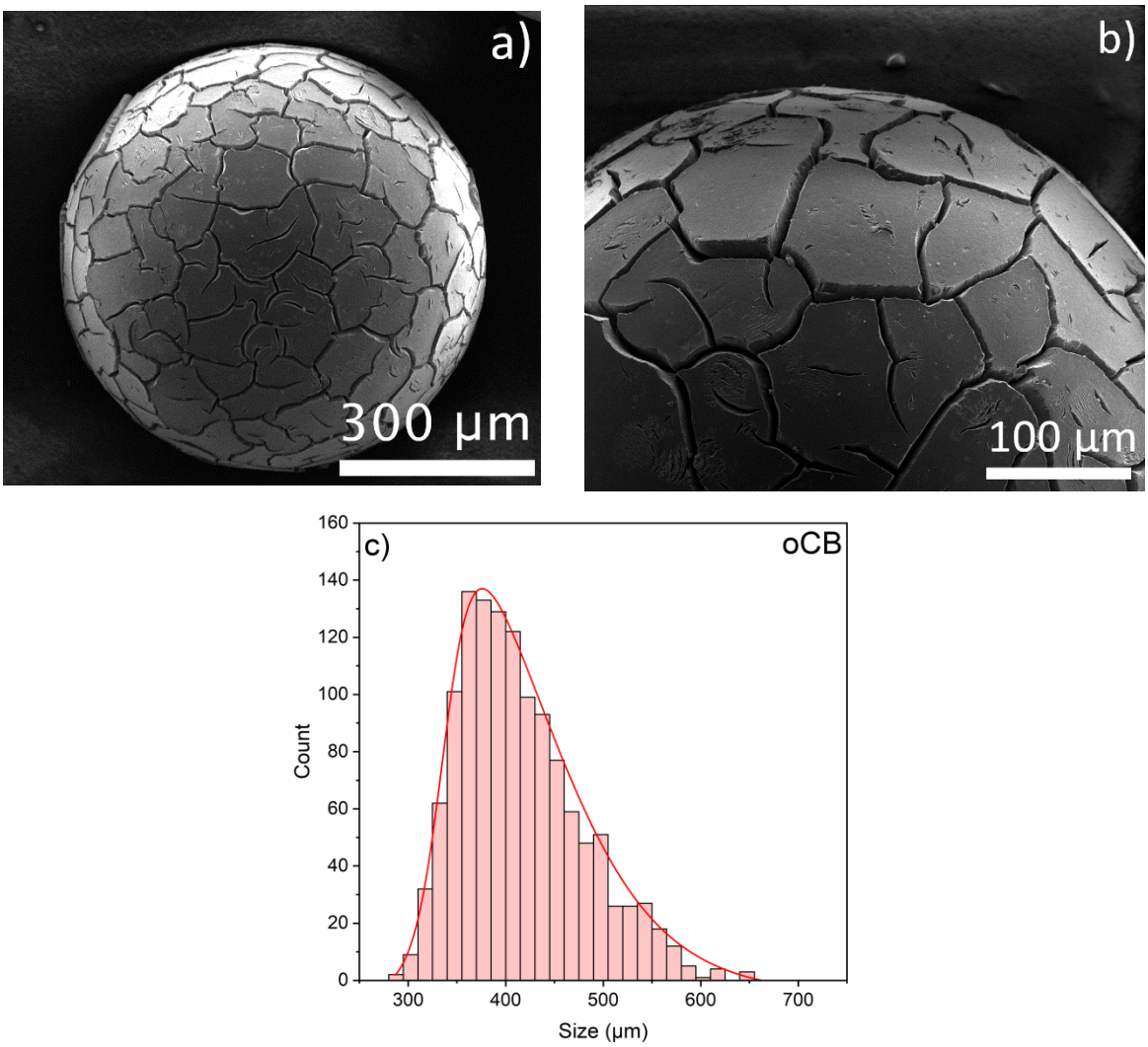

Figure 39 - Size and surface morphology analysis of oCB; **a:** SEM image of a whole bead; **b:** close-up of a bead's surface; **c:** diameter distribution of oCB generated from light microscope images.

Analysis via microscopy did not show intact beads below 300 µm, which means these are fragments that were removed as a result of the acid oxidation. Some acid oxidised beads were cracked in half and imaged using SEM which shows that the surface cracks go 20-30 µm into the body of the bead. The histogram also shows obvious asymmetry, and accordingly was fitted with a log-normal distribution function, which is often used to describe the size distribution of particles that are a product of some type of fragmentation. All of these point towards the main

mechanism of reduction in diameter being the removal of platelets delineated by the newly created cracks.

4.6.2 Bulk Characterisation

The untreated beads (CB) were then analysed via XRD, which shows that this material is made up of carbon of low graphiticity, as illustrated by Figure 40a. The diffractograms show no sharp peaks, which points towards low graphiticity and crystallinity. This is generally in line with results published for ACs, which tend to be of lower graphiticity.[42–44] The two low intensity, broad peaks at 20 and 28 ° likely correspond to two separate populations of stacked graphitic layers of different spacings. The main difference between the XRD patterns of CB and oCB is that there seems to be only one (002) peak in the diffractogram of oCB, but it is still very broad and low intensity. This points towards there having happened some form of rearrangement that brought about a single population of stacked graphitic layers. Since the untreated beads were of low graphiticity it is possible that the heat generated during the acid oxidation led to this rearrangement, but it is not possible to definitively say.

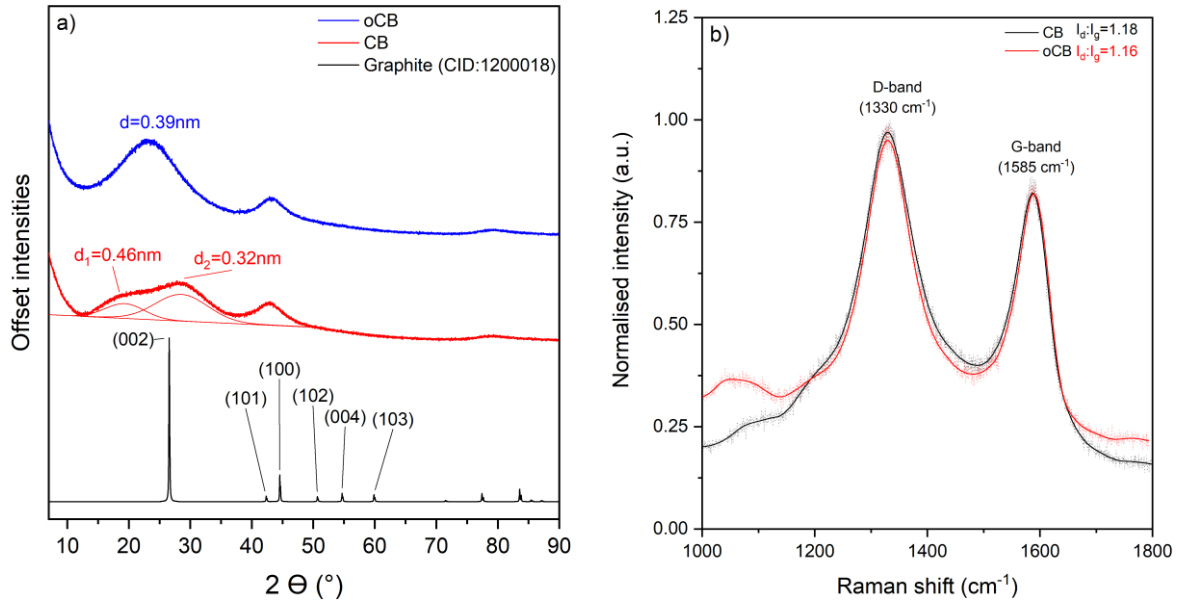

Figure 40 – **a:** X-ray diffractograms of untreated (CB) and acid oxidised carbon beads (oCB); **b:** Raman spectra of untreated (CB) and acid oxidised carbon beads (oCB).

Raman analysis of the untreated beads confirm the findings of XRD analysis, in that these beads are poorly graphitic, and acid oxidation did not change this (see Figure 40b). Signal intensity in the D band is higher than in the G band in the case of both CB and oCB, which is consistent with a carbon material of low graphiticity and very high defect density.

The surface morphology of CB and oCB were characterised using N_2 sorption experiments (see Figure 41a). The initial rise in adsorbed N_2 at low pressures describes the filling of

micropores, and the large amplitude of this step shows significant microporosity. The hysteresis signifies further porosity, in the mesopore range, which is supported by the pore area distribution data, plotted in the inset of Figure 41a. These results show that both the untreated beads and the acid oxidised ones have a very high surface area, with extensive meso-, and micropore systems. The surface areas of 1530 and 1260 m^2/g for CB and oCB, respectively, are quite high even among similar carbon materials. It is worth noting that acid oxidation reduced the surface area of the beads by 18%, but at the same time the micropore area increased by 23%, and surface area stemming from mesopores was only moderately affected. This means that the reduction in surface area is mainly the result of a reduction in macropore area.

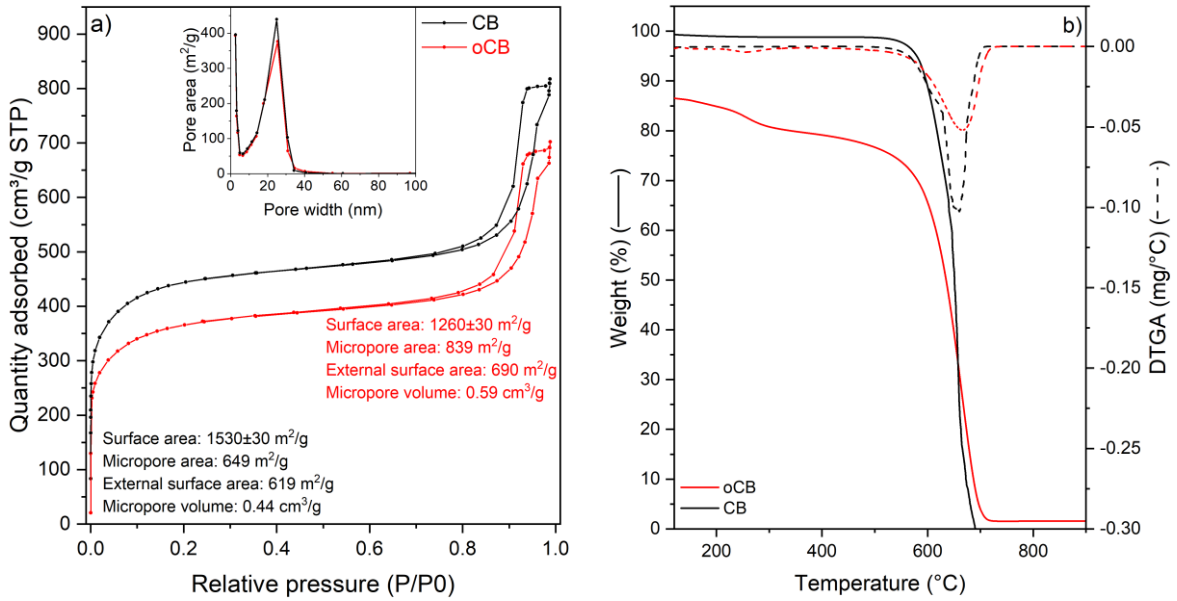

Figure 41 – **a:** Results of N_2 sorption experiments for CB and oCB, analysed via the BET method; **b:** TGA curves recorded in air, for CB and oCB

Thermogravimetric analysis of CB and oCB shows that both materials are completely combustible. The largest difference is that oCB contained much more water, due to its increased hydrophilicity. The main weight change step was recorded as 655 and 670 °C for CB and oCB, respectively, which places this material between graphene nanoplatelets and graphite in terms of thermal stability.[156]

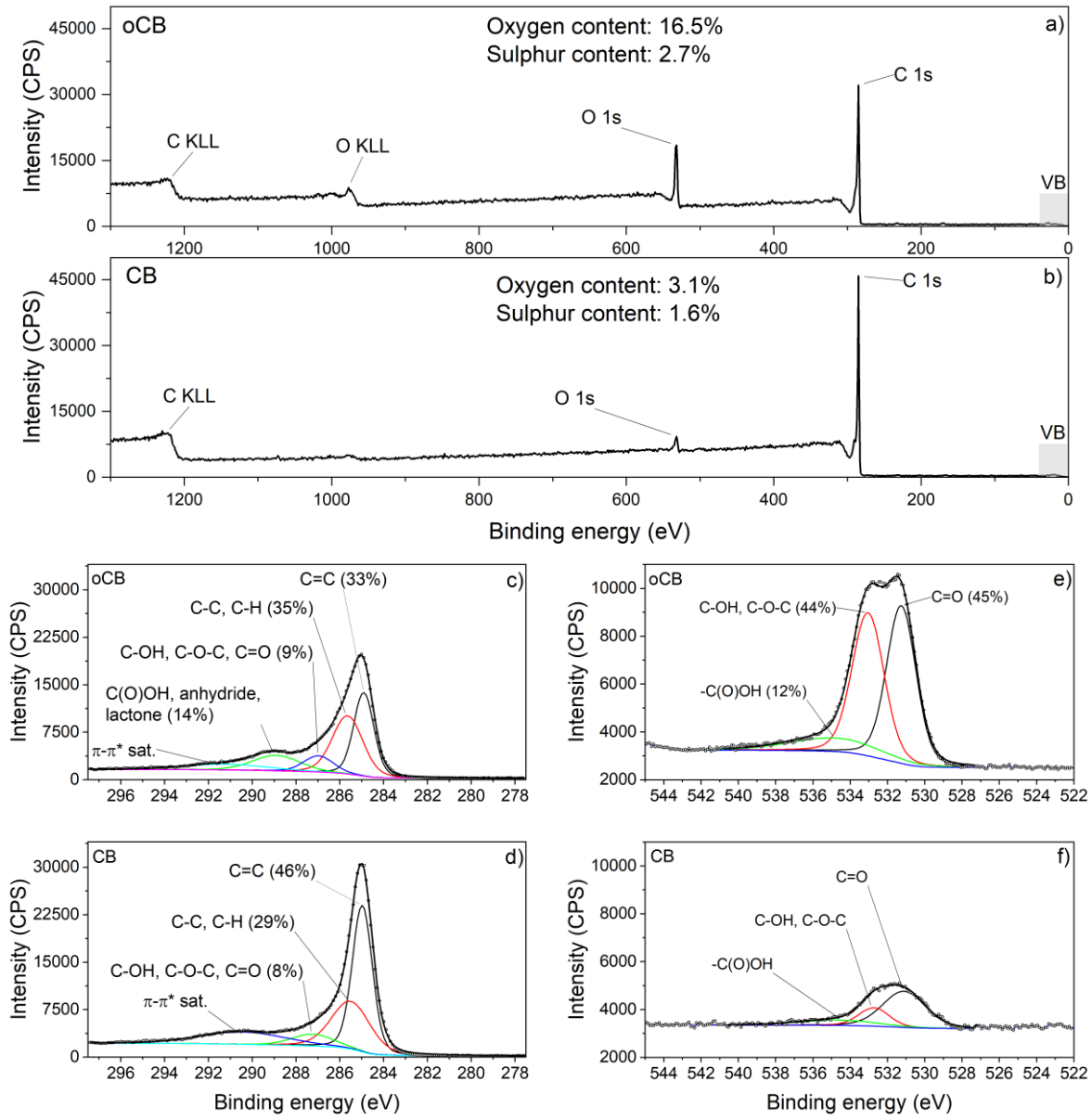

Figure 42 – XPS spectra of CB and oCB; **a,b:** Survey spectra of CB, and oCB; **c,d:** High resolution C 1s spectra of of CB and oCB; **e,f:** High resolution O 1s spectra of CB and oCB.

4.6.3 XPS Analysis

Finally XPS and Boehm titration were used to characterise CB and oCB on an atomic level. The aim of this was to quantify what changes the acid oxidation introduced to the surface chemistry (see Figure 42 and Supplementary figure 11). In the case of the untreated beads there was some oxygen content and traces of sulphur functional groups, but these signals were too low intensity to allow quantification. According to the producer, these beads are made by generating droplets of a resin that contains an organosulphur stabiliser, which explains the presence of the S 2p signal. The O 1s signal increased 5.3-fold and the S 2p signal increased marginally, although in the case of the latter the main difference is just a change in oxidation states. XPS analysis suggests that the untreated beads contain oxygen mostly in the form of

carbonyl groups. The acid oxidation increased the ratio of hydroxyl, ether and carboxyl functional groups, which clearly shows the introduction of new functional groups. This is also corroborated by the C 1s spectra, which overall shows a slight decrease in $C(sp^2)$-$C(sp^2)$ bonds, and a large increase in bonds containing C(sp3), like alkyl chains, hydroxyl groups, ethers, and notably the emergence of carboxylic acids, anhydrides and lactones. The emergence of this last class of functional groups is the most important conclusion of XPS analysis. Unfortunately, the individual quantification of these functional groups is not possible using XPS data due to overlapping binding energies.[157] To solve this problem Boehm titration was used to quantify the newly introduced functional groups.

4.6.4 Boehm Titration

To gain a more complete understanding of how acid oxidation affected the surface chemistry of the beads Boehm titration was also used. The untreated beads show a relatively high number of oxygen functional groups already, although most of these are lactonic groups, which have less of an effect on surface chemistry than carboxylic or phenolic groups due to being uncharged. As a result of the acid oxidation the overall number of oxygen functional groups grew from 1.10 to 1.96 mmol/g, mainly by the introduction of carboxylic groups. Overall, the results of the Boehm-titration support the results of XPS characterisation in that acid oxidation introduced a large number of new oxygen functional groups to the surface of the beads.

It should be pointed out, that the increase in oxygen functional groups according to XPS and Boehm-titration are different. This is due to how these methods work; XPS only analyses a depth of about 5-10 nm, while in the case of Boehm-titration the bases react with all surface functional groups throughout the internal and external structures of the beads.

This discrepancy means that acid oxidation affects the external layers of the beads to a much greater extent than the internal pore structure, likely due to the hydrophobicity of the beads and gaseous by-products of the acid oxidation blocking off the internal pore structure from the reaction mixture. Literature values for surface oxygen functional groups identified via Boehm titration on ACs are in the range of 0.5-2.0 mmol/g. This means that CB shows a relatively high surface oxygen functional group concentration, while oCB contains an extremely high number of these functional groups.

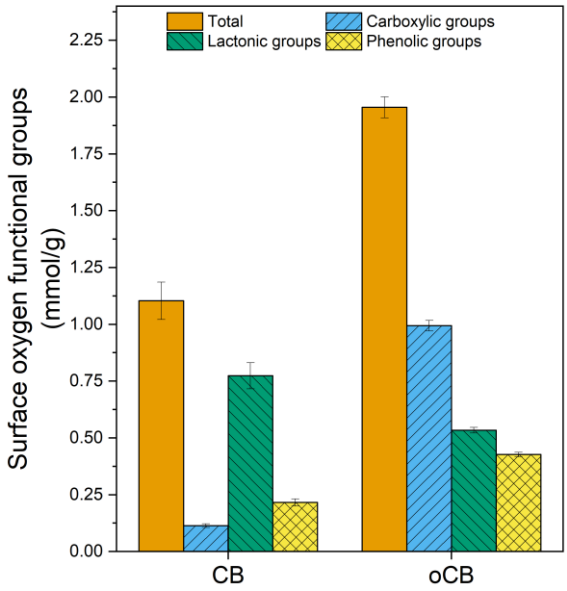

Figure 43 – Results of Boehm-titration for CB and oCB

4.7 Sorption Studies

4.7.1 Adsorption of AO7 on GNF and oGNF

The adsorption of AO7 on GNF and oGNF was studied relatively briefly, as only slight differences were found between these two types of materials. Adsorption happens very quickly under the conditions used in these experiments, which were the same as in all of the other dye degradation experiments in Chapter 1 and Chapter 3. This means that there was a relatively small amount of dye and a comparatively large amount of GNF/oGNF present (roughly 2.7 µmol and 50 mg respectively). These conditions were chosen to make these findings fully comparable to the later dye degradation experiments.

GNF seems to facilitate near instantaneous adsorption, while on oGNF adsorption is slightly less rapid. The rate of adsorption is described by k values generated from the kinetic curves (see Supplementary figure 13); $k_{initial}$ refers to the slope between the first and second point, while $k_{subsequent}$ to the rest of the graph. For reference, 50 mg GNF or oGNF would have a total adsorption capacity of 8.2 µmol, which partly explains the quick, total adsorption of 2.7 µmol of dye. Furthermore, both types of fibres have diameters of 90-150 nm which is two orders of magnitude larger than the size of an AO7 molecule, which means that while the internal tunnel is accessible, it does not get filled up during adsorption. Overall this means that both the external and internal surfaces are quickly being covered by the adsorbate.

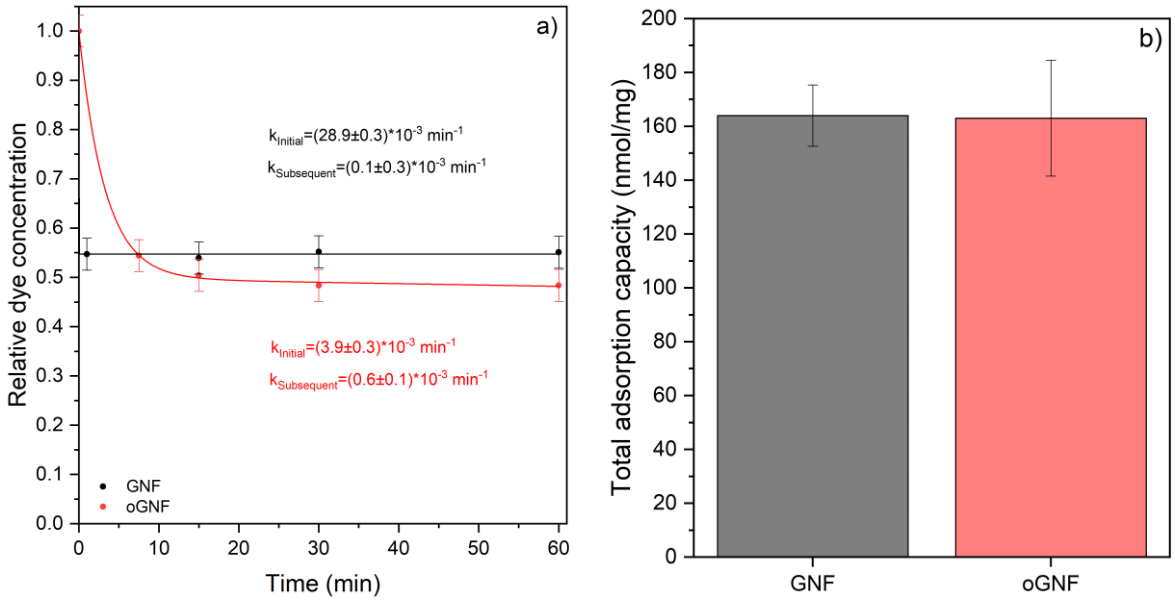

Figure 44 – Graphs showing the adsorption kinetics and capacity for the adsorption of AO7 on GNF and oGNF at neutral pH; **a:** Adsorption kinetics; **b:** Adsorption capacity after 3 days.

Further, the total adsorption capacity was measured to be roughly 163 nmol/mg for both GNF and oGNF. When comparing experimentally measured values against appropriate literature values, it is important to take into consideration that in the case of highly specific materials, like carbon nanofibers, the exact production method will define the surface morphology and chemistry, and by extension the adsorption properties. Additionally, for published values to be relevant, experimental conditions and the adsorbate have to be similar to the results presented in this work. There are no publications that could serve as exact comparisons, but there are works that can still provide a frame of reference. Soberman *et al.* reported that multiwall carbon nanotubes have adsorption capacities of 300-600 nmol/mg against pharmaceuticals, while Yar *et al.* have found that carbon nanotube - polyacrylonitrile composite nanofibres have adsorption capacities of 250-650 nmol/mg against methylene blue.[46-47] Neither of these research groups published surface areas for their materials, but it can be said that compared to these GNF and oGNF are poor adsorbents. As another way of comparison, the work of Santoso *et al.* should be considered, who found that in the case of ACs there is an average ratio of 4.11 between the BET surface area of a material in m^2/g and the adsorption capacity of the material against methylene blue in mg/g.[160] This ratio for GNF and oGNF is 5.6 and 6.8, respectively, which shows that these materials are poor adsorbents compared to the ACs compiled by Santoso *et al.*. The results of adsorption studies with GNF and oGNF underline the findings of characterisations, which is to say that acid oxidation did not change the fibres in any significant way.

4.7.2 Adsorption of AO7 on CB and oCB

The first experiments probing the sorption characteristics of these materials were looking at the adsorption kinetics and capacity of CB and oCB against AO7 at three different pH values: 0.75, 7.0 and 14. The pH of 7.0 is the most relevant for any potential real world application and also for later experiments of this project, but this is also the most complicated in terms of adsorption mechanisms. ACs usually have a wide range of surface functional groups, with pKa values between 3 and 11, which means that at pH=7 some will be protonated, some will be deprotonated, which leads to both repulsive and attractive interactions with adsorbates.[61-62] Thus pH values of 0.75 and 14 were also investigated to probe whether electrostatic interactions play any significant role in adsorption, and to further study how acid oxidation affected adsorption properties.

It is important to note that experiments at pH=7.0 were done at practically zero ionic strength, while the large amount of acid or base present at pH=0.75 and pH=14 respectively, necessarily leads to higher ionic strengths, and so these experiments are not strictly comparable to pH=7.0 experiments.

In adsorption kinetics experiments the starting concentration of the dye is relatively low, which means these experiments are more characteristic of the build-up of the most thermodynamically favourable first adsorption layer or layers. Thus adsorption rates observed in such experiments are mostly defined by the interactions between the surface of the carbon materials and the dye molecules. The main drivers of this are likely electrostatic interactions, mainly ionic interactions between polar functional groups and π-stacking of aromatic rings. An important question of adsorption studies is whether adsorption follows a first or second order kinetic profile. Ho and McKay, in their very influential 1999 article stated that pseudo-first order kinetics only apply to the initial stages of adsorption, whereas the later stages are better described by pseudo-second order kinetics.[127] The adsorption experiments conducted in this work were all done using dilute dye solutions of 0.07 mM in order to make any results directly comparable to dye degradations using the same dye concentration. Accordingly, an assumption was made that pseudo-first order kinetics will describe these experiments the best, and so rates of adsorption were calculated as the slope of ln c(dye) vs time.

As shown by previous characterisation results, the internal pore structure of untreated and acid oxidised beads is not fundamentally different, and so it is assumed that any difference in adsorption mechanism or kinetics is mainly due to a difference in surface chemistry.

At neutral pH and near zero ionic strength there is a significant difference in both adsorption kinetics and capacity between CB and oCB, which means that adsorption is significantly hindered in the case of the latter. It is worth noting that the reduction in total adsorption capacity is roughly twice as large as the reduction in surface area between CB and oCB, which means that surface chemistry must also play a role here. AO7 has two pK_a values of 8.26, and 11.4, and so it is roughly 95% protonated at pH=7.0 as shown on Supplementary figure 16, and although the exact pK_a values of the functional groups on CB and oCB are not known, it is safe to say that at pH=7.0 only some of them are going to be deprotonated. This means that if there is electrostatic repulsion between the dye and the beads it is going to be moderate.

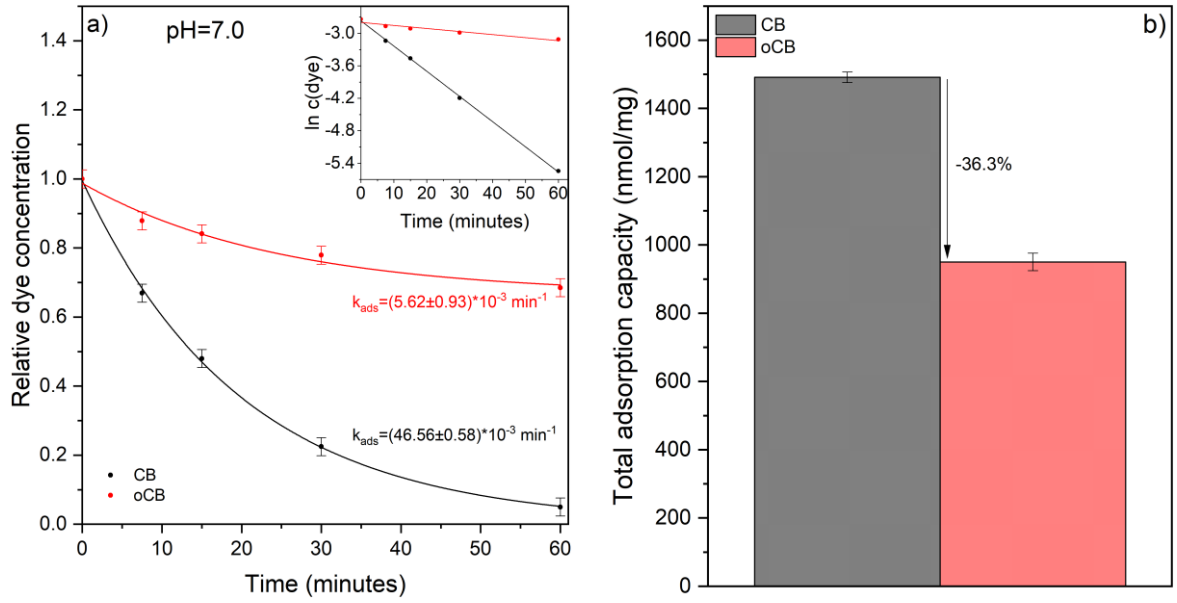

Figure 45 – Kinetic curves for adsorption with AO7 on CB and oCB at neutral pH; **a:** Adsorption kinetics; **b:** Adsorption capacity after 3 days.

The zeta potentials of the beads were measured at neutral pH in order to gain more insight into the electrostatic charge of the surface of these beads. The recorded values were -17.4 ± 3.9 mV and -16.6 ± 3.6 mV for CB and oCB, respectively, which signal a slight negative charge in both cases, but no significant difference between the two materials. It should be noted that the beads had to be ground into a fine dust in order to make the measurements possible. This means that the whole bead has been analysed, not just the areas where the acid oxidation had its effect, which could explain why no difference was detected[9].

[9] For reference, electron microscopy showed that acid oxidation caused roughly 25 µm deep ridges on the surface of oCB. If we assume this is the maximum depth at which acid oxidation had an effects, that corresponds to 14.3% of the total volume of a bead of 500 µm diameter.

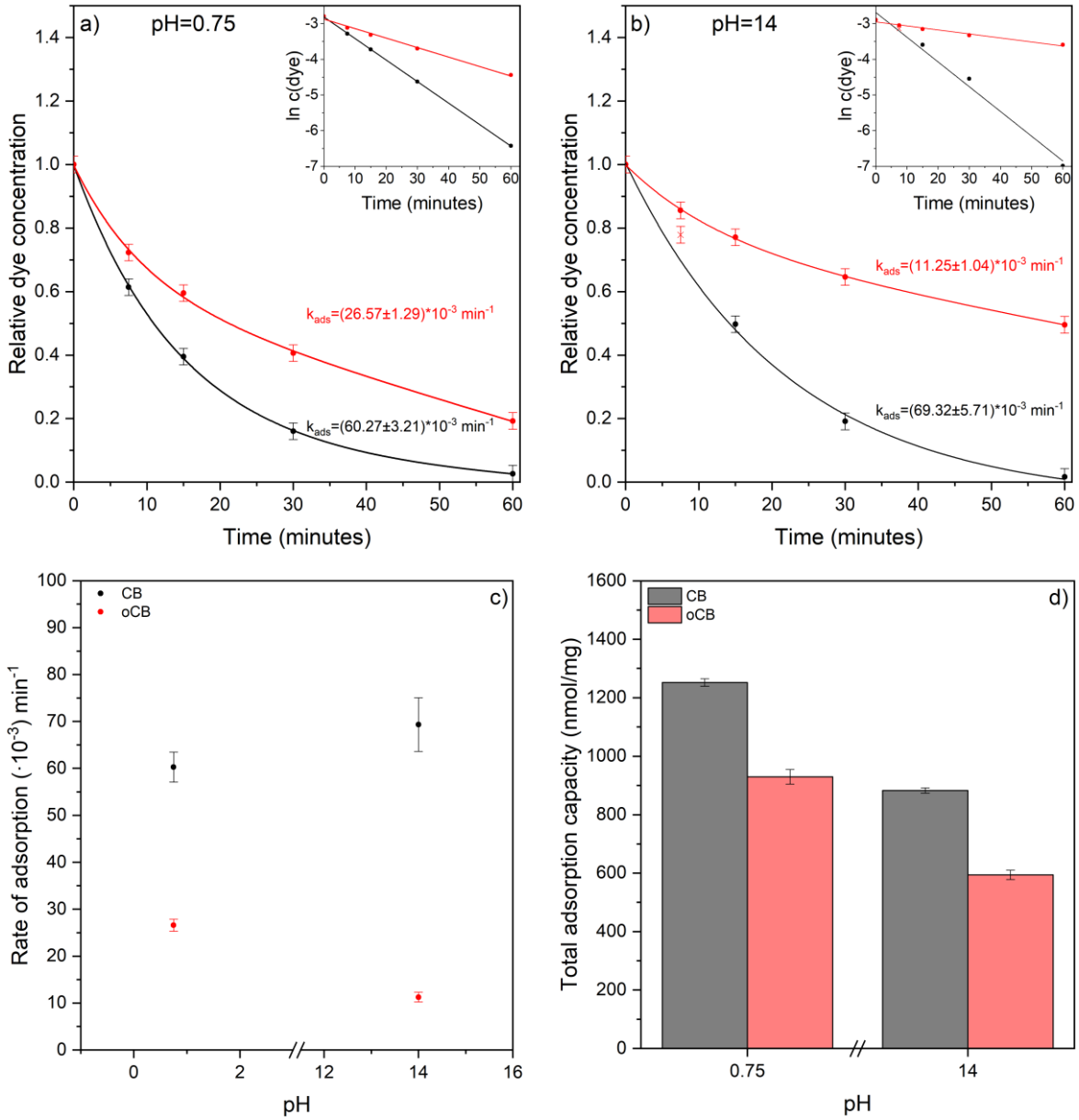

Figure 46 – Results of adsorption studies; **a:** Kinetic curves for the adsorption of AO7 on CB and oCB at pH=0.75; **b:** Kinetic curves for the adsorption of AO7 on CB and oCB at pH=14; **c:** Graph summarising the observed rates of adsorption for CB and oCB at pH values of 0.75 and 14; **d:** Graph summarising the adsorption capacities of CB and oCB at pH values of 0.75 and 14.

Experiments at pH values of 0.75 and 14 also show that adsorption is significantly hindered on oCB, both in terms of adsorptive capacity and adsorption rate (see Figure 46). The adsorption rate of AO7 on CB is only slightly dependent on pH, while in the case of oCB k_{ads} is significantly lower at both pH values, especially at pH=14, than that of CB. This means that in the case of CB the relatively low surface concentration of oxygen functional groups don't create enough electrostatic repulsion, even at pH=14, to hinder adsorption. On the other hand, in the case of oCB the large surface concentration of functional groups on the external surface clearly suppresses adsorption through electrostatic repulsion, since k_{ads} is lower at pH=14 than at

pH=0.75. This suppression is also apparent in the adsorption capacities which are significantly lower at pH=14 in both the case of CB and oCB.

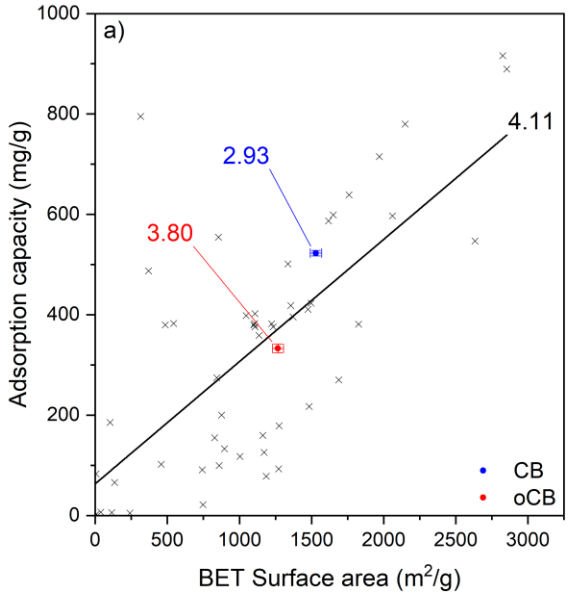

Figure 47 – Graph showing adsorption capacities of ACs against methylene blue along with this work's results. AC datapoints are from [160]

Before continuing the discussion of this chapter it's important to compare the above results against already published adsorption capacities. Santoso *et al.* have compiled a large number of adsorption capacities of methylene blue with different ACs as adsorbents, which serve as good comparisons.[160] These adsorption capacities have been plotted against the surface areas of the material that the numbers belong to, as illustrated by Figure 47, along with the values recorded in this work. This analysis shows that both CB and oCB fit well into the general trend seen with these materials. Furthermore, the average AC material according to Santoso *et al.* have a ratio of BET surface area in m^2/g to adsorption capacity against methylene blue in mg/g of 4.11. Both CB and oCB are below this average which means these materials are better adsorbents than the average of these. This graph also underlines the previous conclusion that the acid oxidation led to both morphological and surface chemistry changes that led to the large decrease in adsorption capacity for oCB compared to CB; the decrease in adsorption capacity is relatively larger than the change in surface area.

4.7.3 Adsorption of Sulfanilic Acid and 2-Naphthol on CB and oCB

To further probe the adsorption mechanisms facilitated by CB and oCB two additional adsorbates were studied. These were initially intended to be sulfanilic acid (SA) and 1-amino-2-naphthol (1-A-2-N) as these are the products of the azo-bond cleavage of AO7.[83]

Additionally, SA contains two polar functional groups on a six membered aromatic ring, so ionic interactions are expected to play a more significant role in the adsorption of it, while 1-A-2-N is a relatively large aromatic molecule where π stacking is expected to play the dominant role in adsorption. Unfortunately, the purchased 1-A-2-N was not suitable for this experiment. A 1.5 mM stock solution was attempted to be made but it did not dissolve in water sufficiently, there was undissolved matter in the flask even after sonication and weeks of storage (see Supplementary figure 14). Because of this 2-naphthol (2-N) was used instead. Both SA and 2-N contain only one functional group that can be deprotonated, as illustrated by Supplementary figure 17 and Supplementary figure 18.

The adsorption of both SA and 2-N were significantly hindered in the case of oCB compared to CB. First, adsorption in neutral media was studied, the results of which can be seen on Figure 48. These results show a similar trend to the adsorption of AO7 on CB and oCB at pH=7, meaning that adsorption is hindered on oCB, although the extent of hindrance is very different in the two cases. Notably, the adsorption of SA on oCB significantly slows down after about 15 minutes, while the adsorption of 1-N is very similar in the case of CB and oCB. This further supports the explanation that Coulombic interactions play a very significant role in the adsorption of organics on CB and oCB, since SA is a much more polar molecule than 2-N.

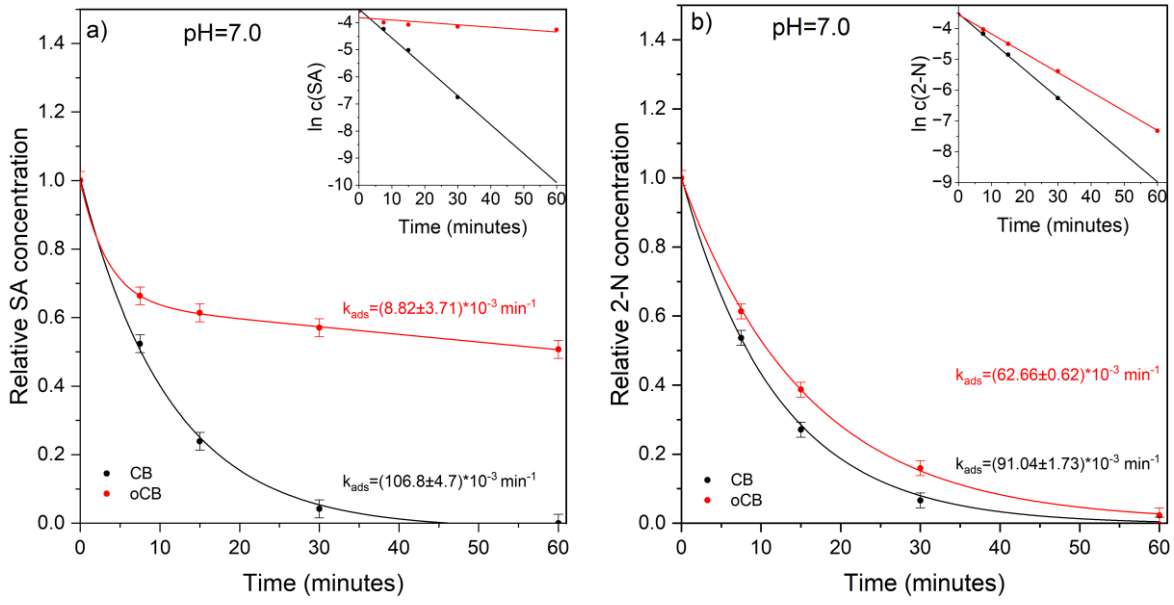

Figure 48 – Kinetics curves for the adsorption of SA (**a**) and 2-N (**b**) on CB and oCB at neutral pH.

After this, the adsorption of SA and 2-N were studied at pH=0.75 and pH=14 at both CB and oCB. In both cases adsorption on CB is independent of pH, which means that ionic interactions don't play a significant role in these processes. The adsorption of SA on oCB on the other hand is strongly affected by pH; the adsorption rate is significantly lower at pH=0.75 when

compared to CB at the same pH, and at pH=14 the adsorption on oCB actually plateaus after about 10 minutes, indicating that the beads are saturated. This means that there must be relatively strong repulsive ionic interactions between the SA molecules and the surface oxygen functional groups. It should also be noted that the ln c(SA) vs time datapoints cannot be fitted with a single line satisfactorily. This means that adsorption in these cases cannot be treated as following pseudo-first order kinetics, but rather something more complex is happening.

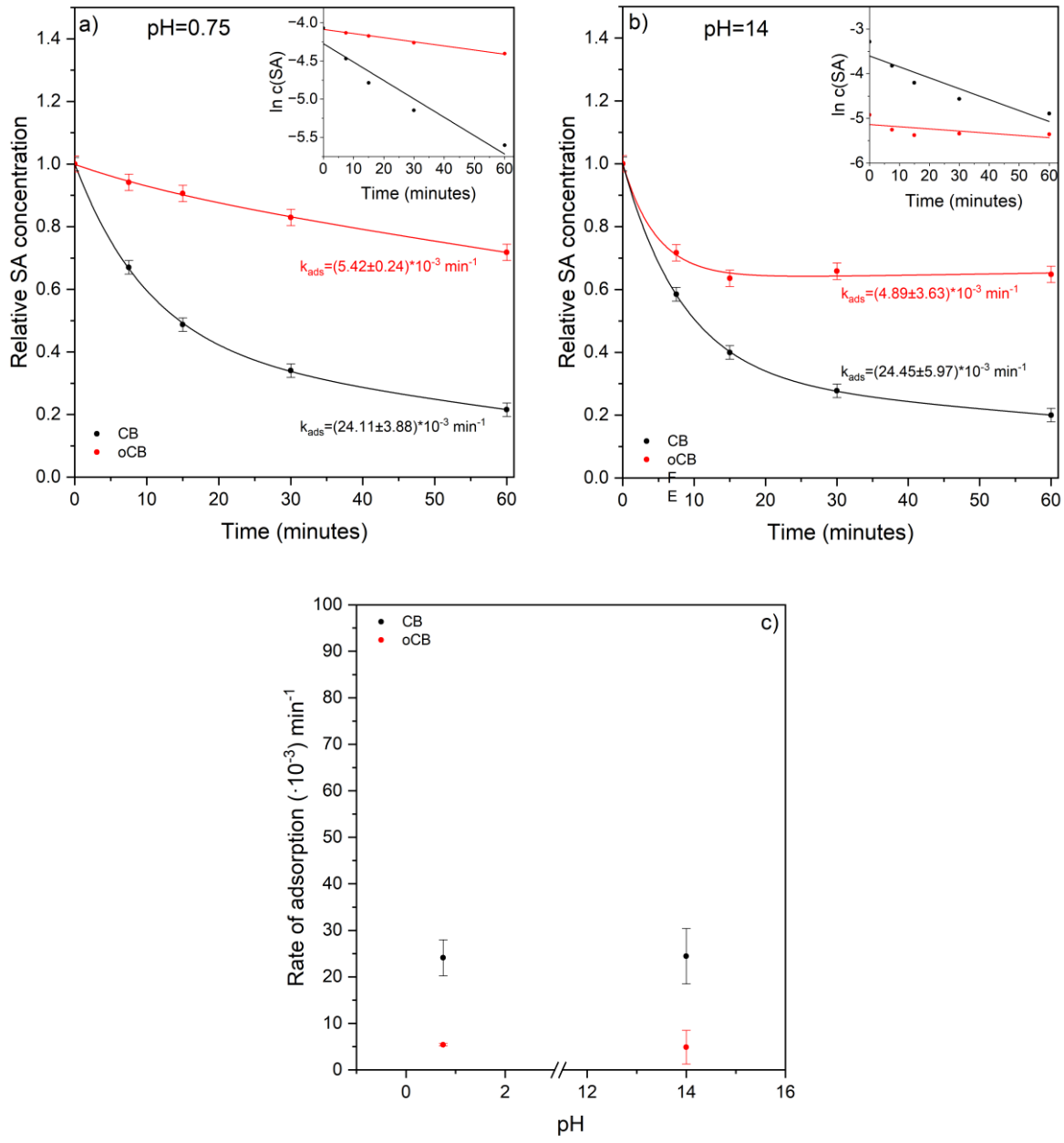

Figure 49 – Kinetic curves for the adsorption of sulfanilic acid (SA) on CB and oCB at different pH values; **a:** pH=0.75; **b:** pH=7.0; **c:** Summary of adsorption rates.

To further probe this both ln c(dye) vs time and 1/c(dye) vs time plots were generated (see Supplementary figure 19). In the case of oCB, adsorption plateaus at about 15 minutes, regardless of what kinetic model is used to interpret the data. The case of CB is more difficult

to interpret, but it is likely that adsorption can be best understood as a process made up of two parts. It is not possible to say whether these are pseudo-first or pseudo-second order processes. In order to enable comparison with other adsorption experiments, a single line was fitted onto ln c(dye) vs time plots as Figure 49 shows, and the slope of these were taken as the rate of adsorption.

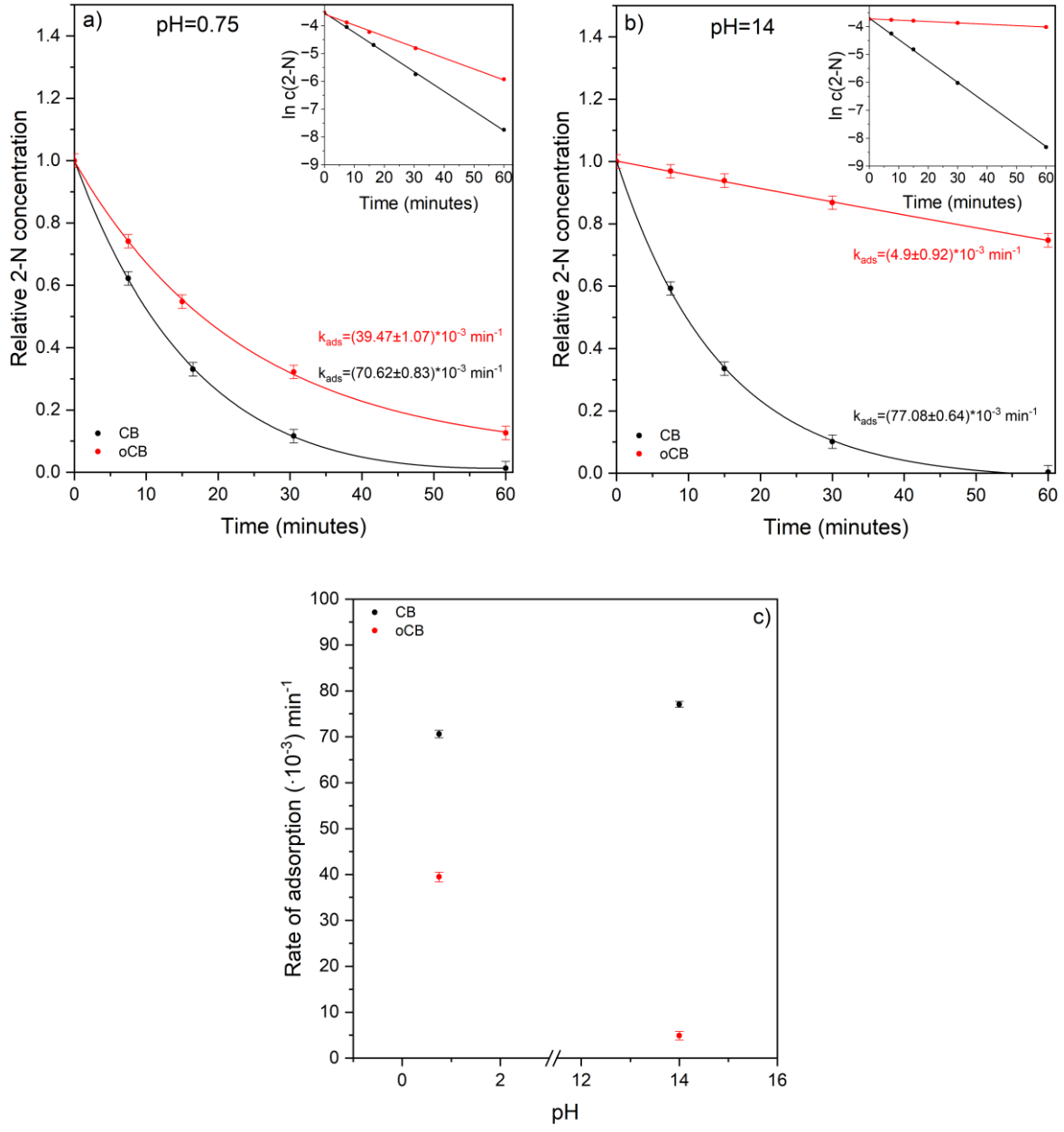

Figure 50 – Kinetic curves for the adsorption of 2-naphthol (2-N) on CB and oCB at different pH values; **a:** pH=0.75; **b:** pH=14; **c:** Summary of adsorption rates;

The kinetic curves for 2-N also show strong hindrance of adsorption on oCB but in this case the difference between pH=0.75 and 14 is much more striking (See Figure 50). Adsorption on CB is independent of pH for 2-N, but in the case of oCB adsorption is strongly hindered at

pH=14. This must be due to the repulsive interaction between the deprotonated surface functional groups of the beads and the electron rich, deprotonated 2-N molecules.

4.7.4 Desorption

Finally, the desorption of dye molecules from the adsorbents was studied in order to gain some insight into whether these materials would be regenerable in a real world setting. To do this a certain amount of untreated and acid oxidised beads were saturated with dye. After this, consecutive hot water washes were used. This method was chosen as water is a good solvent of AO7, and as such is expected to be a suitable regeneration medium.

The adsorption of AO7 on both CB and oCB is largely irreversible, as illustrated by Figure 51. In the case of hot water washes, both for CB and oCB the first wash desorbed the largest amount of dye, but this and by extension the total amount washed off is very small. AO7 is freely soluble in water; its solubility at room temperature is 116 g/L. This means that solubility should not be a barrier to desorption, but to specifically probe this question an additional DMF wash was used.

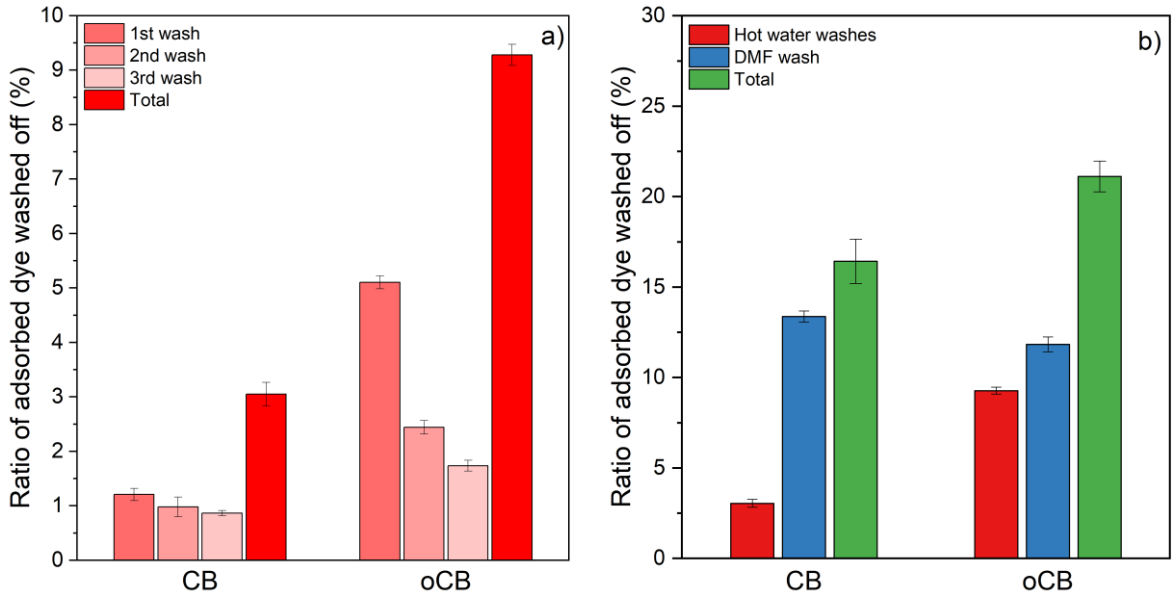

Figure 51 – Graphs showing the results of dye desorption experiments; **a:** Percent of dye having been washed off from CB and oCB in 3 consecutive hot water washes; **b:** Percent of dye having washed of in hot water washed combined, and an additional DMF wash.

According to a literature survey AO7 is most soluble in polar aprotic organic solvents, like DMF and DMSO.[163] The solubility of AO7 in DMF was tested prior to this experiment by adding 5 mg AO7 to 5 mL DMF. AO7 completely dissolved in a matter of seconds, and so its solubility was deemed high enough to not hinder desorption experiments. This additional DMF

wash only removed about 10-12% of the remaining dye so it is safe to say that the overall low desorption is not due to solubility issues. The results of these desorption experiments point to the adsorption of AO7 being mostly irreversible, most likely due to adsorption in micropores. This highlights the need to avoid adsorption as much as possible if composite catalysts are to be made of these beads. The impact of adsorption on catalytic activity will be explored in detail in the next chapter.

4.8 Conclusions and Future Prospects

The work presented in this chapter studies the usage of Piranha solution in the acid oxidation of two macroscale supports. Carbon materials are intensely researched as adsorbents, but their use as catalyst supports is relatively underexplored. Adsorption is not necessarily a desirable process in catalytic processes, like Fenton chemistry, so if these materials are used as supports it is crucial to have a deep understanding of the structure-performance relationships governing sorption characteristics. GNF and CB were chosen as studied carbon materials, since these are macroscale carbon materials of two very common geometry and their acid oxidation with Piranha solution is novel experimental work. GNFs were found to be unchanged by the acid oxidation, while the physico-chemical properties of CB changed drastically. Acid oxidation led to a reduction in surface area, and a disproportionate increase in the concentration of surface functional groups. This led to drastic changes in sorption properties, as well, through the enhancement of repulsive electrostatic interactions between the adsorbate and surface functional groups.

There are some additional studies that could provide a finer grain understanding of adsorption processes on CB and oCB. Diffuse reflectance infrared Fourier-transform spectroscopoy (DRIFTS) could be used to further differentiate the types of functional groups introduced to the surface of CB as a result of acid oxidation. There is a potentiometric titration mentioned in this chapter that could be used to measure the pKa values of surface functional groups, which would help further elucidate how electrostatic interactions affect adsorption processes. Finally, the measurement of heats of adsorption for AO7, SA and 2-N would help in understanding to what extent electrostatic interactions and π-interactions govern adsorption processes.

Chapter 5- Comparative study into the catalytic activity of normal versus acid oxidised macroscale carbon supported mixed metal oxides in Fenton-like organics removal

5.1 Introduction

This project aims to produce a material that has the potential to be exploited industrially, and as such it was an important aspect of experimental design to keep costs and scalability in mind. The aim of this and the next chapter is to create a bifunctional catalyst that can facilitate both the electrocatalytic generation and efficient activation of H_2O_2. After careful consideration, oxides of Co and Mn were chosen as these are commonly used catalysts for H_2O_2 activation and oxygen reduction, respectively. In this chapter the synthesis and usage of neat Co, Mn spinels and their composites with PBSAC and GNF will be discussed. Both the untreated and acid oxidised versions of these supports are used as catalyst supports, in order to study how acid oxidation affects catalytic performance of the resulting composite. Different catalyst loadings were synthesised and tested to gain a deeper understanding of catalytic performance. The metric defined in Chapter 2 will be used here to identify to what extent different removal modes contribute to overall dye removal.

The main aim of this chapter is to describe novel catalyst-support combinations that are intended to be technologically relevant due to their compatibility with packed bed type reactors. Co, Mn spinels in AOPs using H_2O_2 as the oxidant and the usage of macroscale carbon materials as catalyst supports in Fenton-like chemistry are both understudied areas according to a review of the literature; this work aims to contribute to filling this gap.

5.2 Literature Review

5.2.1 Spinels

Spinels are mixed metal oxides that can be generally described as having an $A_xB_{3-x}O_4$ structure. For the sake of simplicity, in this work only spinels containing metal ions of similar sizes will be discussed. All spinels can be categorised as normal or inverse. In normal spinels metal ion A occupies tetrahedral sites, while metal ion B occupies octahedral sites. In inverse spinels half of the ions in the octahedral sites are swapped for ions in the tetrahedral sites. The most common metal centre oxidation states in spinels for sites of A and B are +2, +3, and +4.

[164] The simplest examples of Co and Mn containing spinels are the binary oxides Co_3O_4, and Mn_3O_4.

Co_3O_4 is a normal spinel with a cubic close-packed lattice where Co(II) ions occupy the tetragonal sites, while the Co(III) ions occupy the octahedral sites. [165] The Co(II) ions are in a high spin state, while the Co(III) ions can be high, intermediate or low spin depending on further crystallographic factors. For example, Long *et al.* reported that Co(II) ions can migrate to the surface of Co_3O_4 crystals, forming amorphous islands of CoO phases, which reduces the bulk Co(II) ratio, and by extension affect the solid state properties of Co(III) ions. [166] This process creates crystalline-amorphous interfaces, and an abundance of defects in the crystalline domains, which leads to markedly different adsorption and catalytic activities, and highlights that there can be very large differences in catalytic performance between different Co_3O_4 samples. Co(II,III) oxides are commonly used in experimental work in energy applications, such as Li-ion battery electrode materials. [4-5]

Mn_3O_4 is also a normal spinel, where the Mn(II) ions occupy the tetrahedral sites, while the Mn(III) ions occupy the octahedral ones, but unlike Co_3O_4 it's phase symmetry is reduced to tetragonal. This is due to the tetragonal Jahn-Teller distortion of the relatively large amount of Mn(III) in the lattice. [169] In the case of Mn(II,III) oxides both metal ions are in a high spin state. Mn(II,III) oxides are extensively used as catalysts of many different processes, including Fenton-like chemistry and battery electrode applications. [7–9]

Co, Mn spinels are extensively researched for use in energy applications, which allows for a thorough description of synthetic procedures and the physical properties of resultant materials. Spinels have traditionally been prepared using solid-state methods, but these often produce materials of large, irregular particles. [164][172] It is still quite challenging to produce homogeneous, nanocrystalline spinels under mild conditions, but the most common approaches include hydrothermal, solvothermal, and sol-gel methods. [11-12] In the production of $Co_{3-x}Mn_xO_4$ spinels, one of the most impactful crystallographic issues is that high Mn content reduces the otherwise cubic symmetry to tetragonal due to the Jahn-Teller distortion of Mn(III) ions. Rios *et al.* have reported that in the case of this class of spinels at room temperature cubic phase crystals will form if $x<1.3$, cubic and tetragonal phases coexist if $1.3<x<1.9$, while if $1.9<x<3.0$ then only the tetragonal phase will form. [175] While Mn-rich cubic $Co_{3-x}Mn_xO_4$ spinels have been observed at higher temperatures, these will spontaneously transform into tetragonal phase on quenching, so producing cubic Co, Mn spinels on a wide

composition range is still a challenge. [176] A notable research article that reports the synthesis of such materials was published by Li *et al.* where the authors were able to produce cubic and tetragonal spinels of Co:Mn ratios of 2:1, 1:1, and 1:2. [177] The main way in which Li *et al.* identified these materials is through XRD. Co and Mn ions are roughly similar in ionic radii at the same oxidation states[10], which on one hand means that these ions are interchangeable with minimal crystallographic distortion in the same lattice. On the other hand it means that Co_3O_4 is a good reference for cubic Co, Mn spinels, while Mn_3O_4 is a good reference for tetragonal Co, Mn spinels. Accordingly Li *et al.* have used the binary oxides as their references. The simulated X-ray diffractograms of these materials are shown by Figure 52, along with X-ray diffractograms of Li *et al.* of Co, Mn spinels.

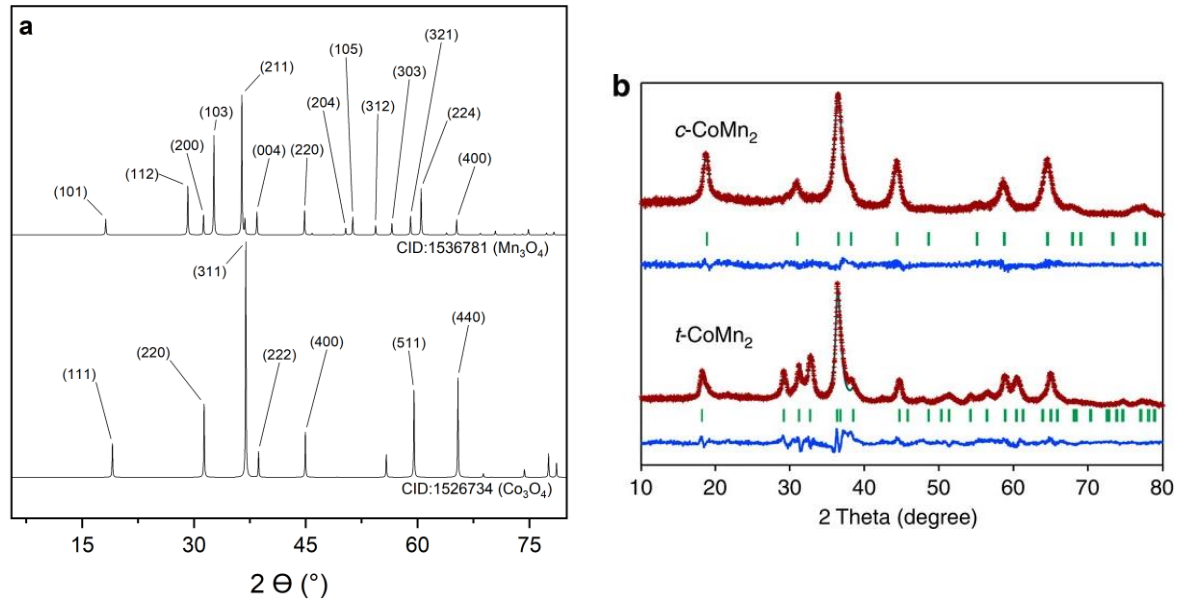

Figure 52 – X-ray diffractograms of Co, Mn spinels; **a:** reference diffractograms generated from published CIFs; **b:** Diffractograms of cubic and tetragonal $CoMn_2O_4$ spinels [177]

5.2.2 Co, Mn Spinels in AOPs

There are very few literature articles about Co, Mn spinels in AOPs using H_2O_2 as the oxidant, so other tangentially relevant publications will also be used to showcase the applications of these materials. When Co, Mn spinels are produced without a template or support, these materials tend to form large aggregates of various morphologies on the order of microns. Many researchers use the Scherrer-equation to give a rough estimate of crystallite

[10] The ionic radius of Co(II) ions in a high spin state and octahedral geometry is 75 pm, while Mn(II) ions in the same state and geometry are 83 pm. Co(III) ions in high spin states and octahedral geometries have ionic radii of 61 pm, while Mn(III) ions in the same state and geometry have ionic radii of 65 pm. Co(III) ion in low spin states and octahedral geometries have ionic radii of 55 pm. [244]

sizes, which are generally in the 5-90 nm range. [16–18] This wide range highlights that one of the main physical properties that researchers target in tailoring materials to an application is crystallinity; Co, Mn spinels can be synthesised from amorphous and nanocrystalline materials to several micron large single crystals. [19-20] This large range in crystallinity also translates to a wide scale of surface areas reported in the literature, with most materials having surface areas of 3-180 m^2/g. [16-17][21–26] The main reason for such a wide range in the crystallinity of a sample is that certain synthetic procedures introduce defects into the lattice, which affects physical and catalytic properties. Yang *et al.* have reported that the ratio of Co to Mn salts used in the synthetic mixture and the calcination temperature of the intermediate product can be used to control the amount of oxygen vacancies in the resulting material. [179] According to these authors calcination temperature is inversely proportional to the amount of oxygen vacancies detected in the sample via XPS; the overall oxygen signal did not change as calcination temperature increased but the ratio of oxygen vacancy to lattice oxygen increased. They also reported that the ratio of Co:Mn defined the local chemical environment of the resulting vacancies, which played a significant role in how active the resulting catalyst is. They found that maximum catalytic activity in AOP experiments using peroxymonosulfate (PMS) as the oxidant was exhibited by the catalyst that had a Co:Mn ratio of 2:1, and contained a good balance of lattice and defective oxygen sites, which in their case meant about 40% oxygen vacancies. The authors claim that this balance of oxygen species allows high catalytic activity through the favourable sorption mechanics of the oxidant, but is also stable enough that the highly oxidising reaction conditions do not change the interface of the catalyst over the course of the reaction. Additionally Co_2MnO_4 contains three redox couples, which can also react internally. This means that catalytically active metal centres can rapidly cycle between oxidation states, explaining the high catalytic activity. Similarly Wang *et al.* have reported in 2016 that the most active catalyst of PMS activation in toluene degradation was one that contained Co and Mn at a ratio of 2:1, with oxygen vacancies of about 32% according to XPS measurements. [180] They claim that these factors allowed the catalyst to rapidly cycle between different oxidation states of both Co and Mn, and by extension generate ROS at a very high rate. It is also worth considering the work of Zhang *et al.*, who studied the catalytic activity of Co, Mn spinels in the activation of peracetic acid for the degradation of antibiotics. [189] In addition findings similar to the aforementioned articles, they have reported that there is a synergistic electronic interaction between Co and Mn ions, which to a large part explains the

high catalytic activity of these mixed metal oxides. They found that the presence of both Co and Mn ions in close proximity enhanced electron transfer between the catalyst and the oxidant, promoting the reduction of Co(III) to Co(II) which is a crucial step of the catalytic cycle. According to their publication the presence of Mn ions close to Co ions also changes the distribution of bonding and antibonding states on Co 3d orbitals which leads to more favourable binding of the oxidant. Finally, an article published by Wang *et al.* in 2022 studied the catalytic activity of Co, Mn spinels in the activation of H_2O_2 for the degradation of ciproflaxin. [190] They found that the generation of $OH^{\cdot}$ radical proceeded through the adsorption of H_2O_2 on the surface of the catalyst, and the subsequent cleavage of the O-O bond. According to this article the high catalytic activity of Co_2MnO_4 when compared to Mn_2O_3 and Co_3O_4 is due to the larger amount of Lewis-acid sites, which in this case means oxygen vacancies, which leads to more energetically favourable adsorption of H_2O_2 and desorption of $OH^{\cdot}$.

5.2.3 Supported Co, Mn Spinel Catalysts

There are very few articles published about supported Co, Mn spinels being used in AOPs, and they are all from the last 5 years. There are some publications about such catalysts where the support is another inorganic material but this is not relevant for this thesis, so these will not be discussed. There is only one article indexed by Scopus at the time of writing that can be used as a good example of carbon supported Co, Mn spinels in AOPs. Researchers Kang and Hwang embedded Co_2MnO_4 into hollow carbon nanofibers, and this composites catalyst was then used in the activation of PMS for the degradation of Rhodamine B. [191] This article is the most relevant for this work, although in the case of Kang and Hwang, the catalyst impregnated carbon nanofibres were made in one step by the researchers instead of decorating commercially available carbon nanofibres. They prepared composite of Co_3O_4, $CoMn_2O_4$ and Mn_3O_4 and nanofibres, and compared their catalytic activity in dye degradation experiments. The structure of the catalyst is illustrated by Figure 53. They found that the presence of the carbonaceous support greatly enhances the catalytic cycling of metal centres by facilitating the transfer of electrons between metal ions of different oxidation states and even metal ions and oxidant molecules. They also reported that the combined leaching of Co and Mn was less than 1 ppm in the case of the most active composite after 80 minutes. For comparison in the case of commercial Co_3O_4 and Mn_3O_4 in the same reaction they recorded leaching of 5 and 3 ppm, respectively. They reported rate constants ranging between 0.0871-0.3406 min^{-1}, as illustrated

by Figure 53. These kinetic curves also serve as a good example of how widely k values can range for the same reaction with changing reaction parameters.

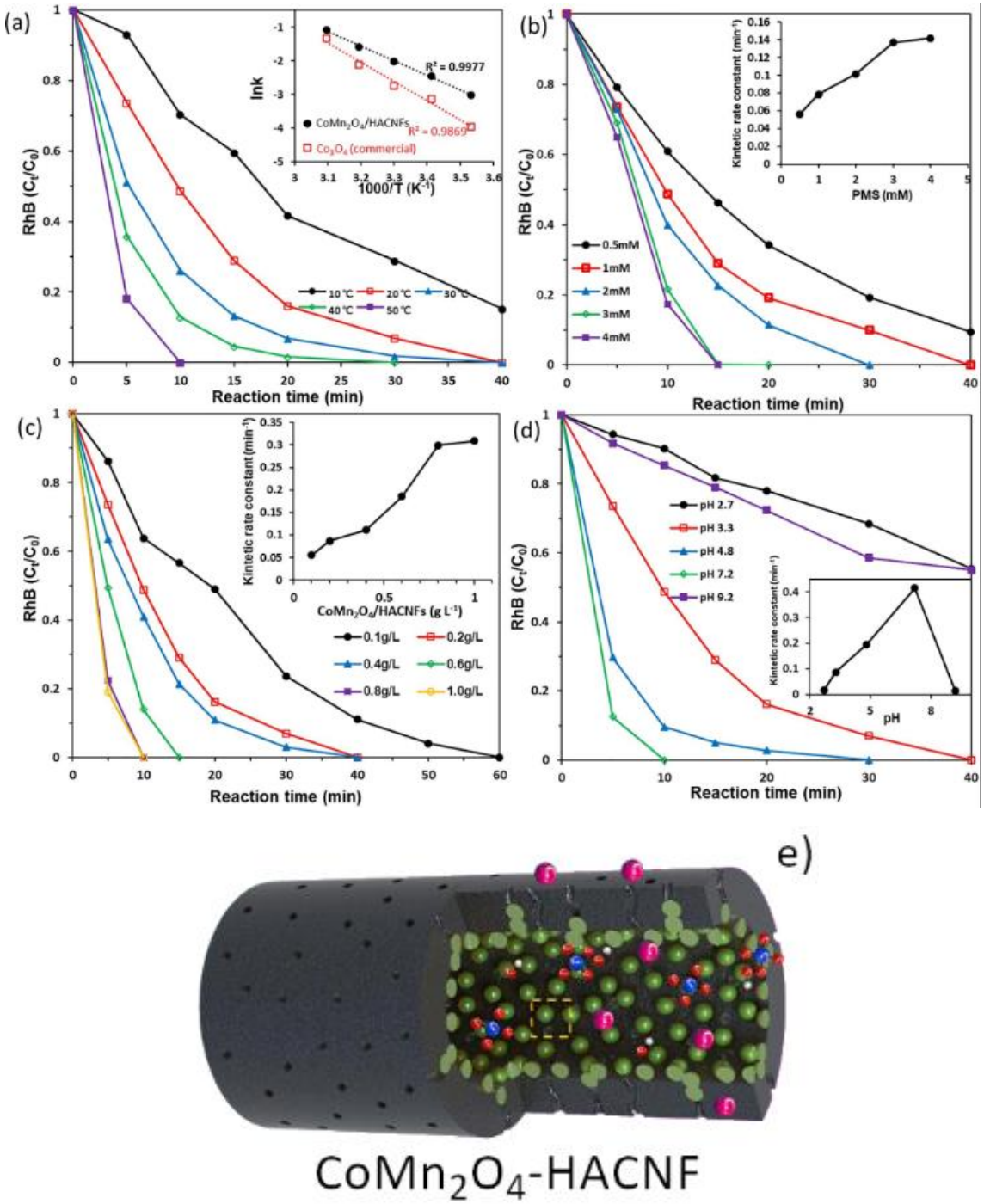

Figure 53 – Results of Kang and Hwang for the study of Co, Mn spinel impregnated carbon fibres in dye degradation experiments; **a-d:** Kinetic curves of dye removal experiments with different experimental conditions using $CoMn_2O_4$-HACNF composite catalyst; **e:** Schematic representation of Co, Mn spinels anchored to hollow activated carbon nanotubes; green spheres represent catalyst particles, purple spheres represent dye molecules, while the red and blue molecules represent the oxidant. [191]
Experimental conditions: 0.02 mg/ml catalyst, c(Rhodamine B)=50 µM, c(PMS)=1 mM, pH=3.28 unless otherwise noted.

Unfortunately, it is quite difficult to properly compare the catalytic activity of different materials in the literature, as there is no single metric that is used for this and researchers often

omit crucial experimental details like pH or catalyst loading. Most researchers simply use the rate of degradation or percentage dye removal in a certain amount of time to assess the catalytic activity of their materials. This can be misleading, as most researchers don't take into consideration dye removal modes other than degradation, but also because this value is highly dependent on the reaction parameters used, and as such is not universally comparable. Traditionally used catalysis metrics like turnover number and frequency are not suitable for this application, at this time, as it is not possible to quantify the number of active sites in these catalysts. In any case, to enable comparison between the work of different groups it is crucial that researchers quantify dye removal by a certain amount of the catalyst instead of simply relying on k values.

In summary, while the field of Fenton-like chemistry is very active, there are very few articles published using Co, Mn spinel catalysts, even though the existing publications identified these materials as highly active in Fenton-like organics removal experiments. The main challenge of this field is generally the same as what was identified in Chapter 1, which is the lack of a unified metric that could serve as an easy way of comparing catalysts. Another gap in published research findings is that despite the diversity of the field there are virtually no publications discussing the usage of composites made with macroscale carbon supports; most supported catalysts contain graphene-derivatives, graphitic carbon nitride and other similar materials which would pose serious challenges in scaling up organics removals towards industrial scales. The work presented in this chapter reports the synthesis of Co, Mn spinels, supported on normal and acid oxidised carbon beads and nanofibres, and the usage of these materials in Fenton-like organics removal experiments. The effect of acid oxidation on catalyst anchoring and catalytic performance is discussed supported by extensive characterisation of these materials. Finally the previously defined metrics are used to evaluate the catalytic performance of the prepared composites catalysts.

5.3 Experimental Details

5.3.1 Chemicals

The H_2O_2 (30% w/v) used in these experiments was purchased from Fischer Scientific and was stored at 5 °C. The Co(II) nitrate (≥97% purity) was purchased from Scientific Laboratory Supplies, while the Mn(II) sulfate (≥99% purity) was purchased from Sigma-Aldrich. The NH_3 solution (35%) was purchased from Fisher Scientific.

5.3.2 Methods

5.3.2.1 Spinel Synthesis

All four spinels were produced using the same method, which is based on the synthesis published by Chun *et al.*. [192] The preparation of the slurry was done by slowly adding NH_3 solution (4.65 mL; 35%) to a 0.2 M Co(II) solution made with ultrapure water while stirring at 600 rpm. After this a 0.2 M Mn(II) solution was added, and the mixture was then kept at 30 °C for 2 h with the same stirring as above. The exact amounts are summarised in Table 4; the overall volume of the reaction mixture was always 24.5 mL. Finally, the reaction mixture was put into a hydrothermal reactor, and was heated to 180 °C for 4 h. The reactor was put into the room temperature furnace, and the specified time was measured from the point of reaching 180 °C. The resulting solids were separated via vacuum filtration, the materials were washed with ultrapure water (3 x 50 mL) and acetone (3 x 50 mL), and were then dried in a vacuum oven overnight at 70 °C, 0.1 bar. This leads to the formation of cubic spinels in the case of the Co, Mn spinels. The spinels that contained Co were collected as a fine black powder, while Mn_3O_4 was a flaky, brown solid. Yields are presented in the Discussion of results subchapter.

Table 4 – Exact make-up of metal salt solutions used in the hydrothermal syntheses

	Spinel to be produced			
	Co_3O_4	**Co_2MnO_4**	**$CoMn_2O_4$**	**Mn_3O_4**
Co(II) solution	3.26 mmol + 24.5 mL water	3.26 mmol + 15.3 mL water	1.63 mmol + 8.15 mL water	0 mmol + 0 mL water
Mn(II) solution	0 mmol + 0 mL water	1.63 mmol + 8.15 mL water	3.26 mmol + 15.3 mL water	0.33 mmol + 24.5 mL water

5.3.2.2 Composite Synthesis

Each composite was produced through a synthetic method adapted from the production of neat Co_2MnO_4. First, a certain amount of the carbon support (see Table 5) was dispersed in NH_3 solution (4.65 mL, 35%), to which then a Co(II) solution (0.2 M, 15.3 mL) made with ultrapure water was added while stirring at 600 rpm. After this a Mn(II) solution (0.2 M, 8.15 mL) was added, and the mixture was then kept at 30 °C for 2 h with the same stirring as above. Finally, the reaction mixture was put into a hydrothermal reactor, and was heated to 180 °C for 4 h. The reactor was put into the room temperature furnace, and the specified time was measured from the point of reaching 180 °C. The resulting solids were separated via

vacuum filtration; the materials were washed with ultrapure water (3 x 150 mL) and acetone (3 x 150 mL), and were then dried in a vacuum oven overnight at 70 °C, 0.1 bar.

The CB and oCB composites were collected as a mixture of matte black beads (as opposed to the shiny undecorated CB and oCB beads) and unsupported catalyst aggregates, while the GNF and oGNF composites were a mixture of unsupported catalyst particles and fibres that were visually identical to undecorated GNF and oGNF. Yields of these syntheses are compiled in Table 6.

Table 5 – Exact amounts of carbon supports used in the production of each composite

Catalyst loading to be produced (%)	**m (GNF or oGNF) (mg)**	**Catalyst loading to be produced (%)**	**m (CB or oCB) (mg)**
23.8	1250	**16.7**	1950
31.3	856	**28.6**	975
38.3	628	**37.6**	650
55.5	313	**42.9**	520
71.3	156	**47.4**	433

5.3.2.3 Estimation of unsupported catalyst percentage

100 mg of CB and oCB supported catalyst was added to 5 mL water, the mixture was then sonicated for 1 min, and all of the liquid decanted. This was repeated three times. Then 5 mL of acetone was added, the vial was closed, shaken for 30 s, and the liquid decanted. The solids were then vacuum dried and the mass loss was measured.

5.3.2.4 Dye Removal Experiments

Dye degradation experiments were done using 1.59 mM AO7 solution, 7.5 mL 30% m/V H_2O_2, and 32.5 mL ultrapure water in a 100 mL roundbottom flask. The reaction vessel was submerged up to its neck in 500 mL 18 °C tap water, held by a 600 mL beaker. Both of these liquids were stirred at 600 rpm in each experiment. The amount of GNF and oGNF composites was such that it always contained the same mass of Co_2MnO_4 (25 mg), as set out by Table 7. This corresponds to 0.6 mg/mL catalyst concentration.

Table 6 – Recorded yields of each composite type

Catalyst loading (%)	**Co_2MnO_4-GNF**	**Co_2MnO_4-GNF**	**Catalyst loading (%)**	**Co_2MnO_4-CB**	**Co_2MnO_4-oCB**
23.8	90.8	90.9	**16.7**	99.2	100.1
31.3	97.6	97.9	**28.6**	102.4	64.1
38.3	99.5	100.2	**37.6**	100.5	39.8
55.5	101.3	101.8	**42.9**	101.1	96
71.3	104.9	104.8	**47.5**	77.9	99.5

Samples of 800 µL were taken before the catalyst was added and at 7.5, 15, 30 and 60 min after the catalyst was added. The sample was passed through a 0.2 µm pore size hydrophilic PTFE syringe filter and its absorbance was measured immediately after the sample was taken.

Similarly, the CB and oCB composites were also used in a way that ensured that there was always the same amount of catalyst present, which in these cases was 12.5 mg Co_2MnO_4. (See Table 8). This corresponds to 0.3 mg/mL catalyst concentration.

5.3.2.5 Saturation of CB, oCB Composites

A batch of 62.5 mg of 16.7% Co_2MnO_4-CB and 16.7% Co_2MnO_4-oCB each were put into 15 mL 1.5mM AO7 solution for 3 days. Then the mixture was centrifuged at 10000 rpm for 10 min and the liquid was decanted. The materials were then resuspended in a dye degradation reaction mixture of the same composition of other such experiments in this chapter. These catalysts are referred to as presaturated in the discussion of results.

Table 7 – Summary of the amount of catalyst used of each loading in any dye degradation or adsorption experiment along with the corresponding active phase content for Co_2MnO_4-GNF and Co_2MnO_4-oGNF composites

Catalyst loading (%)	**m(Co_2MnO_4-GNF) (mg)**	**m(Co_2MnO_4) (mg)**	**m(Co_2MnO_4-oGNF) (mg)**	**m(Co_2MnO_4) (mg)**
23.8	105.7	25.2	105.7	25.2
31.3	80.2	25.1	80.2	25.1
38.3	66.3	25.4	66.3	25.4
55.5	45.2	25.1	45.2	25.1
71.3	35.4	25.2	35.4	25.2

Table 8 – Summary of the amount of catalyst used of each loading in any dye degradation or adsorption experiment along with the corresponding active phase content for Co_2MnO_4-CB and Co_2MnO_4-oCB composites

Catalyst loading (%)	**m(Co_2MnO_4-CB) (mg)**	**m(Co_2MnO_4) (mg)**	**m(Co_2MnO_4-oCB) (mg)**	**m(Co_2MnO_4) (mg)**
16.7	74.9	12.5	74.9	12.5
28.6	43.7	12.5	43.7	12.5
37.6	33.2	12.5	33.2	12.5
42.9	29.1	12.5	29.1	12.5
47.5	26.3	12.5	26.3	12.5

5.4 Discussion of Results

5.4.1 Characterisation of Co, Mn Spinels

In the first part of this project four different Co, Mn spinels were synthesised through the same hydrothermal method. This method can be used to produce any Co, Mn mixed spinels of $Co_{3-x}Mn_xO_4$ structure, but in the case of this project materials of x=0, 1, 2, 3 were produced, which means Co_3O_4, Co_2MnO_4, $CoMn_2O_4$ and Mn_3O_4. This procedure involves the preparation of an intermediate slurry and its subsequent hydrothermal treatment. Chun *et al.*, the original authors of this method, omitted crucial details from their publication, namely how exactly the heat treatment was done; they only published that this step is done at 180 °C for 40 min. An assumption was made that this step is a hydrothermal treatment, since these are very common in the production of Co, Mn spinels. [31–33] This method worked well in the production of Co_3O_4 and Co_2MnO_4, but $CoMn_2O_4$ and Mn_3O_4 were still not possible to produce in a phase-pure way (For a representative diffractogram of early samples see Supplementary figure 20). It was found that both increasing the hydrothermal temperature or length led to the disappearance of MnOOH traces, but it was also found that increasing the temperature significantly affected the estimated crystallite size, so increasing the length of this step to 4 h was chosen (See Supplementary figure 21, Supplementary figure 22) . The reaction steps are also illustrated by schematic equations (36) and (37). [192]

The production of Mn_3O_4 required significantly more optimisation to reach phase-pure production than any of the other spinels. When Mn_3O_4 was attempted to be produced using the method that was used for the other Co:Mn ratios the desired product only formed on the

walls of the PTFE insert of the hydrothermal reactor, with the bulk slurry being mostly unchanged (see Supplementary figure 22). Several changes to the synthetic method were tried like excluding oxygen from the reaction space, or increasing the length and temperature of the hydrothermal treatment but none of these led to the full disappearance of the MnOOH phase. The final synthetic procedure used a reaction mixture that was 10-times more dilute for the Mn(II) salt, but otherwise identical.

$$Co^{2+} + NH_3 + Mn^{2+} + O_2 \rightarrow [Co(NH_3)_6]^{2+} + MnOOH + Mn_7O_{13} \quad (36)$$

$$[Co(NH_3)_6]^{2+} + MnOOH + Mn_7O_{13} \xrightarrow{\text{Hydrothermal treatment}} Co_{3-x}Mn_xO_4 \quad (37)$$

Due to the nature of these spinels, it is difficult to calculate accurate percentage yields for all four materials, since the mixed spinels can precipitate as other ratios than 2:1 and 1:2 Co: Mn, and knowing this ratio is crucial for calculating the yield. Not all batches were analysed with XPS so these ratios are not known for all samples, and the oxygen content can also vary slightly. Nonetheless, if we assume that the product is exactly Co_2MnO_4 or $CoMn_2O_4$ and nothing else, then the average yield of their syntheses are 100.9±3.3 and 100.5±1.6%, respectively. These values were calculated with sample masses after vacuum drying but it has to be assumed that there is still some amount of water bound to the crystals. More discussion of this issue to follow in later subchapters. The yields of Co_3O_4 syntheses were calculated to be 96.7±1.2%, while Mn_3O_4 was produced with a yield of 96.1±2.8% yield. All calculations were based on the products of three identical syntheses.

The general approach producing the materials of this chapter was that the synthetic process of the neat metal oxide would be optimised, and then this would be used to produce composites without further optimisation.

Spinel	**Average production** (mg)	**Standard deviation**
Co_3O_4	252.1	3.1
Co_2MnO_4	391.2	13.2
$CoMn_2O_4$	381.5	5.7
Mn_3O_4	24.0	0.7

5.4.2 Bulk Characterisation

X-ray diffraction was the main tool used in guiding the optimisation of the synthetic procedure, so these results are discussed first.

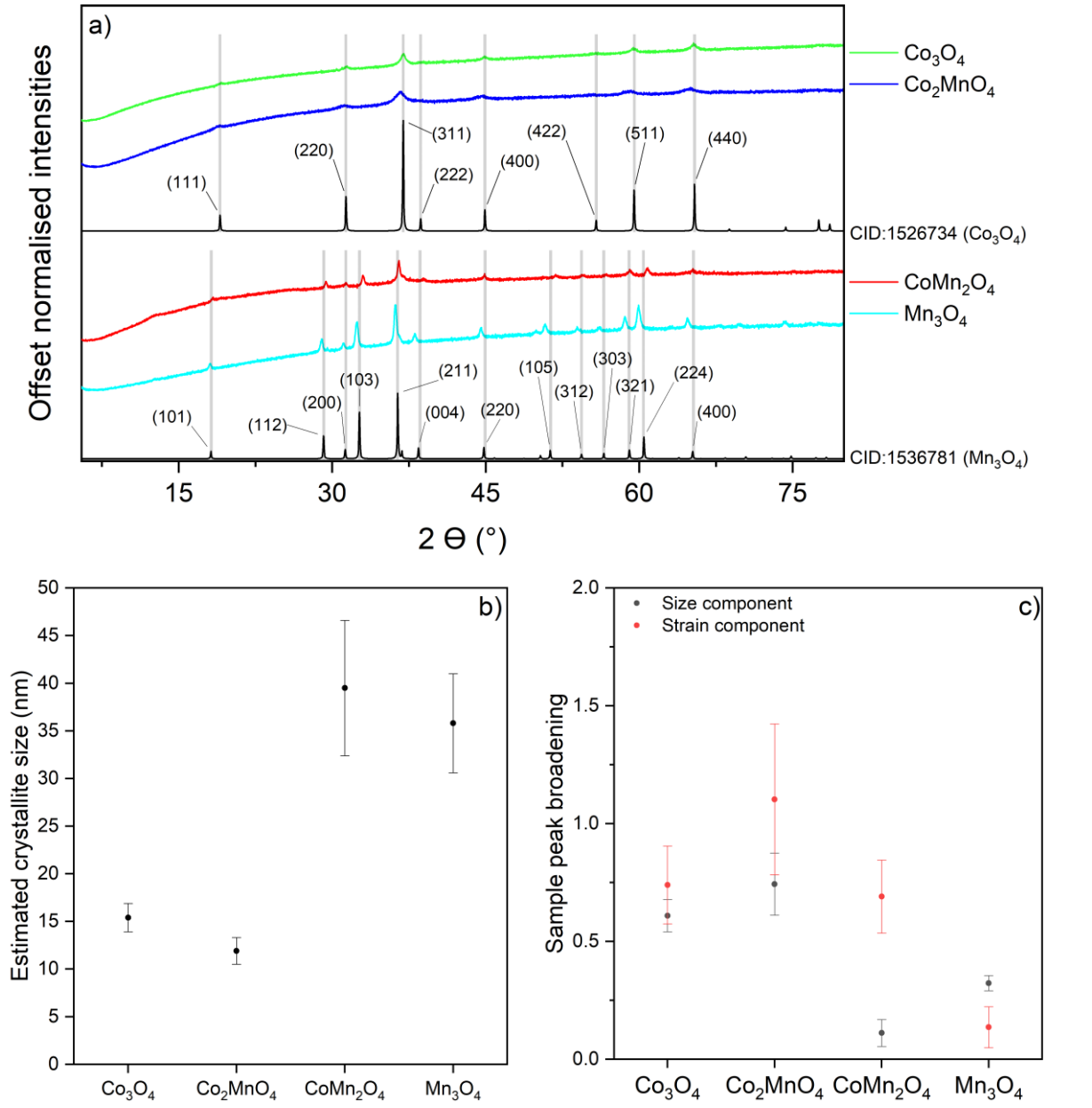

Figure 54 – **a:** X-ray diffractograms of the prepared Co, Mn spinels along with a relevant simulated reference diffractograms; **b:** Results of Williamson-Hall analysis showing different contributions to XRD peak broadening; **c:** Average crystallite sizes estimated using the Scherrer-equation.

The final products of the optimised synthesis produced low intensity XRD peaks, but otherwise the diffraction pattern allowed good identification as illustrated by Figure 54. All diffractograms show significant deviation from a flat baseline, which is due to the X-ray fluorescence of Co and Mn ions when XRD analysis is done with a Cu anode. The two main factors resulting in low intensity of these peaks are poor crystallinity and small crystallite size; this issue will be discussed in more detail later on in this subchapter. The X-ray diffractograms of these Co, Mn spinels were identified using Co_3O_4 or Mn_3O_4 reference patterns (CID:1526734 and CID:1536781, respectively). These matched the binary oxides quite well. The diffractogram of Co_2MnO_4 shows a slight shift towards smaller 2θ values when compared to Co_3O_4, while the

peaks of $CoMn_2O_4$ are slightly shifted towards larger 2θ values compared to Mn_3O_4. According to Bragg's law smaller diffraction angles are associated with larger interatomic spacings, and vice versa. A Co_2MnO_4 lattice can be thought of as a Co_3O_4 lattice where Co(III) ions (61 pm) have been swapped for Mn(III) ions (65 pm), while $CoMn_2O_4$ can be thought of as a Mn_3O_4 lattice where Mn(II) ions (83 pm) were swapped for Co(II) ions (75 pm). This explains the shifts in diffraction patterns. The diffractograms were exaggerated to 3-times the recorded intensities to better show the otherwise low intensity, broad peaks.

Secondary analysis of this data was used to try to uncover the source of peak broadening. Two methods were used, the Scherrer-method and the Williamson-Hall method, but due to the limitations of these methods and the X-ray fluorescence of the samples, only tentative conclusions can be drawn. The Scherrer-method is often used to estimate the size of coherently diffracting crystalline domains, which is a lower limit for particle size. This method is considered rudimentary at best, as it makes a number of assumptions, the two main ones being that particles are spherical and that peak broadening is entirely due to size effects. Nonetheless, it can be used to draw the conclusion that the two Co-containing spinels are significantly different from the Mn-containing spinels, due to some mixture of size and strain effects (see Figure 54b). The Williamson-Hall method is more appropriate for differentiating between size and strain effects, but it works best with diffraction patterns free of distortions like X-ray fluorescence. It is important to note that the Williamson-Hall plot shows the components of line broadening and their extent, but these are often inversely proportional to the physical property that causes the line broadening. For example, a small size component means that the peak broadening is due to size effects only to a small extent, which would mean that the coherently diffracting domains are large. [196] The trend in size components mirrors the trend in crystallite sizes estimated with the Scherrer method. The strain component of these spinels shows a trend where the less Mn is in a sample, the more microstrain it is showing. This trend will be further discussed in the XPS Analysis subchapter. Overall Co_2MnO_4 exhibits the largest size and strain component. This means that this material contains the smallest crystallites, and also has the largest amount of microstrain.

After X-ray diffraction analysis, an attempt was made to image these materials using SEM, but this was relatively uninformative, as all four materials formed large, poorly defined aggregates (see Supplementary figure 24 - Supplementary figure 27). It can be said however

that the more Mn there is in a sample, the more likely it is to show clear particle boundaries and to be heterogeneous in terms of particle size and shape.

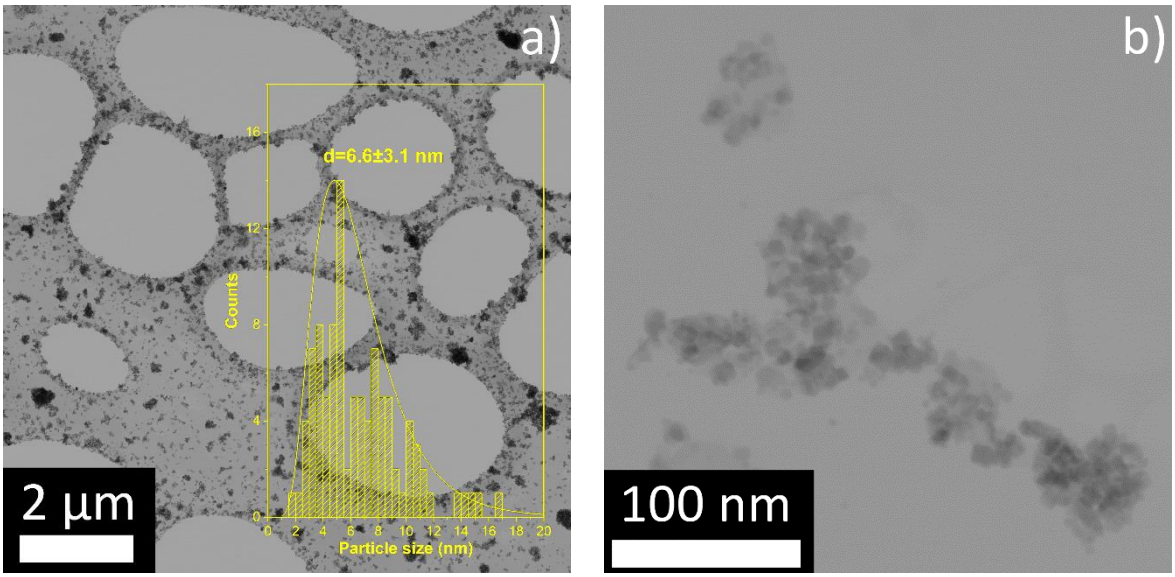

Figure 55 – Bright field STEM images of Co_2MnO_4 samples; **a:** Image at lower magnification, showing the metal oxide particles scattered across the surface of the lacy carbon support film on the sample holder; **b:** Higher magnification image of individual particles.

TEM was also considered in the analysis of these materials, but only in the case of Co_2MnO_4 was it actually used, because as later results show, this spinel showed the highest catalytic activity. The mean particle size was found to be 6.6 ± 3.1 nm. The particles are very small, which partly explains the low intensity, broad XRD peaks. As part of the TEM analysis XRF was used to measure the elemental composition of the sample, which showed a Co:Mn ratio of 1.6:1.0.All four of these Co, Mn spinels were also analysed via N_2 sorption, in order to study how constitution affects surface area. As illustrated by Figure 56, an opposite trend is seen in the measured surface area when compared to estimated crystallite size. This makes sense, since smaller crystallites allow for a more granular surface which in turn leads to a higher surface area. Published surface area values for similar Co_3O_4 materials are in the 20-125 m^2/g range [21-22], while published values for Mn_3O_4 are in the range of 10-180 m^2/g. [23-24] Surface areas for similar Co, Mn spinels are in the range of 30-100 m^2/g, with higher Co content generally leading to higher surface areas. [25-35] The above means that the surface areas of Co_3O_4, $CoMn_2O_4$ and Mn_3O_4 fall within the range of published values, but Co_2MnO_4 exhibits a very high surface area that is among the highest values published for non-templated and non-supported Co_2MnO_4 materials.

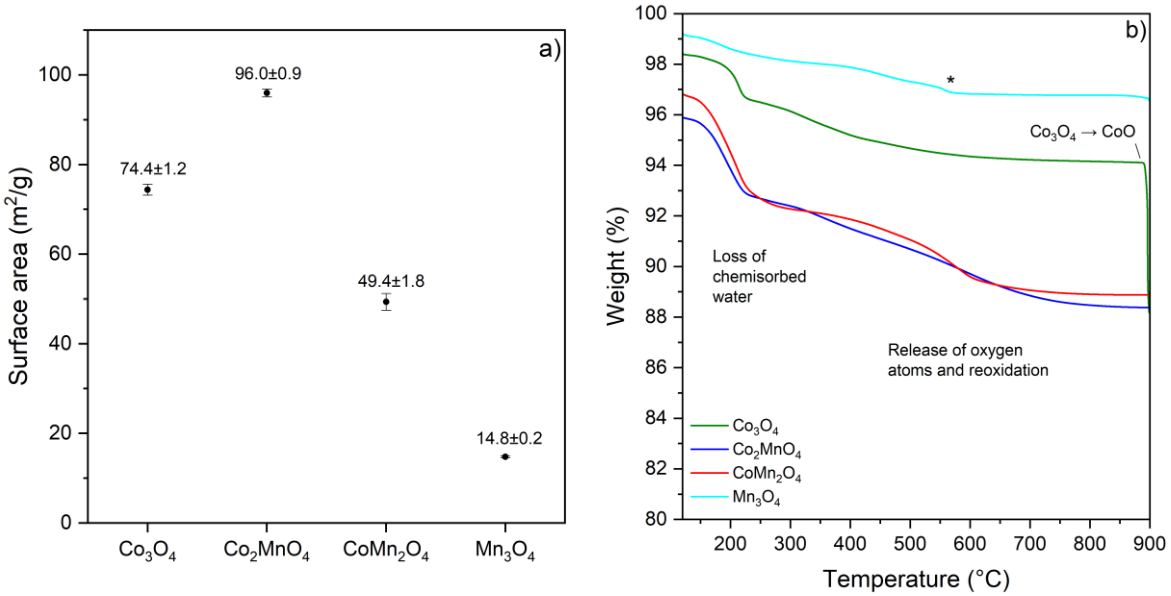

Figure 56 – Surface areas calculated from N_2 sorption experiments via BET theory for all four Co, Mn spinels.

Finally, these four Co, Mn spinels have been studied with thermogravimetric analysis. The heating profile in all cases was such that the sample was first brought to 120 °C, where it was kept for 20 minutes in order to remove all adsorbed water. This explains why some of the graphs below start at values less than 100%. Then the samples were heated to 900 °C at a heating rate of 5 °C/min.

In all four cases only a relatively small weight loss was recorded (note the vertical axis limits). In the case of Co_3O_4 a large drop was seen around 900 °C, which is in good agreement with published values of the thermal reduction of Co(II,III) oxide to Co(II) oxide. [198] On the other hand, the trace of Mn_3O_4 shows a small weight loss step at about 550 °C, marked with an asterisk on Figure 56b. This is most likely due to a trace amount of MnO_2 being present in the sample, which is thermally reducing to Mn_3O_4 at this temperature. [199] In the case of the other spinels one sharper weight loss step can be seen, and then a gradual decline until a plateau between 700 and 900 °C. This is due to the gradual release of oxygen atoms and subsequent reoxidation at high temperature. Wang *et al.* have found that the final weight loss after such a gradual decrease is indicative of oxygen vacancies or defective oxygen sites, with the final weight loss and the amount of oxygen vacancies in the sample being inversely proportional. [200] This would mean that Mn_3O_4 has the largest number of oxygen vacancies, followed by Co_3O_4, with the mixed spinels having the least, but roughly equal amount of oxygen vacancies. This question will be revisited in the next subchapter.

5.4.3 XPS Analysis

Finally, these Co, Mn spinels were assessed on the atomic level using XPS. The main aim of this analysis was to gain further understanding of the constitution of the samples both in terms of elemental make-up and the oxidation states of the present metals.

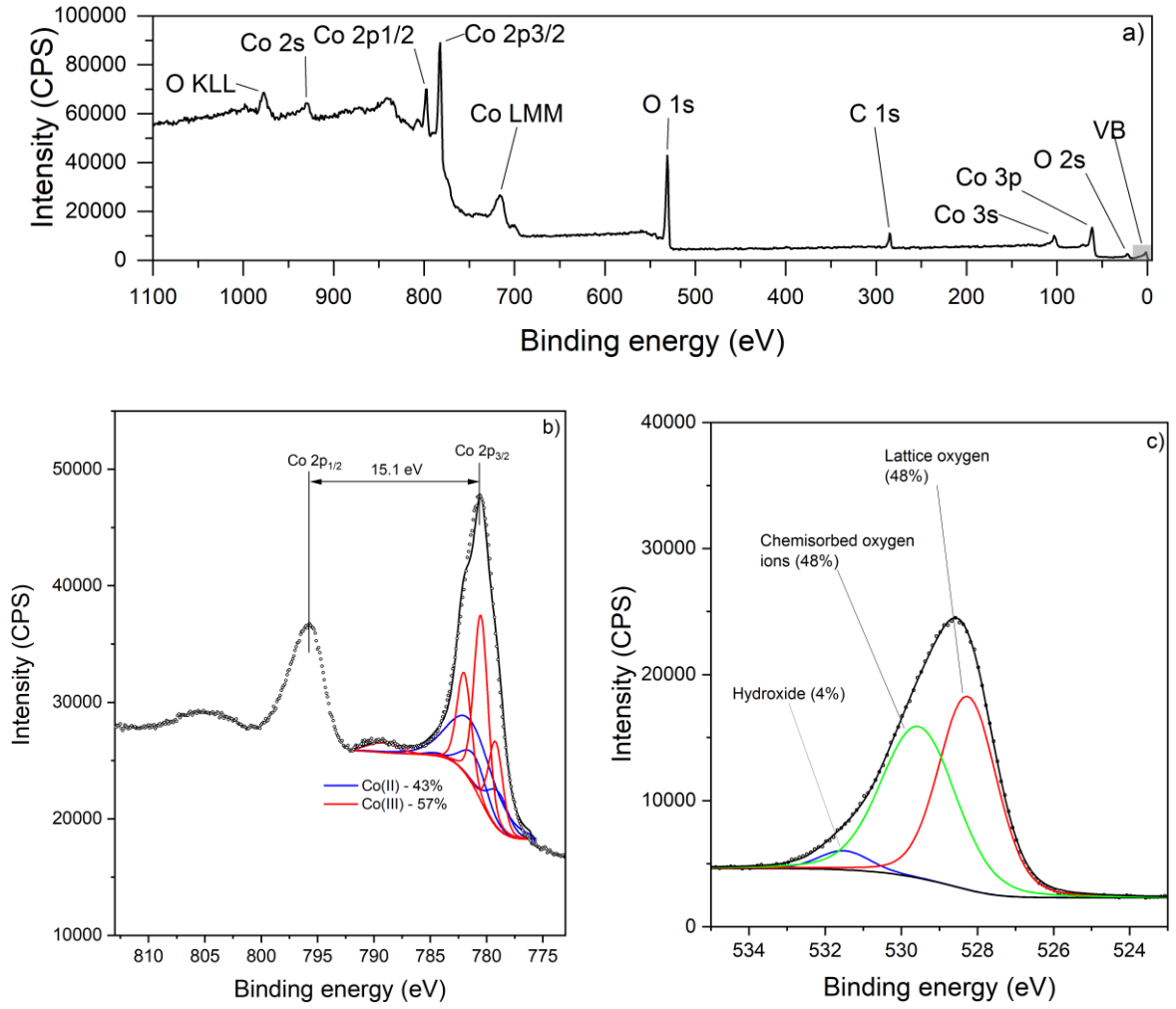

Figure 57 – XPS spectra of a Co_3O_4 sample; **a:** Survey spectrum; **b:** High resolution spectrum of the Co 2p region; **c:** High resolution spectrum of the O 1s region for a Co_3O_4 sample.

The results of XPS analysis for Co_3O_4 is illustrated by Figure 57.The survey spectrum for Co_3O_4 shows no sign of any element other than Co, O and adventitious C. The Co(II) oxides and hydroxides produce strong satellites between the Co $2p_{3/2}$ and Co $2p_{1/2}$ peaks which are not present here. The peak shape of the Co 2p signal is broadly consistent with published results for Co_3O_4 although there is less asymmetry than expected which can be symptomatic of a minor secondary chemical environment, such as terminal metal ions being bound to hydroxide groups or containing oxygen vacancies instead of oxides. Nonetheless this peak was deconvoluted into

Co(II) and Co(III) signals according to Biesinger *et al.*[11], and the ratio was found to be 43% Co(II) to 57% Co(III). [46] This is slightly different than expected for a Co_3O_4 sample, which would normally be 33% Co(II) and 67% Co(III). Notably, it is in line with the findings of Long *et al.* who reported that Co(II) can migrate to the surface of Co_3O_4 crystals. [166] The positions of the Co 2p peaks and the extent of the splitting between them is also consistent with published results for Co_3O_4. [201] The relatively low spin-orbit coupling value of 15.1 eV also points towards low-spin Co(III) being the dominant ion. [41-42]

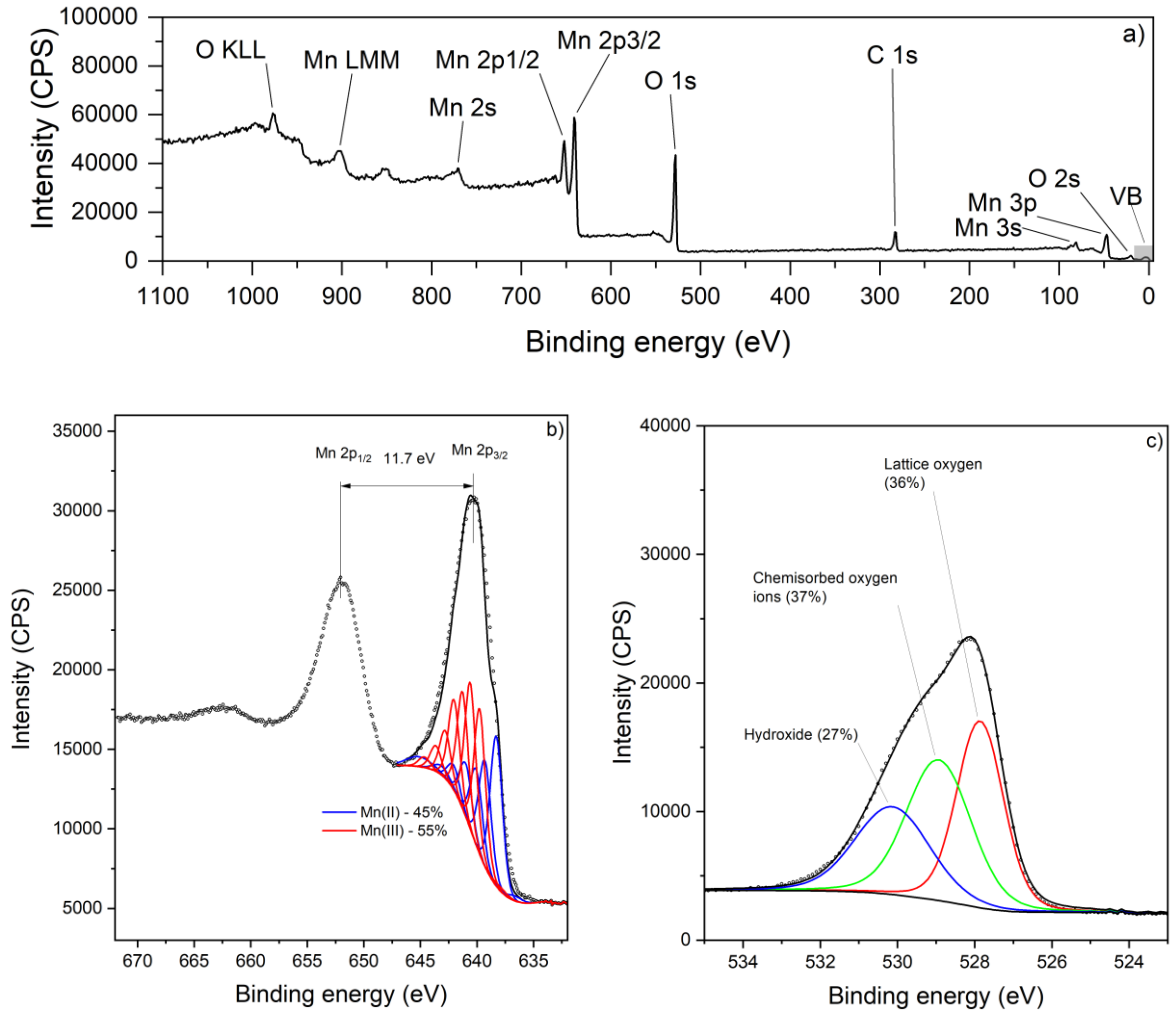

Figure 58 – XPS spectra of a Mn_3O_4 sample; **a:** Survey spectrum; **b:** High resolution spectrum of the Mn 2p region; **c:** High resolution spectrum of the O 1s region of a Mn_3O_4 sample.

The high resolution O 1s signal can be deconvoluted into three separate peaks, which have been identified as the signal of the lattice oxide ions, chemisorbed oxygen ions and

[11] CoO and CoOOH were used as proxies for Co(II) and Co(III) simply because this is what was published by Biesinger *et al.*, and there are no other high quality publications with CoO and Co_2O_3.

hydroxides, where the first two are dominant with roughly equal areas. The deconvolutions of O 1s spectra will be discussed collectively for the four spinels in order to identify any trends.

The results of XPS analysis of a Mn_3O_4 sample is shown by Figure 58. The survey spectrum for Mn_3O_4 shows only Mn, O and adventitious carbon signals. The spin-orbit coupling in the Mn 2p signal is similar to values published by other researchers but this is considered only weak evidence of oxidation state distribution. [43-44] Mn(II) and Mn(IV) oxide phases produce characteristic peak shapes, the former usually has a pronounced satellite peak between Mn $2p_{1/2}$ and Mn $2p_{3/2}$, while the latter shows significant asymmetry in the Mn $2p_{3/2}$ peak, and none of this is visible on the spectrum, which supports the identification of Mn_3O_4. The Mn $2p_{3/2}$ peak has been deconvoluted into Mn(II) and Mn(III) oxide peaks according to Barreto *et al.*. [206] This allows the estimation of the average ratio of Mn(II) and Mn(III) in the analysed depth, which shows 45% Mn(II) and 55% Mn(III). This means there is a slight excess of Mn(II) ions on the surface of the sample, compared to the 33% Mn(II) that would correspond to the constitutional formula Mn_3O_4. It is also worth mentioning that the O 1s spectrum shows substantial hydroxide concentration in the sample, which along with the excess Mn(III) in the sample could indicate small surface deposits of MnOOH.

The survey spectra of Co_2MnO_4 is shown on Figure 59a; it only shows signals of Co, Mn, O and adventitious C. The high resolution spectra of Co_2MnO_4 are shown on Figure 59b-d. When relative sensitivity factors are taken into consideration, the ratio of Co:Mn is 1.76:1.00 for Co_2MnO_4. This is very similar to the 1.6:1.0 ratio measured with XRF, which means the bulk of the catalyst particles are not significantly different from the surface. The high resolution Co 2p spectrum of this sample shows an even amount of Co(II) and Co(III), which is a higher Co(II) concentration than what was seen in Co_3O_4, while the high resolution Mn 2p region shows that the large majority of Mn ions are in a +3 oxidation state. This is significantly different from the ratios seen in the Mn_3O_4 sample. This means that the co-presence of Co and Mn in the synthetic mixture leads to redox processes between the metal ions, which leads to a different ratio of oxidation states when compared to Co_3O_4 and Mn_3O_4, or potentially minor MnOOH deposits on the surface of catalyst particles. The spin-orbit couplings in the Co 2p and Mn 2p spectra are not significantly different from Co_3O_4 and Mn_3O_4, respectively. This means that even though the distribution of oxidation states are different, the mixed spinels have similar overall electronic structures as the binary spinels. Finally the high resolution O 1s spectrum shows a much higher concentration of lattice oxygen when compared to either Co_3O_4

or Mn_3O_4, which means that the presence of both Co and Mn leads to a more ordered material with less defective crystals.

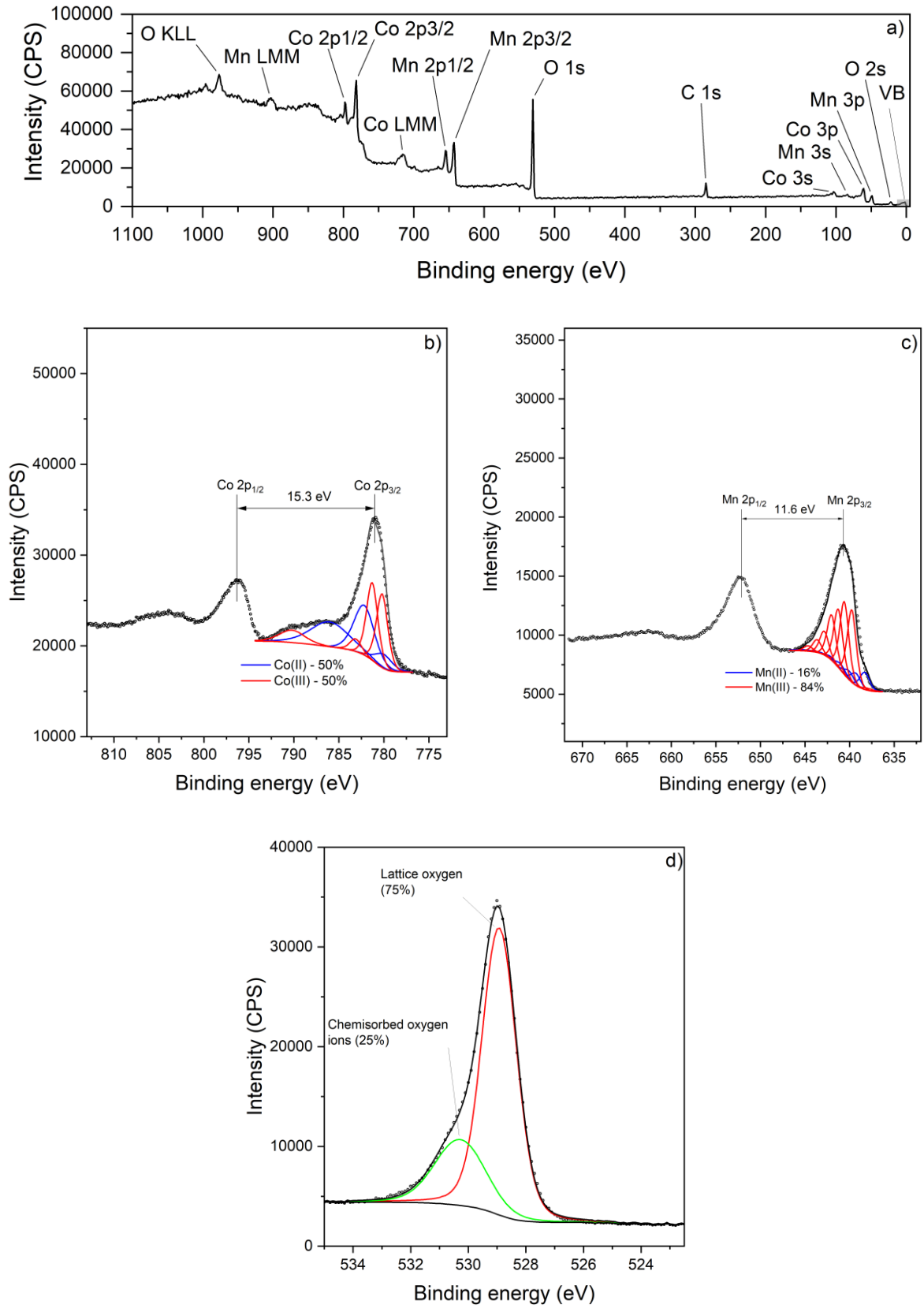

Figure 59 – XPS spectra of a Co_2MnO_4 sample; **a:** Survey spectrum; **b:** High resolution spectrum of the Co 2p region; **c:** High resolution spectrum of the Mn 2p region; **d:** High resolution spectrum of the O 1s region.

The survey and high resolution spectra of $CoMn_2O_4$ are shows on Figure 60. Considering the relative sensitivity factors, the survey spectrum shows a Co:Mn ratio of 0.95:2.00. This is slightly lower than the expected 1:2 ratio, which means that there is an excess of Mn ions in the external layer of the sample. Both the Co 2p and the Mn 2p spectra show a different ratio of oxidation states than what was seen for Co_2MnO_4, likely due to the same redox processes that occur in the synthetic mixture prior to the hydrothermal treatment. This sample shows a large majority of Co(II) and Mn(III) ions in the lattice. Furthermore, the O 1s spectrum shows a similar profile to Co_2MnO_4, namely that there is much more lattice oxygen in the sample, and conversely much less hydroxide/defective oxygen site present compared to the binary oxides.

It is worth finally summarising the findings of XPS analysis for all four Co, Mn spinels. Binary oxides have been identified by both XRD and XPS as M_3O_4, with the corresponding roughly 1:2 M(II):M(III) ratio (M:Co or Mn). The two mixed spinels show a very different spread of oxidation states, likely influenced by the redox processes between the metal ions in the synthetic mixture prior to the hydrothermal treatment. A larger Co concentration correlates with a higher Mn(III) and lower Co(III) content in the mixed spinel, while a larger Mn concentration is correlated with a larger Co(II) content. From this it can be inferred that the main redox processes are excess Co ions oxidising Mn ions, and excess Mn ions reducing Co ions. Figure 61 shows the distribution of oxygen bond types in all four samples. The high resolution O 1s spectra of the binary oxides show the presence of hydroxides in addition to considerable chemisorbed oxygen ions in the case of the binary oxides. The mixed Co, Mn spinels show no signs of hydroxides, and a smaller ratio of chemisorbed oxygen ions. This means these materials are made up of more highly ordered crystals. The trend in these values is in line with the observations of thermogravimetric analysis in the previous subchapter. Additionally when both XPS, TEM and XRD analysis results are taken into consideration it can be said that Co_2MnO_4 is a nanocrystalline material, meaning that it is made up of very small, but crystalline domains, and not a mixture of crystalline and amorphous domains. It is worth comparing the results of Williamson-Hall analysis to the XPS results. The amount of Mn(III) in these spinels mirrors the trend in the strain component that was identified in these materials, which is explained by the strong Jahn-Teller distortion Mn(III) ions are associated with.

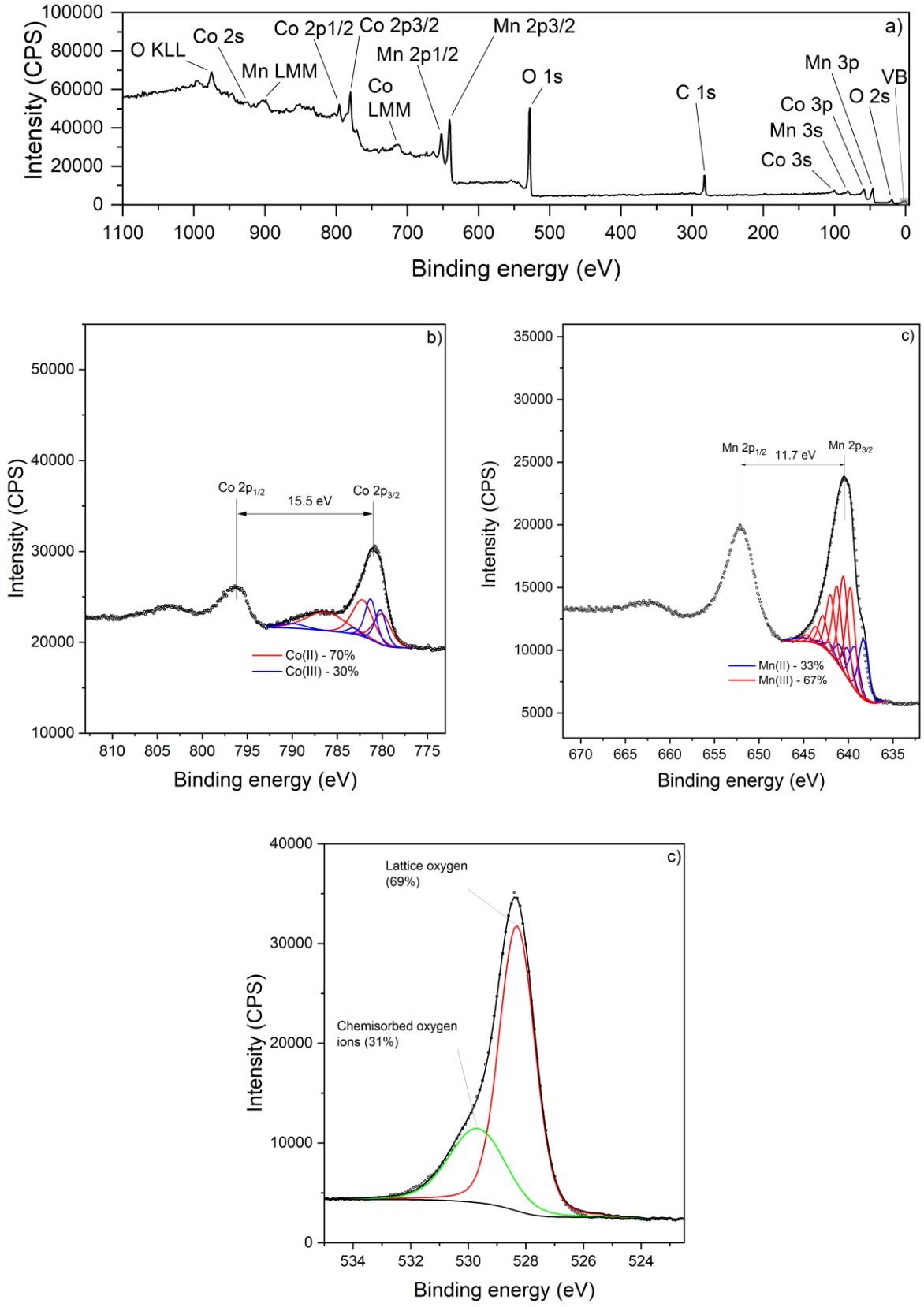

Figure 60 – XPS spectra of a $CoMn_2O_4$ sample; **a:** Survey spectra; **b:** High resolution spectrum of the Co 2p region; **c:** High resolution spectrum of the Mn 2p region; **d:** High resolution spectrum of the O 1s region.

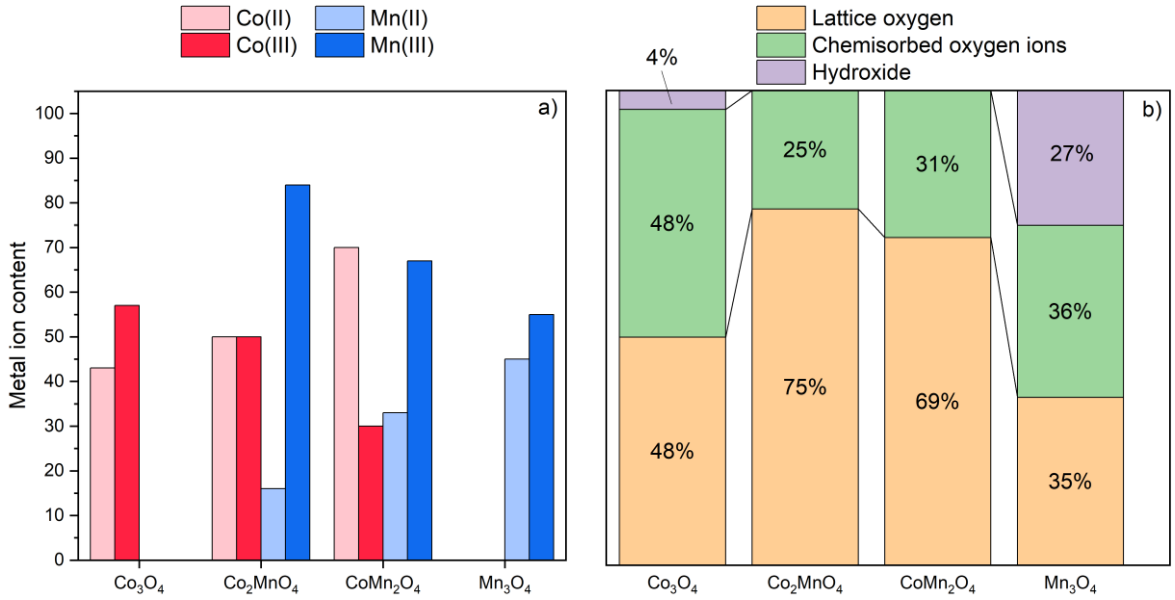

Figure 61 – Summary of XPS analysis for all four Co, Mn spinels; **a:** Ratios of metal ion oxidation states in each sample; **b:** Ratios of different O 1s peak contributions.

5.5 Catalytic Activity of Spinels

The catalytic activity of Co_3O_4, Co_2MnO_4, $CoMn_2O_4$ and Mn_3O_4 were tested in model organics removal experiments where AO7 served as the model pollutant, and H_2O_2 as the precursor to reactive oxygen species which degraded the dye molecules. All four Co, Mn spinels were tested along with a blank, which did not contain any catalyst, only the dye and H_2O_2. To gain a full understand of the catalytic activity of these materials both adsorptive and catalytic properties were tested.

5.5.1 Adsorption Properties

Adsorption capacities were measured in experiments where certain masses of the spinels were added to a dye solution, and the reduction in the amount of dye in solution was then measured after 60 minutes, which is the timeframe of dye degradation experiments, as well. These adsorption capacity experiments used a starting dye concentration of 0.068 mM and a catalyst concentration of 0.6 mg/mL, and the results are illustrated by Figure 62. A decreasing trend between adsorption capacity and Co content can clearly be seen, but overall, Co_3O_4 exhibits a moderate adsorption capacity, while the other three are quite low. Comparison between present experimental results and literature values is difficult, as adsorption capacity strongly depends on particle morphology, adsorbate, and other experimental conditions. Nonetheless it can be said that the adsorption capacity measured here is in line with published results for all four spinels, but all Mn containing spinels exhibit adsorption capacity on the lower

end of published values [46–52] This trend in adsorption is likely explained by a combination of surface area, and surface oxygen vacancy and hydroxide group concentration. To fully understand the driving force in adsorption some additional, targeted research is necessary.

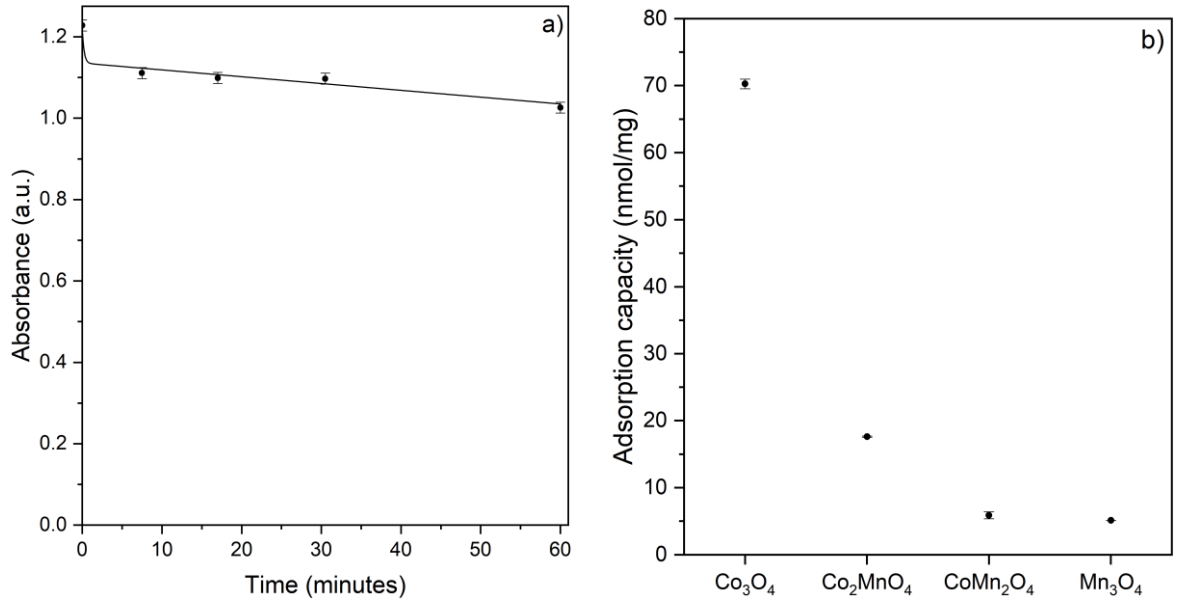

Figure 62 – Results of adsorption studies of AO7 on the neat Co, Mn spinels; **a:** Kinetic curve for the adsorption experiment with Co_2MnO_4; **b:** Summarised adsorption capacities after 60 minutes for all Co, Mn spinels. Experimental conditions: 0.6 mg/mL catalyst, 0.068 mM AO7.

Finally it is worth mentioning that the kinetics of adsorption was also tested in the case of Co_2MnO_4, and a kinetic curve of this experiment can be seen on Figure 62a. The catalyst goes through a rapid initial adsorption which then gives way for a slower, more stable adsorption. A time frame of 60 minutes has been chosen as this fits later dye degradation experiments.

5.5.2 Catalytic Activity in Organics Removal

Next the spinels were tested in dye degradation experiments, the results of which are summarised by Figure 63. All kinetic curves for overall dye removal show a drop in the first minutes, which is likely explained by rapid initial adsorption. Co_3O_4 and Mn_3O_4 seem to facilitate mainly adsorption, and very little additional catalytic activity, and in line with previous observations, the extent of the initial drop matches measured adsorption capacities. Only the two mixed spinels show a long-term gradual degradation. Additionally, if one considers the different contributions to overall dye removal as shown by Figure 63c, it becomes clear that Co_2MnO_4 and $CoMn_2O_4$ facilitate high dye removal with very little adsorption.

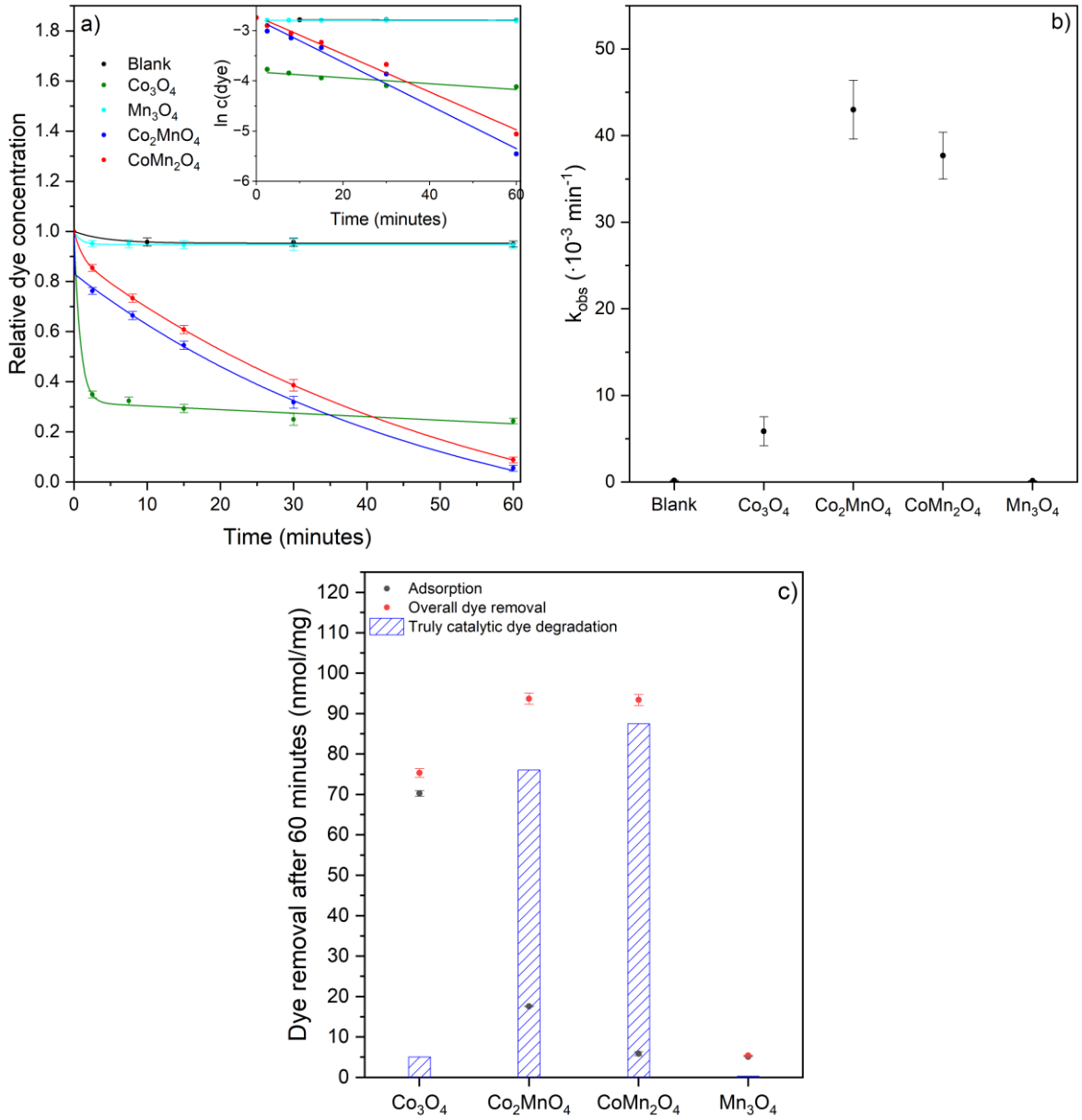

Figure 63 – Graphs showing the catalytic activity of all four Co, Mn spinels in dye degradation experiments; **a:** Kinetic curves of overall dye removal; **b:** Observed rates of reactions, assuming that reactions follow pseudo-first order kinetics; **c:** Comparison of different dye removal contributions.
Experimental conditions: 0.6 mg/mL catalyst, 0.068 mM AO7, 1.8 M H_2O_2.

To further differentiate the two mixed spinels in terms of activity it is worth considering how the whole UV-Vis spectra change versus time. The characteristic absorption peak of the dye (485 nm) only describes the cleavage of the azo-bond in AO7, but that is only the first step of a complex network of parallel and sequential reactions. [83] A more complete picture can be given if one considers the UV-portion of the spectra gathered throughout the dye degradation experiments as illustrated by Figure 64. If a sufficiently low wavelength is chosen where the detector of the spectrometer is not saturated, the change in absorbance can be used as a proxy for the further removal of degradation products.

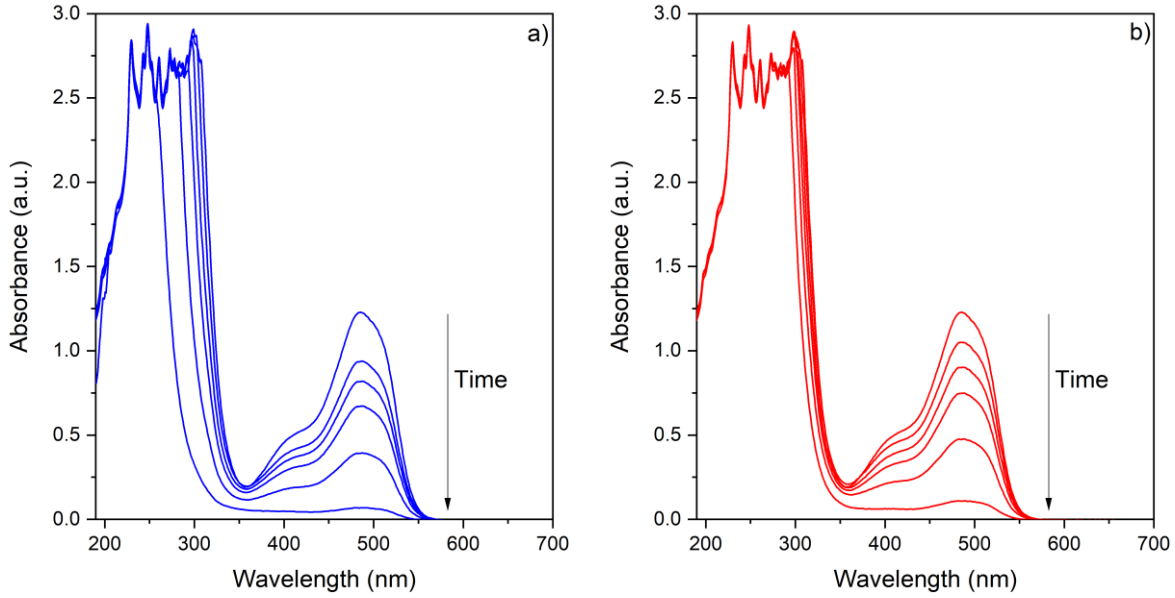

Figure 64 – UV-Vis spectra of dye degradation experiments with Co_2MnO_4 and $CoMn_2O_4$ at times of 0, 7.5, 15, 30 and 60 min; **a:** Co_2MnO_4; **b:** $CoMn_2O_4$.
Experimental conditions: 0.6 mg/mL catalyst, 0.068 mM AO7, 1.8 M H_2O_2.

Zheng *et al.* have reported that after the cleavage of the azo bond, most intermediate degradation products are substituted benzene and naphthalene compounds, indoles and other aromatic molecules, which have strong absorption in the UV region. [83] For reference see Figure 65, which shows the UV-Vis spectrum of AO7 solution without and with H_2O_2 added, with no catalyst present in both cases. It shows that 310 nm is the lowest suitable wavelength to be used as a proxy for the removal of degradation products.

According to the above, Figure 64 shows that over a wider range Co_2MnO_4 facilitates a much greater degree of degradation, since absorbance is strongly declining not only at the characteristic absorption peak of the dye molecule but also at lower wavelength. This, of course, cannot be quantified, since the molar absorptivities of the degradation products, and their ratio in the mixture are unknown, but overall this approach still shows a more complete picture of the catalytic activity of the two mixed spinels. The method described above have been used in the case of all spinels, and the results of this are shown on Figure 66.

These results confirm the findings of the previous catalytic activity experiments and also shows that Co_2MnO_4 is actually much more active than $CoMn_2O_4$. Because of all of the above Co_2MnO_4 has been chosen as the most active catalyst out of these four, and all subsequent experiments will only be using Co_2MnO_4.

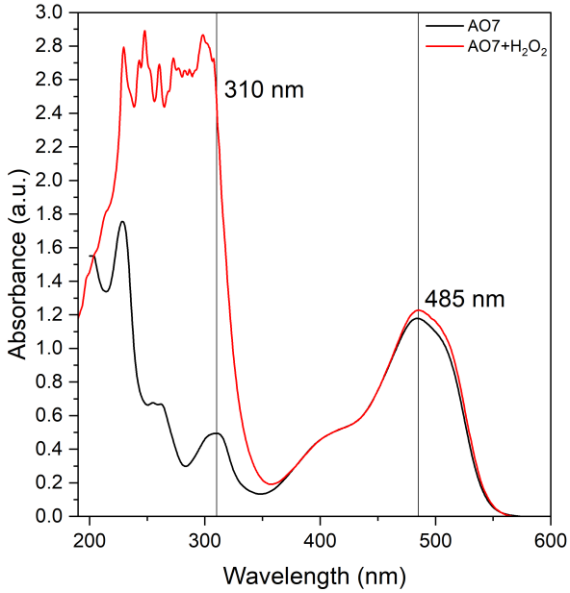

Figure 65 – UV-Vis spectra of AO7 solution (**black trace**) and AO7 solution containing 1.8 M H_2O_2 (**red trace**).

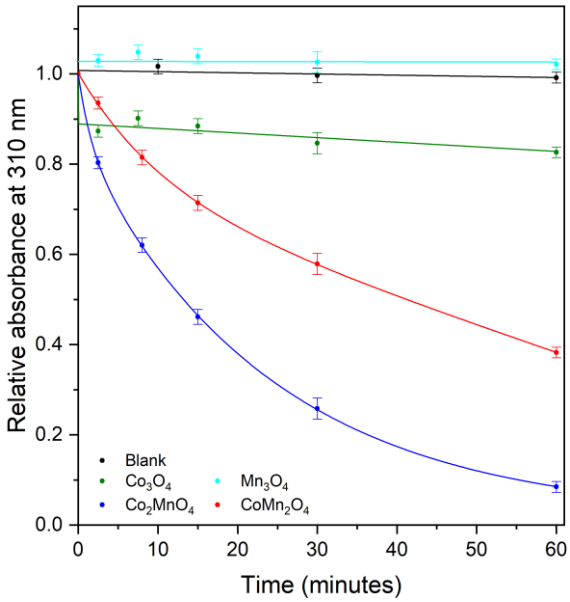

Figure 66 – Summary of further organics degradation facilitated by all four Co, Mn spinels using absorption at 310 nm.
Experimental conditions: 0.6 mg/mL catalyst, 0.068 mM AO7, 1.8 M H_2O_2.

5.6 Co_2MnO_4 Composites

Four types of composites were made altogether, each at five different catalyst loadings. Two carbon supports (GNF and CB) and their acid oxidised versions (oGNF and oCB) were used. GNF and CB were chosen as these are examples of two very common macroscale carbon support types, namely fibrous and spherical. Chapter 2 showed than GNF and CB were affected by acid oxidation differently, and behave differently in adsorption experiments. One of the aims

of this chapter is to probe whether these materials and their acid oxidised versions show fundamental differences when being used as catalyst supports.

5.6.1 Bulk Characterisation

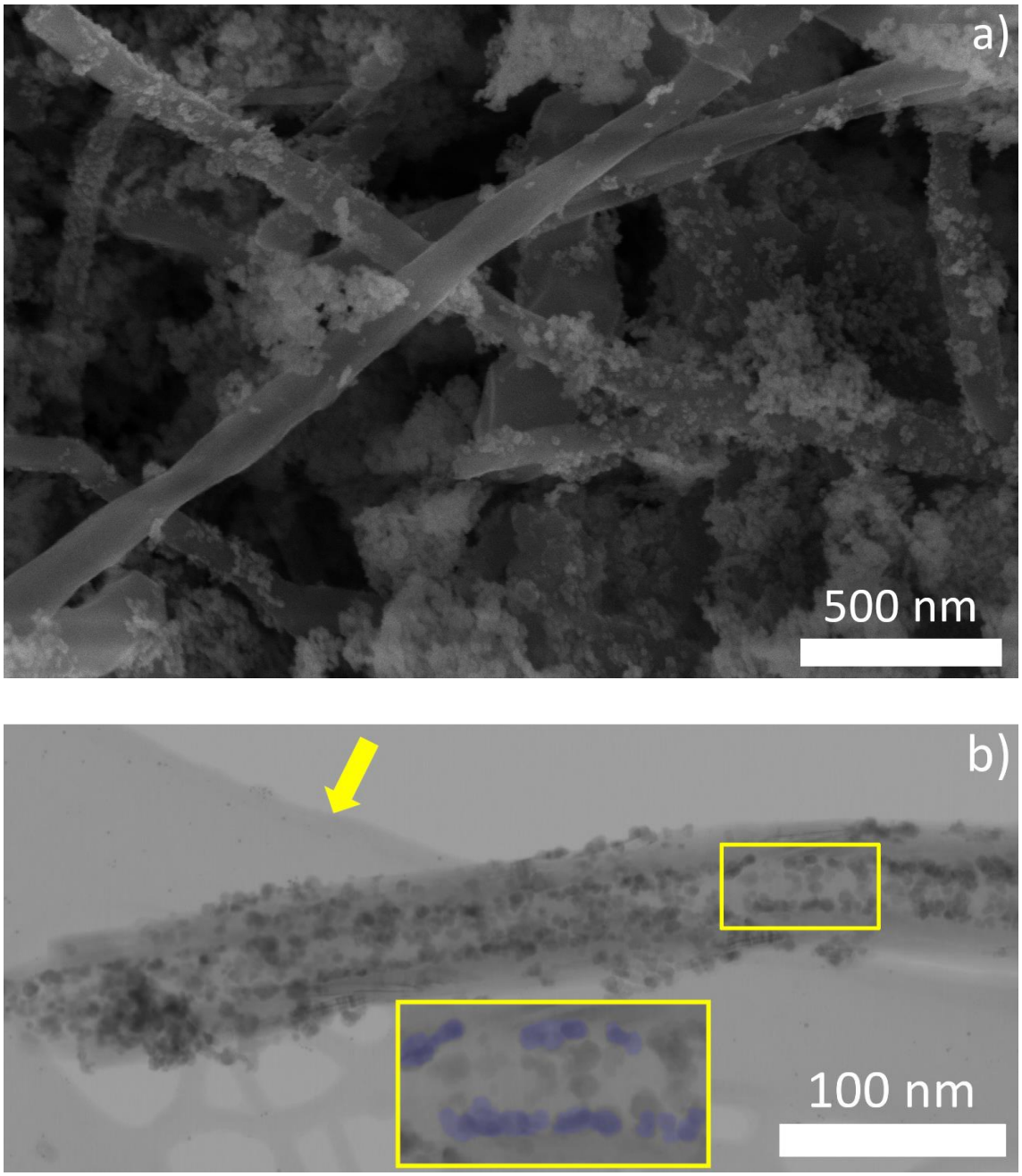

Figure 67 – Electron microscope images of typical Co_2MnO_4-GNF particles of 38.3% catalyst loading showing the distribution of catalyst particles in the composite; **a:** Overview of composite particles imaged using SEM; **b:** TEM image of an individual composite particle;
The yellow arrow highlight the carbon film of the TEM sample holder chip.

Just like the neat spinels, these composites were also analysed with electron microscopy. Only one composite of each type will be discussed in order to highlight the main characteristics of these, with the types being Co_2MnO_4-GNF, Co_2MnO_4-oGNF, Co_2MnO_4-CB and Co_2MnO_4-oCB.

The GNF and oGNF supported catalysts were analysed with both SEM and TEM, but in the case of CB and oCB supported catalysts TEM analysis was not possible due to the size of the beads.

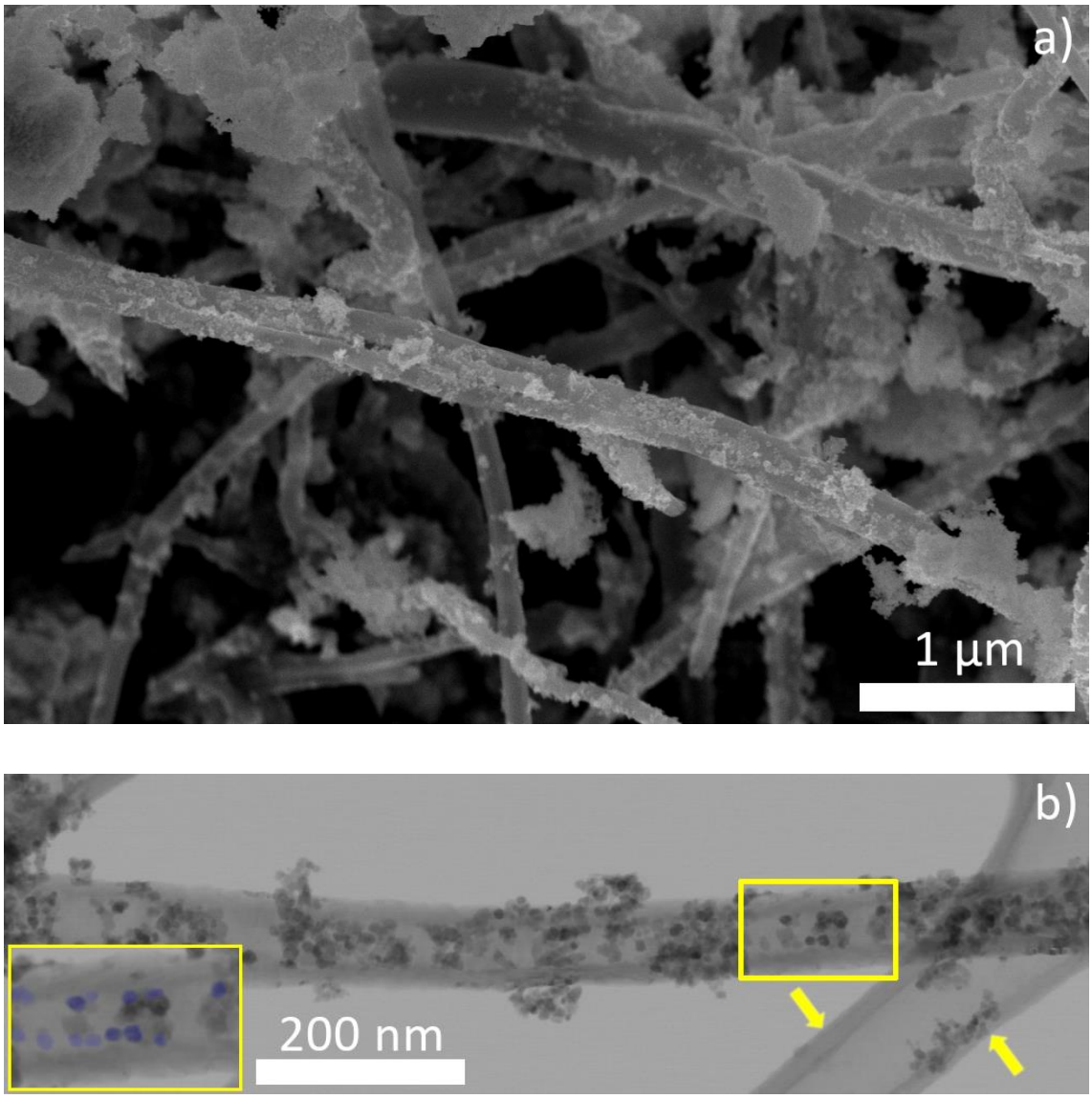

Figure 68 – Electron microscope images of typical Co_2MnO_4-oGNF particles of 38.3% catalyst loading showing the distribution of catalyst particles in the composite; **a:** Overview of composite particles imaged using SEM; **b:** TEM image of an individual composite particle;
The yellow arrows highlight the carbon film of the TEM sample holder chip.

Electron microscopy analysis shows no fundamental difference visible between the GNF and oGNF supported catalysts; in both cases there are masses of unsupported catalyst, and also very small particles dispersed along the length of the fibres, both on the internal and external surfaces of the support. TEM images were also used to generate size distributions of the catalyst particles. In the case of Co_2MnO_4-GNF the particles are 9.2 ± 2.6 nm large, while in the case of Co_2MnO_4-oGNF they are 8.5 ± 2.4 nm. These values are both slightly larger than the 6.6 ± 3.1 nm that was measured for the unsupported catalyst, but the ranges of uncertainty

largely overlap. If there is indeed a difference between particle sizes, it is likely due to the GNF and oGNF providing a slightly better surface for crystal nucleation and growth than the internal wall of the hydrothermal reactor, which could lead to slightly larger particle sizes, but it is not possible to say solely based on these size distributions.

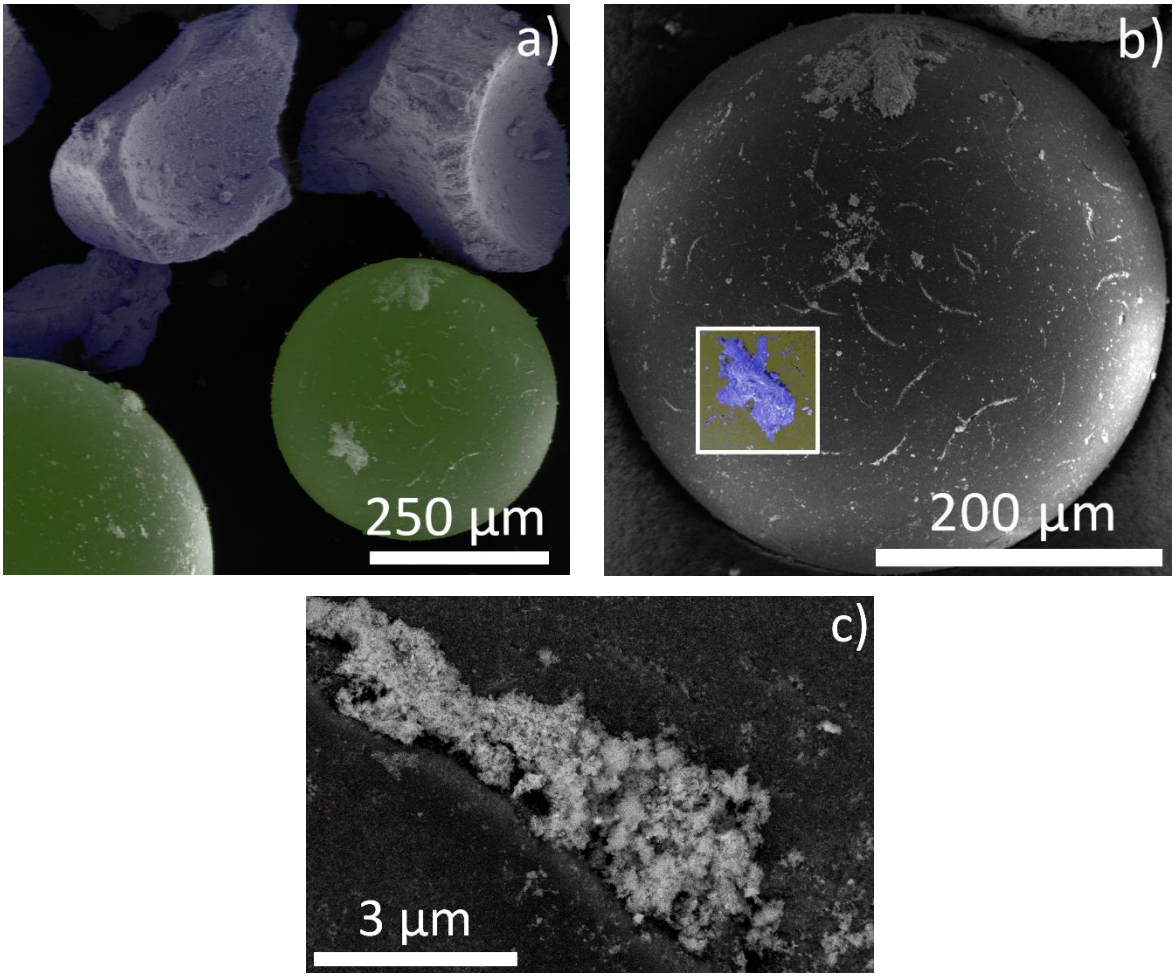

Figure 69 – SEM images of Co_2MnO_4-CB composite (50% catalyst loading) showing poor catalyst anchoring; **a:** Image of a whole bead and unsupported catalyst; **b:** Close-up of a bead; **c:** Close-up of a crack on the surface of a bead; The colour overlays identify different parts of the sample: **Blue:** unsupported catalyst, **Green:** Composite catalyst particle. Yellow: Undecorated carbon surface.

The electron microscopy analysis of the CB and oCB supported catalyst shows a markedly different picture. The untreated carbon beads show a poor anchoring of catalyst particles, as shown on Figure 69. The catalyst particles seem to mostly be localised to the cracks in the surface of the beads which leads to a low overall coverage. On the other hand, the oCB supported composite shows a much more even catalyst coverage both on the external surface and in the surface cracks.

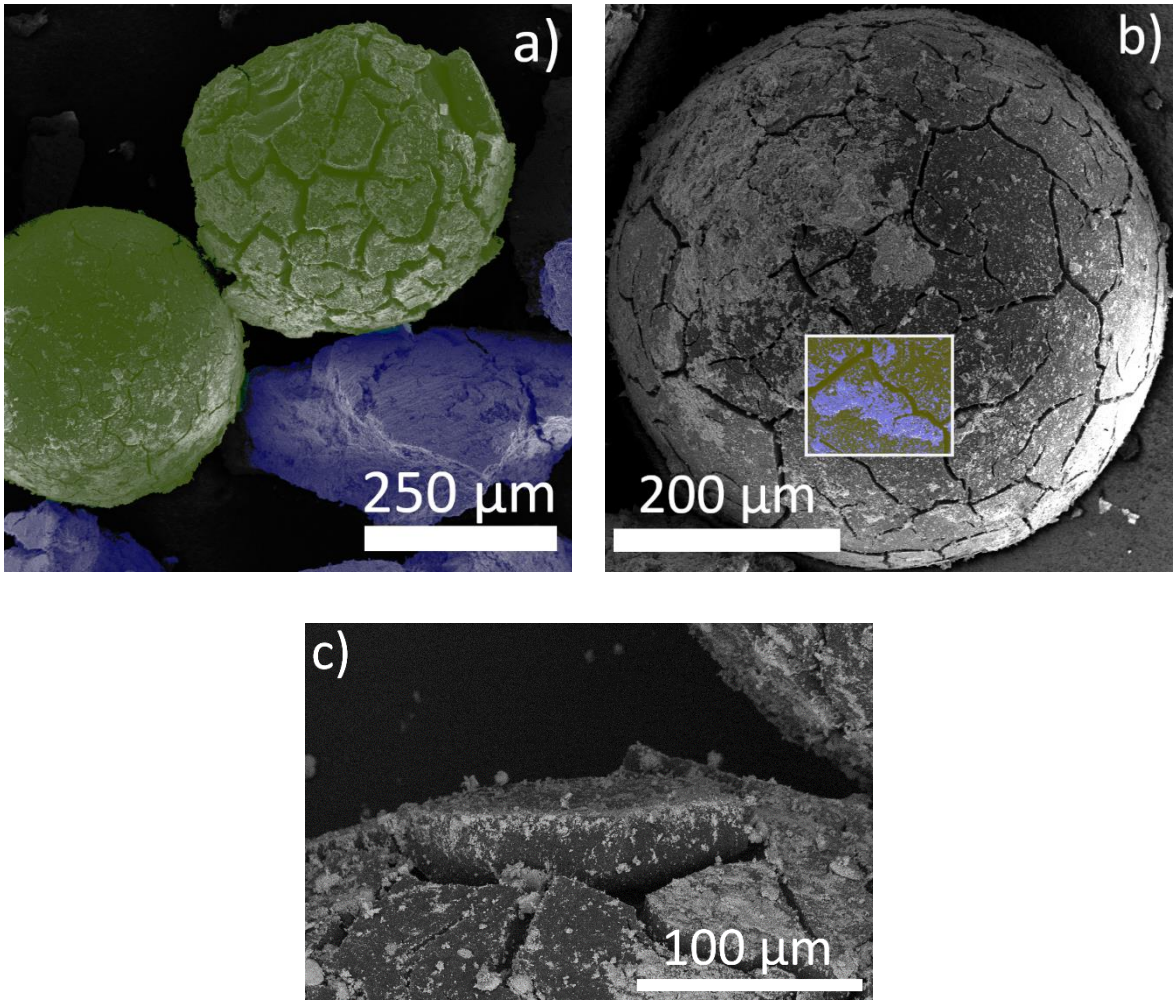

Figure 70 – SEM images of Co_2MnO_4-oCB composite (50% catalyst loading) showing good catalyst anchoring; **a:** Image of multiple beads and unsupported catalyst; **b:** Close-up of one bead; **c:** Close-up of a crack on the surface of a bead; The colour overlays identify different parts of the sample: **Blue:** unsupported catalyst, **Green:** Composite catalyst particle. Yellow: Undecorated carbon surface.

Additionally, it is worth mentioning that there is some unsupported catalyst present on electron micrographs of all composite types. In the case of the CB and oCB based composites, these particles were likely never soundly attached, since their sizes are comparable to the beads, and the catalyst particles also seem to have the negative imprint of the beads on their surface. These unsupported catalyst particles likely gain no benefit from the beads in terms of catalytic activity. The studied GNF and oGNF composites also show aggregates of the catalyst close to a fibre, but these are much smaller. Similarly to *ex situ* MnO_2-GNF composites in Chapter 1, the unsupported aggregates of Co_2MnO_4 in GNF and oGNF based composites are expected to still have some additional catalytic activity compared to neat Co_2MnO_4.

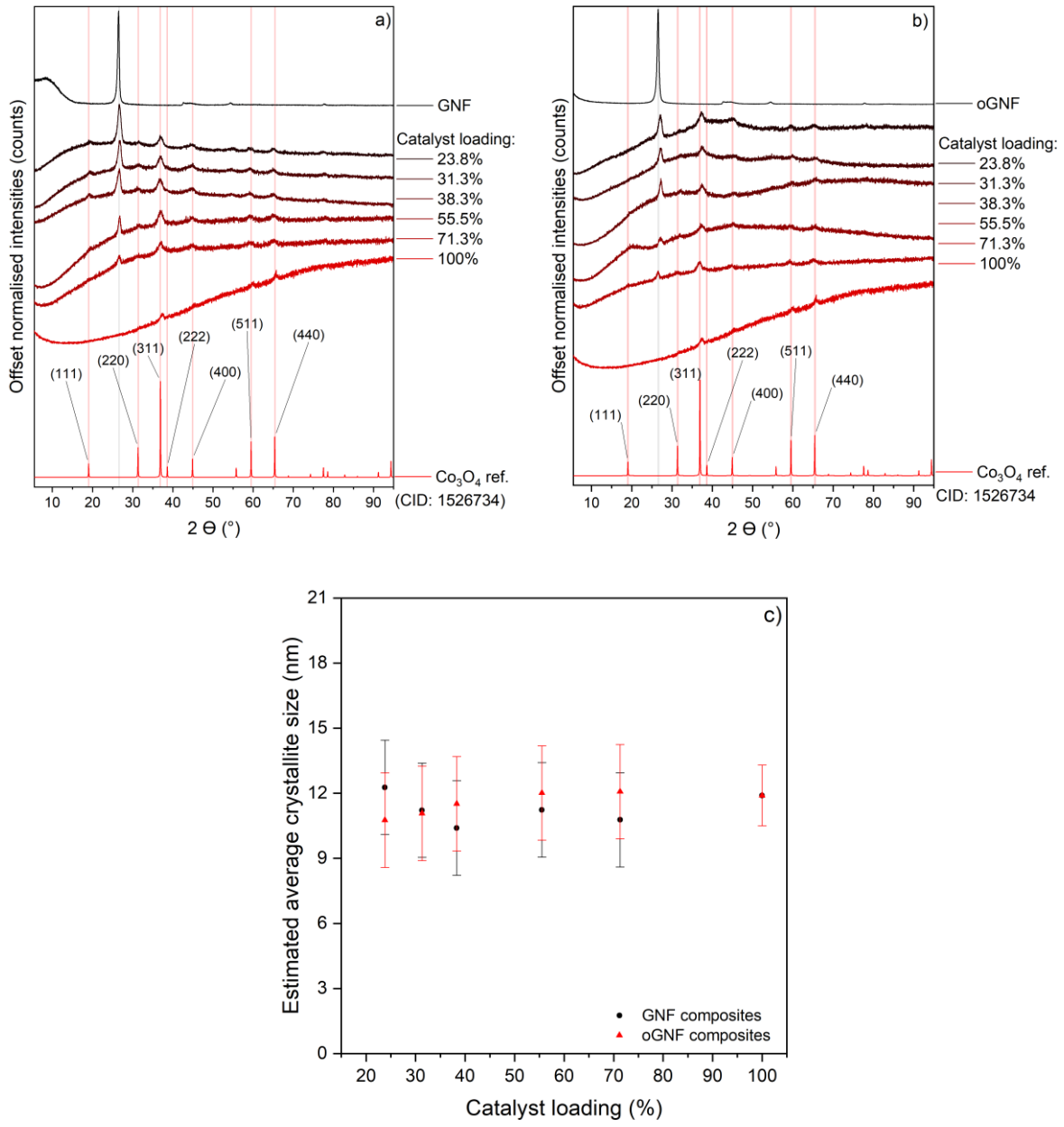

Figure 71 – XRD patterns for all Co_2MnO_4-GNF (**a**) and Co_2MnO_4-oGNF (**b**) composites and estimated crystallite sizes for all GNF and oGNF composites (**c**).

The amount of unsupported catalyst was found to be 22 ± 5% for the lowest loadings, and 38 ± 7% for the highest, with no difference having been detected for CB composites versus oCB composites. The method used to arrive at these values likely overestimated the ratio of unsupported catalyst, since even undecorated oCB lost about 5% of its mass during the same procedure. Still, these values signal that a large ratio of the catalyst in not anchored soundly to the beads, and it also explains the large aggregates of catalyst on the electron micrographs.

The composites were then characterised using bulk analytical methods, of which first XRD is discussed. In both the GNF and oGNF composites' case a gradual transition is seen between the signals of the pure metal oxide and the pure support (see Figure 71). It is worth noting that

the peaks originating from the catalyst are somewhat stronger in the case of the composites when compared to the pure metal oxide's diffractograms. This can be explained by one of two things: the presence of the support in the hydrothermal synthesis facilitates the precipitation of either more crystalline or larger particles. This is in line with the observation made via TEM analysis. The Scherrer-equation was used to estimate crystallite sizes for both GNF and oGNF composites. The exact values are not taken into consideration, only the trend. In the case of both carbon supports no difference is seen in terms of crystallite size between the unsupported catalyst and the composites. Finally, it should be noted that there were not enough high intensity peaks in the diffraction pattern of either the GNF, oGNF, or CB, oCB composites for Williamson-Hall analysis.

In the case of CB and oCB composites, the diffraction peaks originating from the catalyst are similar to the peaks of the unsupported catalyst (See Figure 72). The 16.7% Co_2MnO_4-oCB is a notable exception, where additional peaks are visible. These are peaks originating from a Mn, Co mixed carbonate phase, and a Co_2MnO_4 phase. [214] The explanation for their presence is likely that the synthetic mixture of this composite included a large amount of oCB. This likely led to the neutralisation of a large portion of the NH_3 in solution and by extension the metal ions binding to surface carboxylate groups instead, and the subsequent formation of some amount of Co and Mn carbonates. Lastly, similar to the GNF and oGNF composites the estimated crystallite size of CB and oCB composites show no difference to the same value for the neat catalyst.

All 20 composites were analysed using nitrogen sorption in order to measure their surface areas, as shown by Figure 73. In the case of all composites, there is a broadly linear trend between the surface area values of the pure support and the pure catalyst. This means that the catalyst is simply being dispersed on the surface of the support in the case of GNF and oGNF. In the case of CB and oCB composites, the broadly linear trend likely means that the catalyst is not just being dispersed on the external surface of the beads but also fills up some the internal pore structure, since a large portion of overall surface area is due to micropores.

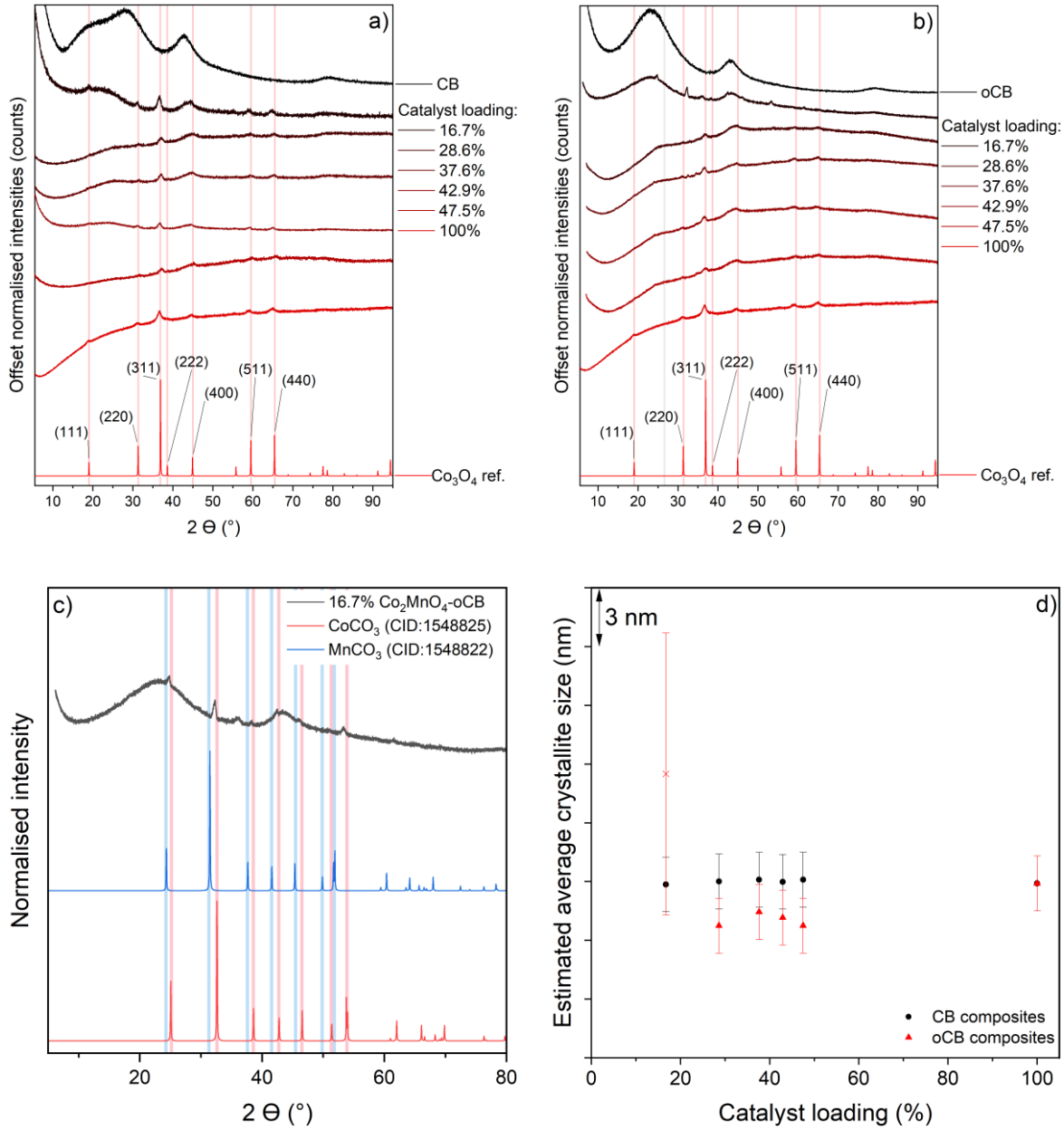

Figure 72 – Results of X-ray diffraction analysis for CB and oCB composites; **a:** Diffraction patterns of Co_2MnO_4-CB composites; **b:** Diffraction patterns of Co_2MnO_4-oCB composites; c: Diffraction pattern of 16.7% Co_2MnO_4-oCB; **d:** Estimated crystallite sizes for CB and oCB composites.

Finally, the composites were studied using a thermogravimetric analyser to probe whether the nominal loading is in agreement with the real loading (see Figure 74).

The GNF and oGNF composites show very good agreement between the expected and real loading, with the largest deviation being less than 1.5%. The CB and oCB composites showed a larger variance, in these cases the largest difference between the nominal and real loading was 4%.

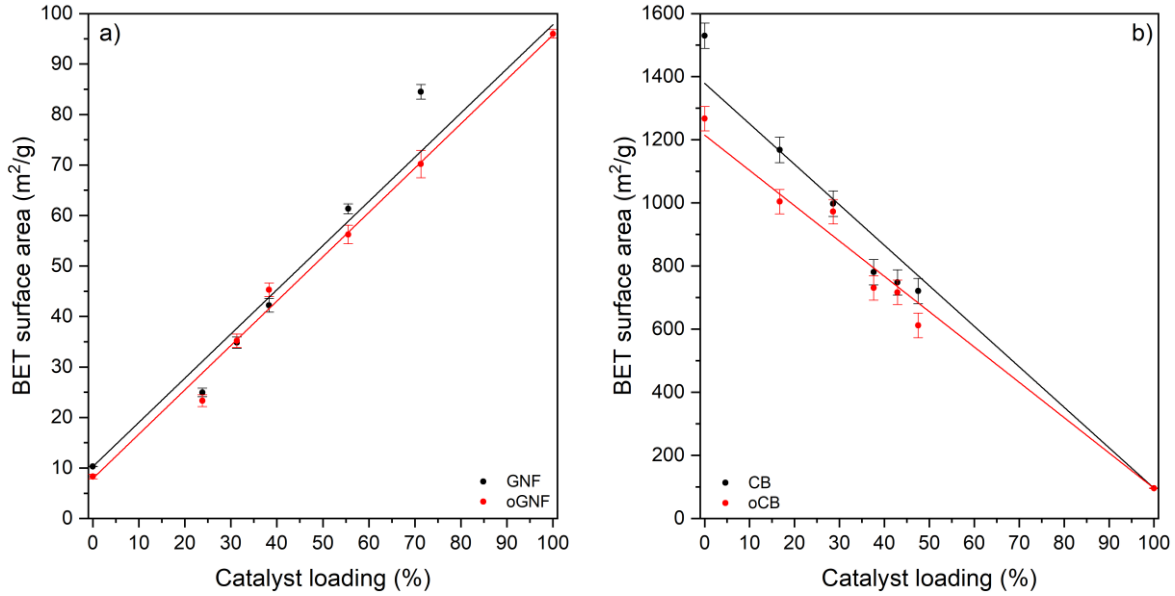

Figure 73 – BET surface areas for all composites measured via N_2 sorption experiments; **a:** GNF and oGNF composites, **b:** CB and oCB composites.

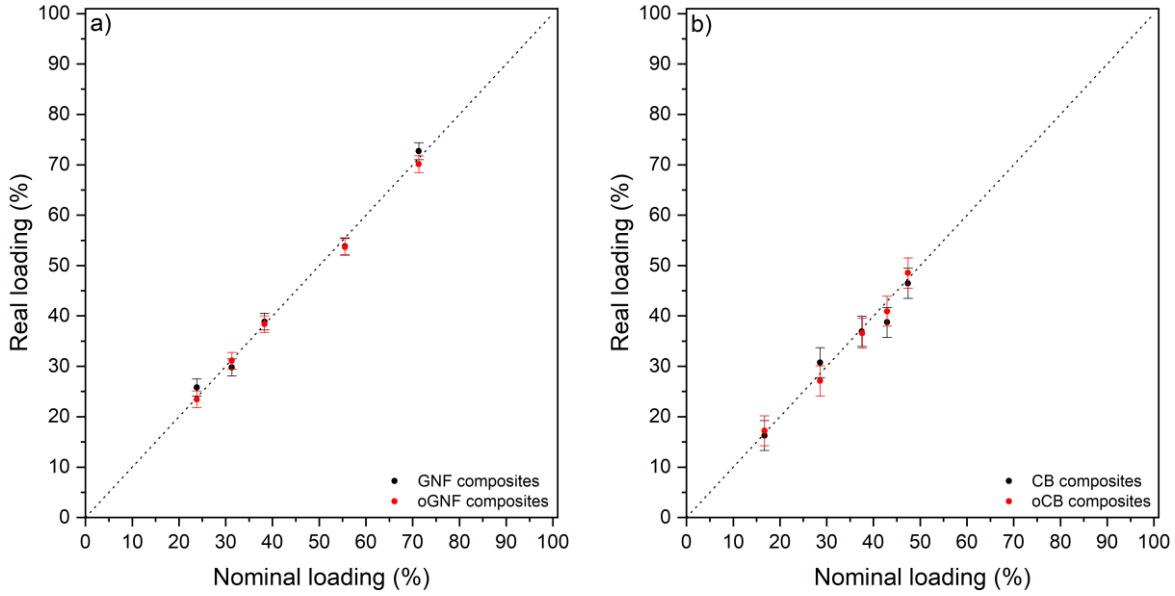

Figure 74 – Graphs showing the nominal vs real loading of composites; **a:** GNF and oGNF composites, **b:** CB and oCB composites.

5.6.2 XPS Analysis

Finally, the prepared composites were characterised on the atomic level using XPS. The survey spectra of the GNF and oGNF composites both show the expected peaks associated with Co, Mn, O and C (see Supplementary figure 28). The high resolution Co and Mn spectra show no significant difference between the GNF and oGNF composite (see Figure 75). There is no significant difference between the Co(II):Co(III) ratio of the neat catalyst and these composites.

The high resolution Mn 2p spectra on the other hand shows a higher ratio of Mn(II) than what was seen for neat Co_2MnO_4.

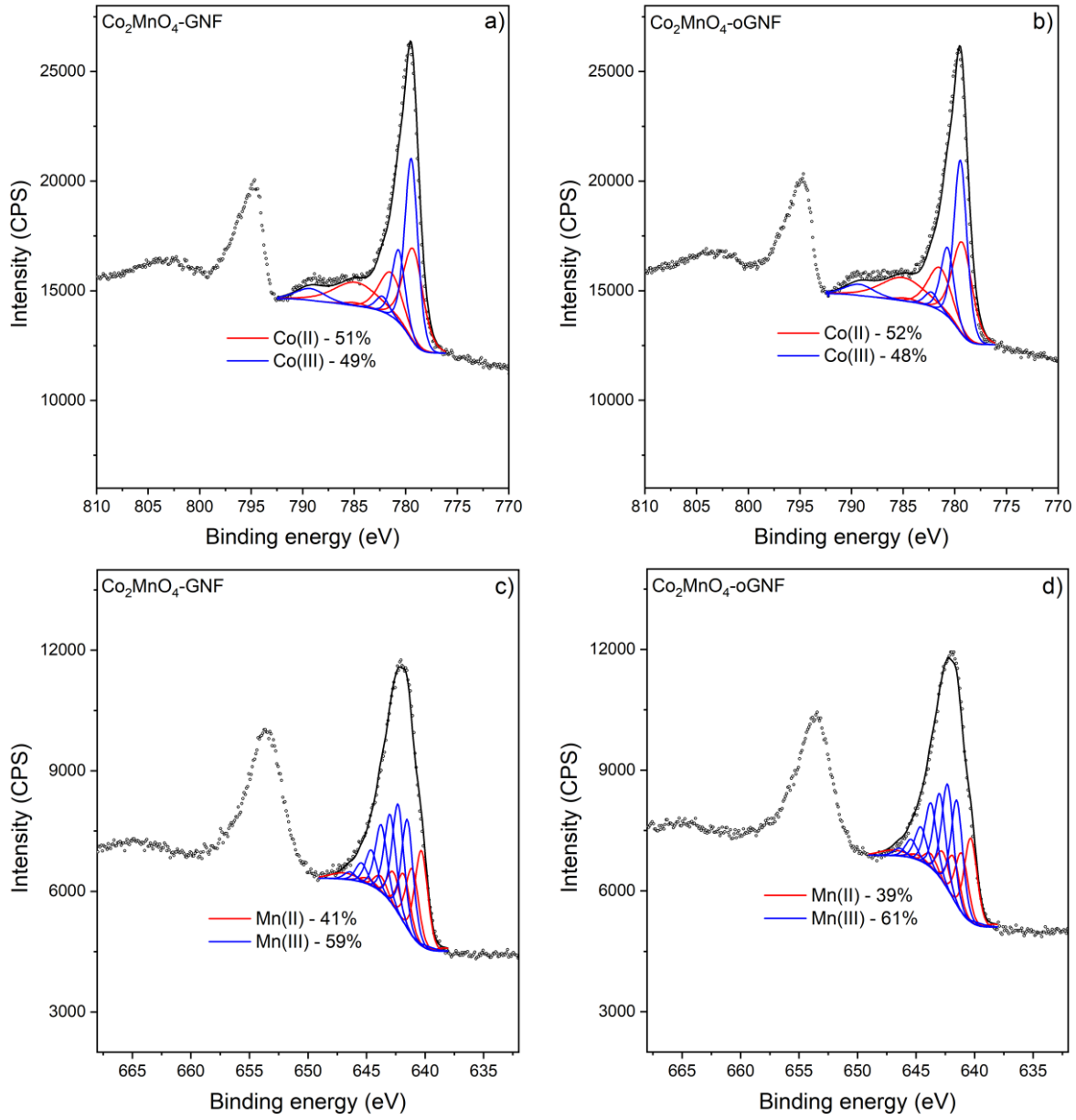

Figure 75 - XPS spectra of 31.3% Co_2MnO_4-GNF and 31.3% Co_2MnO_4-oGNF composites; **a,b**: High resolution Co 2p spectra; **c,d:** High resolution Mn 2p spectra.

This means that if the neat Co_2MnO_4 contained minor surface deposits of MnOOH, these are not present in the case of the GNF and oGNF composites. Overall there are minor differences between the GNF and oGNF composites and neat Co_2MnO_4, and virtually no difference between Co_2MnO_4-GNF and Co_2MnO_4-oGNF. As TEM analysis showed the catalyst particles on GNF and oGNF are in the 5-10 nm range and as such it was not possible to satisfactorily deconvolute the O 1s signal of these composites due to overlapping binding energies.

The XPS analysis of CB and oCB composites proved much more challenging than the GNF and oGNF composites. When UHV XPS was attempted to be used, very little signal was detected, so a near atmospheric pressure instrument was used instead (see Supplementary figure 29). This generally leads to lower signal intensities due to the large amount of N_2 gas particles in the analysis chamber (see Supplementary figure 30). Despite these efforts no XPS spectra was obtainable that would afford the author further analysis of the CB and oCB composites.

5.7 Catalytic Activity

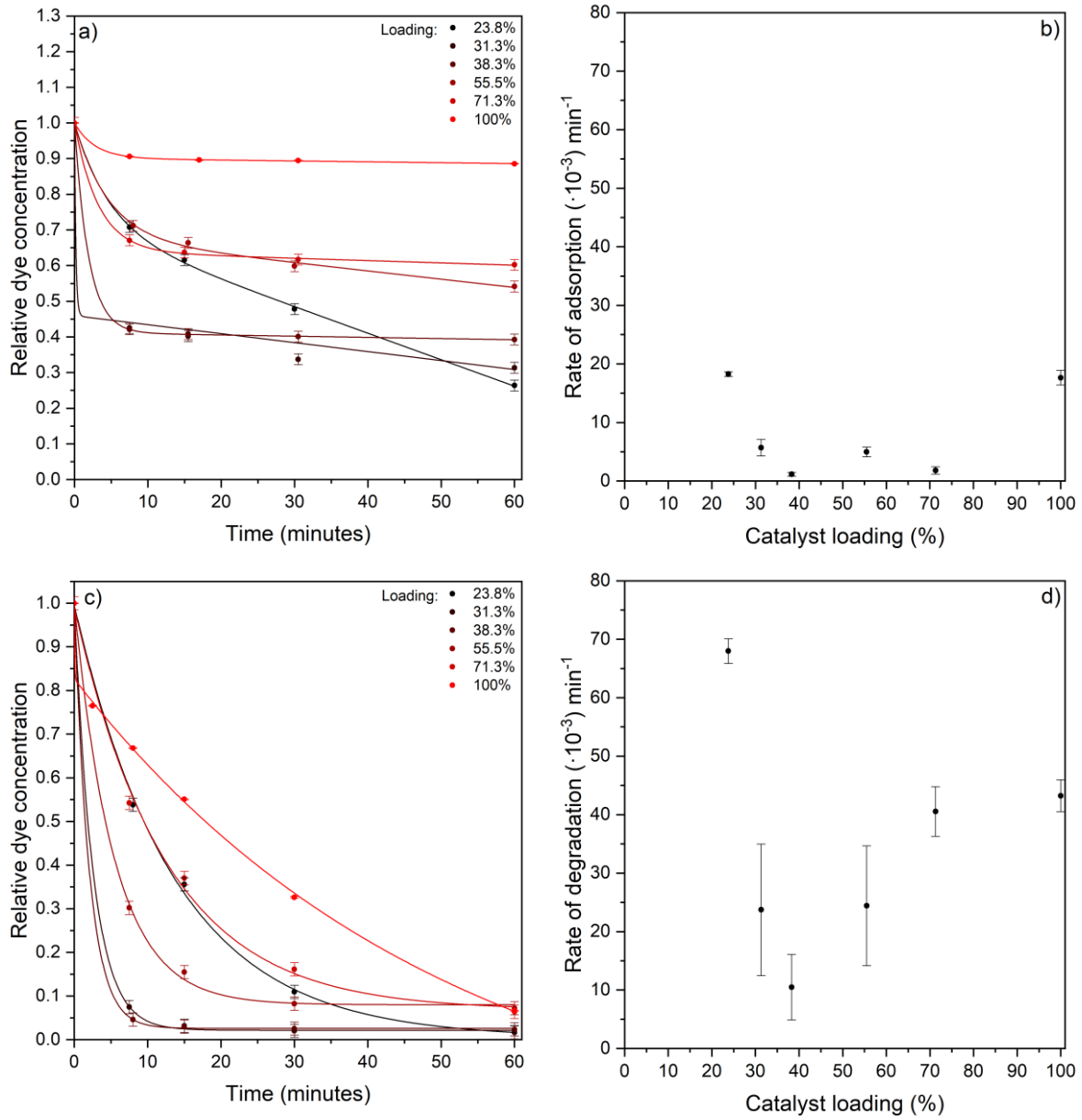

Figure 76 – Kinetic curves of adsorption and degradation of Acid Orange 7 facilitated by Co_2MnO_4-GNF composites; **a:** Kinetic curves for adsorption (without H_2O_2); **b:** Rates of adsorption; **c:** Kinetic curves for dye degradation (with H_2O_2; monitored at 485 nm); **d:** Reaction rates for dye degradation (monitored at 485 nm). Experimental conditions: 0.6 mg/mL equivalent catalyst, 0.068 mM AO7, 1.8 M H_2O_2.

Finally, the catalytic activity of the prepared composites was tested in dye removal experiments. Two types of experiments were conducted, one aimed at testing adsorption capacity and one aimed at testing catalytic activity, both on a 60 min timescale. In dye degradations, the amount of composite catalyst used was such that it always contained the same amount of the catalytically active component. These were then used to generate rates of adsorption and rates of dye degradation. This was done by assuming that all reactions follow a pseudo-first order kinetic profile, and so the slope of ln c(dye) vs time curves were taken to be -k. Different dye removal contributions were also taken into consideration in evaluating the catalytic performance of each composite. The aim of this part of the project was to compare and contrast composites made with normal and acid oxidised supports, while also identifying the composites with the highest truly catalytic degradation. All individual kinetic curves can be seen in the Supplementary information section (Supplementary figure 31 to Supplementary figure 40).

The kinetic curves of Co_2MnO_4-GNF composites are shown on Figure 76, along with rates of adsorption and degradation. The kinetic curves show a similar line shape as adsorption on GNF in Chapter 2. Based on these results there is a short initial phase of rapid decrease in dye concentration, and then a much slower gradual decrease. Overall, these rates of adsorption and degradation are quite low (consider that MnO_2-GNF composites exhibited degradation rates of $(40\text{-}100)\cdot10^{-3}$ min^{-1}), and in almost all cases lower than the neat catalyst. The catalyst facilitating the highest rates of adsorption and degradation is 23.8% Co_2MnO_4-GNF, likely due to the lowest loading being correlated to the highest dispersion of catalyst particles.

After assessing the kinetic aspect of catalytic performance, the dye removal facilitated by each composite was quantified in terms of truly catalytic degradation. In addition to the amount of truly catalytic degradation after 60 minutes, this metric plotted against time is also considered in evaluating catalytic performance.

Figure 77 illustrates that all GNF composites facilitate less overall removal and truly catalytic degradation than the pure catalyst. This is most likely due to the fact that catalyst particles on the internal walls of fibres become less accessible during the reaction due to a combination of the hydrophobicity of the fibres and O_2 gas being produced as a side product of Fenton chemistry. These factors can lead to the internal channel of the fibres being blocked off from the reaction mixture by O_2 gas. It is also apparent, that the truly catalytic degradation

is increasing with time in the case of the pure catalyst and the composite of 71.3% loading, while in the other cases it levels out very quickly.

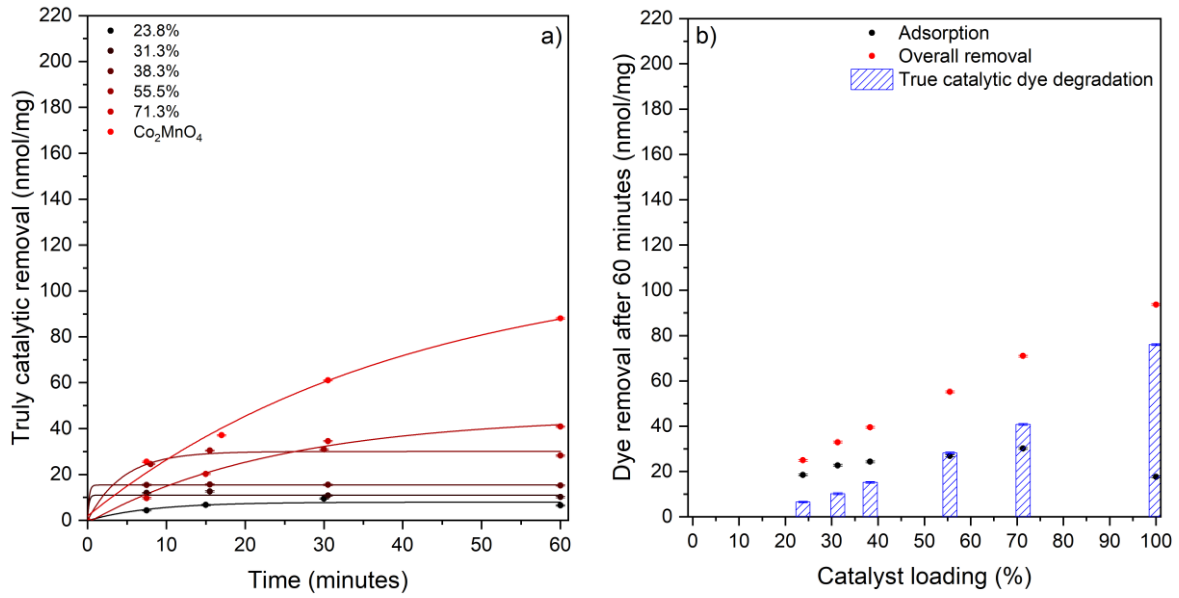

Figure 77 – **a:** Graph showing truly catalytic dye removal versus time for Co_2MnO_4-GNF composites and Co_2MnO_4; **b:** Graph summarising different dye removal contributions at the end of each experiment for Co_2MnO_4-GNF composites and Co_2MnO_4.
Experimental conditions: 0.6 mg/mL equivalent catalyst, 0.068 mM AO7, 1.8 M H_2O_2.

In terms of catalytic activity, the higher the better, of course, but since the activation of H_2O_2 is highly exothermic, heat dissipation would also have to be taken into consideration in any real life application, which would most likely be aided by the presence of a highly thermally conductive support, as it was seen in Chapter 1. Overall, the best performing catalyst is the one of 71.3% loading at roughly 41 nmol/mg over 60 minutes, but these findings also signal that GNF is not a suitable support for this catalyst in this application.

Next, the Co_2MnO_4-oGNF composites are discussed along the same lines of argument as the GNF composites (see Figure 78 and Figure 79). Adsorption on the oGNF composites follow a similar kinetic curve as undecorated oGNF. Similar to oGNF the process reaches a plateau after 15 min, after which there seems to be negligible adsorption happening. This shows that even though Chapter 2 showed that acid oxidation did not significantly change GNF when it comes to surface morphology or chemistry, adsorption on oGNF composites seems to be suppressed compared to GNF composites. The rates of dye degradation signal very low catalytic activity in the case of oGNF composites of up to 55.5% loading, but the 71.3% Co_2MnO_4-oGNF composites facilitates a slightly higher rate of degradation than the neat catalyst. This is surprising, since this composite did not show outstanding physical properties in previous

characterisation; to uncover the source of this observation more characterisation, like electron microscopy analysis, would be necessary.

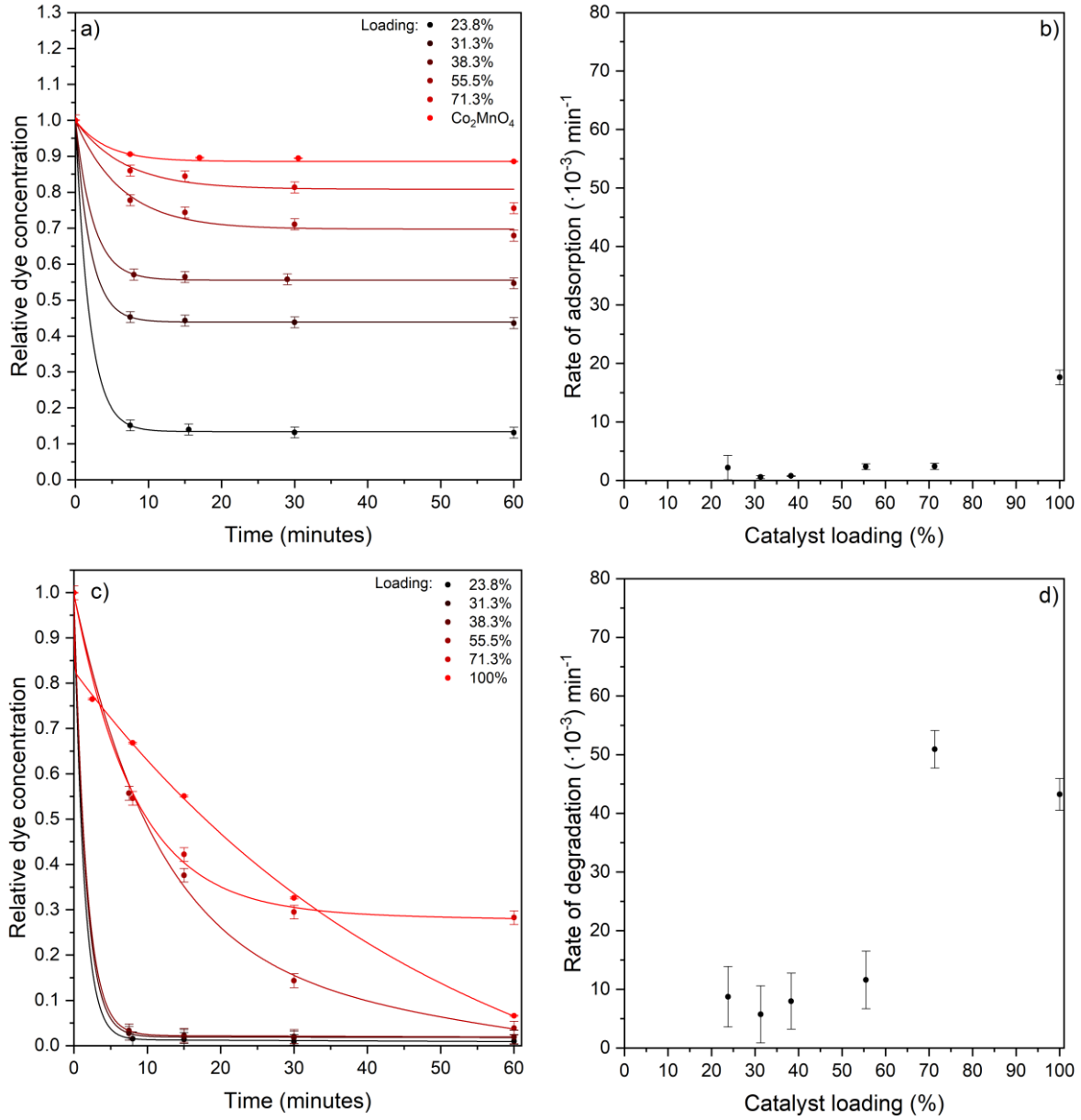

Figure 78 – Kinetic curves of adsorption and degradation of Acid Orange 7 facilitated by Co_2MnO_4-oGNF composites; **a:** Kinetic curves for adsorption (without H_2O_2); **b:** Rates of adsorption; **c:** Kinetic curves for dye degradation (with H_2O_2; monitored at 485 nm); **d:** Reaction rates for dye degradation (monitored at 485 nm). Experimental conditions: 0.6 mg/mL equivalent catalyst, 0.068 mM AO7, 1.8 M H_2O_2.

It should be noted that both the GNF and oGNF composites facilitate a higher rate of reduction in absorbance at 310 nm, and by extension more rapid removal of degradation products than neat Co_2MnO_4 (see Supplementary figure 32). This is a good sign of overall catalytic performance but this removal should be quantified in order to draw any concrete conclusions.

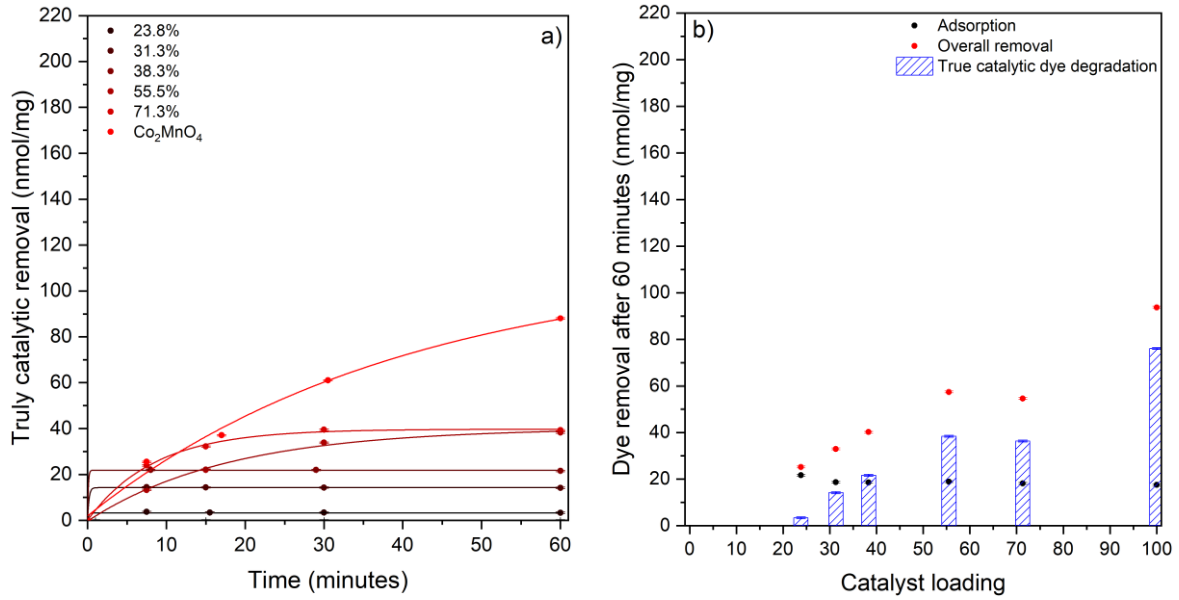

Figure 79 – **a:** Graph showing truly catalytic dye removal versus time for Co_2MnO_4-oGNF composites and Co_2MnO_4; **b:** Graph summarising different dye removal contributions at the end of each experiment for Co_2MnO_4-oGNF composites and Co_2MnO_4.

When considering the different dye removal contributions a similar trend can be seen as with the GNF composites, in that all oGNF composites perform worse than the pure catalyst. The curve shapes on Figure 79a are similar to the GNF composites, but in this case all composites' activity plateaued in the studied timeframe at a much lower value that the pure catalyst. The most active catalyst out of these five materials is the composite of 55.5% loading with a truly catalytic degradation of 38 nmol dye degraded per mg catalyst. All of the above confirms that neither GNF nor oGNF are suitable catalyst supports for this catalyst, in this application. All of the studied indicators of catalytic performance are lower when oGNF composites are compared to GNF composites.

Next the performance of the CB and oCB supported catalysts are evaluated in the same manner as above. The results for the CB composites are shown by Figure 80 and Figure 81. One thing that is immediately apparent when looking at Figure 80a, is that adsorption on the CB composites is more gradual and no step change is visible. The rates of adsorption and catalyst loadings are inversely proportional. The two composites of lowest loadings facilitate higher rates of both adsorption and degradation when compared to the pure catalyst. It has to be noted that rates of degradation describe overall dye removal, which includes adsorption, so it makes sense that the rates of adsorption and rates of degradation follow a similar trend.

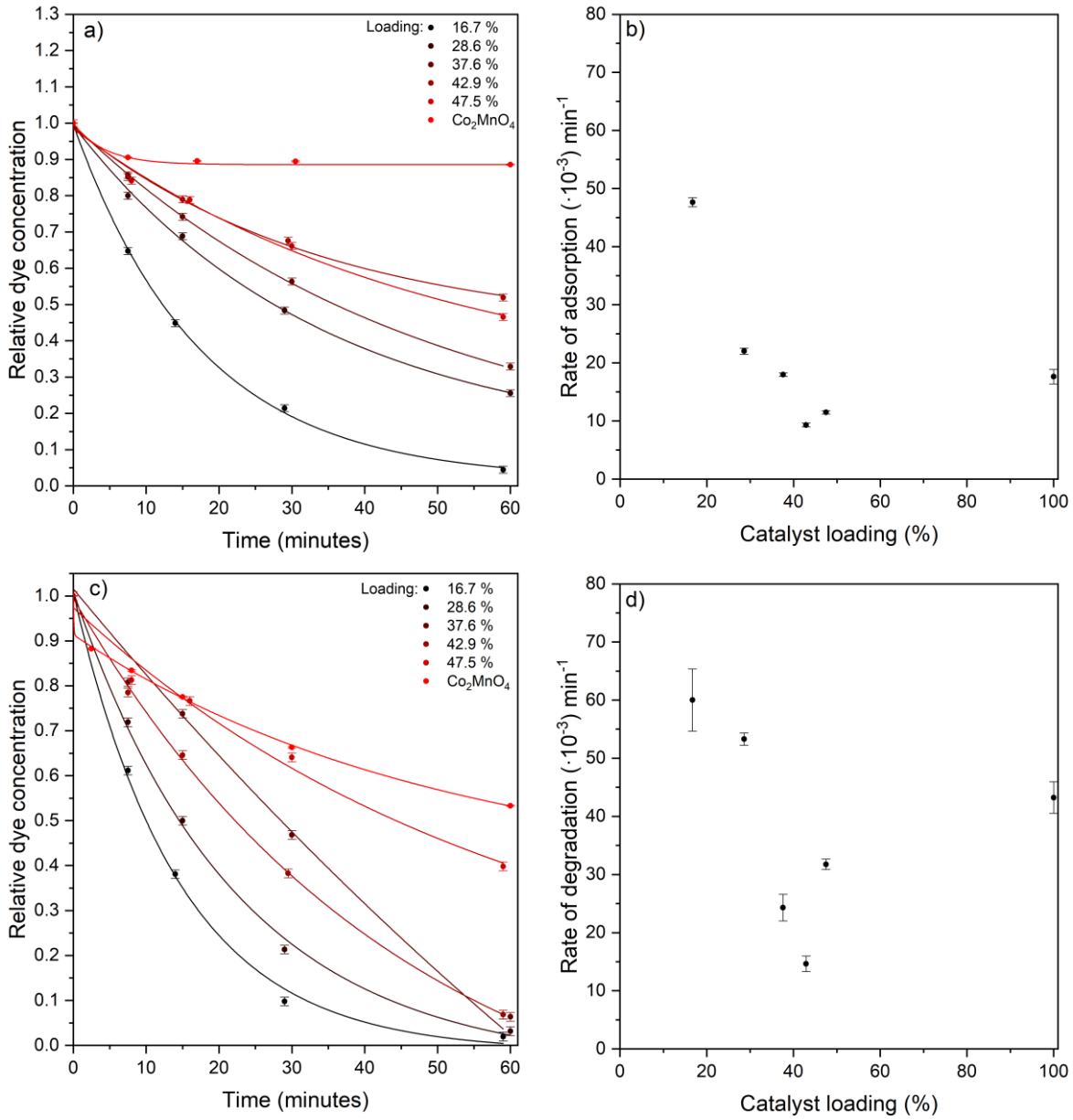

Figure 80 – Kinetic curves of adsorption and degradation of Acid Orange 7 facilitated by Co_2MnO_4-CB composites; **a:** Kinetic curves for adsorption (without H_2O_2); **b:** Rates of adsorption; **c:** Kinetic curves for dye degradation (with H_2O_2; monitored at 485 nm); **d:** Reaction rates for dye degradation (monitored at 485 nm). Experimental conditions: 0.3 mg/mL equivalent catalyst, 0.068 mM AO7, 1.8 M H_2O_2.

By extension it is likely that the composites of 16.7 and 28.6% loadings exhibit these high rates of adsorption and degradation because these contain the highest ratio of undecorated graphitic surfaces.

When considering the amount of dye removed truly catalytically by these composites, it can be seen that the composite of 42.9% loading and the pure catalyst remove 77 and 76 nmol/mg respectively, so based on this metric the most active catalyst is the one of 42.9% loading (see Figure 81).

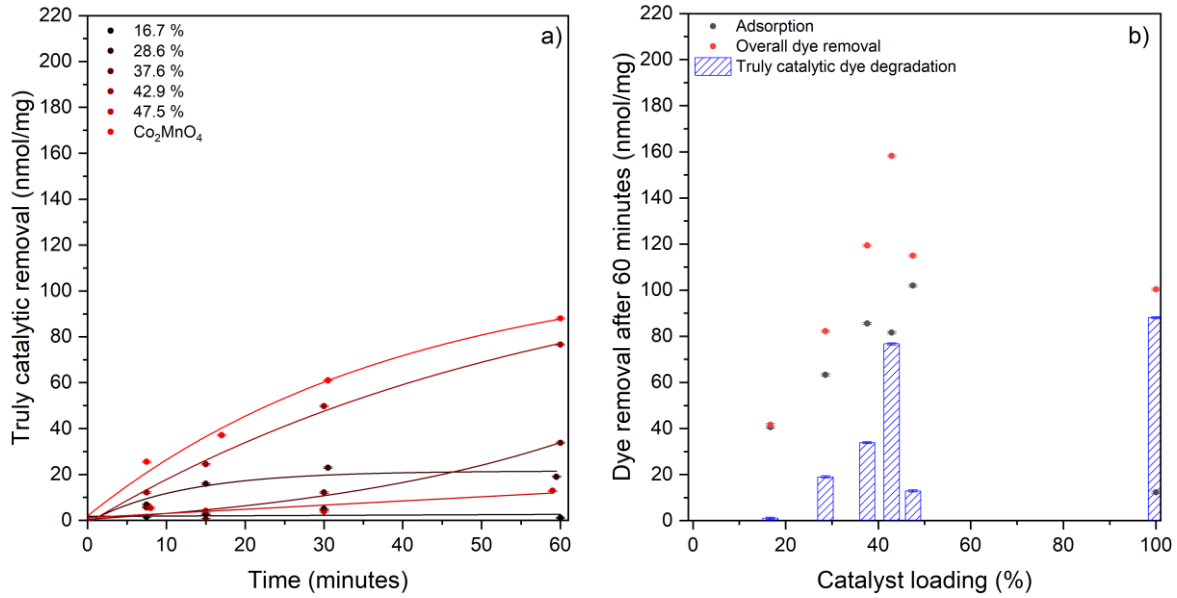

Figure 81 – **a:** Graph showing truly catalytic dye removal versus time for Co_2MnO_4-CB composites, CB and Co_2MnO_4; **b:** Graph summarising different dye removal contributions at the end of each experiment for Co_2MnO_4-CB composites and Co_2MnO_4.

Finally, the oCB supported catalysts are discussed in the same way as above (see Figure 82 and Figure 83). The rates of adsorption show a similar trend as the composites of CB did, meaning that catalyst loading is inversely proportional to rates of adsorption, the highest values belonging to the composite of 16.7% loading. This is likely explained by surface coverage by catalyst particles being directly proportional to catalyst loading, and that the catalyst particles are significantly less adsorptive. These rates are generally lower than those of the CB composites which signals a hindrance to adsorption. The rates of degradation are generally much lower than those of the CB composites, as well, but follow a similar trend as CB composites. The highest values are exhibited by the composites of 16.7, 28.6 and 47.5% loading.

Similarly to GNF and oGNF composites, both the CB and oCB composites exhibit a similar rate of reduction in absorbance at 310 nm as neat Co_2MnO_4, regardless of catalyst loading. This can be a good sign of overall catalytic activity, but further work would be necessary to draw any concrete conclusions.

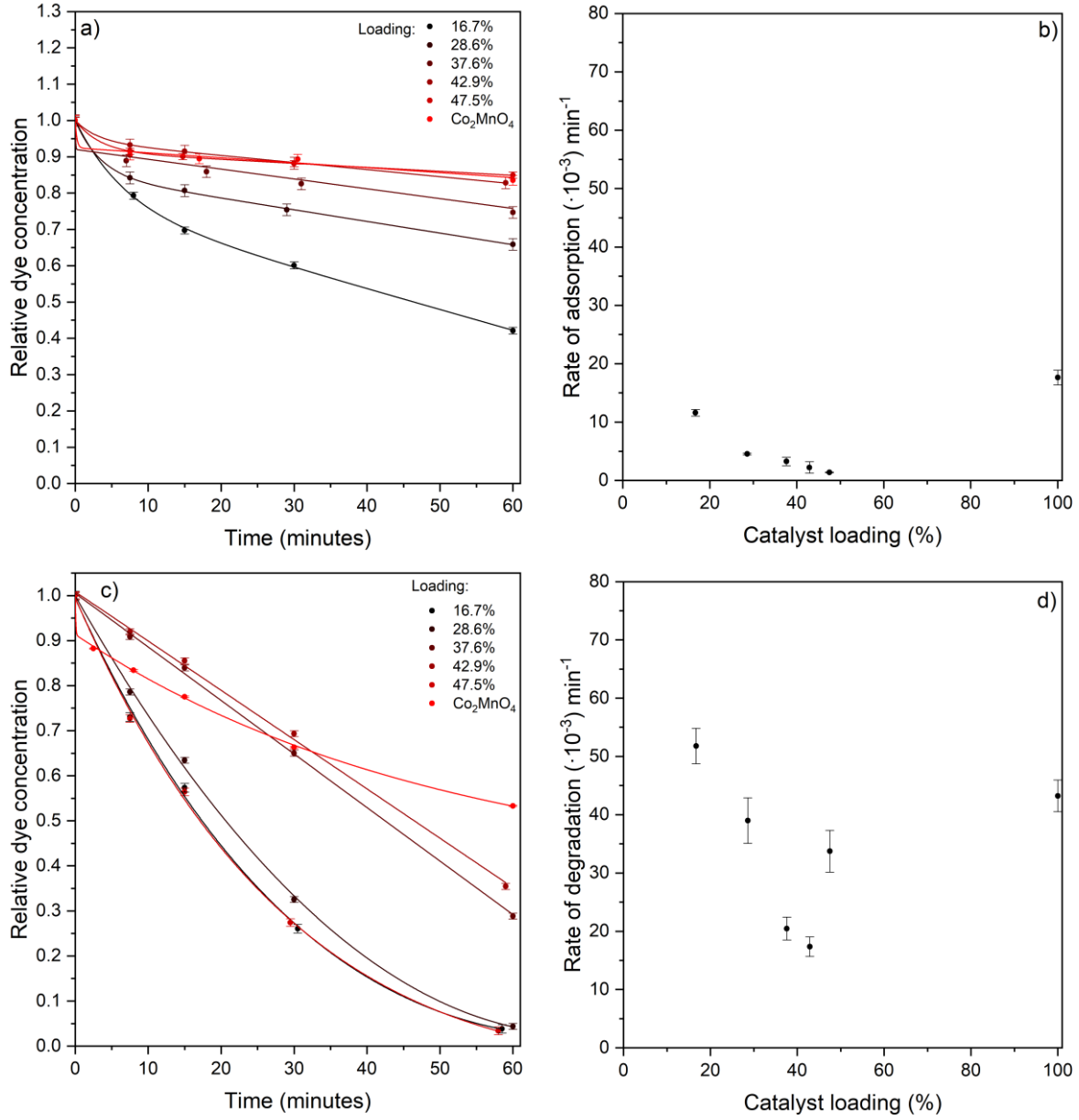

Figure 82 – Kinetic curves of adsorption and degradation of Acid Orange 7 facilitated by Co_2MnO_4-oCB composites; **a:** Kinetic curves for adsorption (without H_2O_2); **b:** Rates of adsorption; **c:** Kinetic curves for dye degradation (with H_2O_2;monitored at 485 nm); **d:** Reaction rates for dye degradation (monitored at 485 nm). Experimental conditions: 0.3 mg/mL equivalent catalyst, 0.068 mM AO7, 1.8 M H_2O_2.

When looking at truly catalytic degradation in the case of oCB supported catalysts there is a catalyst that exhibits a significantly better performance than the pure catalyst, at roughly twice the amount of dye removed by each mg catalyst (76 vs 156 nmol/mg). This fits the trend of the CB supported catalyst in that the higher loadings tend to have higher activity. It also becomes apparent that adsorption is significantly suppressed in the case of all oCB composites when compared to CB composites.

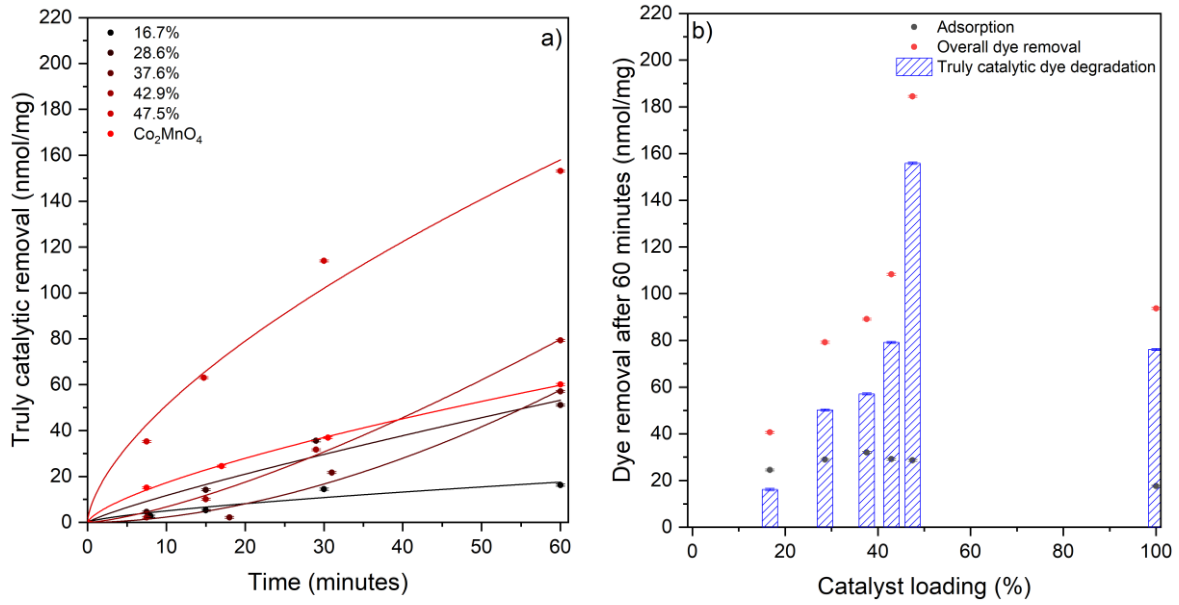

Figure 83 – **a:** Graph showing truly catalytic dye removal versus time for Co_2MnO_4-oCB composites and Co_2MnO_4; **b:** Graph summarising different dye removal contributions at the end of each experiment for Co_2MnO_4-oCB composites and Co_2MnO_4.

In summary, it can be concluded that GNF and oGNF seem to be unsuitable to be used as catalyst supports in this specific application, while CB and especially oCB have good metrics of catalytic performance. Rates of adsorption and degradation follow the same general trend, which is due to the co-occurrence of adsorption and degradation in any dye removal experiment. Truly catalytic dye removal seems to be inversely proportional to the rates facilitated by any catalyst. This makes the development of these catalysts challenging, as the ideal trade-off between rapid degradation and high overall removal will depend on the exact application and its operational parameters. It might be surprising that the best catalyst has such a high loading, as industrial composite catalysts usually have 5-10% catalytically active components at most. One reason why high loadings show such good activity here is that there is a very large discrepancy between the catalytic activity of the pure catalyst and the adsorptive activity of the undecorated carbon beads. Higher loadings will inevitably cover more of the surface of the beads and thus hinder adsorption. Another reason could be that the beads have very large surface areas, most of which stems from the internal pore structures. The catalyst will inevitably occupy both the external surface and the internal pore system. Catalyst particles inside the pore structures are likely less accessible to reactants, especially since one of the side products of H_2O_2 decomposition is O_2 gas, which can block pores. That being said 47.5% Co_2MnO_4-oCB has been identified as the best catalyst in this group of 20 composites.

5.8 Reusability

Finally, as part of this chapter's investigation into the catalytic performance of these composites, specific experiments were conducted to probe the reusability of a CB and an oCB supported catalyst. Based on observation made so far, it is fair to say that in each reaction a batch of catalyst is used, it will irreversibly adsorb some amount of organics. This process eventually leads to the adsorptive saturation of a batch of catalyst over a number of consecutive usages. Considering that a typical experimental mixture contains 2.5 µmol of dye, and that CB and oCB have adsorption capacities of 1500 and 950 nmol/mg, respectively, the saturation of any CB or oCB composite would take dozens of reactions. In order to study the endpoint of this saturation process a 16.7% Co_2MnO_4-CB and a 16.7% Co_2MnO_4-oCB was saturated with AO7. These composites were chosen for two reasons: relatively low saturation times and lower amounts of unsupported catalyst. It was found that saturating these beads with the dye can be quite difficult at higher loadings as the rate of adsorption can be very low, and to overcome this problem composites of 16.7% loading were used.

To prove that the catalysts are saturated, an experiment was done, where a batch of each composite was placed into the same dye solution that was used in other adsorption experiments and the dye concentration was monitored over 60 min. Also, to account for the small reversibility in adsorption, an experiment was done to see how much dye desorbs from both batches of catalyst in ultrapure water of the same volume as typical reaction mixtures. The difference between desorption and adsorption has been named net sorption. As Figure 84 shows net sorption is generally unchanged over the studied timeframe, which means that adsorption and desorption can be assumed to be negligible. These experiments confirm that as the composites get saturated their overall activity decreases, and the truly catalytic activity also decreases somewhat (see Figure 85).

In the case of the CB composite, an unused batch facilitated 1.1 ± 0.5 nmol/mg truly catalytic degradation, while the same metric for the presaturated batch is 0.83 ± 0.5 nmol/mg. This proves that once this CB supported catalyst is adsorptively saturated its truly catalytic activity reaches zero. On the other hand, in the case of the oCB composite, truly catalytic degradation changed from 16.2 ± 0.4 nmol/mg to 14.0 ± 0.4 nmol/mg which signals that even after saturation, roughly the same catalytic activity is still present. These results also highlight the importance of avoiding the adsorption of organics on the catalyst in this application in order

to maintain high truly catalytic activity in the long term. As previous results show, the adsorption of the reactant on the composite catalyst is mostly irreversible.

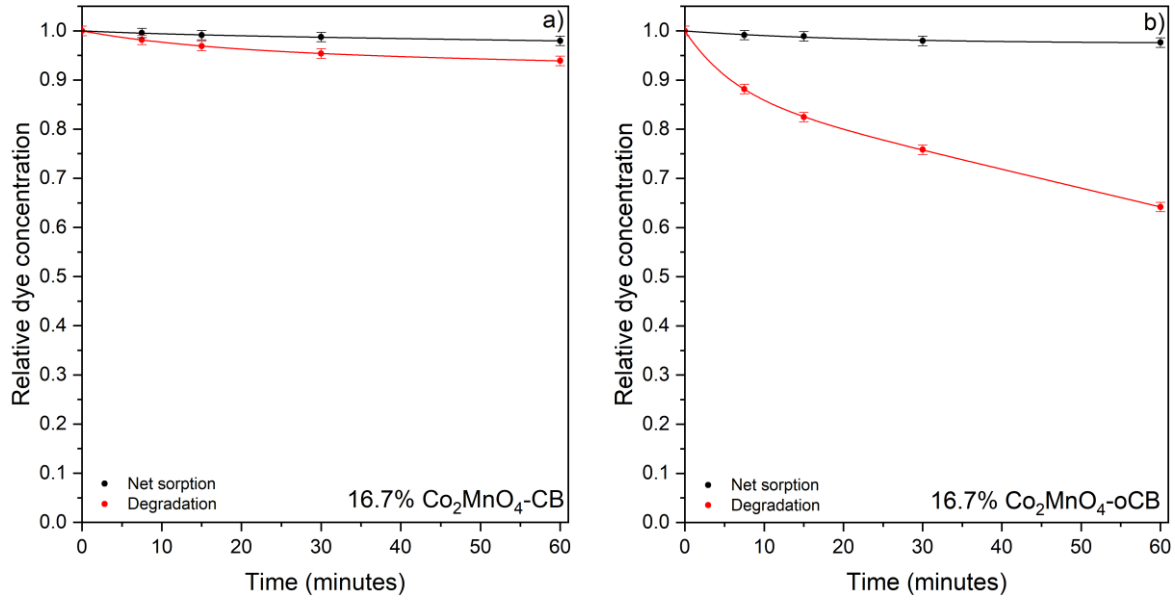

Figure 84 – Kinetic curves for presaturated catalysts in dye degradation experiments; **a:** CB composite; **b:** oCB composite.

Finally, the catalytic efficiency of a new and a presaturated batch of 16.7% Co_2MnO_4-CB and 16.7% Co_2MnO_4-oCB catalysts were quantified. In line with previous experiments, the unused CB composite has negligible catalytic efficiency, which only slightly improves with saturation (from 0.051 ± 0.025 to 0.33 ± 0.053%). On the other hand the catalytic efficiency of the oCB composite changes from 0.78 ± 0.07% for the new batch, to 8.8 ± 0.4% for the presaturated one, which is a roughly tenfold increase and is significantly more than any other value recorded in this work. This practically means that in the case of presaturated composites, the amount of H_2O_2 consumption needed to achieve a certain level of truly catalytic degradation improved significantly.

In the case of 62.5 mg fresh CB composite 1.07 µmol dye was degraded with 2080 µmol H_2O_2 consumed, and this changed to 1.70 µmol dye being degraded with 519 µmol H_2O_2 consumed for the presaturated CB composite. In the case of 62.5 mg oCB composite these values were 16.3 µmol truly catalytically degraded dye with the consumption of 2090 µmol H_2O_2 in the case of the fresh composite, and 14.0 µmol truly catalytic dye degradation with 160 µmol H_2O_2 consumed for the presaturated composite[12]. Since the H_2O_2 consumption

[12] The ratio of dye degraded to H_2O_2 consumed might seem very low, but keep in mind that AO7 is a large molecule, and not a 100% of H_2O_2 decomposition reactions produce ROS. The full mineralisation of AO7 would take dozens of equivalents of ROS, which explains why so much H_2O_2 is needed in these degradation reactions.

decreased in both cases between the fresh and presaturated composites, it is likely that the adsorbing organics cover some catalyst particles, for example in the pore structures, but the full elucidation of this deactivation mechanism would require further, targeted experimentation.

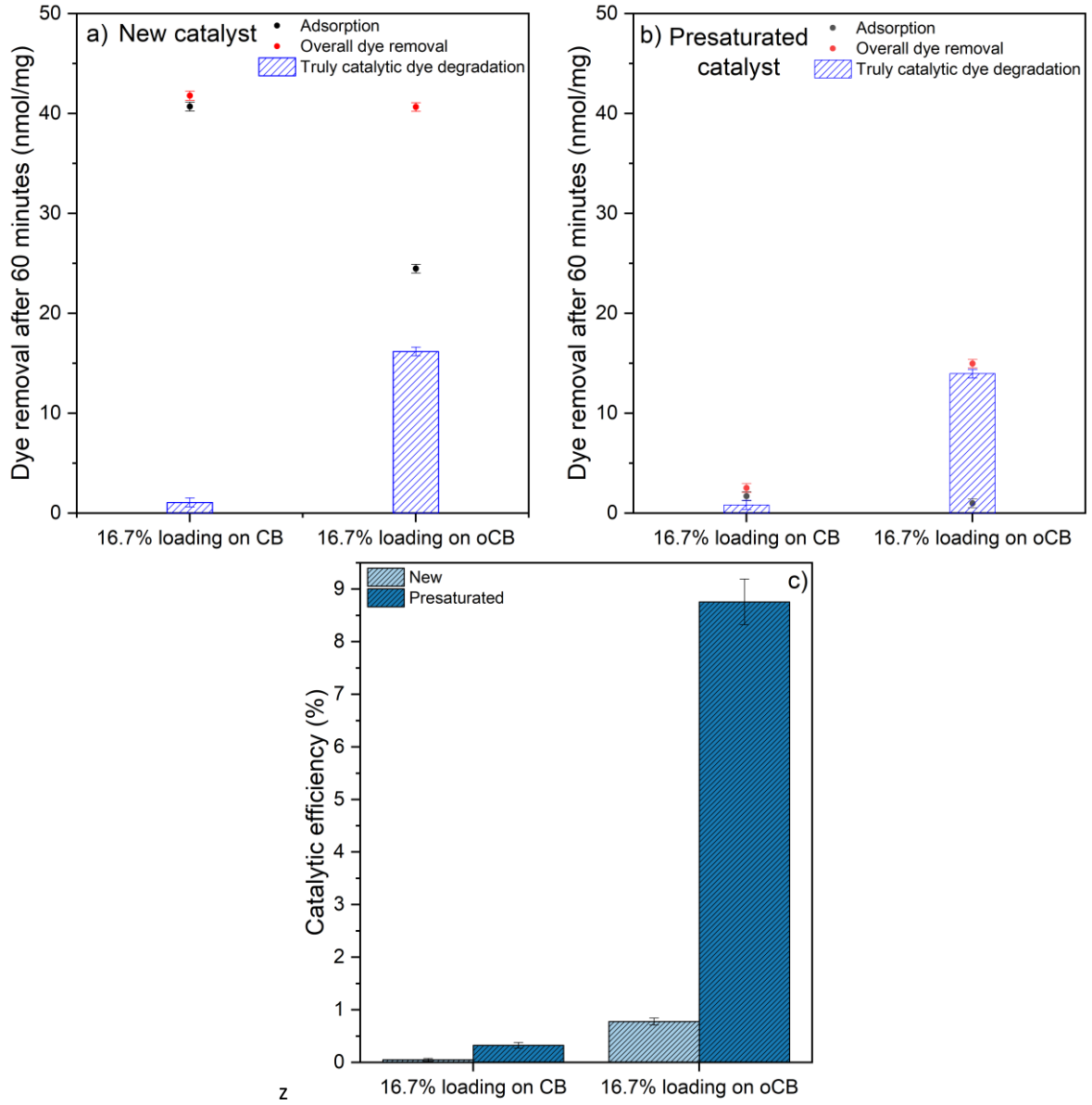

Figure 85 – Graphs describing different contributions to dye removal for a selected CB and oCB composite catalyst using a new and a presaturated batch; **a:** Comparison between net catalyst batches; **b:** Comparison between presaturated catalyst batches; **c:** Comparison between catalytic efficiencies.

The findings of this subchapter underline the importance of having a more detailed understanding of catalytic activity in this field, while also highlighting the significance of suppressing unwanted adsorption in order to maximise catalytic activity.

5.9 Conclusions and Future Prospects

The main question this chapter investigates is how the acid oxidation of GNF and CB change these materials' properties as catalyst supports in Fenton-like organics removal experiments. The chapter starts out by presenting the results of an optimised synthesis for Co, Mn spinels, which have been chosen as the catalyst of interest, since previous literature survey has indicated these materials are suitable catalysts of both the electrochemical generation and activation of H_2O_2. The presented results confirm that the prepared spinels are highly active in Fenton-like organics removal experiments, the most active catalyst having a higher truly catalytic dye removal than the most active MnO_2-GNF composite of the first chapter along with excellent physical properties, like extremely small particle size and a surface area that is among the highest ever published values for Co_2MnO_4 samples.

This metal oxide was then used to produce composite catalysts with GNF, oGNF, CB and oCB which were assessed in similar organics removal experiments. In the case of GNF, oGNF and CB composites the resulting composites showed a catalytic activity that was below that of the neat Co_2MnO_4 both in terms of kinetics and quantified dye removal. The Co_2MnO_4-oCB composites showed a comparable or higher catalytic activity than the unsupported catalyst, while also showing suppression of unwanted adsorption when compared to Co_2MnO_4-CB composites. Finally, the reusability of CB and oCB composites were probed in a proof of concept experiment compared the first use of a catalyst to its adsorptively saturated end state. This experiment showed that the high apparent overall dye removal of a CB composite is mostly due to adsorption at both the unused and saturated stage, while the studied oCB composites showed a sustained activity and even a significant increase in catalytic efficiency.

The work presented in this chapter would benefit from a few, small studied that could lead to a deeper understanding of the studied processes. XRD analysis with an instrument equipped with a Co X-ray anode would allow for the generation of higher quality X-ray diffractograms, and as such unlock the possibility of more precise secondary analysis of XRD data. The ICP-MS analysis of samples taken during organics removal experiments could help quantify the amount of Co and Mn leaching, which would then help identify what extent of catalytic activity is due to a heterogeneous mechanism induced homogeneous mechanism. FIB-SEM analysis could help identify the exact position of catalyst particles in CB and oCB samples, mainly identifying to what extent does the catalyst occupy the internal pore structures vs the external surface. Finally, studying how the pH of the synthetic mixture changes in the

production of oCB composites with the amount of oCB used could help identify any mechanism that led to the emergence of a minor Co, Mn carbonate phase in the case of 16.7% Co_2MnO_4-oCB.

Chapter 6 - Assessment of Electrocatalytic Activity of Carbon Supported Co, Mn Spinels in Oxygen Reduction

6.1 Introduction and Literature Review

This chapter discusses the evaluation of catalytic activity in O_2 reduction of materials previously studied in Chapter 3. The aim is to evaluate what electrochemical processes are being facilitated by these materials and to identify the most catalytically active one. The final aim of this project is to create a bifunctional catalyst that is capable of both efficiently generating and activating H_2O_2 in order to generate ROS for the degradation of aqueous organics.

The research of oxygen reduction reaction (ORR) is a very active field, with over 2500 articles being published in each of the last five years, as indexed by Scopus. According to Yang *et al.* the main motivation for this is that the most commonly used industrial production method of H_2O_2, the Anthraquinone process, has significant drawbacks.[215] High concentration solution have to be produced in order to maximise the economy of the process but this necessitates energy intensive distillation processes, and increases transportation and storage costs further down the value chain, since high concentration H_2O_2 is extremely flammable. H_2O_2 is widely used in paper production, synthetic chemistry, water treatment, etc, so it would be highly desirable if the production of it shifted to a localised, on-demand method, Yang *et al.* argue.

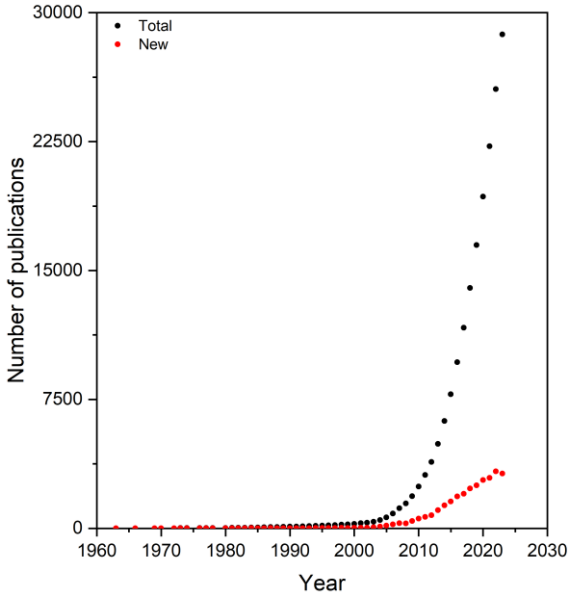

Figure 86 – Graph showing the number of publications with the keywords ‘oxygen reduction reaction’. (Scopus accessed on 2025.03.25.

As discussed in the introduction chapter, the ORR can most commonly follow two reaction pathways: 2 e^- reduction leading to H_2O_2 and 4 e^- reduction leading to H_2O.[216] The most common application of the ORR has been energy storage via the 4 e^- pathway for decades, but in recent years an increasing number of articles are published studying the electrochemical production of H_2O_2 via the 2 e^- pathway.[2-5] Only the latter is relevant for this thesis, so only this will be further discussed.

The 2 e^- ORR can be described with the overall reaction shown by (38). The main steps of this reaction pathway are the diffusion of dissolved O_2 to the vicinity of the catalyst, adsorption onto the surface, electron transfer, desorption of the product, and diffusion into the bulk solution phase.[216] These main steps also identify the parameters governing O_2 reduction on any catalyst: diffusion of O_2 in the electrolyte, mechanism of adsorption, and kinetics of electrode reaction.

$$O_2 + 2\,H^+ + 2\,e^- \rightarrow H_2O_2, E^0 = 0.67\,V \quad (38)$$

A defining step of the ORR mechanism is the manner in which O_2 binds to the surface of the catalyst. Yeager has identified three main modes of this: Griffiths, Pauling and bridge mode, which was later named after Yeager, as illustrated by Figure 87.[218] Adsorption according to the Griffiths and Yeager modes leads to the weakening of the O-O bond due to the interaction between the molecular orbitals of the metal ion centre and the O_2 molecule, which is conducive to direct 4 e^- reduction in a dissociative pathway. In Pauling mode adsorption, only one oxygen atom of the molecule is interacting with the metal ion centre, which is not conducive to the cleavage of the O-O bond, so this adsorption model leads to an associative 2 e^- reduction pathway. Another crucial step that defines the mechanism of ORR on any given material is how strongly the relevant reactants and products of the electron transfers are bound to the surface of the catalyst.[219]

Electrochemical reactions rarely happen at the thermodynamic equilibrium potential of a process. Any difference to this is called an overpotential, and its presence signals that the studied reaction requires more energy to proceed then what the standard redox potentials would suggest. Nørskov *et al.* have studied 4 e^- ORR on a Pt catalyst, where the standard redox potential of this process is 1.23 V.[220] They have found that in this reaction, the origin of the overpotential is that at potentials close to 1.23 V vs RHE the adsorbed O_2 is too stable for any electron or proton transfer between it and the catalyst. Peng *et al.* have found that in Li-O_2 secondary batteries the main processes defining the overpotential of O_2 reduction and

evolution are adsorption-desorption processes and chemical changes to the catalyst species. They reported that an initial ORR can lead to the deposition of Li_2O_2 on the graphene electrode, which then changes sorption characteristics and conductivity, contributing to an increase in overpotential. These findings highlight that the potential at which an electrochemical reaction proceeds is dependent of properties inherent to the catalyst and reactants but also on emergent properties of the studied cell.

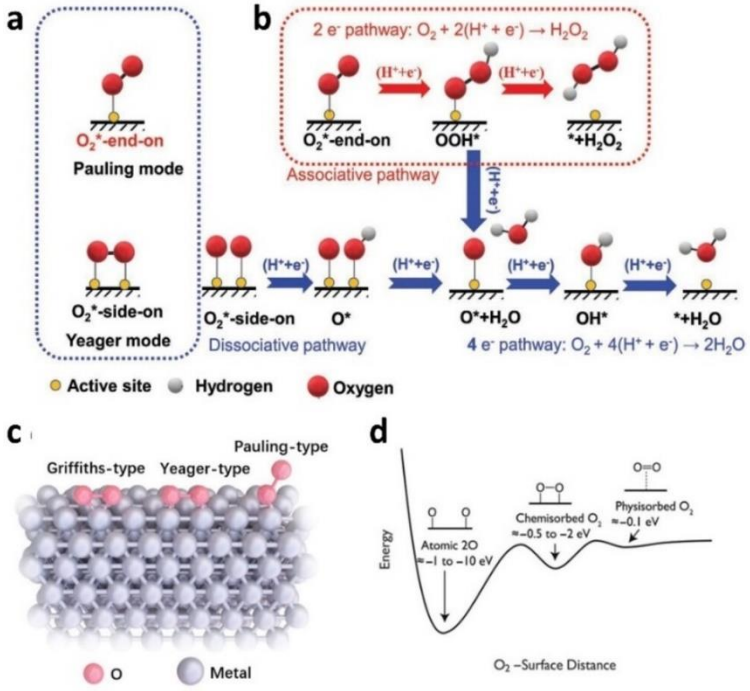

Figure 87 – Graphs showing possible modes of O_2 binding and the reaction pathways these lead to in ORR, according to Byeon *et al.*[221]

The most commonly studied catalysts of ORR include noble metals, mainly Pt, and Pd, transition metal oxides, like ZrO_2 and Co_3O_4, carbon materials and more recently single atom catalysts.[7-8] While Pt catalysts show the highest activity in ORR, Pt is a very expensive material, and it is prone to deactivation in ORR.[167] For this reason, noble metal-free and even metal-free catalysts are actively pursued, where the former category most commonly refers to first row transition metal spinels, while the latter to carbon materials.[40], [224], [225]

The state of the art for the research of ORR on metal oxides, carbon materials and their composites can be understood by considering the work of Hongjie Dai, one of the leading researchers of this field.[173] The Dai Research group has used Co_3O_4, $MnCo_2O_4$, N-doped reduced graphene oxide, and the composites of these, along with a commercial Pt/C catalysts. They use cyclic voltammetry (CV) and rotating ring disk electrode (RRDE) voltammetry to quantify the electrocatalytic activity of their materials in ORR. To do, this they fabricate an

electrode that contains the studied material at a defined surface coverage, and submerge it in an electrolyte.

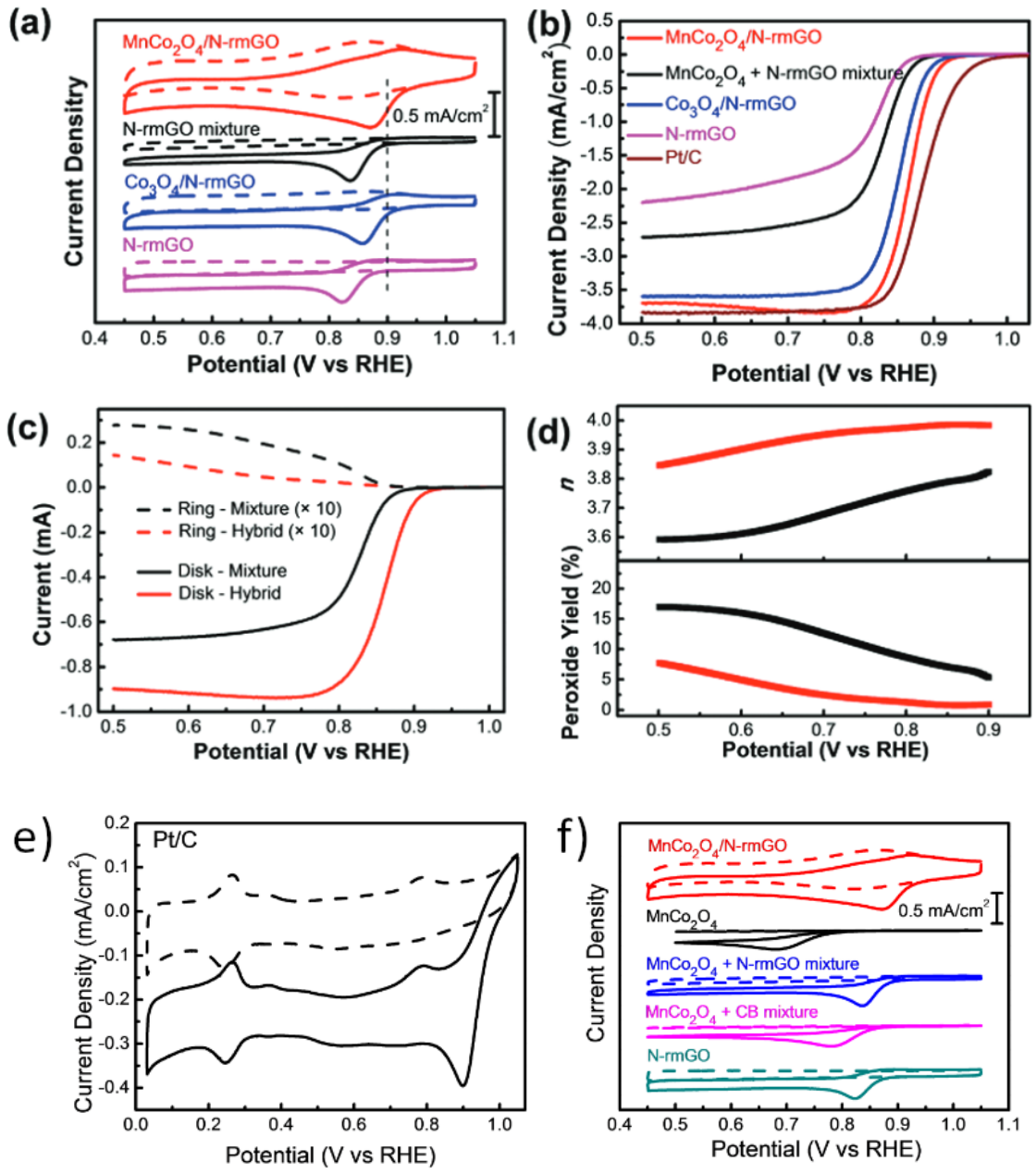

Figure 88 – Results of electrochemical investigations for first row spinel composites commonly used in ORR research; **a:** Cyclic voltammograms; **b:** Rotating disk electrode voltammograms; **c:** Rotating ring disk electrode voltammograms; **d:** Average number of electrons transferred per reaction and the corresponding H_2O_2 yield; **e:** Cyclic voltammogram of Pt/C control; **f:** Additional cyclic voltammograms.[173]

The current response at any given potential applied to this electrode is then studied in electrolytes either purged with N_2, or saturated with O_2. CV can then be used to identify the potential at which ORR occurs under the used experimental parameters, and RRDE can then be used to study the mechanism of ORR, including the number of transferred electrons per reaction, and by extension the H_2O_2 yield of ORR. Liang *et al.* were studying these materials to

be used in energy applications, and as such the target potential was the 1.23 V vs RHE of 4 e^- ORR. Figure 88a and f show that the overpotential on the studied materials were between 0.3 and 0.6 V.

Liang *et al.* identified the $MnCo_2O_4$/N-rmGO hybrid as the most active noble metal free catalyst with an onset potential of 0.9 V vs RHE and an anodic current density of 3.5-4.0 mA/cm^2. The average number of electrons transferred in reactions was between 3.8 and 4.0, corresponding to the 4 e^- reduction being dominant, which is associated with minimal peroxide yields. These results show the most common way of studying ORR catalysts and the magnitude of measured values that can be expected.

The selective production of H_2O_2 via the promotion of 2 e^- ORR is an area that is receiving more and more research interest in recent years.[15–17] The most commonly used materials in this area are graphene-based carbon materials and single atom catalysts, both of which have been reported to facilitate 2 e^- ORR at 0.7 V vs RHE, at selectivities of up to 95% in alkaline media.[18-19] Rarely, oxidised macroscale carbon materials are also used as catalysts, but this is quite recent and so not many publications are available, yet.[16–18] These researchers generally found that oxygen content, especially the concentration of surface carboxylic functional groups, is correlated with electrocatalytic activity.

It is worth briefly summarising the theoretical basis of RRDE voltammetry. The fundamental relationships affecting the measured current in RRDE described by the Levich and Koutecký–Levich equations ((39) and (40) respectively), both of which are described in a form most suitable for O_2 reduction, i.e. an electrochemical process at large negative overpotential with an analyte of low diffusivity. The Levich equation describes the relationship between the limiting current and the square root of the rotation rate, and accordingly, the constant terms of the equation are often condensed into the Levich constant (B_L). In ideal cases the number of electrons transferred can be thought of as a constant, but this is not always the case. Additionally, in a simple half reaction the current measured at different potentials is linearly dependent on the rotation rate, but the equation itself is only valid for the limiting current. The line fitted onto the limiting currents plotted against the square root of the rotation rate should have a y intercept of zero in ideal cases. Finally, it is worth noting that the term 0.620 is a constant stemming from the geometry of the electrodes used for such investigations.

The Koutecký–Levich equation can be used to gain more insight about the electrochemical process of interest, including kinetic and mechanistic details. The use of this

approach if limited to reactions where the rate of electron transfer and mass transport are comparable. In the case of this work, the most important aspect of Koutecký–Levich analysis is that plots at different potentials should all be linear and these lines should be parallel. The slope of these lines are mainly defined by the number of transferred electrons, while the intercept is defined by both the number of transferred electrons and the rate of electron transfer.

These equations are only valid for limiting currents, or in other words currents measured at the plateaus of the sigmoid curves on linear sweep voltammograms. In this work, limiting currents were not easily measurable so instead these were gained by extrapolating the recorded voltammograms until a plateau. As a matter of convention, cathodic currents will be treated as negative numbers and anodic currents as positives.

$$\mathrm{i_L} = 0.620 \cdot \mathrm{n} \cdot \mathrm{F} \cdot \mathrm{A} \cdot \mathrm{D}^{\frac{2}{3}} \cdot \omega^{\frac{1}{2}} \cdot \nu^{-\frac{1}{6}} \cdot \mathrm{c} = B_L \cdot \omega^{\frac{1}{2}} \tag{39}$$

$\mathrm{i_L}$: limiting current (A), n: number of electrons transferred,
F: Faraday constant (C/mol), A: electrode area ($\mathrm{cm^2}$),
D: diffusion coefficient ($\mathrm{cm^2/s}$), ω: angular rotation rate (rad/s),
ν: kinematic viscosity ($\mathrm{cm^2/s}$), c: analyte concentration ($\mathrm{mol/cm^3}$)
$\mathrm{B_L}$: Levich constant

$$\frac{1}{\mathrm{i_m}} = \frac{1}{\mathrm{i_k}} + \frac{1}{\mathrm{i_{mt}}} = \frac{1}{n \cdot F \cdot A \cdot k \cdot c} + \frac{1}{\mathrm{B_L} \cdot \omega^{\frac{1}{2}}} \tag{40}$$

$\mathrm{i_m}$: measured current (A), $\mathrm{i_k}$: kinetic current (A), $\mathrm{i_{mt}}$: mass transport current (A)
k: rate of electron transfer, $\mathrm{B_L}$: Levich constant, ω: angular rotation rate (rad/s)

Finally, it is important to mention that the field of H_2O_2 sensing, while only tangentially relevant, can serve with important information about the reduction potential of H_2O_2 in neutral media. The most commonly used materials are noble metal nanoparticles like Ag, Au, and Pt, and metal oxides, like MnO_2, Co_3O_4, and ZnO and their composites with graphene-based carbon materials.[20–22] These reseachers generally report a limit of detection of 0.01-1 µM, at potentials of -0.5 to 0.5 V vs RHE, with metal chalcogenides exhibiting H_2O_2 reduction potentials of -0.5 to -0.3 V vs RHE.

In summary, the research of noble-metal free catalysts for 2 and 4 e^- ORR is a very active field. The main tools used in identifying high catalytic activities are RRDE and CV. The most common noble metal free catalysts are first row transition metal oxides, including spinels where possible, graphitic carbon materials, and their composites. Most researchers use strongly alkaline or acidic media in their ORR experiments, which means there is a relative lack

of research in ORR at neutral pH values, especially when the generation of H_2O_2 is coupled to its activation for water treatment purposes. Composites of graphitic carbon materials are a popular choice for multicomponent ORR catalysts, but there is a lack of research into macroscale carbon materials being used as the sole catalyst of ORR or as a component of a composite catalyst.

6.2 Experimental Details

6.2.1 Chemicals

The KCl (≥99.5% purity) used in these experiments was purchased from VWR. The Co(II) nitrate (≥97% purity) used in the catalyst synthesis was purchased from Scientific Laboratory Supplies, while the Mn(II) sulfate (≥99% purity) used in the same was purchased from Sigma-Aldrich. The H_2O_2 (30% w/v) used in these experiments was produced by Fischer Scientific, and it was stored at 5 °C. The $FeCl_3$ (≥99% purity) used in the generation of O_2 was purchased from Merck. The $K_3[Fe(CN_6)]$ (≥98.5% purity) used in CV measurements was purchased from Sigma-Aldrich.

6.2.2 Methods

6.2.2.1 Composite synthesis

First a certain amount of GNF or oGNF was dispersed in an aqueous NH_3 solution (4.65 mL, 35%). Then a Co(II) solution (0.2 M) made with ultrapure water was added while the mixture was stirred at 600 rpm. After this, a Mn(II) solution (0.2 M) was added, and the mixture was then kept at 30 °C for 2 h with the same stirring as above. The overall volume of the reaction mixture was always 24.5 mL, and in the case of mixed spinels this was split between the Co(II) and Mn(II) solutions 2:1 for Co_2MnO_4 and 1:2 for $CoMn_2O_4$. Finally, the reaction mixture was hydrothermally treated (180 °C, 4 h). The time of the hydrothermal treatment was measured from the point of reaching the set temperature. The resulting solids were separated via vacuum filtration, the materials were washed with ultrapure water (3 x 150 mL) and acetone (3 x 150 mL), and then was dried in a vacuum oven overnight (70 °C, 0.1 bar). The exact amounts of reactants used are set out in Table 9.

Table 9 – Exact amounts of reactants used in the synthesis of composites

	m (Co(II) salt) (mg)	m (Mn(II) salt) (mg)	m(GNF/oGNF) (mg)	Nominal loading (%)
Co_3O_4	949	0	650	28.7
Co_2MnO_4	949	409	856	31.3
$CoMn_2O_4$	475	818	969	28.2
Mn_3O_4	0	81.8	65	27.0

The yields of syntheses are illustrated by Table 10. Only one batch of each composite type was made, so the variance in yields cannot be calculated. Co_2MnO_4-GNF and Co_2MnO_4-oGNF were not made separately for this chapter, the yield of its synthesis can be found in Chapter 3.

Table 10 – Yields of composite syntheses

Composite type	Yield (%)	Composite type	Yield (%)
Co_3O_4-GNF	94.6	**Co_3O_4-oGNF**	92.6
$CoMn_2O_4$-GNF	87.1	**$CoMn_2O_4$-oGNF**	92.7
Mn_3O_4-GNF	93.4	**Mn_3O_4-oGNF**	97.1

6.2.2.2 Cyclic Voltammetry

CV experiments were done in a three electrode cell connected to a Princeton Applied Research 273a potentiostat. The reference electrode was a Ag/AgCl/3.5 M KCl electrode from Metrohm (Product number: 6.0724.140), while a glassy carbon disk tipped electrode was used as the working electrode, also from Metrohm (Product code: 6.1204.300). For counter electrode a graphite rod was used with a diameter of 6.3 mm, ordered from Alfa Aesar. A conical glass vessel was used to hold 20 mL of the electrolyte, and a specially designed lid kept the electrodes in place and submerged to the same extent. The potentiostat was controlled using a laptop running the proprietary software of Princeton Applied Research called PowerCV.

6.2.2.3 Electrode Fabrication

Before fabricating an electrode the glassy carbon disk tipped electrode was polished in all cases. An alumina powder and a polishing cloth was used; first a slurry was formed with water (5 mL) and the alumina (25 mg) which was pipetted onto the polishing cloth. The electrode tip was then lightly pressed against the polishing cloth and moved in figures of eight for 15 s. The electrode was then washed with water, and acetone, and dried in an oven at 80 °C.

Electrodes were fabricated for CV measurements by making a slurry of the material to be studied, and dropcasting it onto the glassy carbon disk (3 mm in diameter). The slurry was made using the catalytically active material (5 mg or 15 mg), a 5% Nafion solution (40 µL), and a 1:3 isopropanol-water mixture (1 mL or 500 µL). These components were made into a homogeneous slurry using a mortar and pestle. In the case of undecorated carbon materials the mass of catalytically active material and volume of 5% Nafion solution were different (10 mg and 20 µL, respectively). Electrodes were prepared by pipetting the above described mixture (2.5 µL) onto the glassy carbon disk of the working electrode. The electrode was then dried in an oven (80 °C, 15 min). This method leads to a 0.35 mg/cm^2 mass loading of the catalytically active material on electrode in the case of the metal oxides, and 0.70 mg/cm^2 in the case of the carbonaceous materials.

6.2.2.4 O_2 Saturation of Electrolytes

O_2 gas was generated by carefully dosing a H_2O_2 solution (30% m/V, 100 µL) via a needle through a septum into a roundbottom flask containing an $FeCl_3$ solution (1.5 mM, 1 mL). A tube (1/16 in, PTFE) was fed from the septum to the CV electrolyte where initially the gas was bubbled through the electrolyte. After a period of feeding O_2 gas in (5 min), the tube was moved above the liquid level so as to not disturb the measurements or evaporate the electrolyte. The CV vessel was closed down with a lid containing five ports, three of which were used for the electrodes, while the other two were closed with septa. One of these septa were used for dosing the O_2 in, while the other had a syringe needle through it to avoid the build-up of excess pressure inside the vessel.

6.3 Discussion of Results

The materials used in this chapter are using the same synthetic route as Chapters 2 and 3. Acid oxidation, the metal oxide syntheses and composite formation with GNF and oGNF have been thoroughly characterised before, and as such the synthesis or characterisation of the composites used here will not be discussed.

6.3.1 Cyclic Voltammetry

CV has been used as the main tool in assessing the electrocatalytic activity of the studied materials in O_2 reduction. Scanning started at a small positive potential in all cases, the forward scan is the oxidation side, while the backward scan is the reduction side.

For these experiments, first a baseline was recorded in which the working electrode was left bare. Since the reference electrode was Ag/AgCl/3.5 M KCl a prior experiment was done to ascertain the validity of potential readings. For this, a few mg of potassium hexacyano ferrate(III) was used in 0.1 M KCl (see Figure 89). The recorded reduction potential of 0.371 V vs RHE is in good agreement with the literature value for the reduction of hexacyano ferrate (III), which means readings are accurate.[233] All subsequent voltammograms will be shown as current vs potential against the RHE at pH=7, which means potentials are shifted towards more positive values by 0.205 V.

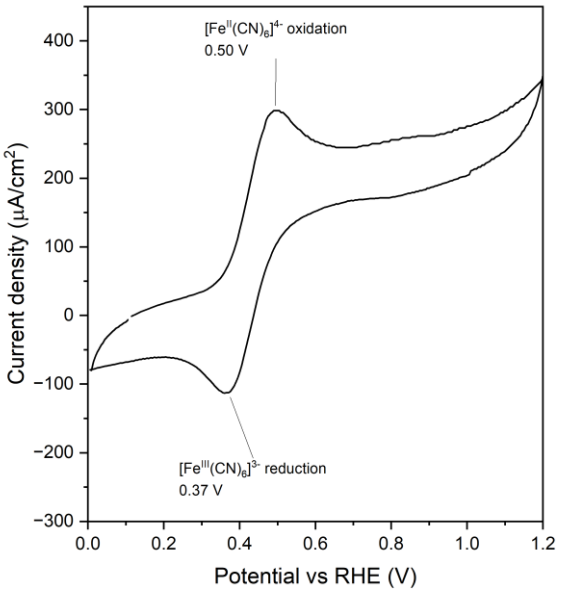

Figure 89 – Graph showing the cyclic voltammogram of the hexacyano ferrate(III)-hexacyano ferrite redox couple.
Experimental conditions: WE: Glassy carbon, CE: graphite, RE: Ag/AgCl/3.5 M KCl; 0.1 M KCl electrolyte.

Electrolytic processes generally need a supporting electrolyte that electrically connects the cathode and the anode. The reaction pathway ORR follows is fundamentally defined by pH through influencing the potential intermediates. In the case of carbon materials and metal oxides, ORR happens at a potential closer to 0 V vs RHE in alkaline media, which translates into a lower energy requirement. Thus, in applied research the most common electrolytes are strong bases (for ex. 0.1-1.0 M KOH).[234] Initial experiments were done using 0.1 M KOH and 0.1 M $NaNO_3$ as electrolytes, but these only served to optimise the experimental conditions, so these will not be discussed (see Supplementary figure 43 to Supplementary figure 46). The main takeaway of these initial experiments is that the only reduction peaks were seen between -1.0 and 0.0 V, so only this potential window was studied further.

Electrolytes like KCl, KNO_3, etc. are increasingly being researched as ORR electrolytes.[24–26] Accordingly, all experiments below were done using 0.1 M KCl as the

electrolyte. This was done in order to make sure that the electrochemical H_2O_2 generation results and the dye degradation experiments' results are compatible, as pH plays a fundamental role in both. The aim of the project is to eventually couple these processes in one device so it is important that the two processes are studied under similar conditions.

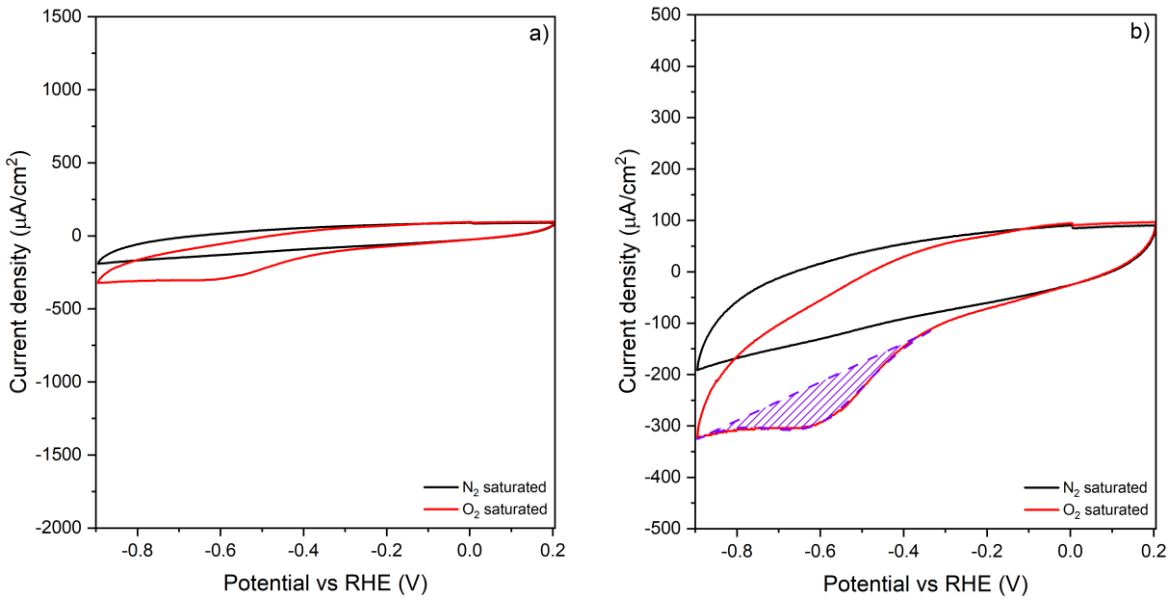

Figure 90 – Cyclic voltammogram of bare glassy carbon electrode.
Experimental conditions: WE: Glassy carbon, CE: graphite, RE: Ag/AgCl/3.5 M KCl; 0.1 M KCl electrolyte.

The general approach in all CV experiments is that first a baseline current vs potential plot is recorded with an electrolyte that has been purged with N_2. Then the electrolyte is saturated with O_2, and so any signal that emerges will necessarily be connected to the reduction of O_2. Figure 90 shows such a measurements with an undecorated glassy carbon working electrode. The N_2 purged electrolyte's signal is quite flat with minimal capacitance or visible redox peaks, while the O_2 saturated electrolyte's signal shows an O_2 reduction peak at -0.6 V. This is consistent with 2 e^- ORR on glassy carbon, and as such it is assumed that this peak is due to O_2 being reduced on the bare working electrode.[238]

Figure 90b also shows the general method of analysing peaks throughout this chapter. In order to make the results comparable, a straight baseline is used between the endpoints of each peak, and then the excess current between the baseline and the maximum extent of the peak is considered to be the reduction current. Next, this setup is used to study the electrocatalytic activity of the previously discussed metal oxides, some carbon materials and their composites. Carbon beads were not used in these experiments since their size did not make electrode fabrication possible.

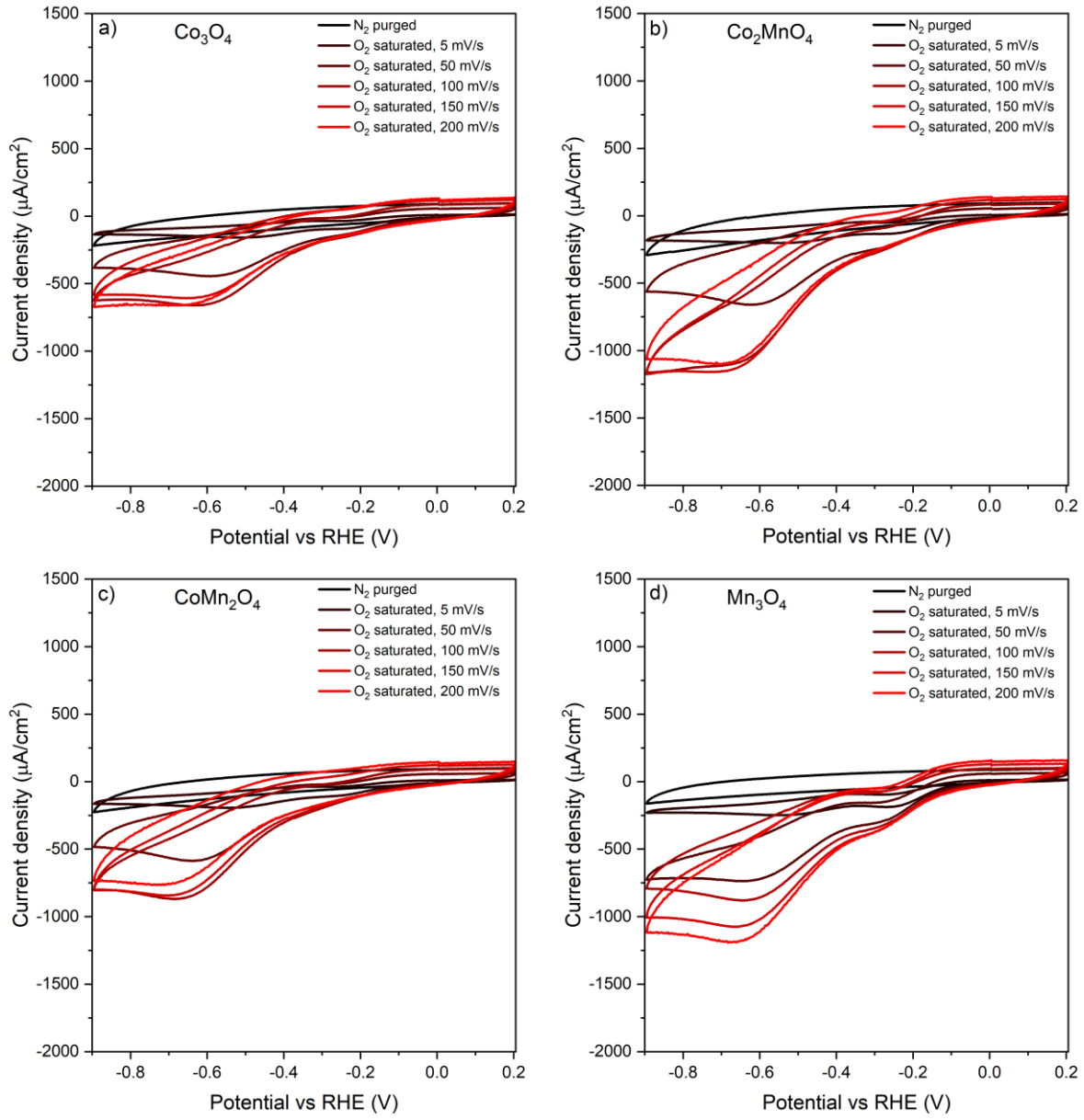

Figure 91 – Cyclic voltammograms for all four spinels in N_2 purged and O_2 saturated electrolytes; **a:** Co_3O_4, **b:** Co_2MnO_4, **c:** $CoMn_2O_4$, **d:** Mn_3O_4, **e:** Commercial Co_3O_4;
Experimental conditions: WE: Glassy carbon, CE: graphite, RE: Ag/AgCl/3.5 M KCl; 0.1 M KCl electrolyte, 0.35 mg/cm^2 coverage on WE.

6.3.2 Metal Oxides

To study the electrocatalytic activity of the Co, Mn oxides and their composites the electrodes were prepared to contain 0.35 mg/cm^2 electrocatalytically active material in each case. This value is similar to the 0.1-0.2 mg/cm^2 coverage researchers usually use in this field.[28–30] Before any cyclic voltammograms are recorded 10 conditioning cycles are run at 100 mV/s. As Figure 91 shows, all four metal oxides produce a distinct reduction peak between -0.6 and -0.7 V which is most likely due to ORR happening on exposed sections of the glassy carbon working electrode. As such, this peak will not be considered to be a sign of

catalytic activity of any sample. In addition to this, the Mn_3O_4 sample consistently shows a secondary reduction peak at -0.26 V at all scan rates. For comparison a commercial Co_3O_4 sample was also analysed under identical conditions, as illustrated by Figure 92. Co_3O_4 was chosen as it is a commonly used catalyst of ORR. This sample shows one strong reduction peak, which is present at all scan rates. Reduction potentials of -0.2 to -0.6 V are significantly more negative than the values published for similar materials, which tend to be 0.8 to 1.0 V. This peak is more in line with potentials of H_2O_2 reduction.[28–30][20–22]

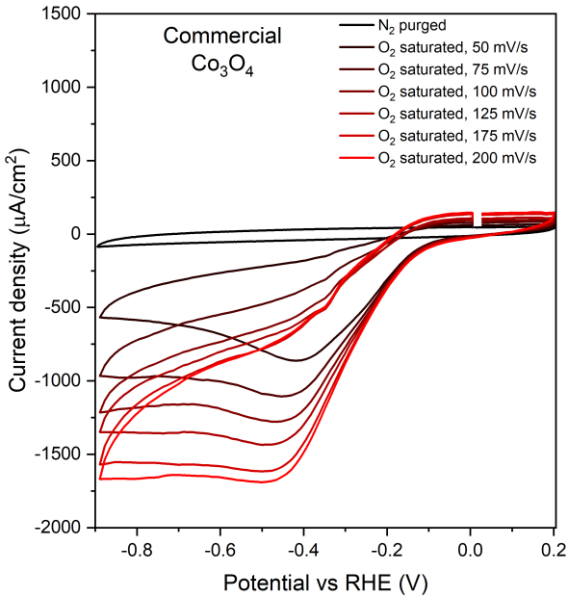

Figure 92 – Cyclic voltammograms of commercial Co_3O_4 sample at different scan rates.
Experimental conditions: WE: Glassy carbon, CE: graphite, RE: Ag/AgCl/3.5 M KCl; 0.1 M KCl electrolyte, 0.35 mg/cm^2 coverage on WE.

The recorded CV data was then further analysed to gain a deeper understanding of the electrocatalytic activity of the prepared materials (see Figure 93). The aim of this secondary analysis was to find the material that facilitates the largest reduction current. The samples of Co_3O_4, Co_2MnO_4, and $CoMn_2O_4$ only have an appreciable reduction peak at -0.25 V at the lowest scan rates. The Mn_3O_4 sample on the other hand shows a peak at -0.25 V at all scan rates. The peak position is mostly independent of the scan rate, which point towards the reaction being Nernstian, ergo exhibiting signs of rapid electron transfer.

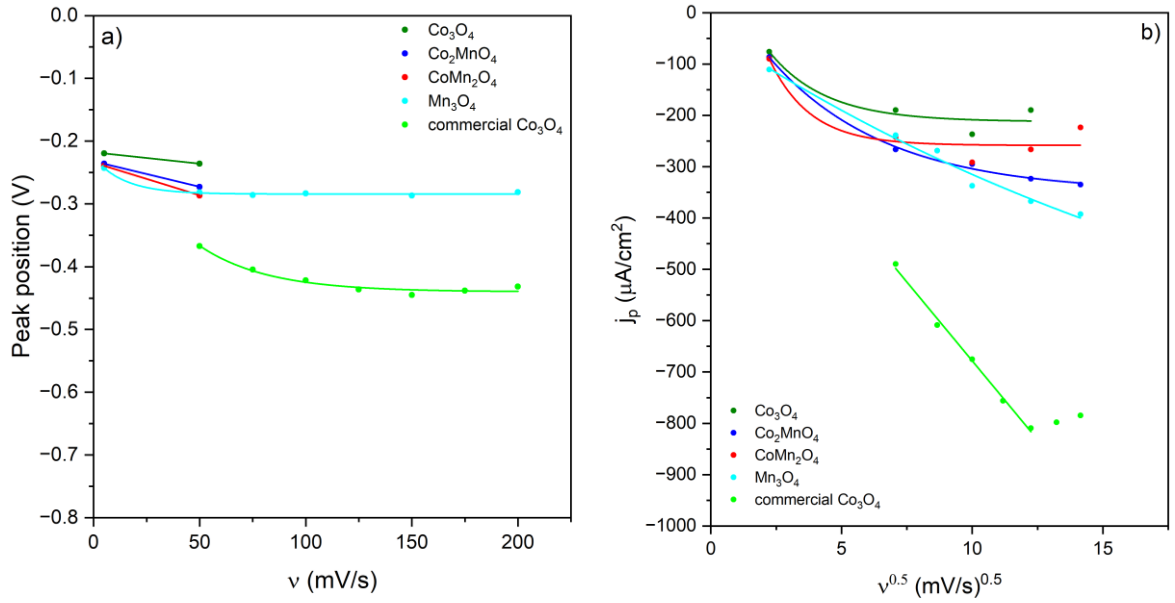

Figure 93 – Graphs summarising the electrocatalytic activity of the neat spinels and a commercial Co_3O_4 sample in O_2 reduction; **a:** Reduction peak positions vs scan rates; **b:** Reduction peak currents versus scan rates.

For comparison the peak positions recorded with the commercial Co_3O_4 sample shows more dependence on the scan rate as its peak position vs scan rate points do not fall along a line. This point towards a slower rate of electron transfer in the case of the commercial Co_3O_4. As Figure 93b illustrates, the highest reduction current was registered in the case of Mn_3O_4, but all four spinels exhibit a significantly lower reduction current than the commercial Co_3O_4. Although it has to be noted that the rate of electron transfer seems to be outpaced by the scanning rate above 150 mV/s in the case of the commercial Co_3O_4, while in the case of Mn_3O_4 no such break can be seen. This means that the rate of electron transfer is likely higher in the case of Mn_3O_4 compared to the commercial Co_3O_4. In summary Mn_3O_4 has been identified as the most active catalyst out of these four, but since the differences between the spinels are quite small, composites of all four were produced and studied.

In addition to the metal oxides, the previously described carbon materials were also studied in similar experimental setups as above. Both carbon materials exhibit high amplitude peaks at -0.6 V, and much smaller peaks at -0.25 V as illustrated by Figure 94.

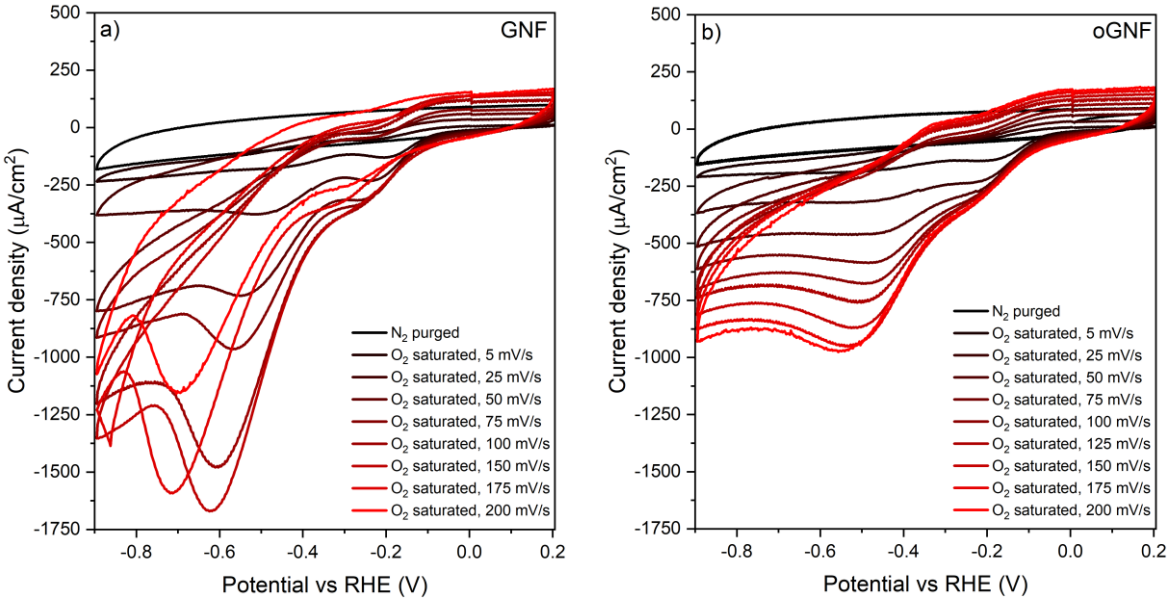

Figure 94 – Cyclic voltammograms of GNF and oGNF in N_2 purged and O_2 saturated electrolytes. **a:** GNF, **b:** oGNF.
Experimental conditions: WE: Glassy carbon, CE: graphite, RE: Ag/AgCl/3.5 M KCl; 0.1 M KCl electrolyte, 0.70 mg/cm^2 coverage on WE.

The peak positions at -0.6 and -0.25 V for GNF and oGNF behave very similarly when compared to the scan rate (see Figure 95). The datapoints in both cases show a linear relationship to the scan rate, with some dependence on it, signalling sluggish electron transfer. On the other hand, there are large differences between the peaks of different potential and the two carbonaceous materials in terms of reduction current versus scan rate.

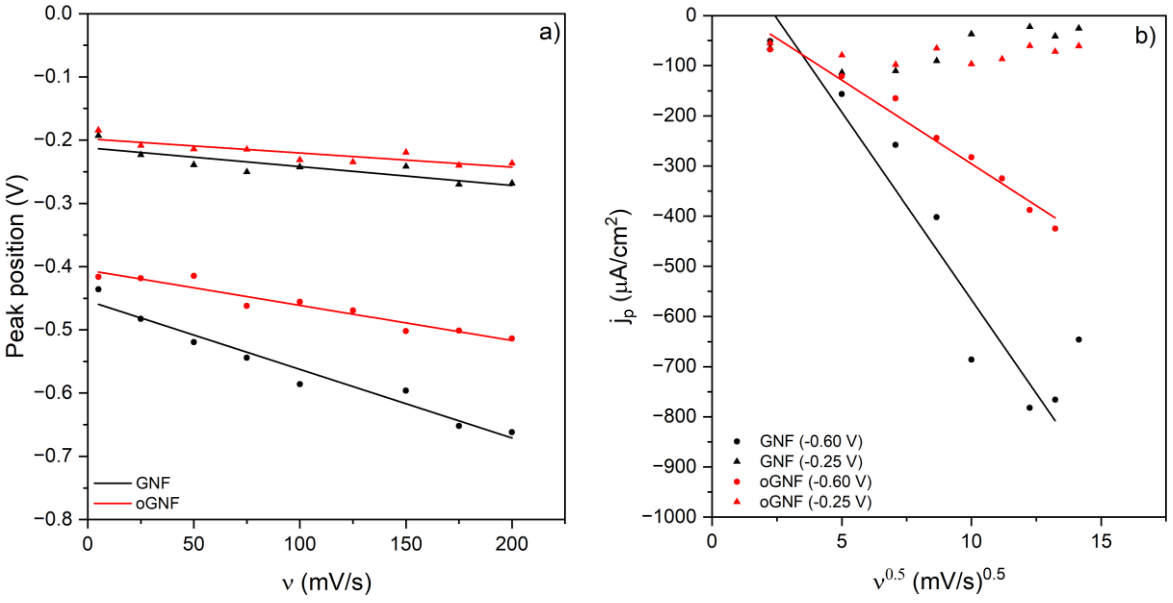

Figure 95 – Graphs summarising the electrocatalytic activity of GNF and oGNF in O_2 oxygen reduction; **a:** Graph showing peak positions vs scan rate; **b:** Reduction peak currents versus scan rates.

The peaks at -0.6 V, which are due to ORR, show signal magnitudes directly proportional to the scan rate, while the peak at -0.25 V shows close to zero currents regardless of scan rate. This means that GNF, and to a lesser extent oGNF facilitate ORR and another electrochemical process at -0.25 V.

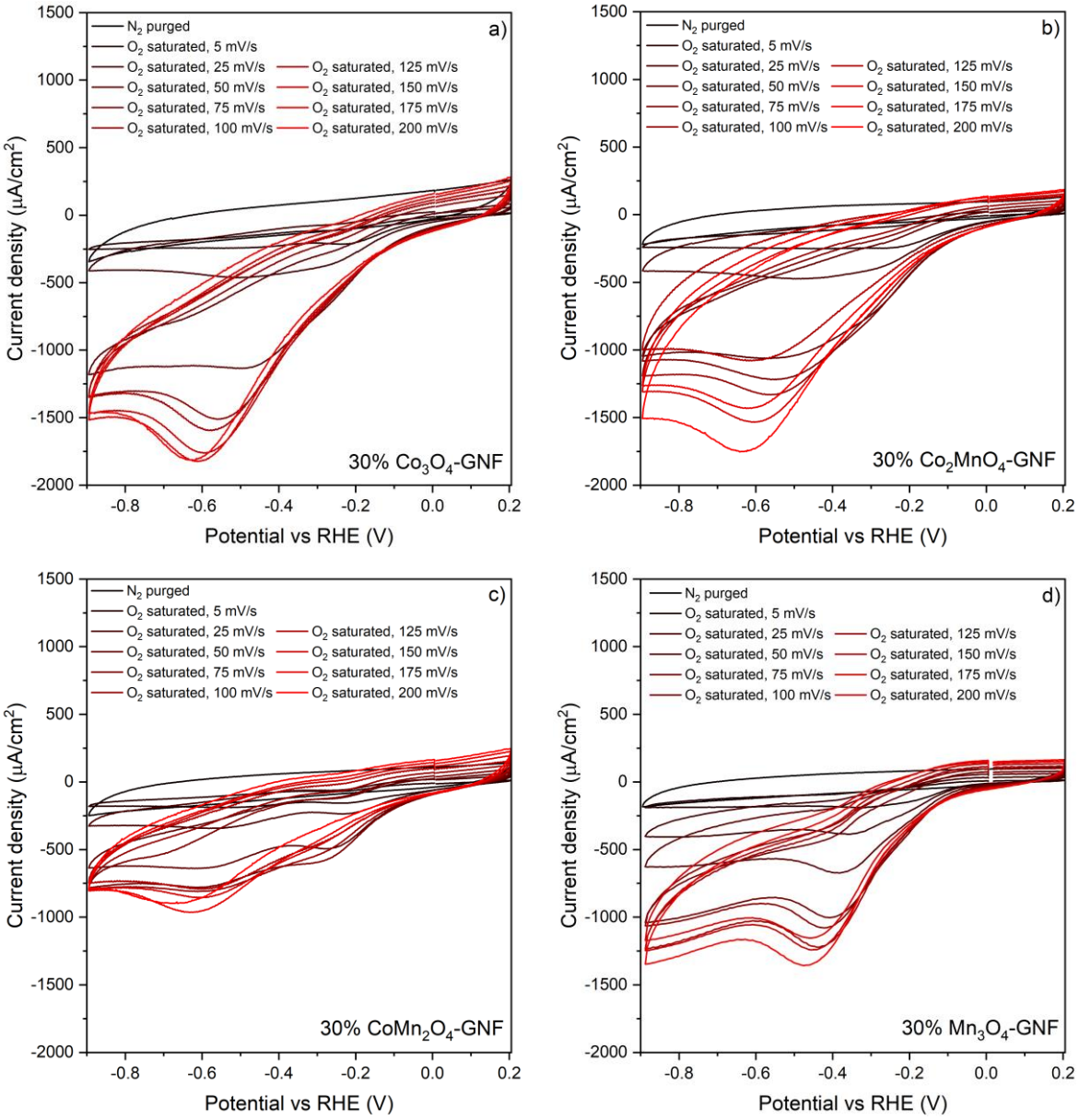

Figure 96 – Cyclic voltammograms of GNF composites of 30% catalyst loading in N_2 purged and O_2 saturated electrolytes. **a:** Co_3O_4-GNF; **b:** Co_2MnO_4-GNF; **c:** $CoMn_2O_4$-GNF; **d:** Mn_3O_4-GNF.
Experimental conditions: WE: Glassy carbon, CE: graphite, RE: Ag/AgCl/3.5 M KCl; 0.1 M KCl electrolyte, 0.35 mg/cm^2 coverage on WE.

Finally, to conclude this subchapter the GNF and oGNF composites of the above metal oxides are studied using CV results recorded the same way as above (see Figure 96). A peak at -0.6 V has been recorded in many cases, which is identified as being associated with the undecorated graphitic surfaces of the support. An additional, often very low magnitude peak

has been recorded in the case of Co_3O_4-GNF, Co_2MnO_4-GNF, and $CoMn_2O_4$-GNF between -0.2 and -0.3 V.

The presence of these two separate peaks signals that two electrochemical processes are being facilitated on these materials, O_2 reduction on carbon surfaces at -0.6 V and another electrochemical process, likely H_2O_2 reduction. Interestingly the Mn_3O_4-GNF sample shows only one peak. This can either mean that this material is facilitating H_2O_2 reduction, although this is unlikely without ORR also happening in the cell, or alternatively that some synergism between Mn_3O_4 and GNF shifted the reduction potential of O_2 to a slightly more positive value. In the case of composites with two main peaks, only the one associated with the metal oxide will be considered for further analysis.

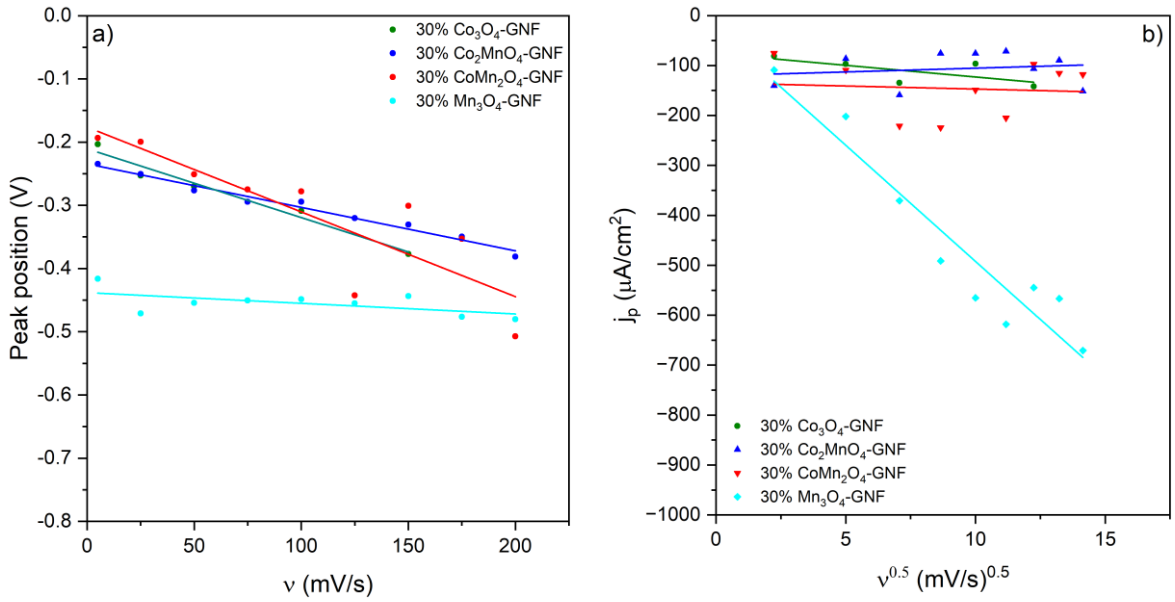

Figure 97 – Graphs summarising the electrocatalytic activity of GNF composites of 30% catalyst loading in O_2 reduction; **a:** Graph showing peak positions vs scan rate; **b:** Reduction peak currents versus scan rates.

When considering the peak positions vs scan rates, as illustrated by Figure 97, it becomes apparent that the Mn_3O_4-GNF is qualitatively different from the other composites. In this case the position of the peak does not change significantly with scan rate. This points towards Nernstian behaviour, which in this case is associated with rapid electron transfer. In the other cases non-Nernstian behaviour is seen which in this case points towards sluggish electron transfers. Additionally, as Figure 97b illustrates, the Mn_3O_4-GNF composite shows the highest peak reduction currents. If this peak was due to H_2O_2 reduction as with the unsupported metal oxides, there should be an ORR peak which would produce the H_2O_2. Since this is not the case, it is not possible to say what exact electrochemical process is associated with this peak based solely on these experimental results.

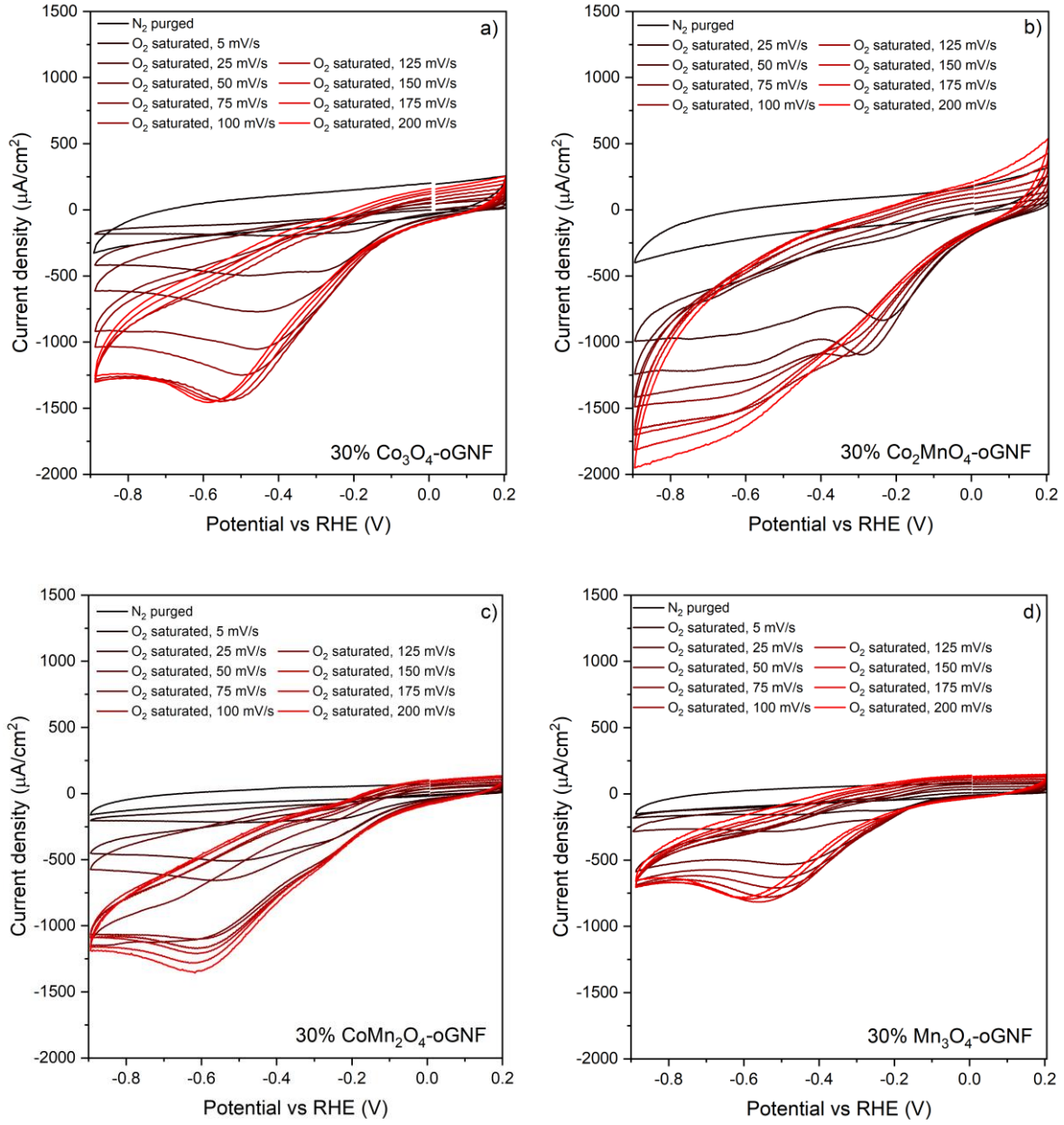

Figure 98 – Cyclic voltammograms of oGNF composites of 30% catalyst loading in N_2 purged and O_2 saturated electrolytes. **a:** Co_3O_4-oGNF; **b:** Co_2MnO_4-oGNF; **c:** $CoMn_2O_4$-oGNF; **d:** Mn_3O_4-oGNF.
Experimental conditions: WE: Glassy carbon, CE: graphite, RE: Ag/AgCl/3.5 M KCl; 0.1 M KCl electrolyte, 0.35 mg/cm^2 coverage on WE.

Figure 98 shows the cyclic voltammograms recorded with the oGNF composites. These composites also show two separate reduction peaks in most cases, which points towards no emergent synergism in any case. The peak associated with oGNF is much larger than the one associated with the metal oxide in the case of Co_3O_4-oGNF, $CoMn_2O_4$-oGNF while in the case of Co_2MnO_4-oGNF the metal oxide's peak is only larger at lower scan rates. This points towards low catalytic performance and no emergent synergism between the catalyst and support.

The graphs shown on Figure 99 further illustrate the catalytic activity of these composites. The peak positions recorded via CV are in all cases dependent on the scan rate, which points towards sluggish electron transfer in all cases. It is also worth mentioning that only the Co, Mn spinel containing composite catalysts show any appreciable catalytic activity. When looking at the plots of reduction current density versus scan rate, Mn_3O_4-oGNF and Co_3O_4-oGNF show very low values, and while Co_2MnO_4-oGNF shows current densities of up to 550 µA/cm^2 the rate of electron transfer is outpaced by the scan rate above 50 mV/s. Based on these plots, it can be concluded that the oGNF composites show lower catalytic activities that the GNF composites, further supporting the observations of previous chapters in that acid oxidation of GNF does not improve its performance as a catalyst support in the studied applications.

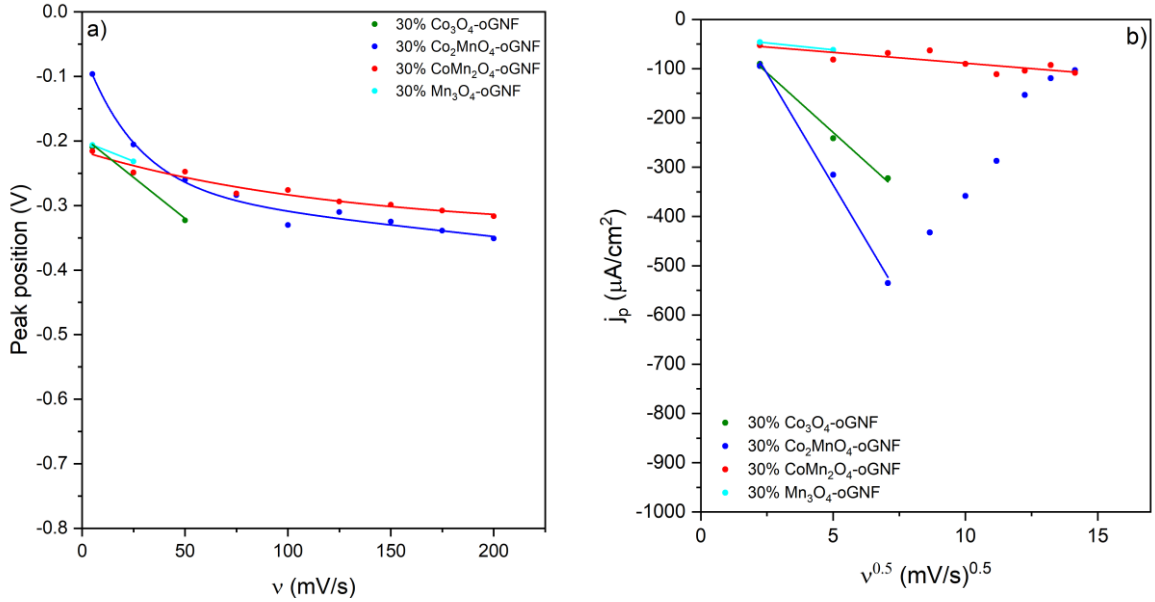

Figure 99 – Graphs summarising the electrocatalytic activity of oGNF composites of 30% catalyst loading in O_2 n reduction; **a:** Graph showing peak positions vs scan rate; **b:** Reduction peak currents versus scan rates.

As noted above the carbon materials were studied with a different electrode coverage than the metal oxides, so to make sure results are completely comparable the three most active materials were studied again under identical experimental conditions. This time the electrode was fabricated by creating a slurry of 15 mg of a sample, 40 µL of Nafion, and 500 mL 1:3 IPA-H_2O. After this, the slurry was homogenised using a mortar and pestle, and 1.5 µL of it was pipetted onto the electrode. It was then similarly dried and then used.

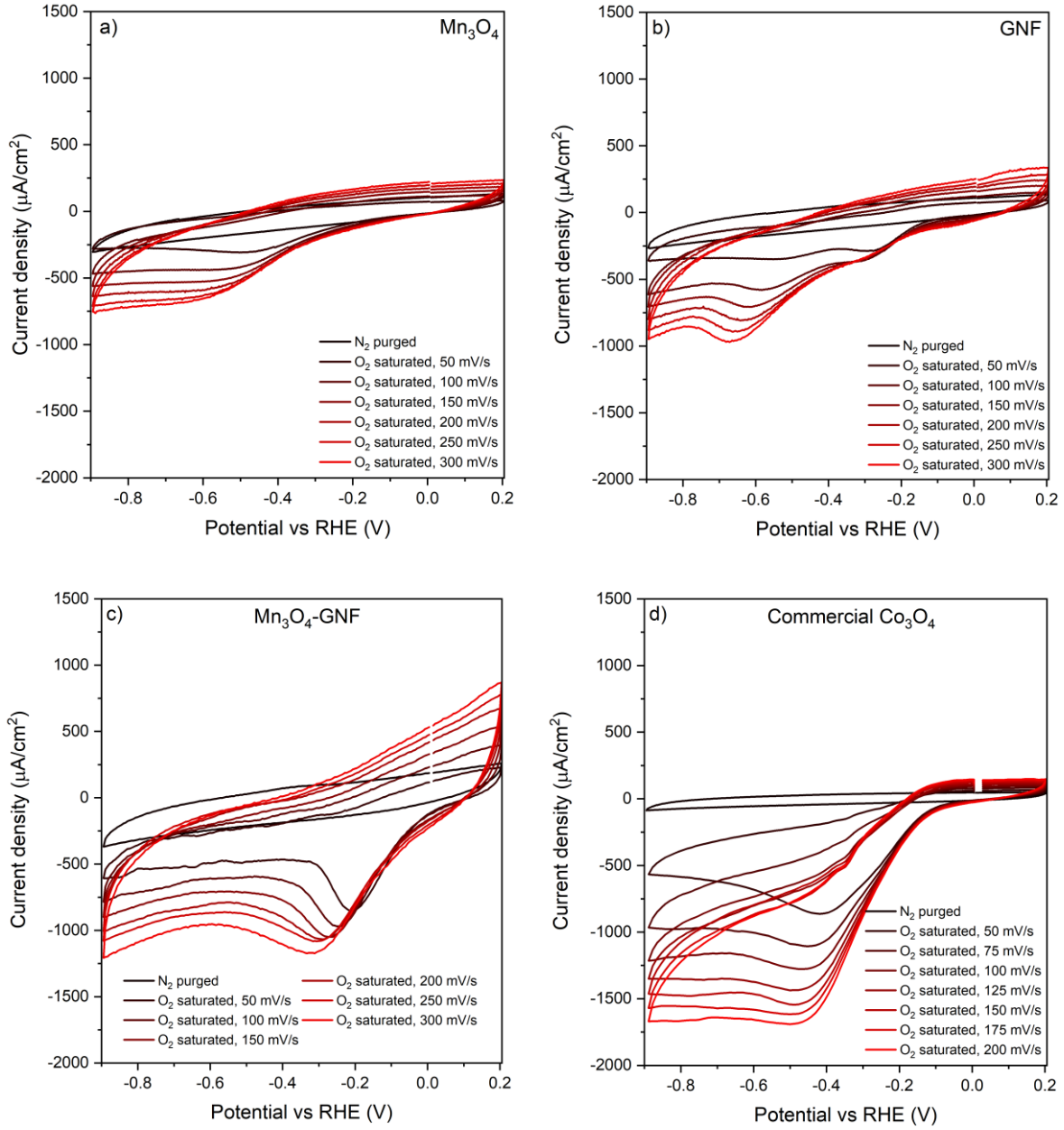

Figure 100 – Cyclic voltammograms of oGNF composites of 30% catalyst loading in N_2 purged and O_2 saturated electrolytes. **a:** Mn_3O_4; **b:** GNF; **c:** Mn_3O_4-GNF.
Experimental conditions: WE: Glassy carbon, CE: graphite, RE: Ag/AgCl/3.5 M KCl; 0.1 M KCl electrolyte, 0.70 mg/cm^2 coverage on WE.

The recorded cyclic voltammograms generally reinforce the previous observations. The peak at -0.25 V for Mn_3O_4-GNF is much more pronounced in this case which is due to the higher mass loading on the working electrode. As Figure 101 shows, these experiments similarly identify Mn_3O_4-GNF as the most active electrocatalyst. The peak position plotted against the scan rate shows good linearity in the case of Mn_3O_4 and GNF and for Mn_3O_4-GNF this plot only deviates from linearity at the lowest scan rate. The peak reduction current is mostly independent of scanning rate, but in general Mn_3O_4-GNF shows good reduction currents of

550-650 µA/cm^2. For reference, literature values for similar materials are in the range of 100-1000 µA/cm^2.[173][28-29]

Based on the above observation it can be concluded that the Mn_3O_4-GNF composite shows the best electrocatalytic activity, but based on these results it is not possible to say whether this is an O_2 reduction or H_2O_2 reduction. To decide this question RRDE voltammetry was used.

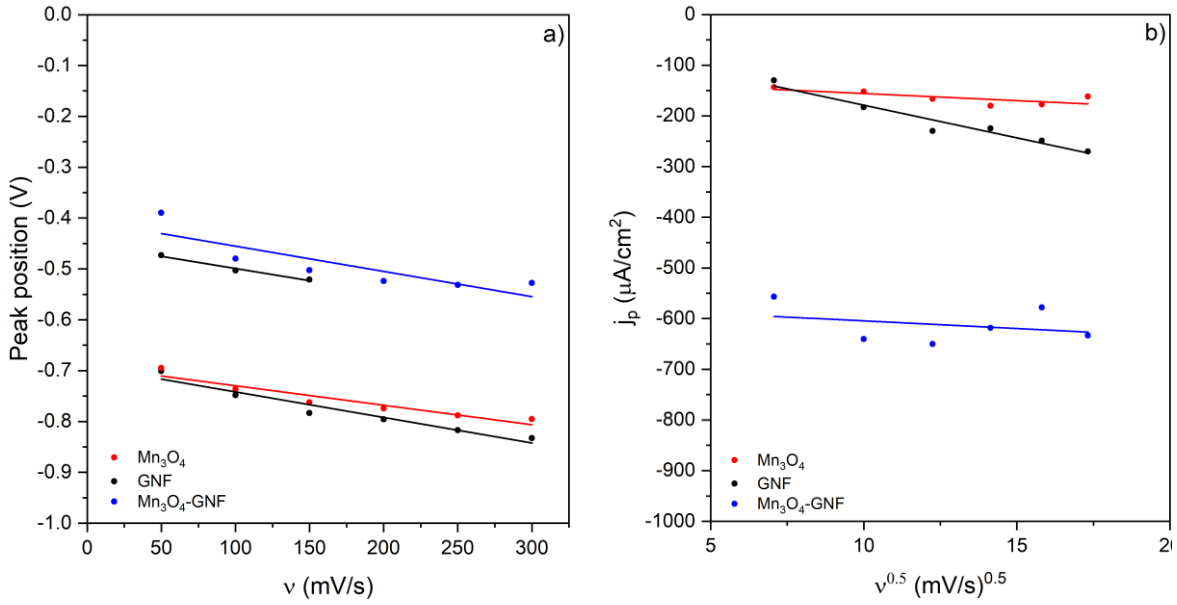

Figure 101 – Graphs summarising the electrocatalytic activity of the most active catalysts in O_2 reduction; **a:** Graph showing peak positions vs scan rate; **b:** Reduction peak currents versus scan rates

6.3.3 Rotating Ring Disk Electrode Voltammetry (RRDE)

This work was done in collaboration with Caillean Convery, a postgraduate researcher of the Mamlouk Research Group at Newcastle University. The author of this thesis provided the materials of interest, was present during initial experiments, and has done all of the data analysis.

Before the experiments themselves the collection efficiency between the disk and ring electrodes has been calculated. This was done by collecting voltammograms with undecorated electrodes and an electrolyte that contains 10 mM $K_3[Fe(CN)_6]$. The ferricyanide-ferrocyanide is a well characterised 1 e^- redox couple with a known redox potential which makes it an ideal analyte in this experiment. The collection efficiency was found to be 26.5±0.19%, which means that if there is an electrochemical reaction happening on the disk, this fraction of the products will go on to take part in a potential second reaction at the ring electrode. These results also

serve as a good example of a simple and electrochemically reversible half reaction that is free of complications, like coupled reactions, or poor mass transfer.

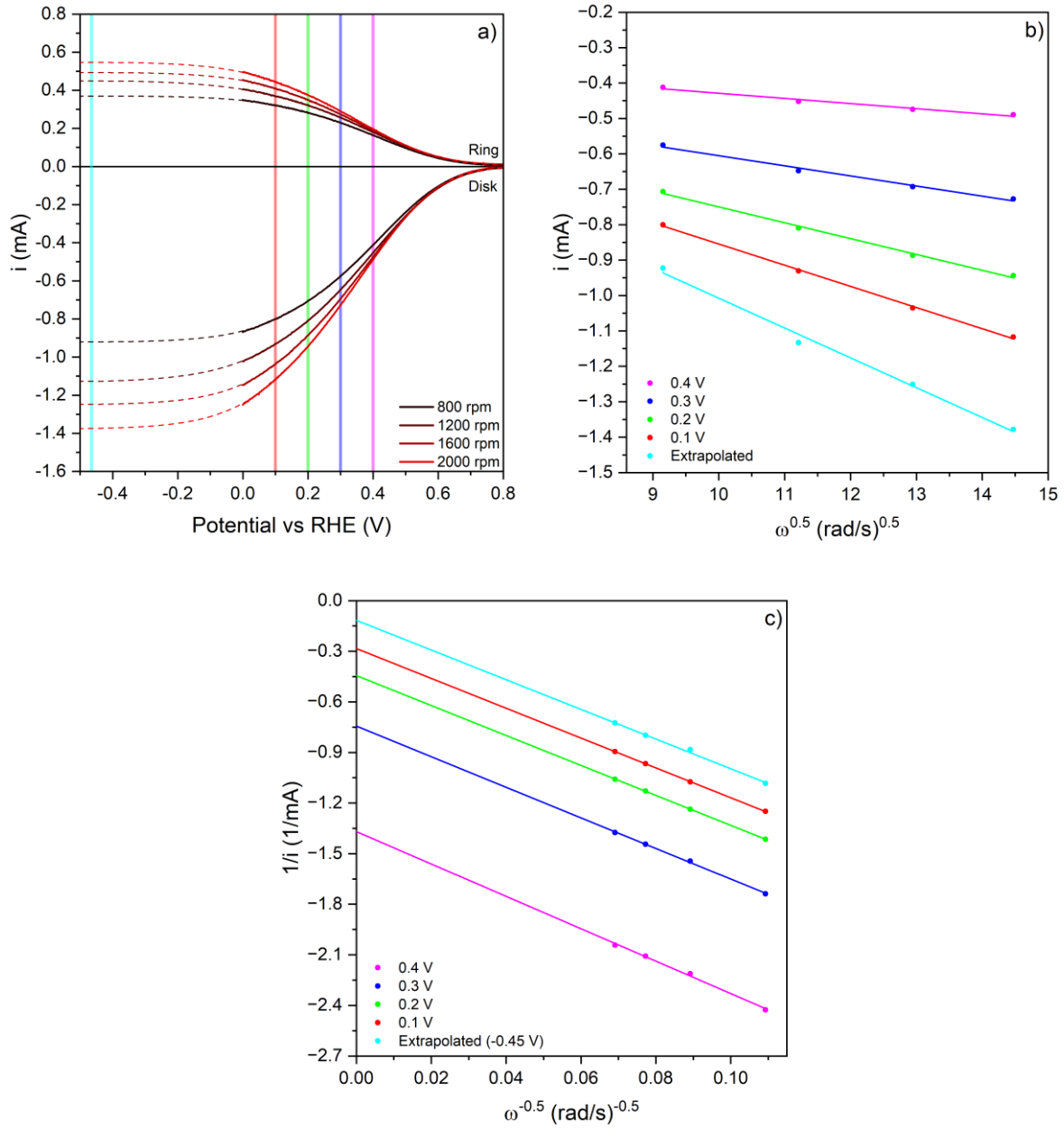

Figure 102 – Rotating ring disk electrode voltammetry results for the bare working electrode with electrolyte containing potassium ferricyanide; **a:** Linear sweep voltammograms; **b:** Levich-plot; **c:** Koutecký-Levich plot. Electrolyte: 0.1 M KCl, WE: Glassy carbon disk and Pt ring, CE: glassy carbon, RE: RHE.

Figure 102 summarises the results of RRDE voltammetry experiments with the bare electrodes and an electrolyte with the ferricyanide-ferrocyanide redox couple added. The curves were extrapolated in order to generate the limiting currents. Figure 102a shows that strong signals were recorded on both the disk and the ring at all rotation rates, which is expected in the case of an easily oxidisable and reducible redox couple. The Levich plot shows

data points falling along a line in the case of all rotation rates, as it would be expected in the case of a simple, electrochemically reversible process (see Figure 102b).

Similarly the Koutecký-Levich plot also shows data points falling along a straight line in all cases (see Figure 102c). It has to be noted though that the intercept is non-zero. This could be due to not having enough datapoints at lower rotation rates, or a genuine kinetic hindrance. More rotation rates below 800 rpm would have to be studied in order to decide. Nonetheless, these graphs show what to expect from the secondary analysis of the RRDE data.

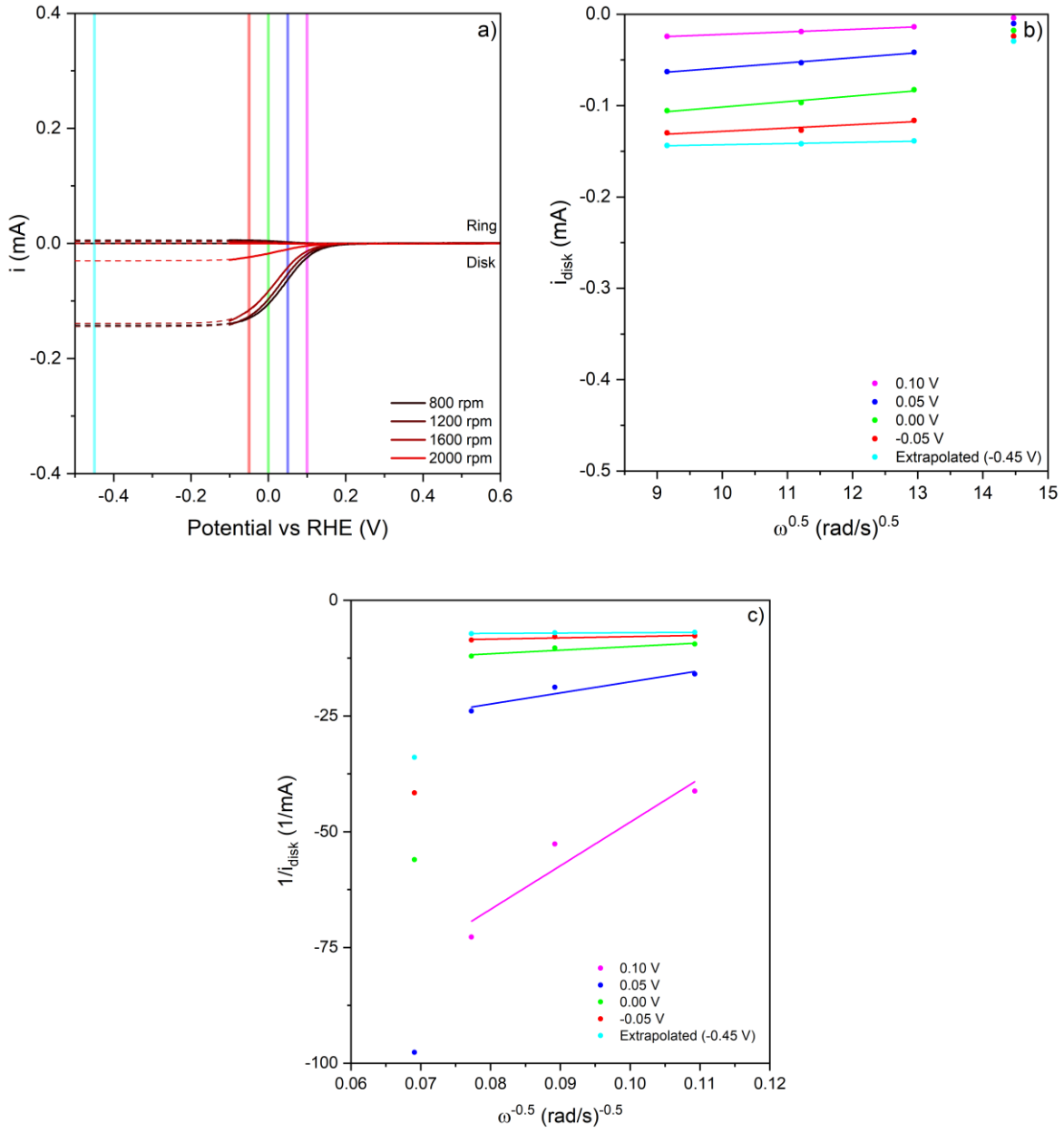

Figure 103 – Rotating ring disk electrode voltammetry results for Mn_3O_4. **a:** Linear sweep voltammograms; **b:** Levich-plot; **c:** Koutecký-Levich plot.
Electrolyte: 0.1 M KCl, WE: Glassy carbon disk, Pt ring, CE: glassy carbon, RE: RHE. 0.35 mg/cm^2 coverage on WE.

The voltammograms recorded with Mn_3O_4 dropcast onto the working electrode, and submerged in 0.1 M KCl show a much lower catalytic activity than what was seen in the case of the bare working electrode; no $K_3[Fe(CN)_6]$ was included in the electrolyte for this or any of the other voltammograms in the remainder of this chapter. The curve of 2000 rpm is significantly different from the other rotation rates, which is likely due to a measurement artefact. Nonetheless, the data recorded at other rotation rates is enough for Levich and Koutecký-Levich analysis. Datapoints on the Levich plot show a linear relationship apart from the 2000 rpm point, which signals that the number of transferred electrons does not change with rotation rate.

The currents recorded are so low that it is safe to say that catalytic activity is negligible. The slope of the Levich plot is 1.3±0.2 μA/(rad/s)$^{0.5}$, but since this value is expected to be negative it is assumed to be zero. The Koutecký-Levich plot shows that lines of different potentials have significantly different slopes. This means that the number of electrons transferred is dependent on the potential, which makes this material unsuitable for Koutecký-Levich analysis. All of these point towards this material showing negligible catalytic activity in O_2 reduction.

Next GNF was studied similar to the above, as illustrated by Figure 104. This and the next material exhibit a significant problem, which is that in the RRDE voltammograms a second reduction step can be seen, partly overlapping with O_2 reduction. This makes finding the limiting current difficult, but could also mean that two electrochemical processes are competing at close potentials, which is not ideal. Nonetheless, Levich and Koutecký-Levich analysis was used to gain a deeper understanding of this data. Similarly to Mn_3O_4, datapoints of the Levich plot fall along a line, which means the number of transferred electrons does not change with rotation rate, but only negligible catalytic activity is seen. The slope of the Levich plot is -7.0±0.4 μA/(rad/s)$^{0.5}$, which is near zero. The lines on the Koutecký-Levich plot show different slopes, which means that the number of electrons transferred per reaction is dependent on potential, and so this material in this reaction was deemed unsuitable for Koutecký-Levich analysis. Based on these observations it can be said that GNF also exhibits signs of negligible electrocatalytic activity.

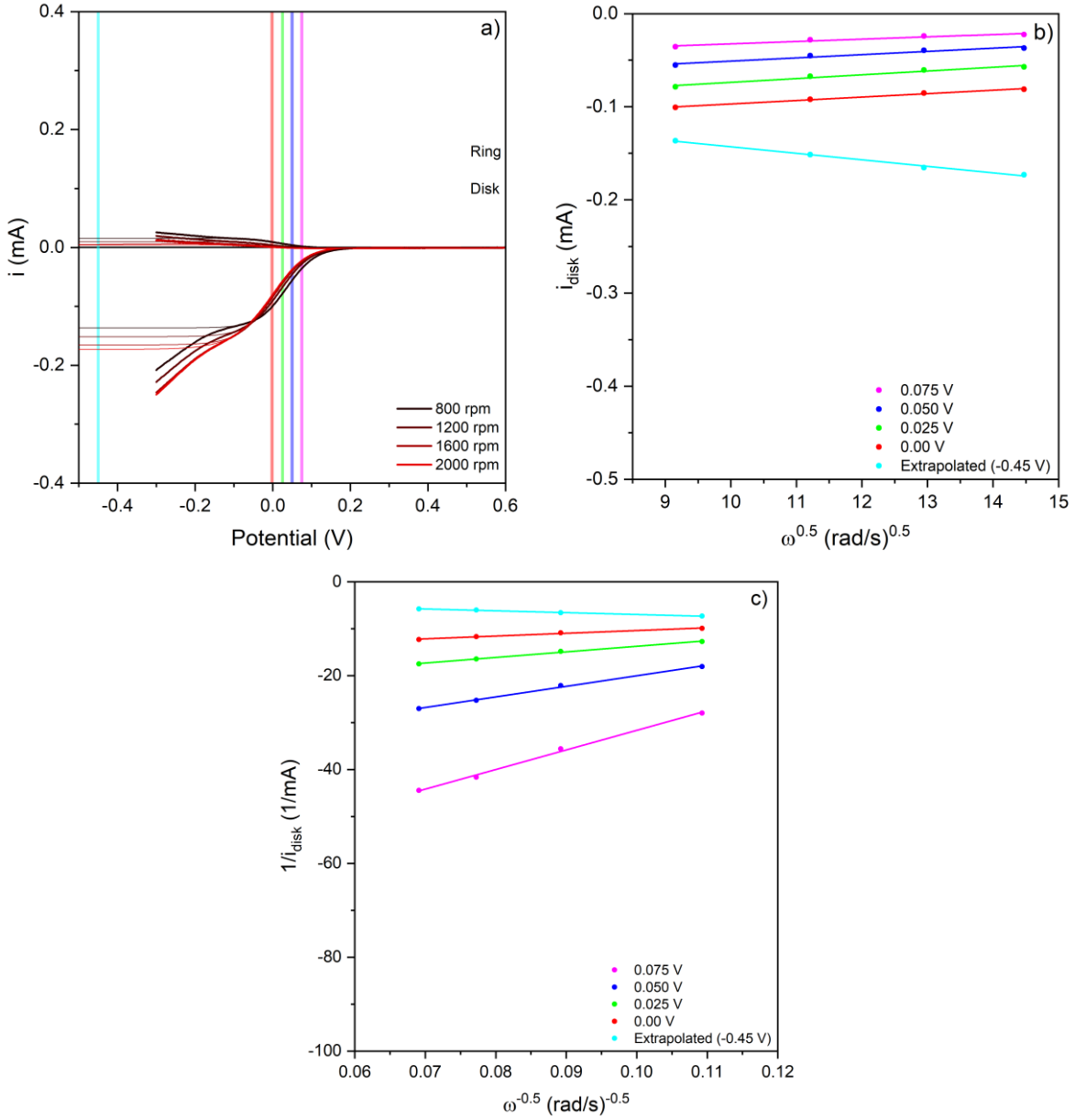

Figure 104 – Rotating ring disk electrode voltammetry results for GNF. **a:** Linear sweep voltammograms; **b:** Levich-plot; **c:** Koutecký-Levich plot.
Electrolyte: 0.1 M KCl, WE: Glassy carbon disk and Pt ring, CE: glassy carbon, RE: RHE. 0.35 mg/cm^2 coverage on WE

Finally, the composite Mn_3O_4-GNF was also studied like the above (see Figure 105). Similarly to GNF, this sample also shows signs of a competing second electrochemical process, which makes data analysis somewhat difficult. Similarly to previous cases, the Levich plot shows a linear relationship between current and the square root of the rotation rate. The slope of the Levich plot is 4.4±0.1 µA/(rad/s)$^{0.5}$. The slope of this plot should be negative, so this has to be assumed to be zero, similar to the results seen with Mn_3O_4.

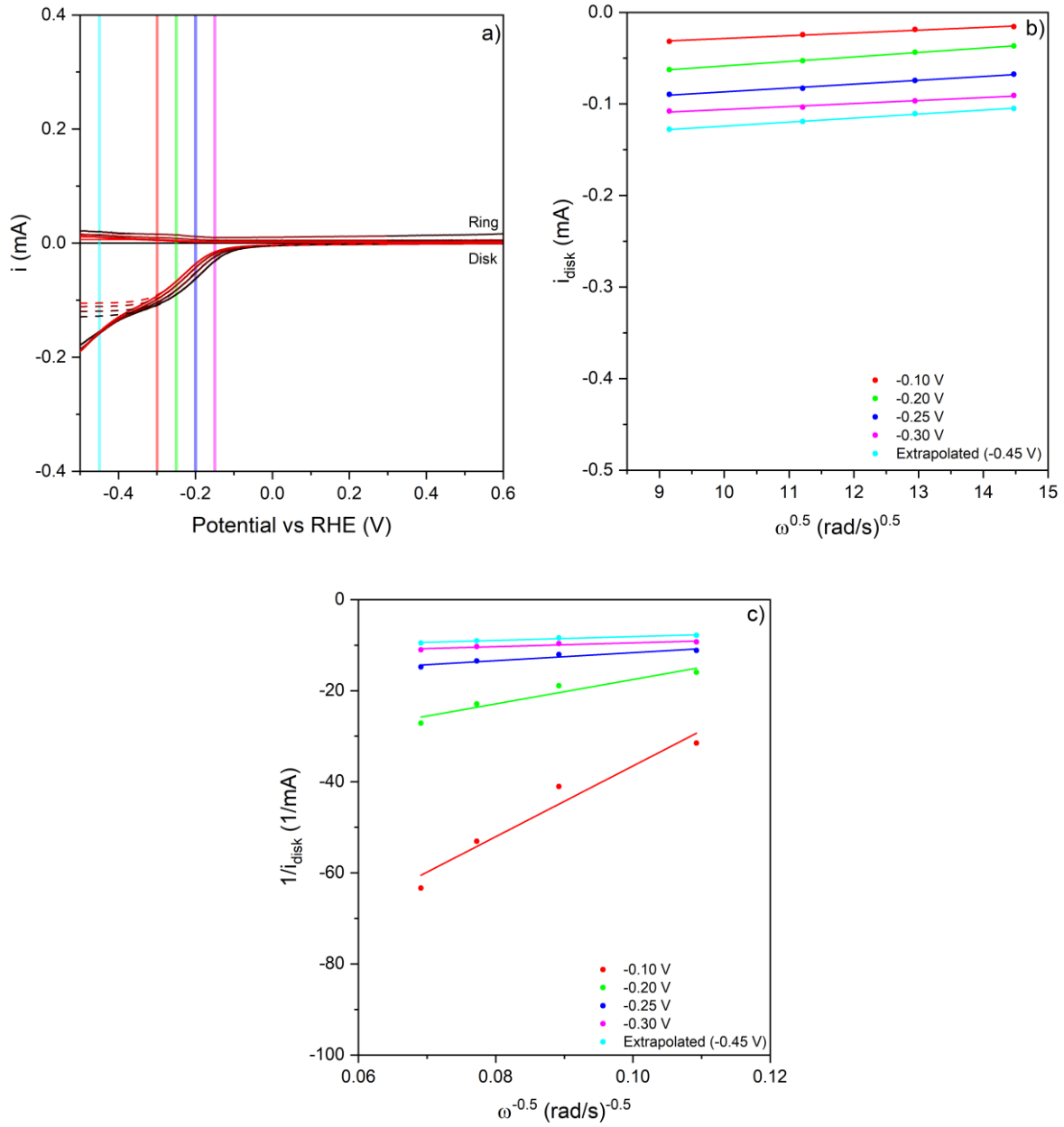

Figure 105 – Rotating ring disk electrode voltammetry results for 30% Mn_3O_4-GNF. **a:** Linear sweep voltammograms; **b:** Levich-plot; **c:** Koutecký-Levich plot.
Electrolyte: 0.1 M KCl, WE: Glassy carbon disk and Pt ring, CE: glassy carbon, RE: RHE. 0.35 mg/cm^2 coverage on WE

The lines on the Koutecký-Levich plot exhibit very different slopes at different potentials, which means there is a strong dependence between the number of electrons transferred and the potential applied. This makes the material in this reaction unsuitable for Koutecký-Levich analysis. The above observations show that this composite shows similar complications from a secondary reaction as GNF, and likely a lower number of transferred electrons per reaction.

It can be concluded based on the above, that these three materials show signs of negligible catalytic activity in O_2 reduction in 0.1 M KCl. Some experimental methods have

shown signs of complications that make the electrochemical process happening at the electrode unsuitable for analysis, like the changing slope in disk current versus the square root of scan rate plots of RRDE voltammetry data. Overall these observations prove that the studied materials exhibit signs of negligible ORR activity, and so it has to be concluded that the reductions seen at -0.25 V in initial cyclic voltammograms is due to H_2O_2 reduction. These findings are also in line with the findings of Chapter 3, where experimental results indicated that forming composites of GNF and oGNF do not improve catalytic activity.

6.4 Conclusions and Future Prospects

The aim of this chapter was to study the electrocatalytic activity of the materials synthesised and tested in previous chapters. Neat metal oxides, normal and acid oxidised fibrous carbon supports and their composites were tested using CV and RRDE voltammetry. The experimental results of CV studies showed moderate electrocatalytic activities in the case of Mn_3O_4, GNF and 30% Mn_3O_4-GNF, and negligible activity in the case of other materials. The reduction potentials recorded on the cyclic voltammograms could be explained by an ORR of extreme overpotential or H_2O_2 reduction. To decide this question RRDE voltammetry was used in a collaboration with Caillean Convery, a PGR of the Mamlouk Group at Newcastle University. This additional analysis showed negligible ORR activity so it was concluded that the reductions observed with CV were due to H_2O_2 reduction, and by extension that the studied materials have negligible catalytic activity in ORR under the studied experimental conditions.

There are some studies that could improve this chapter, keeping in mind that the aim is to produce a bifunctional catalyst that facilitates the generation and the activation of H_2O_2 in the same reaction medium. Synthesis of the used materials could be optimised towards electrocatalytic activity, by incorporating a different surface modification of the carbon support, or through some additional synthetic step, like annealing the composite sample after synthesis. If these do not lead to improvement in catalytic activity, a different carbon support could be used, like graphene, GO, or rGO. Another relatively short study that could improve this chapter is to use the Randles–Ševčík equation in order to compare recorded graphs of reduction current vs the square root of the scan rate to theoretical plots of 2 e^- and 4 e^- ORR. This would require the measurement of dissolved O_2 concentration via fluorimetry for example, and its diffusion coefficient using the Randles–Ševčík equation.

Concluding remarks

This thesis explores the development of carbon-supported bifunctional catalysts that are capable of both generating H_2O_2 and decomposing it into reactive oxygen species, which can then be used to efficiently degrade aqueous organics. The research presented here identifies highly active catalyst of Fenton-like chemistry, and probes the structure-performance relationships that govern their catalytic performance. Previously, this field lacked a unified metric that would enable wide-scale comparison between different catalysts, and so to address this, the concept of truly catalytic degradation has been proposed.

Chapter 1 explores the synergism that emerges in composite catalysts by studying a MnO_2-GNF composite in dye removal experiments. Observations show that the most active MnO_2-GNF composite facilitated a twice as high rate of degradation and three times as much truly catalytic degradation as the unsupported catalyst. The enhanced catalytic activity of these composite catalysts can be mainly attributed to a significantly higher dispersion of the catalyst, and the ability to dissipate heat generated during these experiments. The temperature of the reaction mixture in such contexts is an aspect of catalytic activity that is rarely discussed. The most active MnO_2-GNF catalyst facilitates a rate of degradation of $(104 \cdot 10^{-3})$ min^{-1}, which is in the midrange of published values $(5 \cdot 10^{-3}\text{-}200 \cdot 10^{-3})$ min^{-1}.

Chapter 2 presents the usage of Piranha solution in the acid oxidation of two macroscale supports, GNF and CB in order to modify sorption characteristics and catalyst anchoring. It was observed that both the surface morphology and surface chemistry of CB was significantly altered as a result of this treatment, while GNF was mostly unaffected. The most impactful change that was seen is that the concentration of acidic surface functional groups doubled in the case of oCB versus CB. The adsorption of organics on oCB was significantly suppressed, due to the increased electrostatic interactions, and the disruption of π-π stacking, that are associated with the increased concentration of polar functional groups. The 1.96 mmol/g concentration of acidic surface functional groups in oCB is extremely high compared to 0.5-2.0 mmol/g range found in the literature.

The carbon materials produced above were subsequently used to produce composite catalysts in Chapter 3. Four different Co, Mn spinels were produced via an optimised synthetic route, and were then tested in dye removal experiments. The most active of these spinels, Co_2MnO_4, was then used to produce composites with GNF, oGNF, CB and oCB. It was concluded that most GNF, oGNF and CB composites did not surpass the unsupported catalyst in terms of

rate of degradation, or truly catalytic degradation, but 47.5% Co_2MnO_4-oCB did. This composite facilitated a similar rate of degradation to the unsupported catalyst, but twice the truly catalytic degradation. These findings highlight why it is important to prevent the mostly irreversible adsorption of organics on PBSAC type materials in similar applications. The highest rates of degradation observed with Co_2MnO_4 composites, ($50 \cdot 10^{-3}$-$60 \cdot 10^{-3}$) are in the lower half of the ($5 \cdot 10^{-3}$-$200 \cdot 10^{-3}$) min^{-1} literature range, but this chapter has showed that acid oxidation can be used to suppress the unwanted adsorption of organics on carbon supported catalysts. This leads to truly catalytic degradation making up a much larger portion of overall dye removal (2.6% vs 40% in the case of 16.7% Co_2MnO_4-CB vs 16.7% Co_2MnO_4-oCB).

Finally, the electrocatalytic activity of GNF and oGNF supported Co_2MnO_4 was investigated via cyclic and rotating ring disk electrode voltammetry. It was found that none of these materials facilitate any appreciable O_2 reduction, only signs of H_2O_2 reduction were observed.

Future prospects

This project has opened up a line of scientific inquiry into macroscale carbon supported noble metal-free Fenton-like chemistry. In addition to the more focused smaller studies, this line of work could be further developed in three areas via subsequent postgraduate research. While the kinetic analysis of the discussed Co_2MnO_4 composites was sufficiently extensive to allow conclusions to be drawn, it could be expanded via using a design of experiments approach. Using such an approach would be a step-change in the evaluation of Fenton-like catalysts, as one-variable-at-a-time experimentation often finds a local maximum in catalytic activity, but not necessarily the global maximum in terms of rate of degradation or truly catalytic degradation versus experimental conditions. It would be important to conduct targeted studies into producing an active catalyst of 2 e^- ORR using some combination of one of the Co, Mn spinels and one of the carbon supports, since this would allow a subsequent reactor to forego the need for the input of H_2O_2 and thus significantly reduce costs. Finally, the culmination of this line of research would be adapting the generation and activation of H_2O_2 to a packed bed, continuous flow reactor, where one module contains the most active 2 e^- ORR catalyst, while a subsequent module the most active Fenton-like catalyst. This would contribute to filling a gap in academic research, as publications exploring Fenton-like chemistry in continuous flow reactors is currently lacking. It would also open up the possibility of scaling up towards a pilot plant scale, which is a currently unexplored area of this field. This would require

extensive research, with the most obvious challenge being the presence of bubbles from the recombination of ROS.

The wider field of Fenton-like chemistry has gone through a long and very extensive science and engineering research path from the discovery of Fenton chemistry in 1870's to the first pilot scale water treatment plants expected to be online in the near future. The most significant drawback of Fenton-chemistry is the generation of a toxic sludge when using Fe based catalysts, so the field has largely moving to other 3rd row transition metals. The excessive leaching of Fe also shows that it is crucial to immobilise the catalyst on a support. The state of the art in terms of the synthesis of advanced hybrid Fenton-like catalysts is to use single atom catalysts, or extremely small zero valent metal or metal oxide nanoparticles supported on graphene-like supports. While these materials facilitate orders of magnitudes higher rates of degradation, scaling these up for even a pilot plant without a significant loss of catalytic activity would likely be extremely challenging, if not impossible. It is the opinion of the author of this thesis that the scale-up of macroscale carbon supported metal oxide catalysts should be a more feasible route for the large scale production of catalysts for tertiary water treatment. It would also be imperative to utilise the considerable research into 2 e^- ORR in order to eliminate the most significant chemical input of any potential Fenton-based water treatment plant, which is H_2O_2. The wider chemical industry is moving from continuously stirred tank reactors towards continuous flow reactors from being the standard reactor configuration, and so it is reasonable to assume that Fenton-like water treatment will follow a similar path. This thesis contributes to the field by reporting of the emergent synergism between a fibrous graphitic carbon support and a Fenton-like catalyst, while also discussing a highly active macroscale carbon supported Fenton-like catalyst on which the unwanted adsorption of organics is greatly suppressed, and is expected to be suitable for packed bed reactor configurations.

Bibliography

[1] UNICEF and WHO, “Progress on household drinking water, sanitation and hygiene 2000-2017. Special focus on inequalities,” New York, NY, USA, 2019.

[2] Environment Agency, “Poly- and perfluoroalkyl substances (PFAS): sources, pathways and environmental data: summary,” 2021.

[3] J. O. Tijani, O. O. Fatoba, and L. F. Petrik, “A Review of Pharmaceuticals and Endocrine-Disrupting Compounds: Sources, Effects, Removal, and Detections,” *Water, Air, Soil Pollut.*, vol. 224, no. 11, p. 1770, Nov. 2013, doi: 10.1007/s11270-013-1770-3.

[4] A. Ismanto, T. Hadibarata, R. A. Kristanti, L. Maslukah, N. Safinatunnajah, and W. Kusumastuti, “Endocrine disrupting chemicals (EDCs) in environmental matrices: Occurrence, fate, health impact, physio-chemical and bioremediation technology,” *Environ. Pollut.*, vol. 302, p. 119061, Jun. 2022, doi: 10.1016/j.envpol.2022.119061.

[5] `

[6] R. Andreozzi, “Advanced oxidation processes (AOP) for water purification and recovery,” *Catal. Today*, vol. 53, no. 1, pp. 51–59, Oct. 1999, doi: 10.1016/S0920-5861(99)00102-9.

[7] J. J. Pignatello, E. Oliveros, and A. MacKay, “Advanced oxidation processes for organic contaminant destruction based on the fenton reaction and related chemistry,” *Crit. Rev. Environ. Sci. Technol.*, vol. 36, no. 1, pp. 1–84, 2006, doi: 10.1080/10643380500326564.

[8] Y. Mokhbi, M. Korichi, and Z. Akchiche, “Combined photocatalytic and Fenton oxidation for oily wastewater treatment,” *Appl. Water Sci.*, vol. 9, no. 2, p. 35, Mar. 2019, doi: 10.1007/s13201-019-0916-x.

[9] A. K. Bińand S. Sobera-Madej, “Comparison of the Advanced Oxidation Processes (UV, UV/H 2 O 2 and O 3) for the Removal of Antibiotic Substances during Wastewater Treatment,” *Ozone Sci. Eng.*, vol. 34, no. 2, pp. 136–139, Mar. 2012, doi: 10.1080/01919512.2012.650130.

[10] H. J. H. Fenton, “16 Oxidation of Tartatic Acid in Presence of Iron,” *J. Chem. Soc. Trans.*, vol. 65, no. 0, pp. 899–910, 1894.

[11] F. Haber, J. Weiss, and P. R. S. L. A, “The catalytic decomposition of hydrogen peroxide by iron salts,” *Proc. R. Soc. London. Ser. A - Math. Phys. Sci.*, vol. 147, no. 861, pp. 332–351, 1934, doi: 10.1098/rspa.1934.0221.

[12] J. H. Baxendale, M. G. Evans, and C. S. Park, “The mechanism and kinetics of the initiation of polymerisation by systems containing hydrogen peroxide,” *Trans. Faraday Soc.*, vol. 42, pp. 155–169, 1946, doi: 10.1039/TF9464200155.

[13] G. V. Buxton, C. L. Greenstock, W. P. Helman, and A. B. Ross, “Critical Review of rate constants for reactions of hydrated electrons, hydrogen atoms and hydroxyl radicals (·OH/·O− in Aqueous Solution,” *J. Phys. Chem. Ref. Data*, vol. 17, no. 2, pp. 513–886, Apr. 1988, doi: 10.1063/1.555805.

[14] G. R. Buettner, L. W. Oberley, and S. W. H. C. Leuthauser, “THE EFFECT OF IRON ON THE DISTRIBUTION OF SUPEROXIDE AND HYDROXYL RADICALS AS SEEN BY SPIN TRAPPING AND ON THE SUPEROXIDE DISMUTASE ASSAY,” *Photochem. Photobiol.*, vol. 28, no. 4–5, pp. 693–695, Oct. 1978, doi: 10.1111/j.1751-1097.1978.tb07001.x.

[15] E. Finkelstein, G. M. Rosen, and E. J. Rauckman, “Spin trapping of superoxide and hydroxyl radical: Practical aspects,” *Arch. Biochem. Biophys.*, vol. 200, no. 1, pp. 1–16, Mar. 1980, doi: 10.1016/0003-9861(80)90323-9.

[16] S. Croft, B. C. Gilbert, J. R. Lindsay Smith, and A. C. Whitwood, “An E.S.R. Investigation

of the Reactive Intermediate Generated in the Reaction Between Fe II and H 2 O 2 in Aqueous Solution. Direct Evidence for the Formation of the Hydroxyl Radical," *Free Radic. Res. Commun.*, vol. 17, no. 1, pp. 21–39, Jan. 1992, doi: 10.3109/10715769209061086.

[17] D. Barnes, M. O'Hara, E. Samuel, and D. Waters, "The treatment of paint-stripping wastewaters which contain phenol and chromium," *Environ. Technol. Lett.*, vol. 2, no. 2, pp. 85–94, Feb. 1981, doi: 10.1080/09593338109384027.

[18] B. N. Aronstein, R. A. Lawal, and A. Maka, "Chemical degradation of cyanides by fenton's reagent in aqueous and soil-containing systems," *Environ. Toxicol. Chem.*, vol. 13, no. 11, pp. 1719–1726, Nov. 1994, doi: 10.1002/etc.5620131102.

[19] Bigda Richard J., "Fenton's chemistry: an effective advanced oxidation process," *Adams/Green Ind. Publ. Inc.*, 1996.

[20] R. S. Greenberg, T. Andrews, P. K. C. Kakarla, and R. J. Watts, "In-Situ Fenton-Like Oxidation of Volatile Organics: Laboratory, Pilot, and Full-Scale Demonstrations," *Remediat. J.*, vol. 8, no. 2, pp. 29–42, Jan. 1998, doi: 10.1002/rem.3440080205.

[21] W. H. Glaze, J.-W. Kang, and D. H. Chapin, "The Chemistry of Water Treatment Processes Involving Ozone, Hydrogen Peroxide and Ultraviolet Radiation," *Ozone Sci. Eng.*, vol. 9, no. 4, pp. 335–352, Sep. 1987, doi: 10.1080/01919518708552148.

[22] J. J. Pignatello, E. Oliveros, and A. MacKay, "Advanced Oxidation Processes for Organic Contaminant Destruction Based on the Fenton Reaction and Related Chemistry," *Crit. Rev. Environ. Sci. Technol.*, vol. 36, no. 1, pp. 1–84, Jan. 2006, doi: 10.1080/10643380500326564.

[23] A. D. Bokare and W. Choi, "Review of iron-free Fenton-like systems for activating H2O2 in advanced oxidation processes," *J. Hazard. Mater.*, vol. 275, pp. 121–135, Jun. 2014, doi: 10.1016/j.jhazmat.2014.04.054.

[24] J. He, X. Yang, B. Men, and D. Wang, "Interfacial mechanisms of heterogeneous Fenton reactions catalyzed by iron-based materials: A review," *J. Environ. Sci.*, vol. 39, pp. 97–109, Jan. 2016, doi: 10.1016/j.jes.2015.12.003.

[25] I. Langmuir, "The mechanism of the catalytic action of platinum in the reactions 2Co + O2= 2Co2 and 2H2+ O2= 2H2O," *Trans. Faraday Soc.*, vol. 17, p. 621, 1922, doi: 10.1039/tf9221700621.

[26] H. S. Taylor, "A theory of the catalytic surface," *Proc. R. Soc. London. Ser. A, Contain. Pap. a Math. Phys. Character*, vol. 108, no. 745, pp. 105–111, May 1925, doi: 10.1098/rspa.1925.0061.

[27] R. M. Mironenko and A. V. Lavrenov, "An Essay on the History of Catalytic Hydrogenation of Organic Compounds. From P. Sabatier and V. N. Ipatieff to the Present Days," *Catal. Ind.*, vol. 14, no. 1, pp. 131–144, Mar. 2022, doi: 10.1134/S2070050422010056.

[28] P. Sabatier, *La catalyse en chimie organique*. 1920.

[29] E. F. A., "Reactions of Hydrogen with Organic Compounds over Copper-Chromium Oxide and Nickel Catalysts," *Nature*, vol. 141, no. 3575, pp. 811–811, May 1938, doi: 10.1038/141811d0.

[30] J. J. B. van Eijk Van Voorthuijsen and P. Franzen, "Structure and properties of compounds formed during the preparation of nickel-on-silica catalysts," *Recl. des Trav. Chim. des Pays-Bas*, vol. 70, no. 9, pp. 793–812, Jan. 1951, doi: 10.1002/recl.19510700906.

[31] G. C. A. Schuit and L. L. Van Reijen, "The Structure and Activity of Metal-on-Silica Catalysts," 1958, pp. 242–317. doi: 10.1016/S0360-0564(08)60409-5.

[32] J. W. E. Coenen and P. B. Wells, “Research Group On Catalysis, Council Of Europe. Standard Catalyst Projects,” 1983, pp. 801–814. doi: 10.1016/S0167-2991(09)60069-0.
[33] F. Rodríguez-reinoso, “The role of carbon materials in heterogeneous catalysis,” *Carbon N. Y.*, vol. 36, no. 3, pp. 159–175, 1998, doi: 10.1016/S0008-6223(97)00173-5.
[34] E. Zavoisky, “Spin-magnetic resonance in paramagnetics,” *Fiz. Zhurnal*, vol. 9, pp. 211–245, 1945.
[35] A. Damjanovic, M. A. Genshaw, and J. O. Bockris, “The Mechanism of Oxygen Reduction at Platinum in Alkaline Solutions with Special Reference to H[sub 2]O[sub 2],” *J. Electrochem. Soc.*, vol. 114, no. 11, p. 1107, 1967, doi: 10.1149/1.2426425.
[36] A. Damjanovic, “Progress in the Studies of Oxygen Reduction during the Last Thirty Years,” in *Electrochemistry in Transition*, Boston, MA: Springer US, 1992, pp. 107–126. doi: 10.1007/978-1-4615-9576-2_9.
[37] T. Toda, H. Igarashi, H. Uchida, and M. Watanabe, “Enhancement of the Electroreduction of Oxygen on Pt Alloys with Fe, Ni, and Co,” *J. Electrochem. Soc.*, vol. 146, no. 10, pp. 3750–3756, Oct. 1999, doi: 10.1149/1.1392544.
[38] W. J. King and A. C. C. Tseung, “The reduction of oxygen on nickel-cobalt oxides—I,” *Electrochim. Acta*, vol. 19, no. 8, pp. 485–491, Aug. 1974, doi: 10.1016/0013-4686(74)87029-5.
[39] W. J. King and A. C. C. Tseung, “The reduction of oxygen on nickel-cobalt oxides—II,” *Electrochim. Acta*, vol. 19, no. 8, pp. 493–498, Aug. 1974, doi: 10.1016/0013-4686(74)87030-1.
[40] C. W. B. Bezerra *et al.*, “A review of Fe–N/C and Co–N/C catalysts for the oxygen reduction reaction,” *Electrochim. Acta*, vol. 53, no. 15, pp. 4937–4951, Jun. 2008, doi: 10.1016/j.electacta.2008.02.012.
[41] ASTM D1193-06(2018), “Standard Specification for Reagent Water.” doi: 10.1520/D1193-06R18.
[42] P. Scherrer, “Bestimmung der Größe und der inneren Struktur von Kolloidteilchen mittels Röntgenstrahlen,” *Nachrichten von der Gesellschaft der Wissenschaften zu Göttingen, Math. Klasse*, pp. 98–100, 1918.
[43] J. I. Langford and A. J. C. Wilson, “Scherrer after sixty years: A survey and some new results in the determination of crystallite size,” *J. Appl. Crystallogr.*, vol. 11, no. 2, pp. 102–113, Apr. 1978, doi: 10.1107/S0021889878012844.
[44] T. Ungar, *Industrial Applications of X-ray Diffraction*. CRC Press, 2000.
[45] G. . Williamson and W. . Hall, “X-ray line broadening from filed aluminium and wolfram,” *Acta Metall.*, vol. 1, no. 1, pp. 22–31, Jan. 1953, doi: 10.1016/0001-6160(53)90006-6.
[46] M. C. Biesinger, B. P. Payne, A. P. Grosvenor, L. W. M. Lau, A. R. Gerson, and R. S. C. Smart, “Resolving surface chemical states in XPS analysis of first row transition metals, oxides and hydroxides: Cr, Mn, Fe, Co and Ni,” *Appl. Surf. Sci.*, vol. 257, no. 7, pp. 2717–2730, Jan. 2011, doi: 10.1016/j.apsusc.2010.10.051.
[47] G. Greczynski and L. Hultman, “Reliable determination of chemical state in x-ray photoelectron spectroscopy based on sample-work-function referencing to adventitious carbon: Resolving the myth of apparent constant binding energy of the C 1s peak,” *Appl. Surf. Sci.*, vol. 451, pp. 99–103, Sep. 2018, doi: 10.1016/j.apsusc.2018.04.226.
[48] N. Thomas, D. D. Dionysiou, and S. C. Pillai, “Heterogeneous Fenton catalysts: A review of recent advances,” *J. Hazard. Mater.*, vol. 404, p. 124082, Feb. 2021, doi: 10.1016/j.jhazmat.2020.124082.

[49] A. A. Frost, “Oxidation Potential-Free Energy Diagrams,” *J. Am. Chem. Soc.*, vol. 73, no. 6, pp. 2680–2682, Jun. 1951, doi: 10.1021/ja01150a074.
[50] X. Liu, C. Chen, Y. Zhao, and B. Jia, “A Review on the Synthesis of Manganese Oxide Nanomaterials and Their Applications on Lithium-Ion Batteries,” *J. Nanomater.*, vol. 2013, no. 1, Jan. 2013, doi: 10.1155/2013/736375.
[51] “https://www.mindat.org/min-43551.html.”
[52] “https://www.mindat.org/min-1164.html”.
[53] “https://www.mindat.org/min-1921.html”.
[54] “https://www.mindat.org/min-1134.html”.
[55] S. L. Brock, N. Duan, Z. R. Tian, O. Giraldo, H. Zhou, and S. L. Suib, “A Review of Porous Manganese Oxide Materials,” *Chem. Mater.*, vol. 10, no. 10, pp. 2619–2628, Oct. 1998, doi: 10.1021/cm980227h.
[56] T. Gao, M. Glerup, F. Krumeich, R. Nesper, H. Fjellvåg, and P. Norby, “Microstructures and Spectroscopic Properties of Cryptomelane-type Manganese Dioxide Nanofibers,” *J. Phys. Chem. C*, vol. 112, no. 34, pp. 13134–13140, Aug. 2008, doi: 10.1021/jp804924f.
[57] T. Gao, H. Fjellvåg, and P. Norby, “A comparison study on Raman scattering properties of α- and β-MnO2,” *Anal. Chim. Acta*, vol. 648, no. 2, pp. 235–239, Aug. 2009, doi: 10.1016/j.aca.2009.06.059.
[58] V. P. Santos, M. F. R. Pereira, J. J. M. Órfão, and J. L. Figueiredo, “The role of lattice oxygen on the activity of manganese oxides towards the oxidation of volatile organic compounds,” *Appl. Catal. B Environ.*, vol. 99, no. 1–2, pp. 353–363, Aug. 2010, doi: 10.1016/j.apcatb.2010.07.007.
[59] B. Lan *et al.*, “The art of balance: Engineering of structure defects and electrical conductivity of α-MnO2 for oxygen reduction reaction,” *Electrochim. Acta*, vol. 283, pp. 459–466, Sep. 2018, doi: 10.1016/j.electacta.2018.06.195.
[60] S. Dawadi, A. Gupta, M. Khatri, B. Budhathoki, G. Lamichhane, and N. Parajuli, “Manganese dioxide nanoparticles: synthesis, application and challenges,” *Bull. Mater. Sci.*, vol. 43, no. 1, p. 277, Dec. 2020, doi: 10.1007/s12034-020-02247-8.
[61] M. Huang, F. Li, F. Dong, Y. X. Zhang, and L. L. Zhang, “MnO 2 -based nanostructures for high-performance supercapacitors,” *J. Mater. Chem. A*, vol. 3, no. 43, pp. 21380–21423, 2015, doi: 10.1039/C5TA05523G.
[62] M. Toupin, T. Brousse, and D. Bélanger, “Influence of Microstucture on the Charge Storage Properties of Chemically Synthesized Manganese Dioxide,” *Chem. Mater.*, vol. 14, no. 9, pp. 3946–3952, Sep. 2002, doi: 10.1021/cm020408q.
[63] R. Zhang, T. S. Arthur, C. Ling, and F. Mizuno, “Manganese dioxides as rechargeable magnesium battery cathode; synthetic approach to understand magnesiation process,” *J. Power Sources*, vol. 282, pp. 630–638, May 2015, doi: 10.1016/j.jpowsour.2015.02.067.
[64] J. Jia, P. Zhang, and L. Chen, “Catalytic decomposition of gaseous ozone over manganese dioxides with different crystal structures,” *Appl. Catal. B Environ.*, vol. 189, pp. 210–218, Jul. 2016, doi: 10.1016/j.apcatb.2016.02.055.
[65] D. M. Robinson *et al.*, “Photochemical Water Oxidation by Crystalline Polymorphs of Manganese Oxides: Structural Requirements for Catalysis,” *J. Am. Chem. Soc.*, vol. 135, no. 9, pp. 3494–3501, Mar. 2013, doi: 10.1021/ja310286h.
[66] J. Luo, Q. Zhang, A. Huang, and S. L. Suib, “Total oxidation of volatile organic compounds with hydrophobic cryptomelane-type octahedral molecular sieves,” *Microporous Mesoporous Mater.*, vol. 35–36, pp. 209–217, Apr. 2000, doi: 10.1016/S1387-1811(99)00221-8.

[67] R. Cerc Korošec, P. Umek, A. Gloter, J. Padežnik Gomilšek, and P. Bukovec, “Structural properties and thermal stability of cobalt- and chromium-doped α-MnO 2 nanorods,” *Beilstein J. Nanotechnol.*, vol. 8, pp. 1032–1042, May 2017, doi: 10.3762/bjnano.8.104.

[68] E. S. Ilton, J. E. Post, P. J. Heaney, F. T. Ling, and S. N. Kerisit, “XPS determination of Mn oxidation states in Mn (hydr)oxides,” *Appl. Surf. Sci.*, vol. 366, pp. 475–485, Mar. 2016, doi: 10.1016/j.apsusc.2015.12.159.

[69] C. Tomon *et al.*, “Core-shell structure of LiMn2O4 cathode material reduces phase transition and Mn dissolution in Li-ion batteries,” *Commun. Chem.*, vol. 5, no. 1, p. 54, Apr. 2022, doi: 10.1038/s42004-022-00670-y.

[70] G. Greczynski and L. Hultman, “Compromising Science by Ignorant Instrument Calibration—Need to Revisit Half a Century of Published XPS Data,” *Angew. Chemie Int. Ed.*, vol. 59, no. 13, pp. 5002–5006, Mar. 2020, doi: 10.1002/anie.201916000.

[71] M. C. Militello and S. W. Gaarenstroom, “Manganese Dioxide (MnO2) by XPS,” *Surf. Sci. Spectra*, vol. 8, no. 3, pp. 200–206, Jul. 2001, doi: 10.1116/11.20020401.

[72] H. W. Nesbitt and D. Banerjee, “Interpretation of XPS Mn(2p) spectra of Mn oxyhydroxides and constraints on the mechanism of MnO 2 precipitation,” *Am. Mineral.*, vol. 83, no. 3–4, pp. 305–315, Apr. 1998, doi: 10.2138/am-1998-3-414.

[73] M. A. Stranick, “MnO2 by XPS,” *Surf. Sci. Spectra*, vol. 6, no. 1, pp. 31–38, Jan. 1999, doi: 10.1116/1.1247888.

[74] “http://www.xpslibrary.com.”

[75] “https://www.xpsfitting.com/”.

[76] S. Ziembowicz and M. Kida, “Limitations and future directions of application of the Fenton-like process in micropollutants degradation in water and wastewater treatment: A critical review,” *Chemosphere*, vol. 296, p. 134041, Jun. 2022, doi: 10.1016/j.chemosphere.2022.134041.

[77] Y. Zhao *et al.*, “Cobalt-doped MnO2 ultrathin nanosheets with abundant oxygen vacancies supported on functionalized carbon nanofibers for efficient oxygen evolution,” *Nano Energy*, vol. 54, pp. 129–137, Dec. 2018, doi: 10.1016/j.nanoen.2018.10.008.

[78] J. Ye, M. Zhou, Y. Le, B. Cheng, and J. Yu, “Three-dimensional carbon foam supported MnO2/Pt for rapid capture and catalytic oxidation of formaldehyde at room temperature,” *Appl. Catal. B Environ.*, vol. 267, p. 118689, Jun. 2020, doi: 10.1016/j.apcatb.2020.118689.

[79] F. Cheng, J. Shen, B. Peng, Y. Pan, Z. Tao, and J. Chen, “Rapid room-temperature synthesis of nanocrystalline spinels as oxygen reduction and evolution electrocatalysts,” *Nat. Chem.*, vol. 3, no. 1, pp. 79–84, Jan. 2011, doi: 10.1038/nchem.931.

[80] F. Wang, H. Dai, J. Deng, G. Bai, K. Ji, and Y. Liu, “Manganese Oxides with Rod-, Wire-, Tube-, and Flower-Like Morphologies: Highly Effective Catalysts for the Removal of Toluene,” *Environ. Sci. Technol.*, vol. 46, no. 7, pp. 4034–4041, Apr. 2012, doi: 10.1021/es204038j.

[81] N. Sui, Y. Duan, X. Jiao, and D. Chen, “Large-Scale Preparation and Catalytic Properties of One-Dimensional α/β-MnO 2 Nanostructures,” *J. Phys. Chem. C*, vol. 113, no. 20, pp. 8560–8565, May 2009, doi: 10.1021/jp810452k.

[82] E. O. Alegbe and T. O. Uthman, “A review of history, properties, classification, applications and challenges of natural and synthetic dyes,” *Heliyon*, vol. 10, no. 13, p. e33646, Jul. 2024, doi: 10.1016/j.heliyon.2024.e33646.

[83] J. Zheng, Z. Gao, H. He, S. Yang, and C. Sun, “Efficient degradation of Acid Orange 7 in

aqueous solution by iron ore tailing Fenton-like process," *Chemosphere*, vol. 150, pp. 40–48, May 2016, doi: 10.1016/j.chemosphere.2016.02.001.

[84] J. Wang and R. Zhuan, "Degradation of antibiotics by advanced oxidation processes: An overview," *Sci. Total Environ.*, vol. 701, p. 135023, Jan. 2020, doi: 10.1016/j.scitotenv.2019.135023.

[85] E.-J. Kim, D. Oh, C.-S. Lee, J. Gong, J. Kim, and Y.-S. Chang, "Manganese oxide nanorods as a robust Fenton-like catalyst at neutral pH: Crystal phase-dependent behavior," *Catal. Today*, vol. 282, pp. 71–76, Mar. 2017, doi: 10.1016/j.cattod.2016.03.034.

[86] X. Wang and Y. Li, "Synthesis and Formation Mechanism of Manganese Dioxide Nanowires/Nanorods," *Chem. – A Eur. J.*, vol. 9, no. 1, pp. 300–306, Jan. 2003, doi: 10.1002/chem.200390024.

[87] M. Johnsson, P. Pettersson, and M. Nygren, "Thermal decomposition of fibrous TiOSO4·2H2O to TiO2," *Thermochim. Acta*, vol. 298, no. 1–2, pp. 47–54, Sep. 1997, doi: 10.1016/S0040-6031(97)00206-2.

[88] G. Eisenberg, "Colorimetric Determination of Hydrogen Peroxide," *Ind. Eng. Chem. Anal. Ed.*, vol. 15, no. 5, pp. 327–328, May 1943, doi: 10.1021/i560117a011.

[89] Y. Zhang, Y. Yang, Y. Zhang, T. Zhang, and M. Ye, "Heterogeneous oxidation of naproxen in the presence of α-MnO2 nanostructures with different morphologies," *Appl. Catal. B Environ.*, vol. 127, pp. 182–189, Oct. 2012, doi: 10.1016/j.apcatb.2012.08.014.

[90] H. Luo *et al.*, "Synthesis of dual function Fe 3 O 4 @MnO 2 @HKUST-1 magnetic micromotors for efficient colorimetric detection and degradation of hydroquinone," *New J. Chem.*, vol. 47, no. 3, pp. 1094–1104, 2023, doi: 10.1039/D2NJ03909E.

[91] D. M. Tinsley and J. H. Sharp, "Thermal analysis of manganese dioxide in controlled atmospheres," *J. Therm. Anal.*, vol. 3, no. 1, pp. 43–48, Mar. 1971, doi: 10.1007/BF01911769.

[92] G. Xie *et al.*, "The evolution of α-MnO2 from hollow cubes to hollow spheres and their electrochemical performance for supercapacitors," *J. Mater. Sci.*, vol. 52, no. 18, pp. 10915–10926, Sep. 2017, doi: 10.1007/s10853-017-1116-4.

[93] J. Hou, Y. Li, L. Liu, L. Ren, and X. Zhao, "Effect of giant oxygen vacancy defects on the catalytic oxidation of OMS-2 nanorods," *J. Mater. Chem. A*, vol. 1, no. 23, p. 6736, 2013, doi: 10.1039/c3ta11566f.

[94] W. E. Richmond and M. Fleischer, "Cryptomelane, a new name for the commonest of the 'psilomelane' minerals," *Am. Mineral.*, vol. 27, pp. 607–610, 1942.

[95] L. T. Larson, "Geology and mineralogy of certain manganese oxide deposits," *Econ. Geol.*, vol. 59, pp. 54–78, 1964.

[96] P. R. B. J. E. Post, R.B. Von Dreele, "Symmetry and cation displacements in hollandites: structure refinements of hollandite, cryptomelane, and priderite.," *Acta Cryst.*, vol. 38, pp. 1056–165, 1982.

[97] C. L. Lake and P. D. Lake, "Carbon Nanofiber Multifunctional Mat," in *Nanotube Superfiber Materials*, Elsevier, 2014, pp. 313–331. doi: 10.1016/B978-1-4557-7863-8.00011-6.

[98] Z. Q. Li, C. J. Lu, Z. P. Xia, Y. Zhou, and Z. Luo, "X-ray diffraction patterns of graphite and turbostratic carbon," *Carbon N. Y.*, vol. 45, no. 8, pp. 1686–1695, Jul. 2007, doi: 10.1016/j.carbon.2007.03.038.

[99] "Applied Sciences Inc. Data sheet for Pyrograf III, PR-19-XT-HHT", [Online]. Available: https://www.knowde.com/stores/applied-sciences-inc/products/applied-sciences-inc-pr-19-xt-hht

[100] J.-P. Tessonnier *et al.*, “Analysis of the structure and chemical properties of some commercial carbon nanostructures,” *Carbon N. Y.*, vol. 47, no. 7, pp. 1779–1798, Jun. 2009, doi: 10.1016/j.carbon.2009.02.032.

[101] L. A. Turkevich, J. Fernback, A. G. Dastidar, and P. Osterberg, “Potential explosion hazard of carbonaceous nanoparticles: screening of allotropes,” *Combust. Flame*, vol. 167, pp. 218–227, May 2016, doi: 10.1016/j.combustflame.2016.02.010.

[102] J. Xu, J. P. Donohoe, and C. U. Pittman, “Preparation, electrical and mechanical properties of vapor grown carbon fiber (VGCF)/vinyl ester composites,” *Compos. Part A Appl. Sci. Manuf.*, vol. 35, no. 6, pp. 693–701, Jun. 2004, doi: 10.1016/j.compositesa.2004.02.016.

[103] G. W. Smith, “Oxidation resistance of pyrolytically grown carbon fibers,” *Carbon N. Y.*, vol. 22, no. 6, pp. 477–479, 1984, doi: 10.1016/0008-6223(84)90078-2.

[104] Y. Jiang, Z. Yang, X. Bi, N. Yao, P. Zhao, and X. Meng, “Mediated electron transfer process in α-MnO2 catalyzed Fenton-like reaction for oxytetracycline degradation,” *Chinese Chem. Lett.*, vol. 35, no. 8, p. 109331, Aug. 2024, doi: 10.1016/j.cclet.2023.109331.

[105] Y. Wang *et al.*, “Fenton-like catalysis by MnO2 membrane reactor with oxygen vacancies for carbamazepine degradation,” *Appl. Catal. B Environ. Energy*, vol. 353, p. 124106, Sep. 2024, doi: 10.1016/j.apcatb.2024.124106.

[106] S. Shen *et al.*, “Understanding the nonradical activation of peroxymonosulfate by different crystallographic MnO2: The pivotal role of MnIII content on the surface,” *J. Hazard. Mater.*, vol. 439, p. 129613, Oct. 2022, doi: 10.1016/j.jhazmat.2022.129613.

[107] A. Bonilla-Petriciolet, D. I. Mendoza-Castillo, and H. E. Reynel-Ávila, Eds., *Adsorption Processes for Water Treatment and Purification*. Cham: Springer International Publishing, 2017. doi: 10.1007/978-3-319-58136-1.

[108] Y. Zhou, J. Lu, Y. Zhou, and Y. Liu, “Recent advances for dyes removal using novel adsorbents: A review,” *Environ. Pollut.*, vol. 252, pp. 352–365, Sep. 2019, doi: 10.1016/j.envpol.2019.05.072.

[109] B. Böhringer *et al.*, “Polymer-based Spherical Activated Carbons – From Adsorptive Properties to Filter Performance,” *Chemie Ing. Tech.*, vol. 83, no. 1–2, pp. 53–60, Jan. 2011, doi: 10.1002/cite.201000166.

[110] M. Tagliavini, F. Engel, P. G. Weidler, T. Scherer, and A. I. Schäfer, “Adsorption of steroid micropollutants on polymer-based spherical activated carbon (PBSAC),” *J. Hazard. Mater.*, vol. 337, pp. 126–137, Sep. 2017, doi: 10.1016/j.jhazmat.2017.03.036.

[111] Y.-A. Boussouga, J. Joseph, H. Stryhanyuk, H. H. Richnow, and A. I. Schäfer, “Adsorption of uranium (VI) complexes with polymer-based spherical activated carbon,” *Water Res.*, vol. 249, p. 120825, Feb. 2024, doi: 10.1016/j.watres.2023.120825.

[112] M. Monthioux and V. L. Kuznetsov, “Who should be given the credit for the discovery of carbon nanotubes?,” *Carbon N. Y.*, vol. 44, no. 9, pp. 1621–1623, Aug. 2006, doi: 10.1016/j.carbon.2006.03.019.

[113] T. V. HUGHES & CHAMBERS., “MANUFACTURE OF CARBON FILAMENTS.,” No. 405,480, 1889

[114] S. L. Schüetzenberger P, “Sur quelques faits relatifs a` l’histoire du carbone.,” *C R Acad Sci Paris*, vol. 111, pp. 774–8, 1890.

[115] P. H. Pélabon C, “Sur une variété de carbone filamenteux,” *C R Acad Sci Paris*, vol. 137, pp. 706–8, 1903.

[116] L. V. Radushkevich LV, “O strukture ugleroda, obrazujucegosja pri termiceskom razlozenii okisi ugleroda na zeleznom kontakte.,” *Zurn Fis. Chim*, vol. 26, pp. 88–95,

1952.
[117] L. N. Hillert M, “The structure of graphite filaments.,” *Z Krist.*, vol. 111, pp. 24–34, 1958.
[118] L. J. E. Hofer, E. Sterling, and J. T. McCartney, “Structure of Carbon Deposited from Carbon Monoxide on Iron, Cobalt and Nickel,” *J. Phys. Chem.*, vol. 59, no. 11, pp. 1153–1155, Nov. 1955, doi: 10.1021/j150533a010.
[119] R. T. K. Baker, “Catalytic growth of carbon filaments,” *Carbon N. Y.*, vol. 27, no. 3, pp. 315–323, 1989, doi: 10.1016/0008-6223(89)90062-6.
[120] Iijima S., “Helical microtubules of graphite carbon.,” *Nature*, vol. 354, pp. 56–8, 1991.
[121] P. Santos, A. P. Silva, and P. N. B. Reis, “The Effect of Carbon Nanofibers on the Mechanical Performance of Epoxy-Based Composites: A Review,” *Polymers (Basel).*, vol. 16, no. 15, p. 2152, Jul. 2024, doi: 10.3390/polym16152152.
[122] T. Yanagisawa, T. Hayashi, Y. A. Kim, Y. Fukai, and M. Endo, “Structure and basic properties of cup-stacked type carbon nanofiber,” *Mol. Cryst. Liq. Cryst.*, vol. 387, no. 1, pp. 167–171, Jan. 2002, doi: 10.1080/10587250215246.
[123] Y. A. Kim, T. Hayashi, Y. Fukaiand, M. Endo, and T. Yanagisawa, “Microstructural change of cup-stacked carbon nanofiber by post-treatment,” *Mol. Cryst. Liq. Cryst.*, vol. 387, no. 1, pp. 157–161, Jan. 2002, doi: 10.1080/10587250215232.
[124] Y. A. Kim, T. Hayashi, Y. Fukai, M. Endo, T. Yanagisawa, and M. S. Dresselhaus, “Effect of ball milling on morphology of cup-stacked carbon nanotubes,” *Chem. Phys. Lett.*, vol. 355, no. 3–4, pp. 279–284, Apr. 2002, doi: 10.1016/S0009-2614(02)00248-8.
[125] J. P. Vareda, “On validity, physical meaning, mechanism insights and regression of adsorption kinetic models,” *J. Mol. Liq.*, vol. 376, p. 121416, Apr. 2023, doi: 10.1016/j.molliq.2023.121416.
[126] Y. . Ho and G. McKay, “The sorption of lead(II) ions on peat,” *Water Res.*, vol. 33, no. 2, pp. 578–584, Feb. 1999, doi: 10.1016/S0043-1354(98)00207-3.
[127] Y. . Ho and G. McKay, “Pseudo-second order model for sorption processes,” *Process Biochem.*, vol. 34, no. 5, pp. 451–465, Jul. 1999, doi: 10.1016/S0032-9592(98)00112-5.
[128] A. Bhatnagar, W. Hogland, M. Marques, and M. Sillanpää, “An overview of the modification methods of activated carbon for its water treatment applications,” *Chem. Eng. J.*, vol. 219, pp. 499–511, Mar. 2013, doi: 10.1016/j.cej.2012.12.038.
[129] W. Shen, Z. Li, and Y. Liu, “Surface Chemical Functional Groups Modification of Porous Carbon,” *Recent Patents Chem. Eng.*, vol. 1, no. 1, pp. 27–40, Jan. 2008, doi: 10.2174/2211334710801010027.
[130] C. Moreno-Castilla, M. . López-Ramón, and F. Carrasco-Marín, “Changes in surface chemistry of activated carbons by wet oxidation,” *Carbon N. Y.*, vol. 38, no. 14, pp. 1995–2001, 2000, doi: 10.1016/S0008-6223(00)00048-8.
[131] M. V. Lopez-Ramon, F. Stoeckli, C. Moreno-Castilla, and F. Carrasco-Marin, “On the characterization of acidic and basic surface sites on carbons by various techniques,” *Carbon N. Y.*, vol. 37, no. 8, pp. 1215–1221, Jan. 1999, doi: 10.1016/S0008-6223(98)00317-0.
[132] M. F. R. Pereira, S. F. Soares, J. J. . Órfão, and J. L. Figueiredo, “Adsorption of dyes on activated carbons: influence of surface chemical groups,” *Carbon N. Y.*, vol. 41, no. 4, pp. 811–821, 2003, doi: 10.1016/S0008-6223(02)00406-2.
[133] D. H. da S. Santos *et al.*, “Regeneration of dye-saturated activated carbon through advanced oxidative processes: A review,” *Heliyon*, vol. 8, no. 8, p. e10205, Aug. 2022, doi: 10.1016/j.heliyon.2022.e10205.
[134] F. Salvador, N. Martin-Sanchez, R. Sanchez-Hernandez, M. J. Sanchez-Montero, and C.

Izquierdo, “Regeneration of carbonaceous adsorbents. Part II: Chemical, Microbiological and Vacuum Regeneration,” *Microporous Mesoporous Mater.*, vol. 202, pp. 277–296, Jan. 2015, doi: 10.1016/j.micromeso.2014.08.019.

[135] W. Won, R. R. Hudgins, A. Lohi, and P. L. Silveston, “The solubility of SO 3 and sulfuric acid in acetone and MEK,” *Can. J. Chem. Eng.*, vol. 79, no. 2, pp. 287–288, Apr. 2001, doi: 10.1002/cjce.5450790212.

[136] J. C. Oxley, J. Brady, S. A. Wilson, and J. L. Smith, “The risk of mixing dilute hydrogen peroxide and acetone solutions,” *J. Chem. Heal. Saf.*, vol. 19, no. 2, pp. 27–33, Mar. 2012, doi: 10.1016/j.jchas.2011.07.010.

[137] Y. Bai, Z.-H. Huang, and F. Kang, “Surface oxidation of activated electrospun carbon nanofibers and their adsorption performance for benzene, butanone and ethanol,” *Colloids Surfaces A Physicochem. Eng. Asp.*, vol. 443, pp. 66–71, Feb. 2014, doi: 10.1016/j.colsurfa.2013.10.057.

[138] M. L. Toebes, J. M. . van Heeswijk, J. H. Bitter, A. Jos van Dillen, and K. P. de Jong, “The influence of oxidation on the texture and the number of oxygen-containing surface groups of carbon nanofibers,” *Carbon N. Y.*, vol. 42, no. 2, pp. 307–315, 2004, doi: 10.1016/j.carbon.2003.10.036.

[139] A. La Torre *et al.*, “Assembly, Growth, and Catalytic Activity of Gold Nanoparticles in Hollow Carbon Nanofibers,” *ACS Nano*, vol. 6, no. 3, pp. 2000–2007, Mar. 2012, doi: 10.1021/nn300400z.

[140] M. Aygün, T. W. Chamberlain, M. del C. Gimenez-Lopez, and A. N. Khlobystov, “Magnetically Recyclable Catalytic Carbon Nanoreactors,” *Adv. Funct. Mater.*, vol. 28, no. 34, Aug. 2018, doi: 10.1002/adfm.201802869.

[141] D. B. Schuepfer *et al.*, “Assessing the structural properties of graphitic and non-graphitic carbons by Raman spectroscopy,” *Carbon N. Y.*, vol. 161, pp. 359–372, May 2020, doi: 10.1016/j.carbon.2019.12.094.

[142] A. C. Ferrari *et al.*, “Raman Spectrum of Graphene and Graphene Layers,” *Phys. Rev. Lett.*, vol. 97, no. 18, p. 187401, Oct. 2006, doi: 10.1103/PhysRevLett.97.187401.

[143] A. Jorio and R. Saito, “Raman spectroscopy for carbon nanotube applications,” *J. Appl. Phys.*, vol. 129, no. 2, Jan. 2021, doi: 10.1063/5.0030809.

[144] A. Gupta, G. Chen, P. Joshi, S. Tadigadapa, and Eklund, “Raman Scattering from High-Frequency Phonons in Supported n -Graphene Layer Films,” *Nano Lett.*, vol. 6, no. 12, pp. 2667–2673, Dec. 2006, doi: 10.1021/nl061420a.

[145] Z. Li, L. Deng, I. A. Kinloch, and R. J. Young, “Raman spectroscopy of carbon materials and their composites: Graphene, nanotubes and fibres,” *Prog. Mater. Sci.*, vol. 135, p. 101089, Jun. 2023, doi: 10.1016/j.pmatsci.2023.101089.

[146] X. Yang *et al.*, “The role of electric conductivity and water wettability of carbon nanotubes cathodes on electrocatalytic reductive-oxidative degradation of chlorinated organic pollutants under aerobic conditions,” *Electrochim. Acta*, vol. 524, p. 145999, Jun. 2025, doi: 10.1016/j.electacta.2025.145999.

[147] J. H. Lehman, M. Terrones, E. Mansfield, K. E. Hurst, and V. Meunier, “Evaluating the characteristics of multiwall carbon nanotubes,” *Carbon N. Y.*, vol. 49, no. 8, pp. 2581–2602, Jul. 2011, doi: 10.1016/j.carbon.2011.03.028.

[148] R. A. Paleo AJ, Krause B, Cerqueira MF, Muñoz E, Pötschke P, “Nonlinear Thermopower Behaviour of N-Type Carbon Nanofibres and Their Melt Mixed Polypropylene Composites,” *Polymers (Basel).*, vol. 14(2), p. 269, 2022, [Online]. Available: https://doi.org/10.3390/polym14020269

[149] A. J. Paleo *et al.*, “Thermoelectric Properties of Cotton Fabrics Dip-Coated in

Pyrolytically Stripped Pyrograf® III Carbon Nanofiber Based Aqueous Inks," *Materials (Basel).*, vol. 16, no. 12, p. 4335, Jun. 2023, doi: 10.3390/ma16124335.

[150] S.-X. Zhao, N. Ta, and X.-D. Wang, "Effect of Temperature on the Structural and Physicochemical Properties of Biochar with Apple Tree Branches as Feedstock Material," *Energies*, vol. 10, no. 9, p. 1293, Aug. 2017, doi: 10.3390/en10091293.

[151] M. Seredych, D. Hulicova-Jurcakova, G. Q. Lu, and T. J. Bandosz, "Surface functional groups of carbons and the effects of their chemical character, density and accessibility to ions on electrochemical performance," *Carbon N. Y.*, vol. 46, no. 11, pp. 1475–1488, Sep. 2008, doi: 10.1016/j.carbon.2008.06.027.

[152] A. C. Martins *et al.*, "Removal of tetracycline by NaOH-activated carbon produced from macadamia nut shells: Kinetic and equilibrium studies," *Chem. Eng. J.*, vol. 260, pp. 291–299, Jan. 2015, doi: 10.1016/j.cej.2014.09.017.

[153] D. Dittmann *et al.*, "Characterization of activated carbons for water treatment using TGA-FTIR for analysis of oxygen-containing functional groups," *Appl. Water Sci.*, vol. 12, no. 8, p. 203, Aug. 2022, doi: 10.1007/s13201-022-01723-2.

[154] S. Sonal, P. Prakash, B. K. Mishra, and G. C. Nayak, "Synthesis, characterization and sorption studies of a zirconium(<scp>iv</scp>) impregnated highly functionalized mesoporous activated carbons," *RSC Adv.*, vol. 10, no. 23, pp. 13783–13798, 2020, doi: 10.1039/C9RA10103A.

[155] X.-Y. Liu *et al.*, "Preparation of a Carbon-Based Solid Acid Catalyst by Sulfonating Activated Carbon in a Chemical Reduction Process," *Molecules*, vol. 15, no. 10, pp. 7188–7196, Oct. 2010, doi: 10.3390/molecules15107188.

[156] G. Sádovská *et al.*, "The thermal stability of carbon materials in the air: Quantitative structural investigation of thermal stability of carbon materials in air," *Carbon N. Y.*, vol. 206, pp. 211–225, Mar. 2023, doi: 10.1016/j.carbon.2023.02.042.

[157] H. Vatankhah *et al.*, "Simultaneous ozone and granular activated carbon for advanced treatment of micropollutants in municipal wastewater effluent," *Chemosphere*, vol. 234, pp. 845–854, Nov. 2019, doi: 10.1016/j.chemosphere.2019.06.082.

[158] M. J. Soberman, R. R. Farnood, and S. Tabe, "A low pressure SWCNT-ENM sandwich membrane system for the removal of PPCPs from water," *Can. J. Chem. Eng.*, vol. 98, no. 5, pp. 1047–1058, May 2020, doi: 10.1002/cjce.23703.

[159] A. Yar and Ş. Parlayici, "Carbon nanotubes/ polyacrylonitrile composite nanofiber mats for highly efficient dye adsorption," *Colloids Surfaces A Physicochem. Eng. Asp.*, vol. 651, p. 129703, Oct. 2022, doi: 10.1016/j.colsurfa.2022.129703.

[160] E. Santoso, R. Ediati, Y. Kusumawati, H. Bahruji, D. O. Sulistiono, and D. Prasetyoko, "Review on recent advances of carbon based adsorbent for methylene blue removal from waste water," *Mater. Today Chem.*, vol. 16, p. 100233, Jun. 2020, doi: 10.1016/j.mtchem.2019.100233.

[161] B. Cagnon, S. Chatelain, T. F. de Oliveira, F. Versaveau, S. Delpeux, and O. Chedeville, "Adsorption of Phthalates on Activated Carbons in Monosolute Solution and in Mix Within Complex Matrices," *Water, Air, Soil Pollut.*, vol. 228, no. 4, p. 144, Apr. 2017, doi: 10.1007/s11270-017-3315-7.

[162] Z. Zhang and D. W. Flaherty, "Modified potentiometric titration method to distinguish and quantify oxygenated functional groups on carbon materials by pKa and chemical reactivity," *Carbon N. Y.*, vol. 166, pp. 436–445, Sep. 2020, doi: 10.1016/j.carbon.2020.05.040.

[163] M. Aboughaly, "Polymer and their derivative biocomposites for dye adsorption," in *Engineered Biocomposites for Dye Adsorption*, Elsevier, 2025, pp. 223–235. doi:

10.1016/B978-0-443-29877-6.00014-7.

[164] J. S. Armijo, “The kinetics and mechanism of solid-state spinel formation ? A review and critique,” *Oxid. Met.*, vol. 1, no. 2, pp. 171–198, 1969, doi: 10.1007/BF00603514.

[165] L. Suchow, “A detailed, simple crystal field consideration of the normal spinel structure of Co3O4,” *J. Chem. Educ.*, vol. 53, no. 9, p. 560, Sep. 1976, doi: 10.1021/ed053p560.

[166] Y. Long, X. Zhu, C. Gao, W. Si, J. Li, and Y. Peng, “Modulation of Co spin state at Co3O4 crystalline-amorphous interfaces for CO oxidation and N2O decomposition,” *Nat. Commun.*, vol. 16, no. 1, p. 1048, Jan. 2025, doi: 10.1038/s41467-025-56487-5.

[167] Y. Liang *et al.*, “Co3O4 nanocrystals on graphene as a synergistic catalyst for oxygen reduction reaction,” *Nat. Mater.*, vol. 10, no. 10, pp. 780–786, 2011, doi: 10.1038/nmat3087.

[168] Z.-S. Wu *et al.*, “Graphene Anchored with Co 3 O 4 Nanoparticles as Anode of Lithium Ion Batteries with Enhanced Reversible Capacity and Cyclic Performance,” *ACS Nano*, vol. 4, no. 6, pp. 3187–3194, Jun. 2010, doi: 10.1021/nn100740x.

[169] P. R. Garcês Gonçalves, H. A. De Abreu, and H. A. Duarte, “Stability, Structural, and Electronic Properties of Hausmannite (Mn 3 O 4) Surfaces and Their Interaction with Water,” *J. Phys. Chem. C*, vol. 122, no. 36, pp. 20841–20849, Sep. 2018, doi: 10.1021/acs.jpcc.8b06201.

[170] H. Wang *et al.*, “Mn 3 O 4 −Graphene Hybrid as a High-Capacity Anode Material for Lithium Ion Batteries,” *J. Am. Chem. Soc.*, vol. 132, no. 40, pp. 13978–13980, Oct. 2010, doi: 10.1021/ja105296a.

[171] M. Liang and X. Yan, “Nanozymes: From New Concepts, Mechanisms, and Standards to Applications,” *Acc. Chem. Res.*, vol. 52, no. 8, pp. 2190–2200, Aug. 2019, doi: 10.1021/acs.accounts.9b00140.

[172] J. Lu *et al.*, “Effectively suppressing dissolution of manganese from spinel lithium manganate via a nanoscale surface-doping approach,” *Nat. Commun.*, vol. 5, no. 1, p. 5693, Dec. 2014, doi: 10.1038/ncomms6693.

[173] Y. Liang *et al.*, “Covalent Hybrid of Spinel Manganese–Cobalt Oxide and Graphene as Advanced Oxygen Reduction Electrocatalysts,” *J. Am. Chem. Soc.*, vol. 134, no. 7, pp. 3517–3523, Feb. 2012, doi: 10.1021/ja210924t.

[174] P. Lavela, J. L. Tirado, and C. Vidal-Abarca, “Sol–gel preparation of cobalt manganese mixed oxides for their use as electrode materials in lithium cells,” *Electrochim. Acta*, vol. 52, no. 28, pp. 7986–7995, Nov. 2007, doi: 10.1016/j.electacta.2007.06.066.

[175] E. Rios, J.-L. Gautier, G. Poillerat, and P. Chartier, “Mixed valency spinel oxides of transition metals and electrocatalysis: case of the MnxCo3−xO4 system,” *Electrochim. Acta*, vol. 44, no. 8–9, pp. 1491–1497, Dec. 1998, doi: 10.1016/S0013-4686(98)00272-2.

[176] E. Vila, R. M. Rojas, J. L. Martín de Vidales, and O. García-Martínez, “Structural and Thermal Properties of the Tetragonal Cobalt Manganese Spinels Mn x Co 3 - x O 4 (1.4 < x < 2.0),” *Chem. Mater.*, vol. 8, no. 5, pp. 1078–1083, Jan. 1996, doi: 10.1021/cm950503h.

[177] C. Li, X. Han, F. Cheng, Y. Hu, C. Chen, and J. Chen, “Phase and composition controllable synthesis of cobalt manganese spinel nanoparticles towards efficient oxygen electrocatalysis,” *Nat. Commun.*, vol. 6, no. 1, p. 7345, Jun. 2015, doi: 10.1038/ncomms8345.

[178] A. S. Diez, S. Schlichter, V. Tomanech, E. V. P. Miner, M. Alvarez, and M. Dennehy, “Spinel manganites synthesized by combustion method: Structural characterization and catalytic activity in the oxidative degradation of organic pollutants,” *J. Environ.*

Chem. Eng., vol. 5, no. 4, pp. 3690–3697, Aug. 2017, doi: 10.1016/j.jece.2017.07.013.
[179] F. Yang *et al.*, “Interfacial engineering coupling with tailored oxygen vacancies in Co2Mn2O4 spinel hollow nanofiber for catalytic phenol removal,” *J. Hazard. Mater.*, vol. 424, p. 127647, Feb. 2022, doi: 10.1016/j.jhazmat.2021.127647.
[180] S. Wang *et al.*, “Mn-Co bimetallic spinel catalyst towards activation of peroxymonosulfate for deep mineralization of toluene: The key roles of SO4•- and O2•- in the ring-opening and mineralization of toluene,” *Chem. Eng. J.*, vol. 453, p. 139901, Feb. 2023, doi: 10.1016/j.cej.2022.139901.
[181] J. Sun *et al.*, “A Facile Strategy to Construct Amorphous Spinel-Based Electrocatalysts with Massive Oxygen Vacancies Using Ionic Liquid Dopant,” *Adv. Energy Mater.*, vol. 8, no. 27, Sep. 2018, doi: 10.1002/aenm.201800980.
[182] A. Dutta *et al.*, “Evolution of Spinel LiMn 2 O 4 Single Crystal Morphology Induced by the Li 2 MnO 3 Phase during Sintering,” *ACS Energy Lett.*, vol. 9, no. 3, pp. 888–895, Mar. 2024, doi: 10.1021/acsenergylett.3c02644.
[183] X. Liu *et al.*, “Hierarchical Zn x Co 3– x O 4 Nanoarrays with High Activity for Electrocatalytic Oxygen Evolution,” *Chem. Mater.*, vol. 26, no. 5, pp. 1889–1895, Mar. 2014, doi: 10.1021/cm4040903.
[184] D. U. Lee, J. Choi, K. Feng, H. W. Park, and Z. Chen, “Advanced Extremely Durable 3D Bifunctional Air Electrodes for Rechargeable Zinc-Air Batteries,” *Adv. Energy Mater.*, vol. 4, no. 6, Apr. 2014, doi: 10.1002/aenm.201301389.
[185] T. Peng, L. Xu, and H. Chen, “Preparation and characterization of high specific surface area Mn3O4 from electrolytic manganese residue,” *Open Chem.*, vol. 8, no. 5, pp. 1059–1068, Oct. 2010, doi: 10.2478/s11532-010-0081-4.
[186] M. Kang, E. D. Park, J. M. Kim, and J. E. Yie, “Manganese oxide catalysts for NOx reduction with NH3 at low temperatures,” *Appl. Catal. A Gen.*, vol. 327, no. 2, pp. 261–269, Aug. 2007, doi: 10.1016/j.apcata.2007.05.024.
[187] D. Wang, X. Chen, D. G. Evans, and W. Yang, “Well-dispersed Co3O4/Co2MnO4 nanocomposites as a synergistic bifunctional catalyst for oxygen reduction and oxygen evolution reactions,” *Nanoscale*, vol. 5, no. 12, p. 5312, 2013, doi: 10.1039/c3nr00444a.
[188] Q. Ni, J. Ma, C. Fan, Y. Kong, M. Peng, and S. Komarneni, “Spinel-type cobalt-manganese oxide catalyst for degradation of Orange II using a novel heterogeneous photo-chemical catalysis system,” *Ceram. Int.*, vol. 44, no. 16, pp. 19474–19480, Nov. 2018, doi: 10.1016/j.ceramint.2018.07.184.
[189] L. Zhang *et al.*, “Co–Mn spinel oxides trigger peracetic acid activation for ultrafast degradation of sulfonamide antibiotics: Unveiling critical role of Mn species in boosting Co activity,” *Water Res.*, vol. 229, p. 119462, Feb. 2023, doi: 10.1016/j.watres.2022.119462.
[190] S. Wang *et al.*, “Hydroxyl radical induced from hydrogen peroxide by cobalt manganese oxides for ciprofloxacin degradation,” *Chinese Chem. Lett.*, vol. 33, no. 12, pp. 5208–5212, Dec. 2022, doi: 10.1016/j.cclet.2022.01.055.
[191] S. Kang and J. Hwang, “CoMn2O4 embedded hollow activated carbon nanofibers as a novel peroxymonosulfate activator,” *Chem. Eng. J.*, vol. 406, p. 127158, Feb. 2021, doi: 10.1016/j.cej.2020.127158.
[192] C. Li, X. Han, F. Cheng, Y. Hu, C. Chen, and J. Chen, “Phase and composition controllable synthesis of cobalt manganese spinel nanoparticles towards efficient oxygen electrocatalysis,” *Nat. Commun.*, vol. 6, pp. 1–8, 2015, doi: 10.1038/ncomms8345.
[193] N. Garg, M. Mishra, Govind, and A. K. Ganguli, “Electrochemical and magnetic

properties of nanostructured CoMn2O4 and Co2MnO4," *RSC Adv.*, vol. 5, no. 103, pp. 84988–84998, 2015, doi: 10.1039/c5ra16937b.

[194] F. Xiang, X. Zhou, X. Yue, Q. Hu, Q. Zheng, and D. Lin, "An oxygen-deficient cobalt-manganese oxide nanowire doped with P designed for high performance asymmetric supercapacitor," *Electrochim. Acta*, vol. 379, p. 138178, May 2021, doi: 10.1016/j.electacta.2021.138178.

[195] R.-L. Zhang *et al.*, "Straw-like phosphorus-doped Co2MnO4 nanoneedle arrays supported on nickel foam for high-efficiency hydrogen evolution reaction in wide pH range of electrolytes," *Appl. Surf. Sci.*, vol. 548, p. 149280, May 2021, doi: 10.1016/j.apsusc.2021.149280.

[196] A. Khorsand Zak, W. H. Abd. Majid, M. E. Abrishami, and R. Yousefi, "X-ray analysis of ZnO nanoparticles by Williamson–Hall and size–strain plot methods," *Solid State Sci.*, vol. 13, no. 1, pp. 251–256, Jan. 2011, doi: 10.1016/j.solidstatesciences.2010.11.024.

[197] Q. Ni, J. Ma, C. Fan, Y. Kong, M. Peng, and S. Komarneni, "Spinel-type cobalt-manganese oxide catalyst for degradation of Orange II using a novel heterogeneous photo-chemical catalysis system," *Ceram. Int.*, vol. 44, no. 16, pp. 19474–19480, 2018, doi: 10.1016/j.ceramint.2018.07.184.

[198] M. A. Hassaan, M. R. Elkatory, M. A. El-Nemr, S. Ragab, and A. El Nemr, "Optimization strategy of Co3O4 nanoparticles in biomethane production from seaweeds and its potential role in direct electron transfer and reactive oxygen species formation," *Sci. Rep.*, vol. 14, no. 1, p. 5075, Mar. 2024, doi: 10.1038/s41598-024-55563-y.

[199] Y. Munaiah, B. G. Sundara Raj, T. Prem Kumar, and P. Ragupathy, "Facile synthesis of hollow sphere amorphous MnO2: the formation mechanism, morphology and effect of a bivalent cation-containing electrolyte on its supercapacitive behavior," *J. Mater. Chem. A*, vol. 1, no. 13, p. 4300, 2013, doi: 10.1039/c3ta01089a.

[200] Z. Wang, W. Wang, L. Zhang, and D. Jiang, "Surface oxygen vacancies on Co 3 O 4 mediated catalytic formaldehyde oxidation at room temperature," *Catal. Sci. Technol.*, vol. 6, no. 11, pp. 3845–3853, 2016, doi: 10.1039/C5CY01709B.

[201] A. Indra, P. W. Menezes, I. Zaharieva, H. Dau, and M. Driess, "Detecting structural transformation of cobalt phosphonate to active bifunctional catalysts for electrochemical water-splitting," *J. Mater. Chem. A*, vol. 8, no. 5, pp. 2637–2643, 2020, doi: 10.1039/C9TA09775A.

[202] P. W. Menezes *et al.*, "High-Performance Oxygen Redox Catalysis with Multifunctional Cobalt Oxide Nanochains: Morphology-Dependent Activity," *ACS Catal.*, vol. 5, no. 4, pp. 2017–2027, Apr. 2015, doi: 10.1021/cs501724v.

[203] C. A. Kent *et al.*, "Water Oxidation and Oxygen Monitoring by Cobalt-Modified Fluorine-Doped Tin Oxide Electrodes," *J. Am. Chem. Soc.*, vol. 135, no. 23, pp. 8432–8435, Jun. 2013, doi: 10.1021/ja400616a.

[204] B. Gnana Sundara Raj, A. M. Asiri, J. J. Wu, and S. Anandan, "Synthesis of Mn3O4 nanoparticles via chemical precipitation approach for supercapacitor application," *J. Alloys Compd.*, vol. 636, pp. 234–240, Jul. 2015, doi: 10.1016/j.jallcom.2015.02.164.

[205] Z.-Y. Tian, P. Mountapmbeme Kouotou, N. Bahlawane, and P. H. Tchoua Ngamou, "Synthesis of the Catalytically Active Mn 3 O 4 Spinel and Its Thermal Properties," *J. Phys. Chem. C*, vol. 117, no. 12, pp. 6218–6224, Mar. 2013, doi: 10.1021/jp312444s.

[206] J. Barreto, P. S. Bagus, and F. Stavale, "Multiplet XPS analysis of the Mn 2p for Mn 3 O 4 thin films," *J. Phys. Condens. Matter*, vol. 37, no. 4, p. 045001, Jan. 2025, doi: 10.1088/1361-648X/ad8b91.

[207] A. Lammini *et al.*, "Experimental and theoretical evaluation of synthetized cobalt oxide

for phenol adsorption: Adsorption isotherms, kinetics, and thermodynamic studies," *Arab. J. Chem.*, vol. 15, no. 12, p. 104364, Dec. 2022, doi: 10.1016/j.arabjc.2022.104364.

[208] R. Voda, "ADSORPTION PERFORMANCE OF CO3O4 IN THE REMOVAL PROCESS OF PHENOL AND LEAD FROM AQUEOUS SOLUTIONS," Nov. 2017. doi: 10.5593/sgem2017H/33/S12.003.

[209] S. A. Singh, B. Vemparala, and G. Madras, "Adsorption kinetics of dyes and their mixtures with Co 3 O 4 –ZrO 2 composites," *J. Environ. Chem. Eng.*, vol. 3, no. 4, pp. 2684–2696, Dec. 2015, doi: 10.1016/j.jece.2015.09.029.

[210] K. Kishore *et al.*, "Efficient removal of toxic dyes from water using Mn3O4 nanoparticles: Synthesis, characterization, and adsorption mechanisms," *J. Mol. Struct.*, vol. 1333, p. 141756, Jun. 2025, doi: 10.1016/j.molstruc.2025.141756.

[211] A. Chouchaine *et al.*, "SYNTHESIS, CHARACTERIZATION OF MN3O4: ADSORPTION APPLICATION AND ANTIBACTERIAL EVALUATION," *J. Chil. Chem. Soc.*, vol. 67, no. 3, pp. 5582–5586, Sep. 2022, doi: 10.4067/S0717-97072022000305582.

[212] T. Van Tran, D. T. C. Nguyen, P. S. Kumar, A. T. M. Din, A. S. Qazaq, and D.-V. N. Vo, "Green synthesis of Mn3O4 nanoparticles using Costus woodsonii flowers extract for effective removal of malachite green dye," *Environ. Res.*, vol. 214, p. 113925, Nov. 2022, doi: 10.1016/j.envres.2022.113925.

[213] M. Y. Nassar and S. Abdallah, "Facile controllable hydrothermal route for a porous CoMn 2 O 4 nanostructure: synthesis, characterization, and textile dye removal from aqueous media," *RSC Adv.*, vol. 6, no. 87, pp. 84050–84067, 2016, doi: 10.1039/C6RA12424K.

[214] H. Jiu *et al.*, "Hierarchical porous CoMn2O4 microspheres with sub-nanoparticles as advanced anode for high-performance lithium-ion batteries," *J. Solid State Electrochem.*, vol. 22, no. 9, pp. 2747–2755, Sep. 2018, doi: 10.1007/s10008-018-3987-y.

[215] S. Yang *et al.*, "Toward the Decentralized Electrochemical Production of H 2 O 2 : A Focus on the Catalysis," *ACS Catal.*, vol. 8, no. 5, pp. 4064–4081, May 2018, doi: 10.1021/acscatal.8b00217.

[216] Z. Zhao and P. K. Shen, "Mechanism of Oxygen Reduction Reaction," in *Electrochemical Oxygen Reduction*, Singapore: Springer Singapore, 2021, pp. 11–27. doi: 10.1007/978-981-33-6077-8_2.

[217] Y. Jiang *et al.*, "Selective Electrochemical H 2 O 2 Production through Two-Electron Oxygen Electrochemistry," *Adv. Energy Mater.*, vol. 8, no. 31, Nov. 2018, doi: 10.1002/aenm.201801909.

[218] E. Yeager, "Electrocatalysts for O2 reduction," *Electrochim. Acta*, vol. 29, no. 11, pp. 1527–1537, Nov. 1984, doi: 10.1016/0013-4686(84)85006-9.

[219] P. S. Ruvinskiy, A. Bonnefont, C. Pham-Huu, and E. R. Savinova, "Using Ordered Carbon Nanomaterials for Shedding Light on the Mechanism of the Cathodic Oxygen Reduction Reaction," *Langmuir*, vol. 27, no. 14, pp. 9018–9027, Jul. 2011, doi: 10.1021/la2006343.

[220] J. K. Nørskov *et al.*, "Origin of the Overpotential for Oxygen Reduction at a Fuel-Cell Cathode," *J. Phys. Chem. B*, vol. 108, no. 46, pp. 17886–17892, Nov. 2004, doi: 10.1021/jp047349j.

[221] A. Byeon, W. C. Yun, J. M. Kim, and J. W. Lee, "Non-precious Metal Catalysts for Two-Electron Oxygen Reduction Reaction," *ChemElectroChem*, vol. 10, no. 17, Sep. 2023, doi: 10.1002/celc.202300234.

[222] M. Shao, Q. Chang, J.-P. Dodelet, and R. Chenitz, “Recent Advances in Electrocatalysts for Oxygen Reduction Reaction,” *Chem. Rev.*, vol. 116, no. 6, pp. 3594–3657, Mar. 2016, doi: 10.1021/acs.chemrev.5b00462.

[223] X. Guo, S. Lin, J. Gu, S. Zhang, Z. Chen, and S. Huang, “Simultaneously Achieving High Activity and Selectivity toward Two-Electron O 2 Electroreduction: The Power of Single-Atom Catalysts,” *ACS Catal.*, vol. 9, no. 12, pp. 11042–11054, Dec. 2019, doi: 10.1021/acscatal.9b02778.

[224] R. Bashyam and P. Zelenay, “A class of non-precious metal composite catalysts for fuel cells,” *Nature*, vol. 443, no. 7107, pp. 63–66, Sep. 2006, doi: 10.1038/nature05118.

[225] M. Lefèvre, E. Proietti, F. Jaouen, and J.-P. Dodelet, “Iron-Based Catalysts with Improved Oxygen Reduction Activity in Polymer Electrolyte Fuel Cells,” *Science (80-.).*, vol. 324, no. 5923, pp. 71–74, Apr. 2009, doi: 10.1126/science.1170051.

[226] E. Jung *et al.*, “Atomic-level tuning of Co–N–C catalyst for high-performance electrochemical H2O2 production,” *Nat. Mater.*, vol. 19, no. 4, pp. 436–442, Apr. 2020, doi: 10.1038/s41563-019-0571-5.

[227] Z. Lu *et al.*, “High-efficiency oxygen reduction to hydrogen peroxide catalysed by oxidized carbon materials,” *Nat. Catal.*, vol. 1, no. 2, pp. 156–162, Jan. 2018, doi: 10.1038/s41929-017-0017-x.

[228] K.-H. Wu *et al.*, “Highly Selective Hydrogen Peroxide Electrosynthesis on Carbon: In Situ Interface Engineering with Surfactants,” *Chem*, vol. 6, no. 6, pp. 1443–1458, Jun. 2020, doi: 10.1016/j.chempr.2020.04.002.

[229] J. Biemolt, K. van der Veen, N. J. Geels, G. Rothenberg, and N. Yan, “Efficient oxygen reduction to H2O2 in highly porous manganese and nitrogen co-doped carbon nanorods enabling electro-degradation of bulk organics,” *Carbon N. Y.*, vol. 155, pp. 643–649, Dec. 2019, doi: 10.1016/j.carbon.2019.09.034.

[230] S. Kumar *et al.*, “Electrochemical Sensors and Biosensors Based on Graphene Functionalized with Metal Oxide Nanostructures for Healthcare Applications,” *ChemistrySelect*, vol. 4, no. 18, pp. 5322–5337, May 2019, doi: 10.1002/slct.201803871.

[231] S. Raja, V. Ramesh, and V. Thivaharan, “Green biosynthesis of silver nanoparticles using Calliandra haematocephala leaf extract, their antibacterial activity and hydrogen peroxide sensing capability,” *Arab. J. Chem.*, vol. 10, no. 2, pp. 253–261, Feb. 2017, doi: 10.1016/j.arabjc.2015.06.023.

[232] H. Liu, L. Weng, and C. Yang, “A review on nanomaterial-based electrochemical sensors for H2O2, H2S and NO inside cells or released by cells,” *Microchim. Acta*, vol. 184, no. 5, pp. 1267–1283, May 2017, doi: 10.1007/s00604-017-2179-2.

[233] P. A. Rock, “The Standard Oxidation Potential of the Ferrocyanide-Ferricyanide Electrode at 25° and the Entropy of Ferrocyanide Ion,” *J. Phys. Chem.*, vol. 70, no. 2, pp. 576–580, Feb. 1966, doi: 10.1021/j100874a042.

[234] F. Si *et al.*, “Electrochemical Oxygen Reduction Reaction,” in *Rotating Electrode Methods and Oxygen Reduction Electrocatalysts*, Elsevier, 2014, pp. 133–170. doi: 10.1016/B978-0-444-63278-4.00004-5.

[235] H. Karimi-Maleh *et al.*, “Nanochemistry approach for the fabrication of Fe and N co-decorated biomass-derived activated carbon frameworks: a promising oxygen reduction reaction electrocatalyst in neutral media,” *J. Nanostructure Chem.*, vol. 12, no. 3, pp. 429–439, Jun. 2022, doi: 10.1007/s40097-022-00492-3.

[236] F. Wu *et al.*, “Single-Atom Co–N 4 Electrocatalyst Enabling Four-Electron Oxygen Reduction with Enhanced Hydrogen Peroxide Tolerance for Selective Sensing,” *J. Am.*

Chem. Soc., vol. 142, no. 39, pp. 16861–16867, Sep. 2020, doi: 10.1021/jacs.0c07790.

[237] Z. Wang *et al.*, “Cobalt-Embedded Nitrogen Doped Carbon Nanotubes: A Bifunctional Catalyst for Oxygen Electrode Reactions in a Wide pH Range,” *ACS Appl. Mater. Interfaces*, vol. 7, no. 7, pp. 4048–4055, Feb. 2015, doi: 10.1021/am507744y.

[238] H. Zhang, C. Lin, L. Sepunaru, C. Batchelor-McAuley, and R. G. Compton, “Oxygen reduction in alkaline solution at glassy carbon surfaces and the role of adsorbed intermediates,” *J. Electroanal. Chem.*, vol. 799, pp. 53–60, Aug. 2017, doi: 10.1016/j.jelechem.2017.05.037.

[239] Y. Liang *et al.*, “Co3O4 nanocrystals on graphene as a synergistic catalyst for oxygen reduction reaction,” *Nat. Mater.*, vol. 10, no. 10, pp. 780–786, Oct. 2011, doi: 10.1038/nmat3087.

[240] Y. Liang *et al.*, “Oxygen Reduction Electrocatalyst Based on Strongly Coupled Cobalt Oxide Nanocrystals and Carbon Nanotubes,” *J. Am. Chem. Soc.*, vol. 134, no. 38, pp. 15849–15857, Sep. 2012, doi: 10.1021/ja305623m.

[241] Y. Wang *et al.*, “Reduced Mesoporous Co 3 O 4 Nanowires as Efficient Water Oxidation Electrocatalysts and Supercapacitor Electrodes,” *Adv. Energy Mater.*, vol. 4, no. 16, Nov. 2014, doi: 10.1002/aenm.201400696.

[242] V. K. Singh, P. Singh, M. Karmakar, J. Leta, and P. Mayr, “The journal coverage of Web of Science, Scopus and Dimensions: A comparative analysis,” *Scientometrics*, vol. 126, no. 6, pp. 5113–5142, Jun. 2021, doi: 10.1007/s11192-021-03948-5.

[243] L. G. Cançado *et al.*, “Quantifying Defects in Graphene via Raman Spectroscopy at Different Excitation Energies,” *Nano Lett.*, vol. 11, no. 8, pp. 3190–3196, Aug. 2011, doi: 10.1021/nl201432g.

[244] R. D. Shannon, “Revised effective ionic radii and systematic studies of interatomic distances in halides and chalcogenides,” *Acta Crystallogr. Sect. A*, vol. 32, no. 5, pp. 751–767, Sep. 1976, doi: 10.1107/S0567739476001551.

Appendices

Supporting Information – Chapter 3

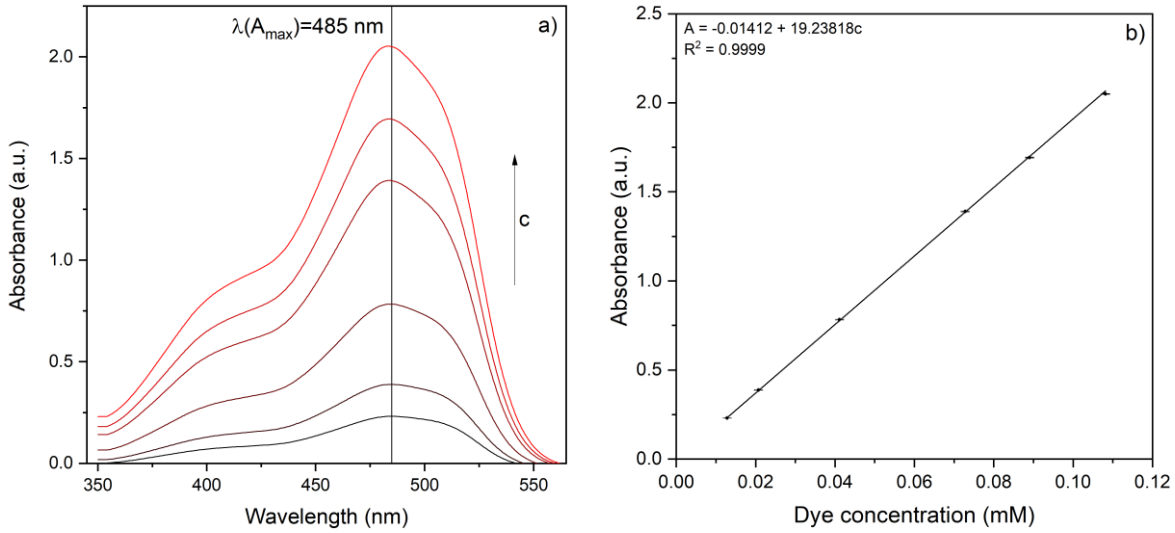

Supplementary figure 1 – **a:** Relevant sections of high resolution UV-Vis spectra of AO7 solutions at certain dye concentrations; **b:** UV-Vis calibration curve for AO7 in water.

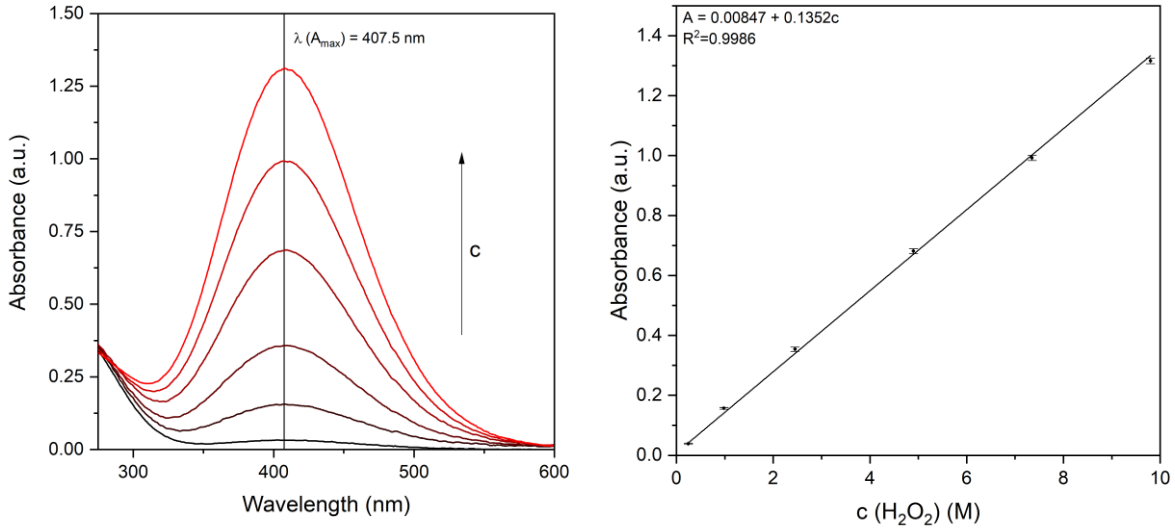

Supplementary figure 2 – **a:** Relevant section of high resolution UV-Vis spectrum for aqueous, acidic $[Ti(O_2)SO_4]^{2+}$ solutions, which form during the determination of H_2O_2 concentration; **b:** calibration curve for the determination of H_2O_2 concentration using the $TiOSO_4$ method.

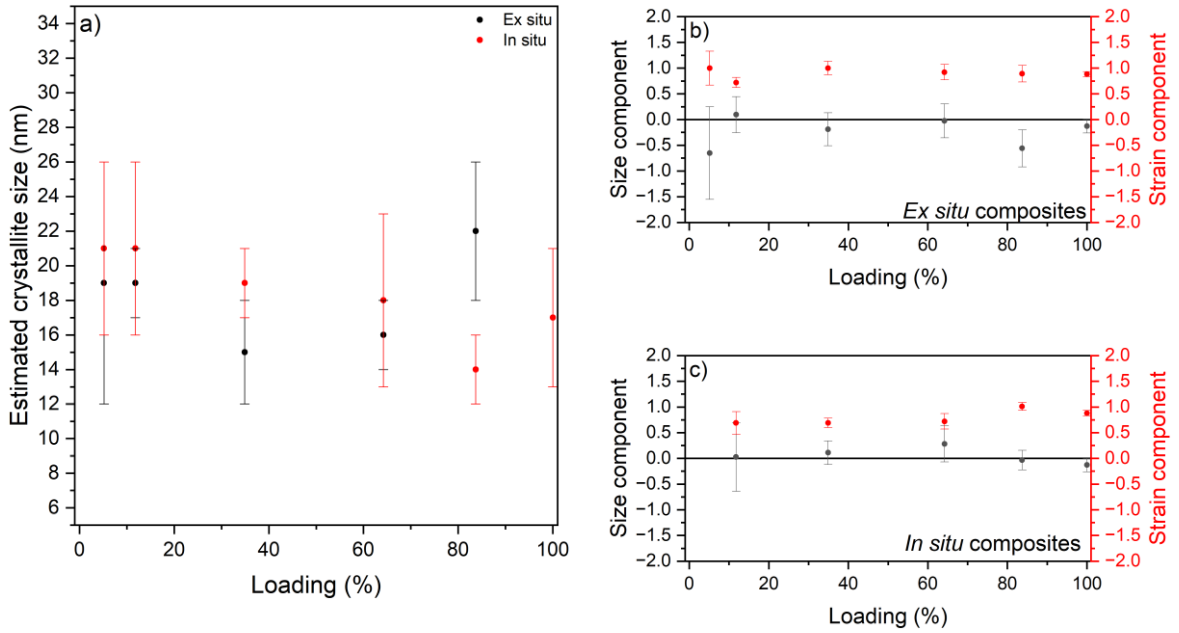

Supplementary figure 3 – Secondary analysis of XRD results for both types of composites; **a:** Crystallite sizes estimated with the Scherrer-method; **b,c:** Results of Williamson-Hall analysis.

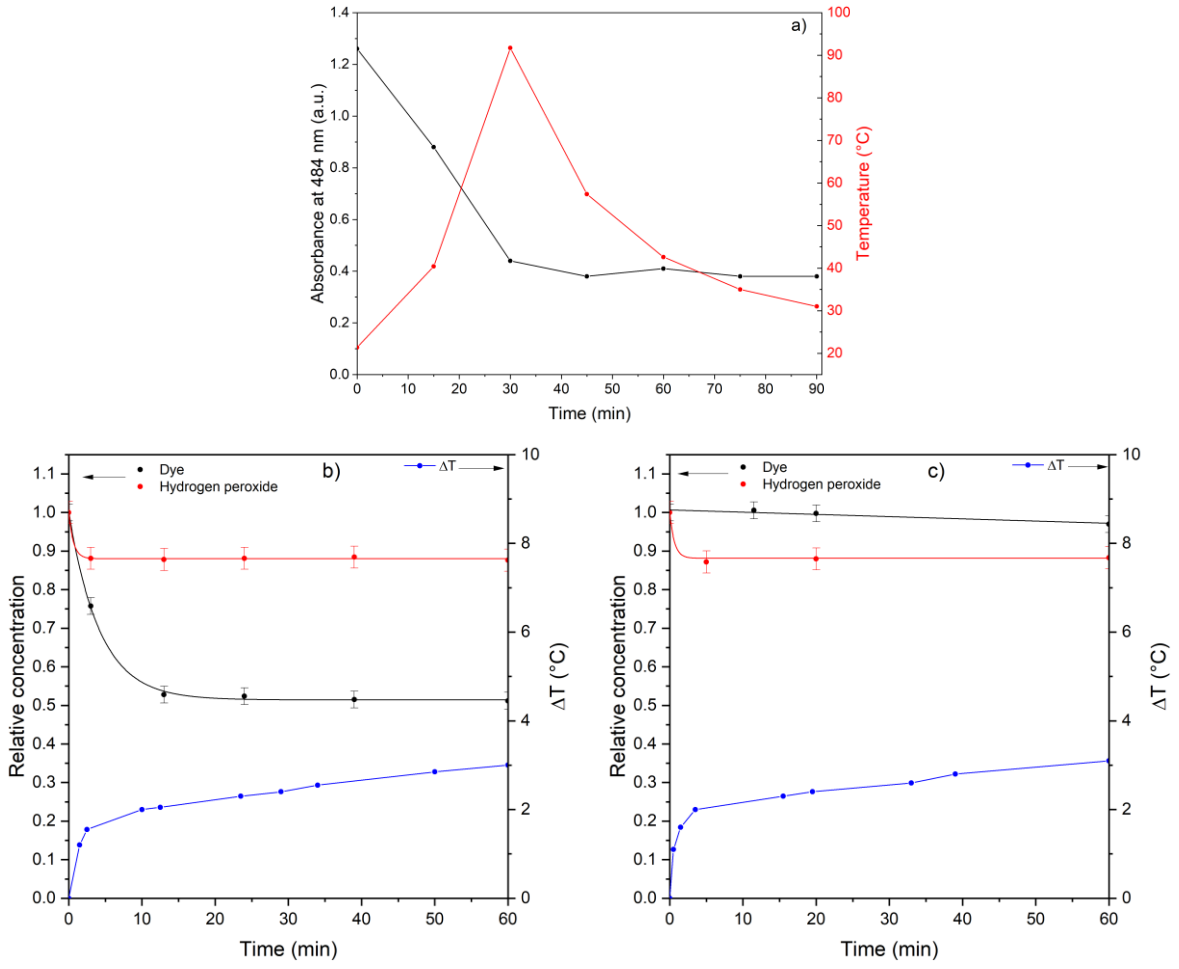

Supplementary figure 4 – Kinetic curves for control dye degradation experiments; **a:** Kinetic curve for the degradation of AO7 by 1.0 mg/mL MnO_2 with no heat sink; **b:** Experiment with 0.6 mg/mL GNF and no H_2O_2; **c:** Experiment with no catalyst or GNF added.

The large heat sink around the reaction vessel made sure that all reactions started from roughly the same temperature, which was 18 °C. There are small differences between starting temperature, but to make the graphs easier to compare ΔT is shown instead of T.

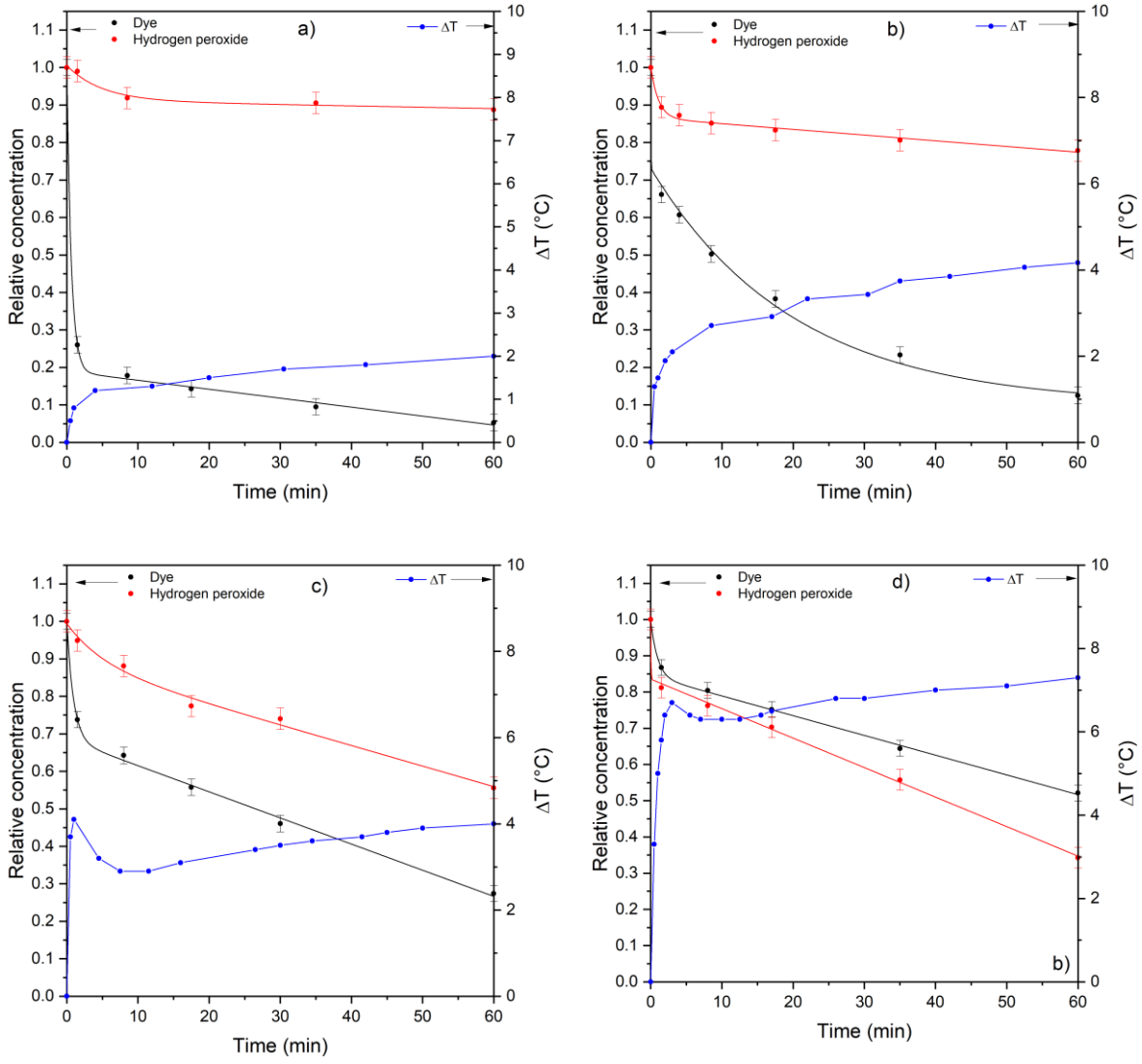

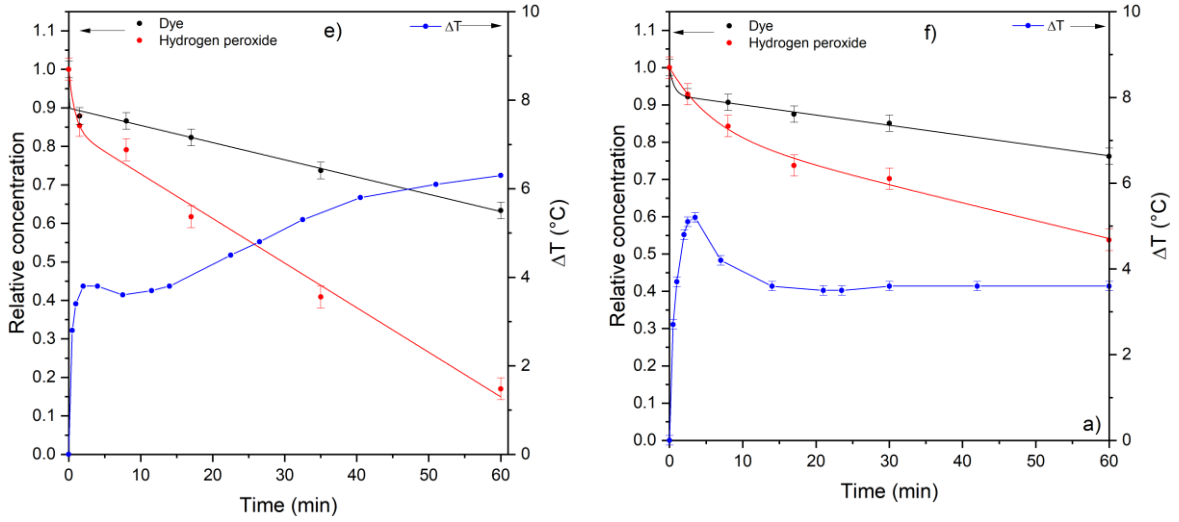

Supplementary figure 5 – Kinetic curves for all composites and for 100% MnO_2; MnO_2 loadings on GNF: **a:** 5.2%, **b:** 11.8%, **c:** 34.9%, **d:** 64.2%, **e:** 83.7%, **f:** 100% MnO_2.

Supporting Information – Chapter 4

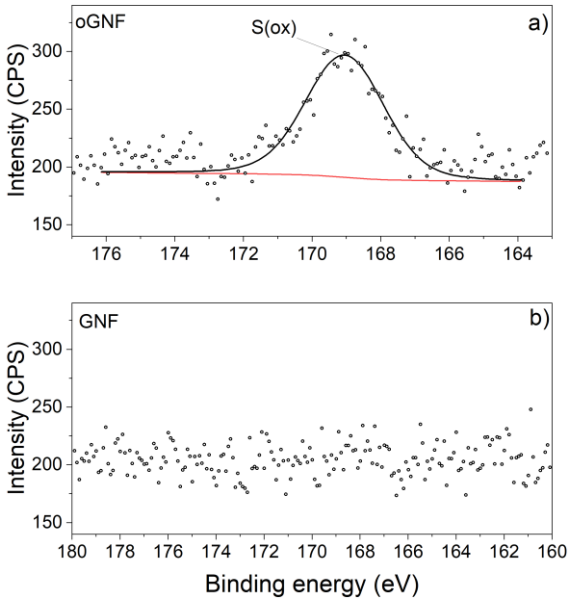

Supplementary figure 6 – High resolution XPS spectra of the S 2p region for GNF, and oGNF.

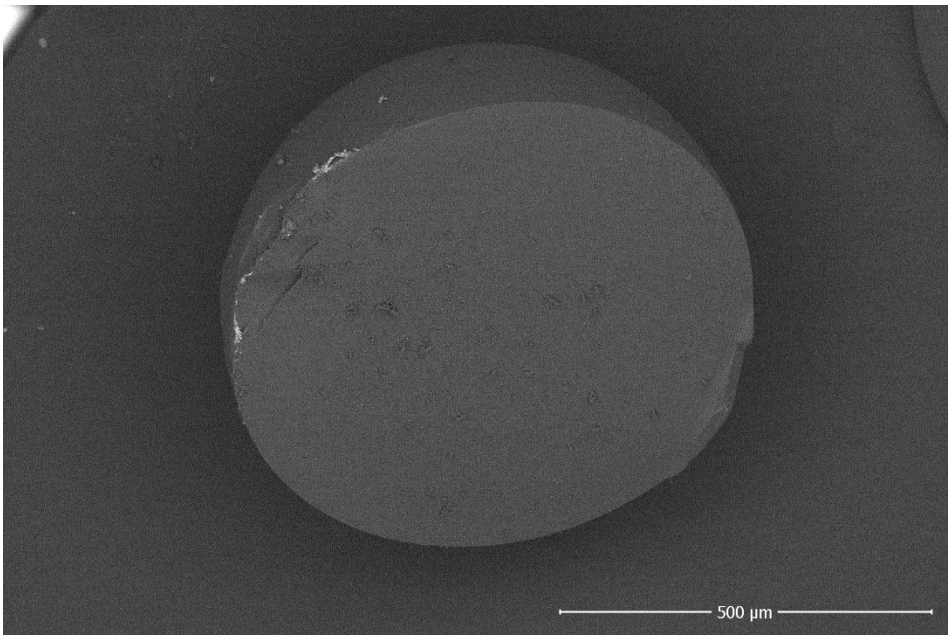

Supplementary figure 7 – SEM image of an untreated bead cracked in half; Image recorded from backscattered electrons.

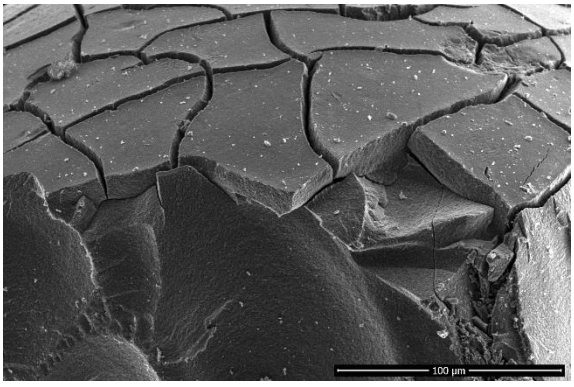

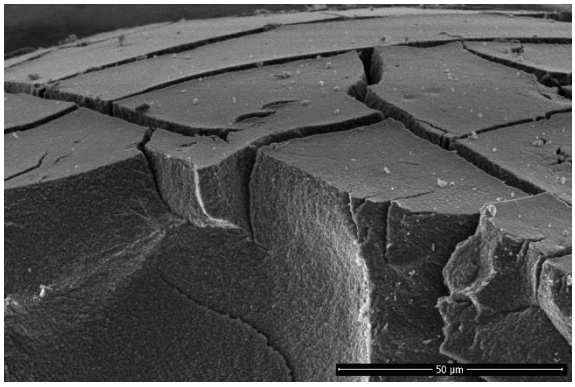

Supplementary figure 8 – SEM images of acid oxidised beads cracked in half.

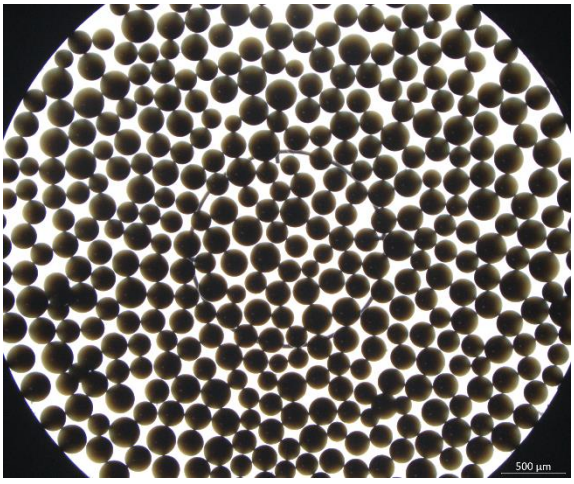

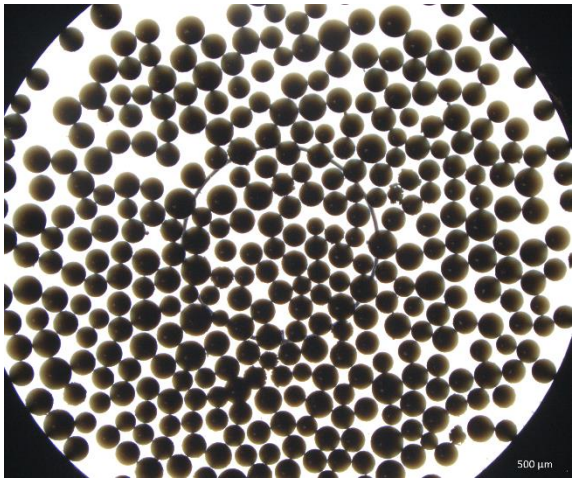

Supplementary figure 9 – Light microscope images that serve as examples of what was used for the generation of diameter distribution; Left: Image of CB; Right: Image of oCB.

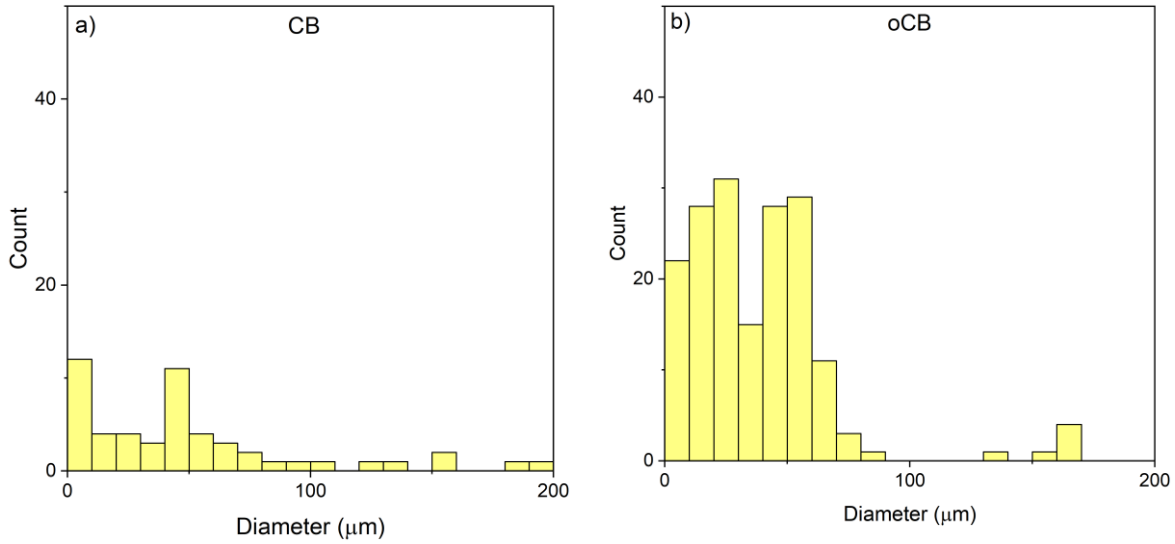

Supplementary figure 10 – Size distribution of particles below 200 μm from light microscopy images for: **a:** CB, and **b:** oCB.

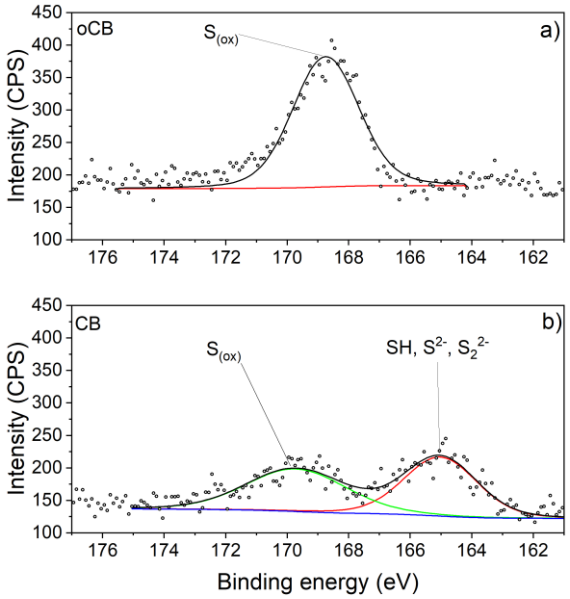

Supplementary figure 11 – High resolution XPS spectra for CB and oCB in the S 2p region.

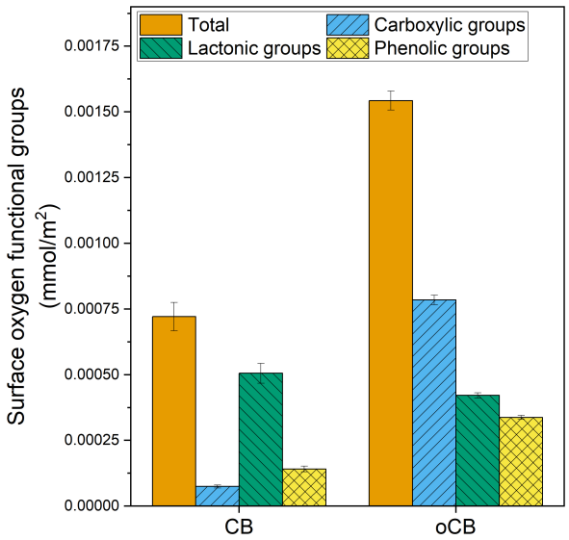

Supplementary figure 12 – Results of Boehm-titration for CB and oCB in mmol/m^2 unit.

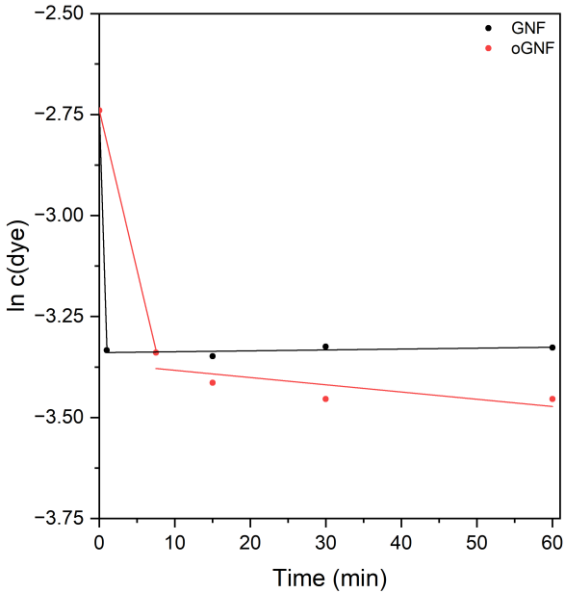

Supplementary figure 13 – Kinetic curves for GNF and oGNF, assuming adsorption follows a pseudo-first order kinetics.

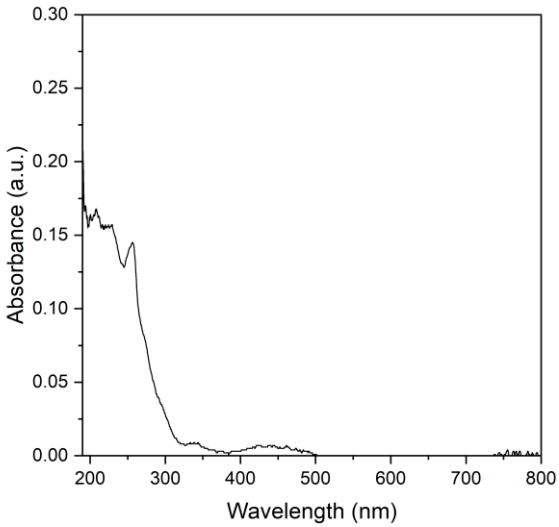

Supplementary figure 14 – UV-Vis spectrum of 1.5 mM 1-amino-2-naphthol stock solution.

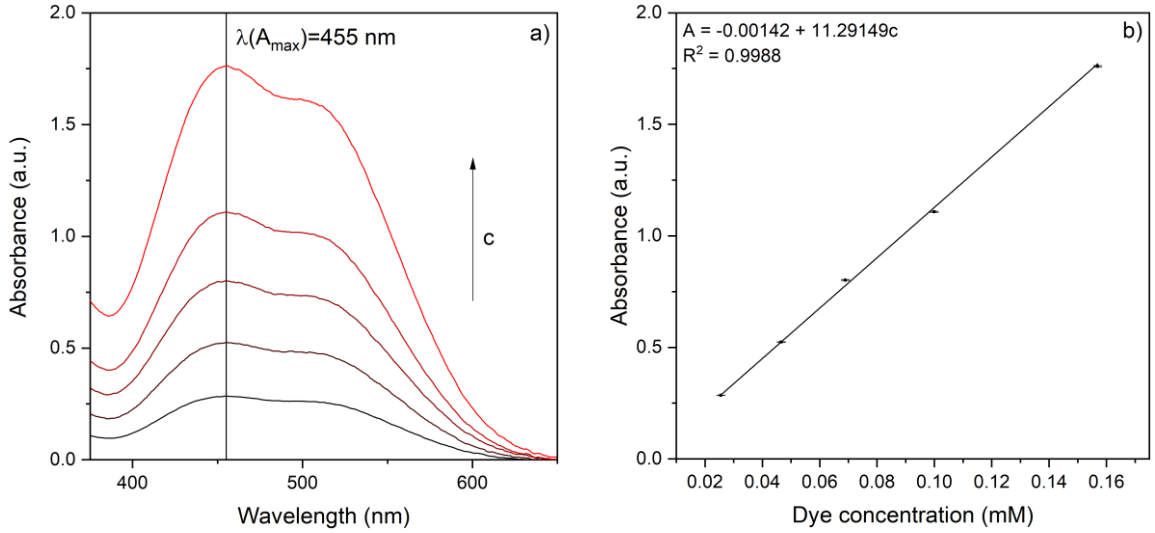

Supplementary figure 15 – **a:** Relevant sections of high resolution UV-Vis spectra of AO7 solutions at pH=14; **b:** UV-Vis calibration curve for AO7 at pH=14.

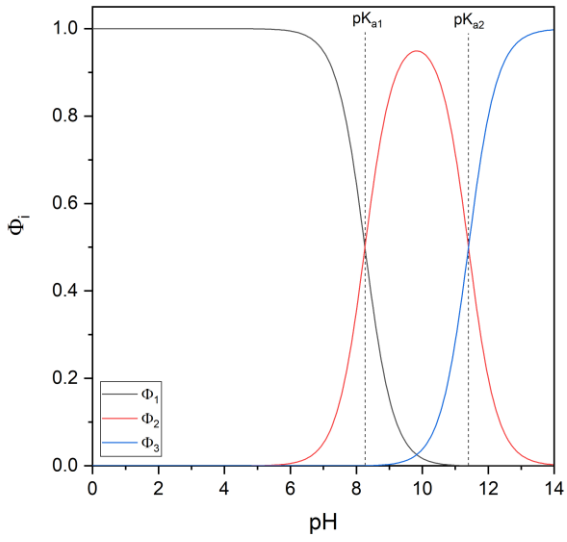

Supplementary figure 16 – Partial more fraction diagram of AO7 (AO7) versus pH where ϕ_1 refers to $H_2[AO7]$, ϕ_2 to $H[AO7]^+$, and ϕ_3 to $[AO7]^{2+}$.

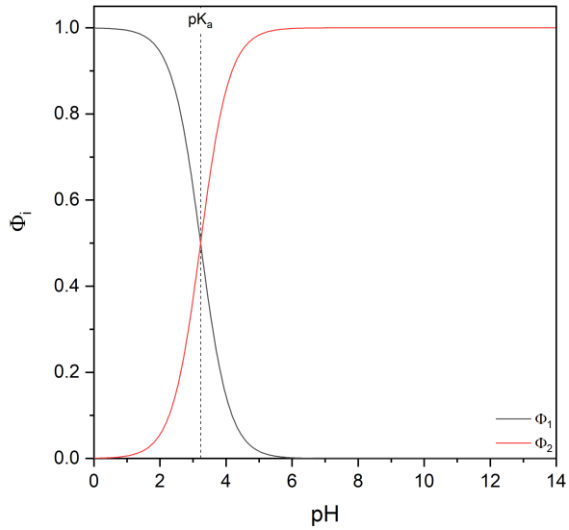

Supplementary figure 17 - Partial more fraction diagram of sulfanilic acid (SA) versus pH where ϕ_1 refers to H[SA], ϕ_2 to $[SA]^+$.

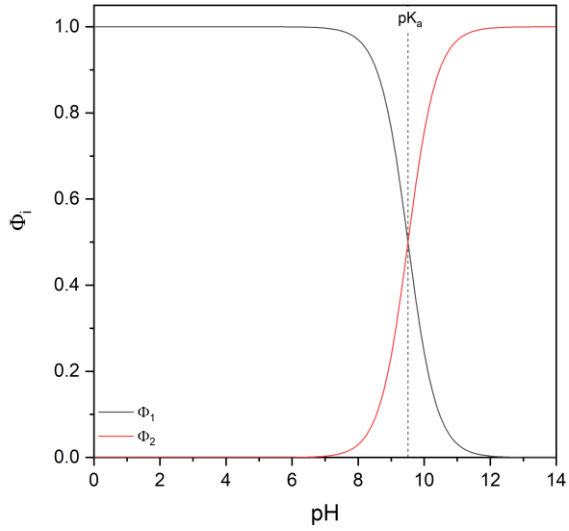

Supplementary figure 18 - Partial more fraction diagram of 2-naphthol (2-N) versus pH where ϕ_1 refers to H[2-N], ϕ_2 to $[2\text{-}N]^+$.

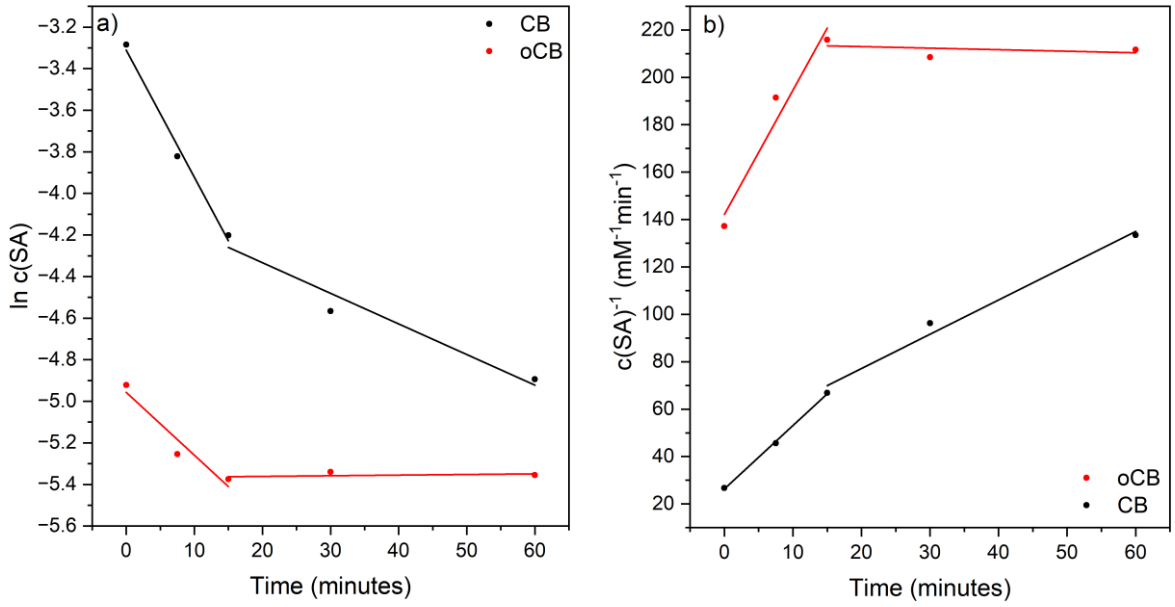

Supplementary figure 19 – Kinetic curves for the adsorption of SA on CB and oCB; **a:** Interpretation of the reactions as following pseudo-first order kinetics; **b:** Interpretation of the reactions as following pseudo-second order kinetics.

Supporting Information – Chapter 5

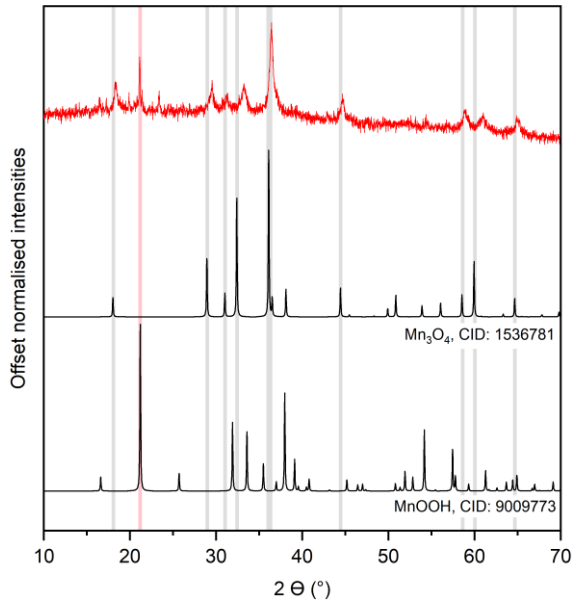

Supplementary figure 20 – XRD pattern of an early spinel produced through open air, open vessel oxidation as the second step.

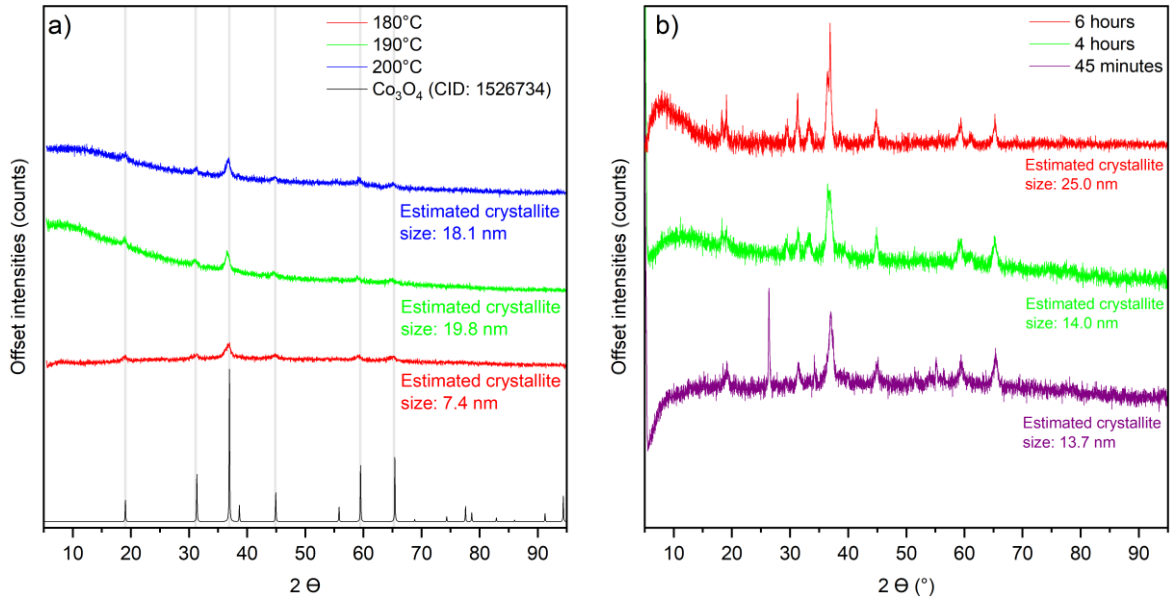

Supplementary figure 21 – XRD patterns of early spinels produced during the optimisation of the synthesis. **a:** Cubic Co_2MnO_4 samples made using different hydrothermal temperatures; **b:** Tetragonal Co_2MnO_4 samples produced via different duration hydrothermal treatments.

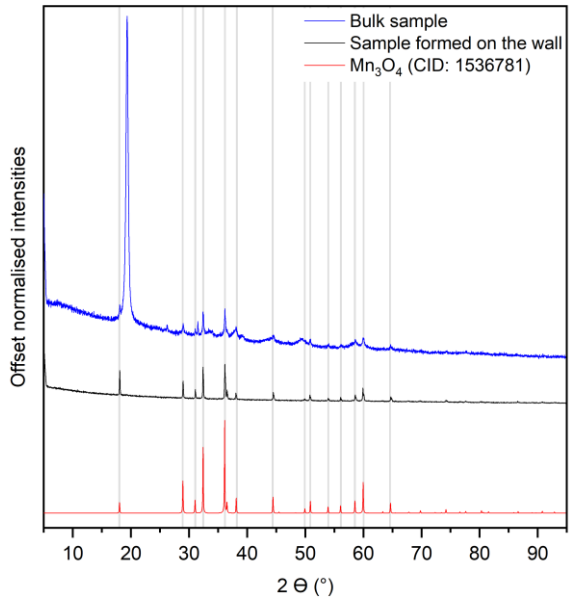

Supplementary figure 22 – XRD pattern of early Mn_3O_4 samples.

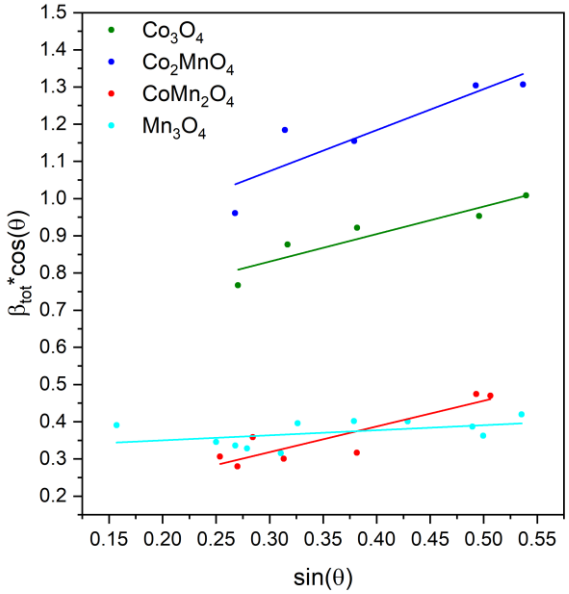

Supplementary figure 23 – Williamson-Hall plots of all four Co, Mn spinels.

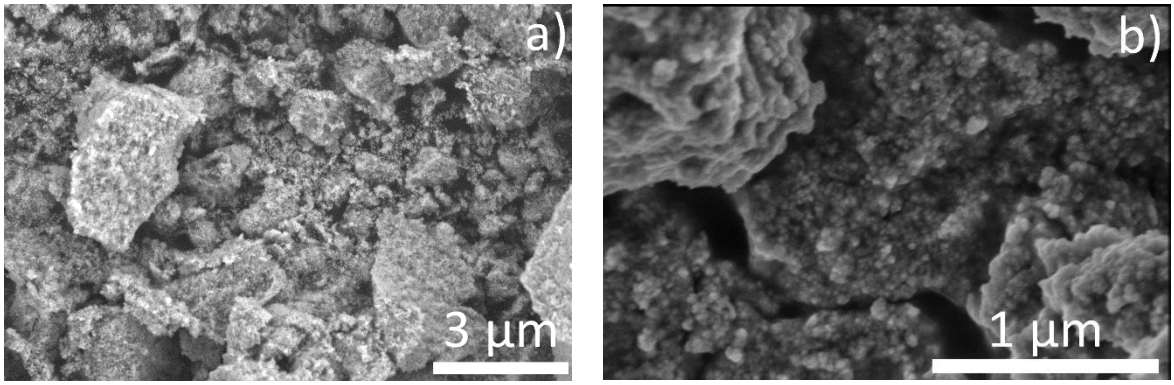

Supplementary figure 24 – SEM images of Co_3O_4 samples

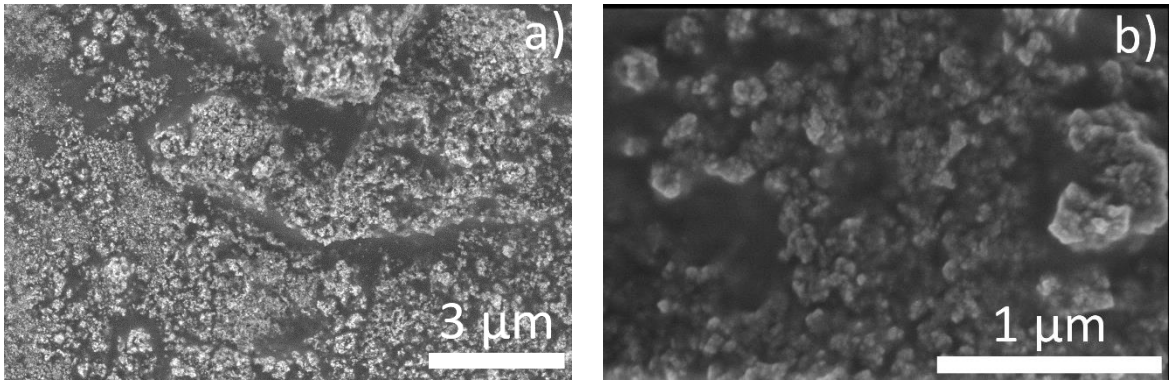

Supplementary figure 25 – SEM images of Co_2MnO_4 samples

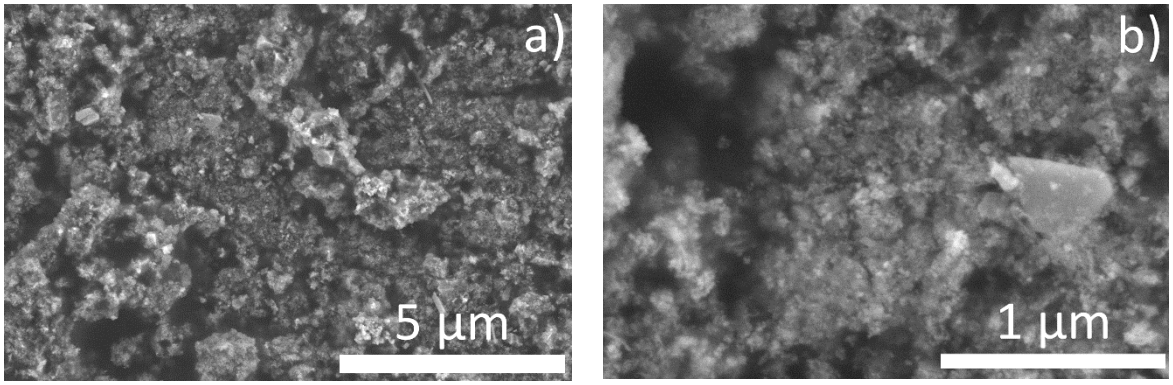

Supplementary figure 26 – SEM images of $CoMn_2O_4$ samples

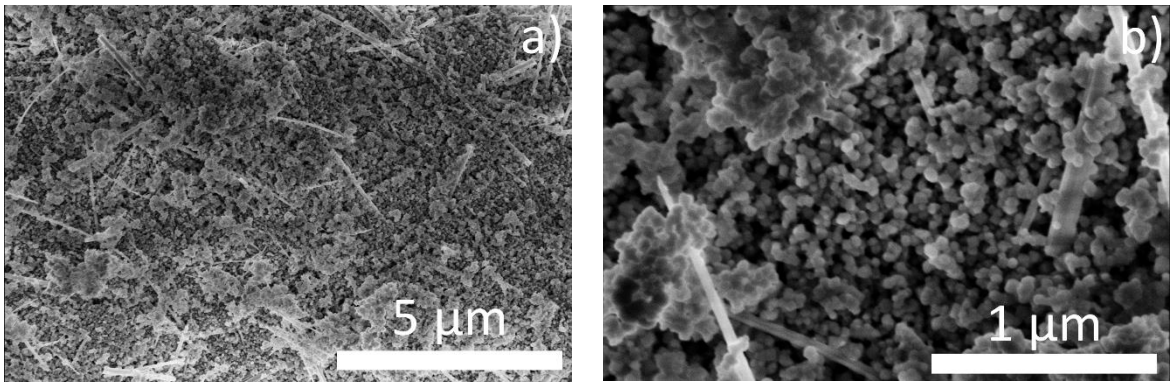

Supplementary figure 27 – SEM images of Mn_3O_4 samples

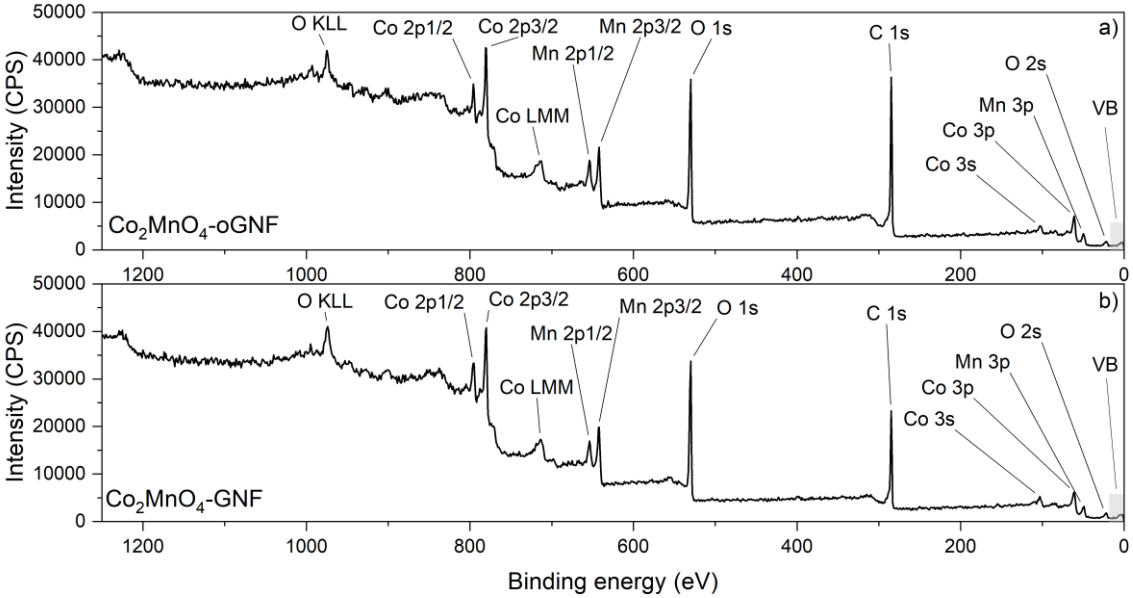

Supplementary figure 28 – Survey XPS spectra of Co_2MnO_4-GNF and Co_2MnO_4-oGNF.

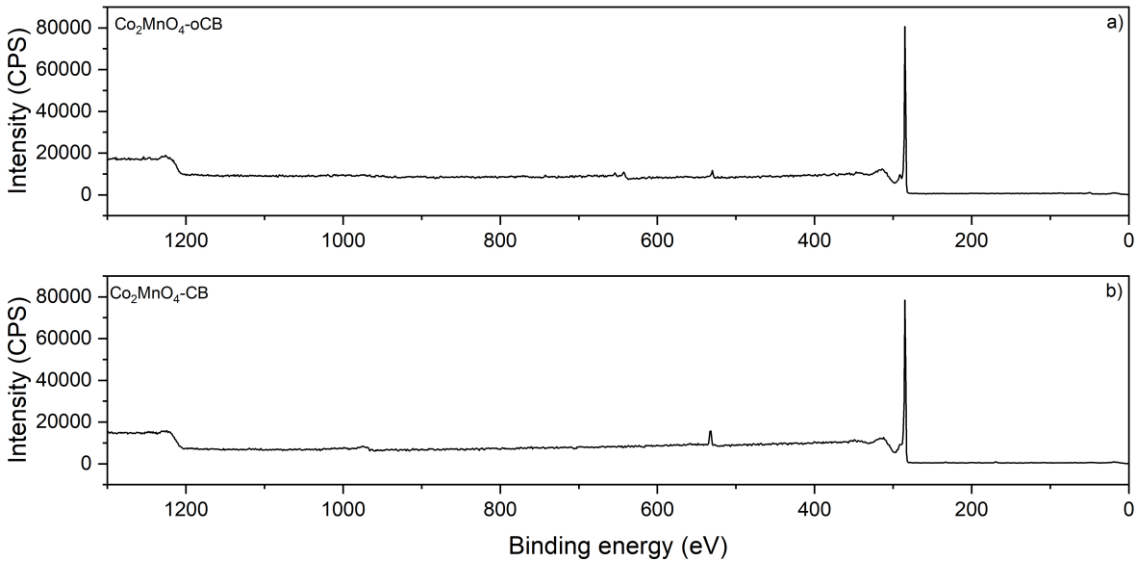

Supplementary figure 29 – Survey XPS spectra of 28.6% Co_2MnO_4-CB and 23.6% Co_2MnO_4-oCB collected using a UHV XPS instrument.

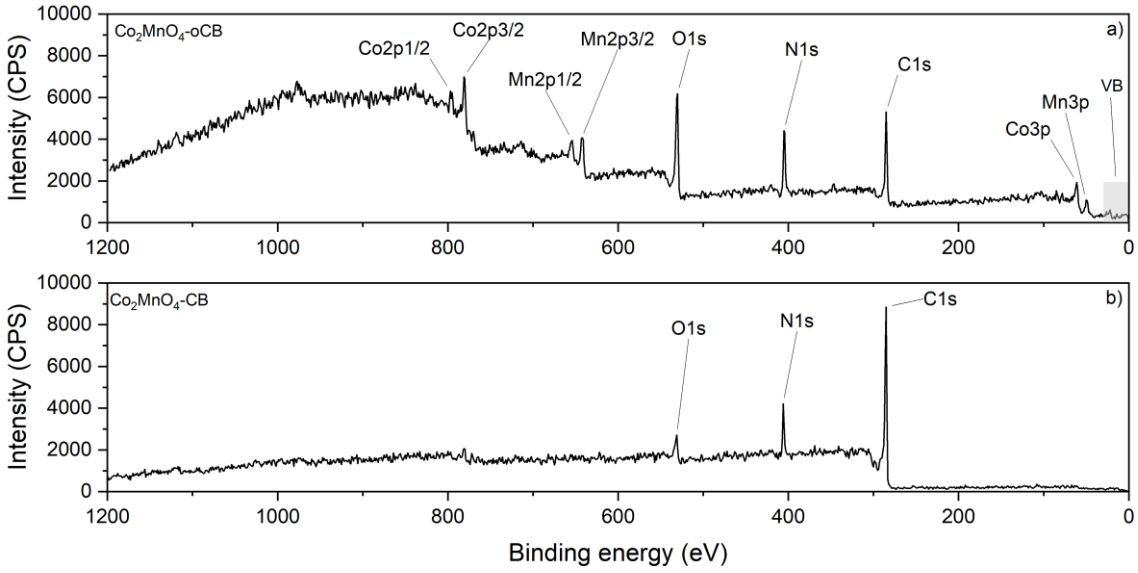

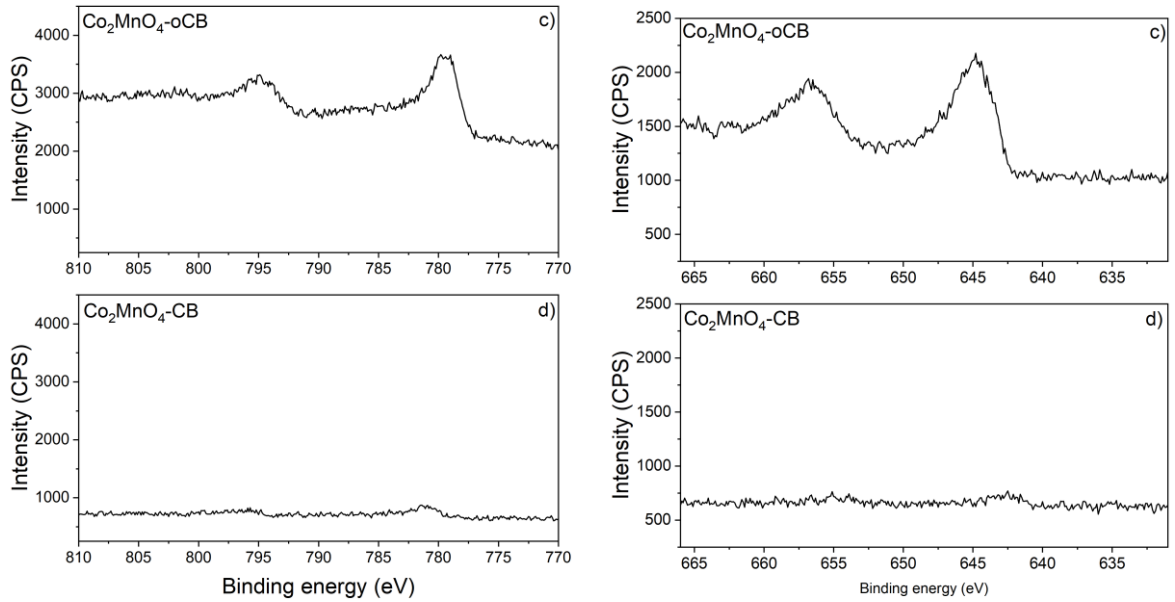

Supplementary figure 30 – XPS spectra of 28.6% Co_2MnO_4-CB and 28.6% Co_2MnO_4-oCB composites collected using a NAP XPS; **a,b:** Survey spectra of Co_2MnO_4-CB and Co_2MnO_4-oCB composites respectively; **c,d:** High resolution Co 2p spectrum of Co_2MnO_4-oCB and Co_2MnO_4-oCB composites respectively; **e,f**: High resolution Mn 2p spectrum of Co_2MnO_4-oCB and Co_2MnO_4-oCB composites respectively

The presence of a N 1s peak is explained by the N_2 gas used to set the pressure in the analysis chamber.

Absorbances at 310 nm were used as a proxy for further organics degradation. In the absence of a known molar absorptivity it was not possible to calculate instantaneous concentrations and by extension k values. Instead the slope of the decrease in absorbance was used, noted –dA/dt. This metric shows only small differences between individual composites, which likely means that the removal of further degradation products happens to a similar extent in all cases. Nonetheless these graphs are shown on Supplementary figure 32, Supplementary figure 35, Supplementary figure 38 and Supplementary figure 41.

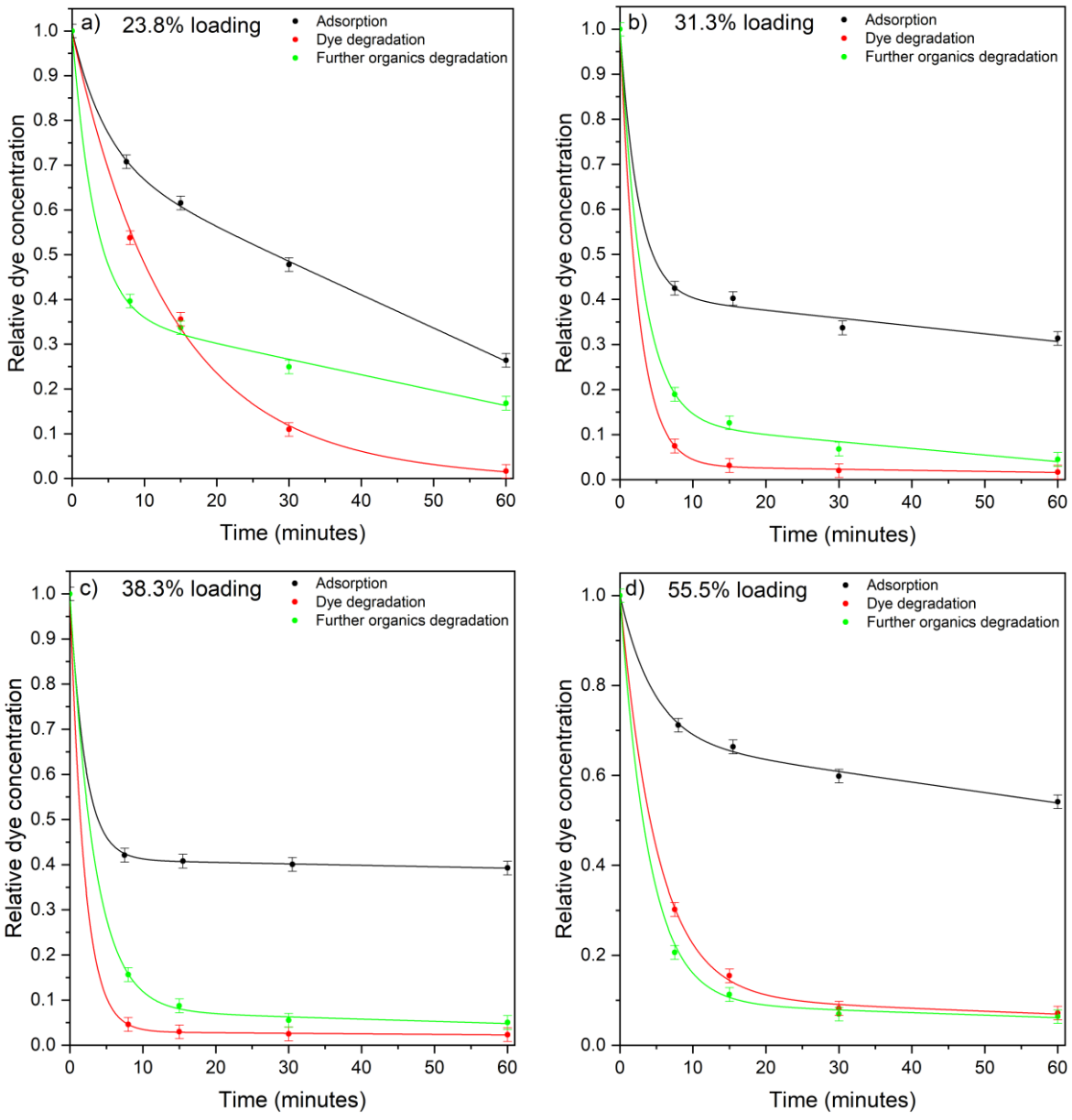

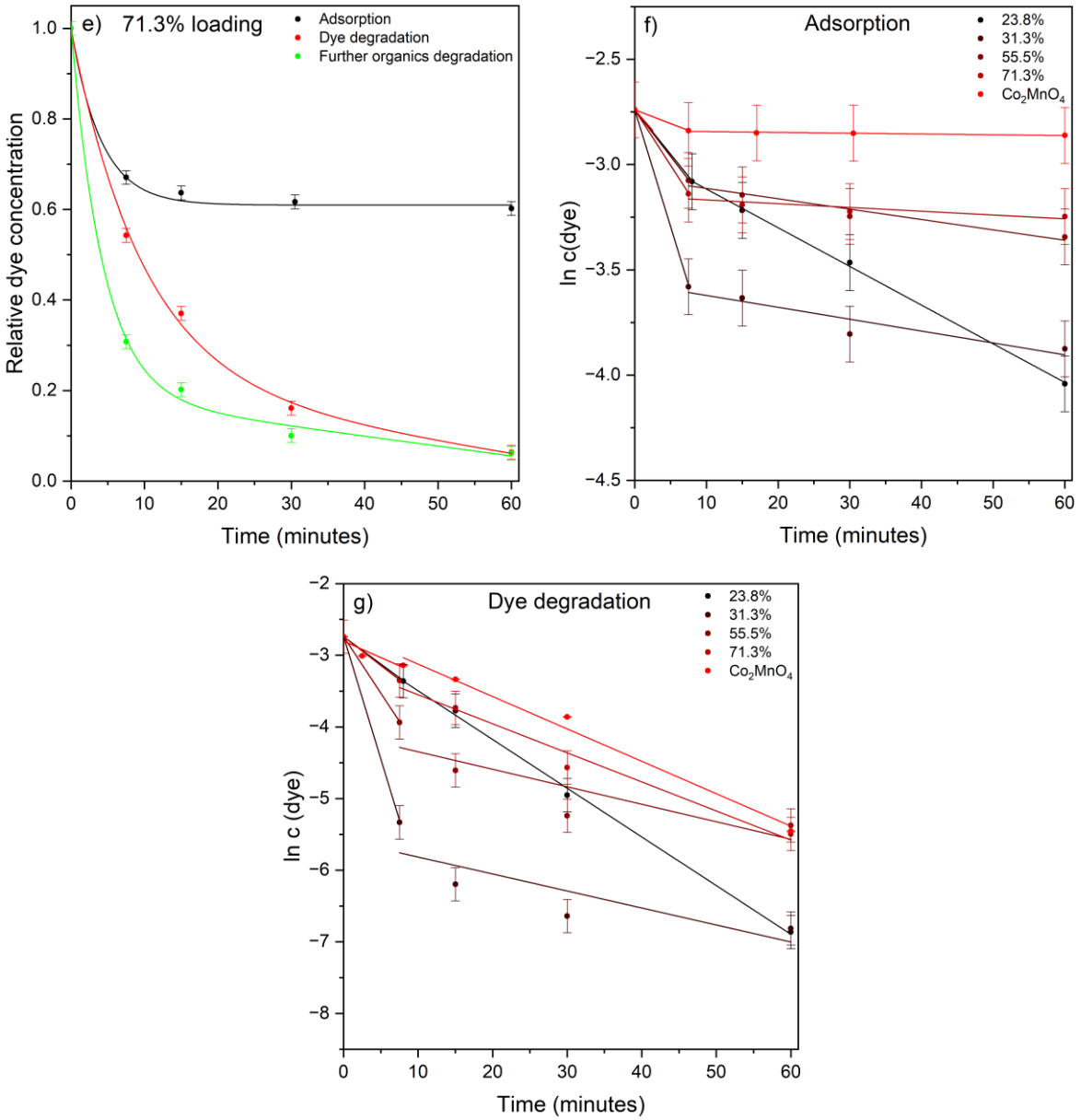

Supplementary figure 31 – Kinetic curves for Co_2MnO_4-GNF composites of different catalyst loadings showing the relative dye concentrations versus time in adsorption and dye degradation experiments; **a:** 23.8% loading, **b:** 31.3% loading; **c:** 38.3% loading; **d:** 55.5% loading; **e:** 71.3% loading; **f:** Summary of ln c(dye) vs time curves for adsorption on all composites; **g:** Summary of ln c(dye) vs time curves for dye degradation on all composites.

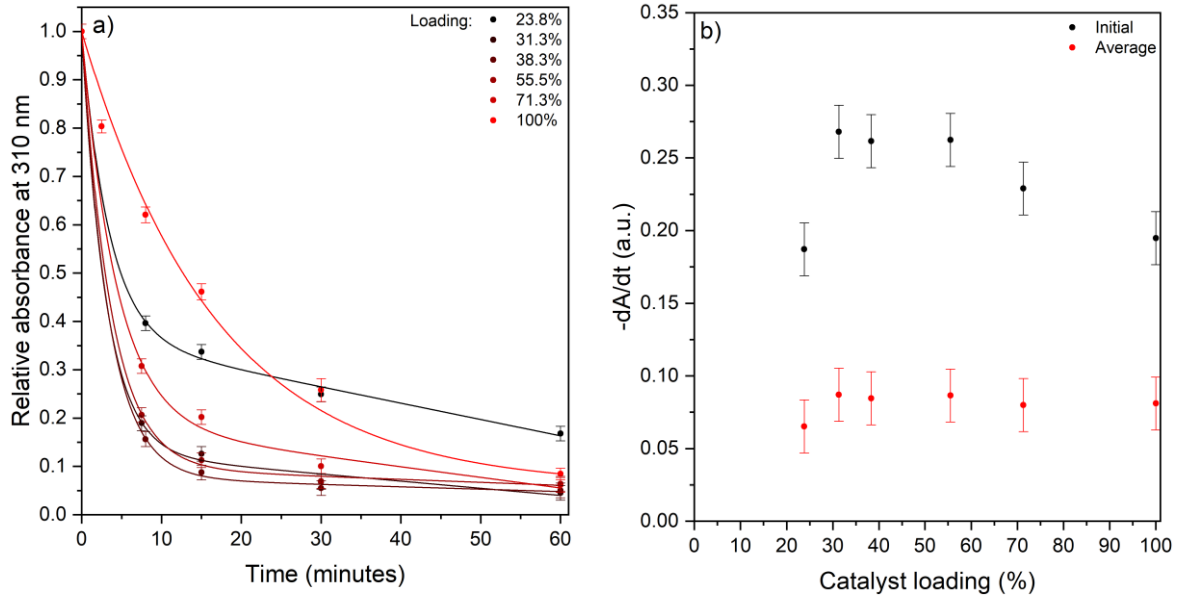

Supplementary figure 32 – Kinetic curves for Co_2MnO_4-GNF composites; **a:** Relative absorbances at 310 nm; **b:** The rate of change in absorbance at 310 nm versus time, used as a proxy of reaction rate.

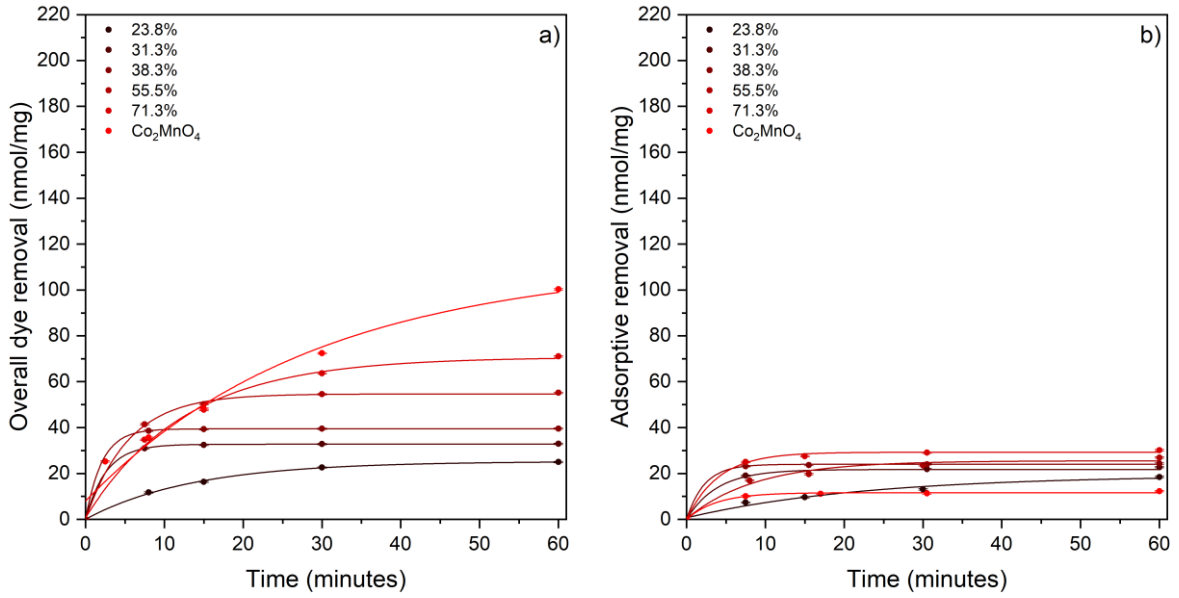

Supplementary figure 33 – Graphs showing overall (**a**) and adsorptive (**b**) dye removal versus time for Co_2MnO_4-GNF composites and Co_2MnO_4.

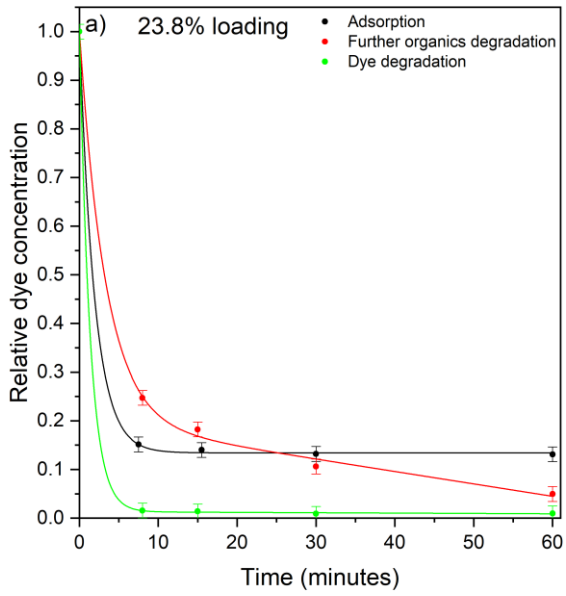
a)
23.8% loading
Adsorption
Further organics degradation
Dye degradation
Relative dye concentration
Time (minutes)

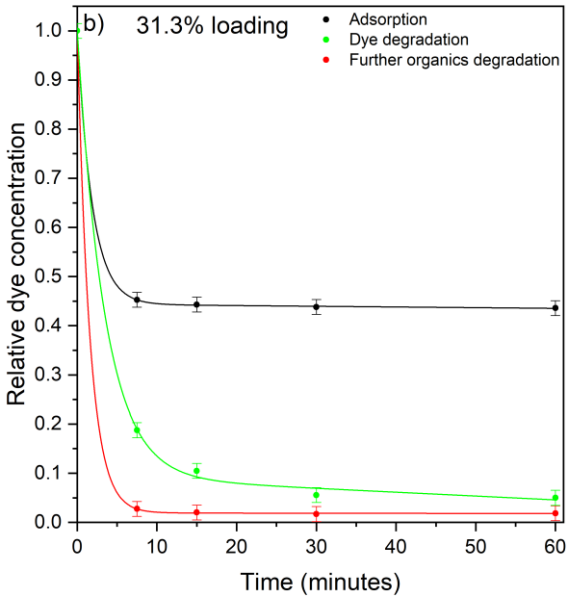
b)
31.3% loading
Adsorption
Dye degradation
Further organics degradation
Relative dye concentration
Time (minutes)

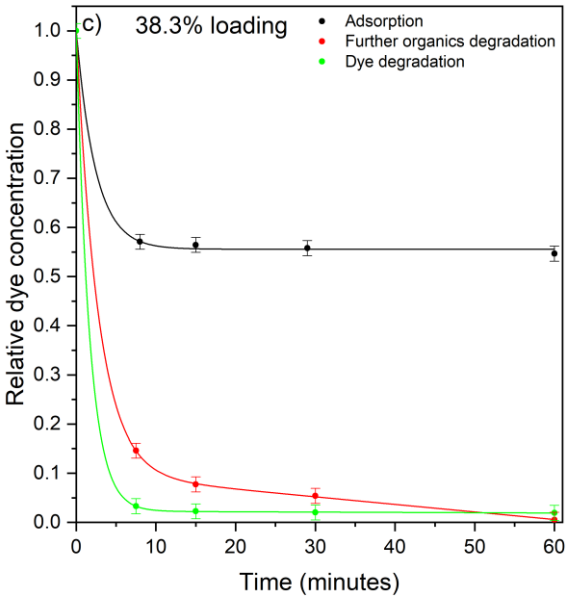
c)
38.3% loading
Adsorption
Further organics degradation
Dye degradation
Relative dye concentration
Time (minutes)

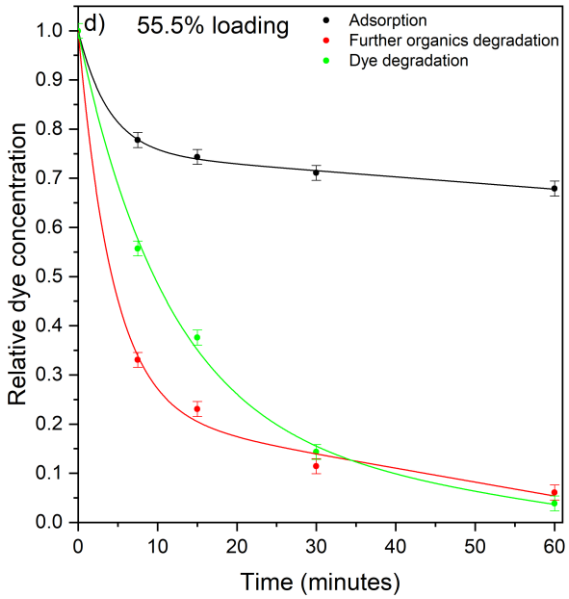
d)
55.5% loading
Adsorption
Further organics degradation
Dye degradation
Relative dye concentration
Time (minutes)

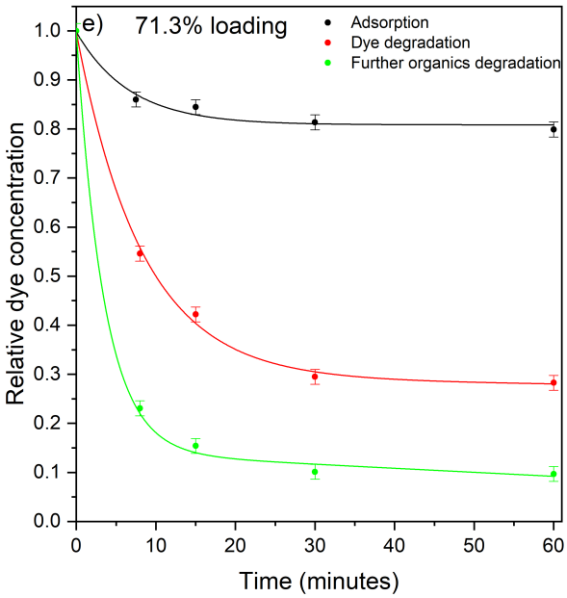
e)
71.3% loading
Adsorption
Dye degradation
Further organics degradation
Relative dye concentration
Time (minutes)

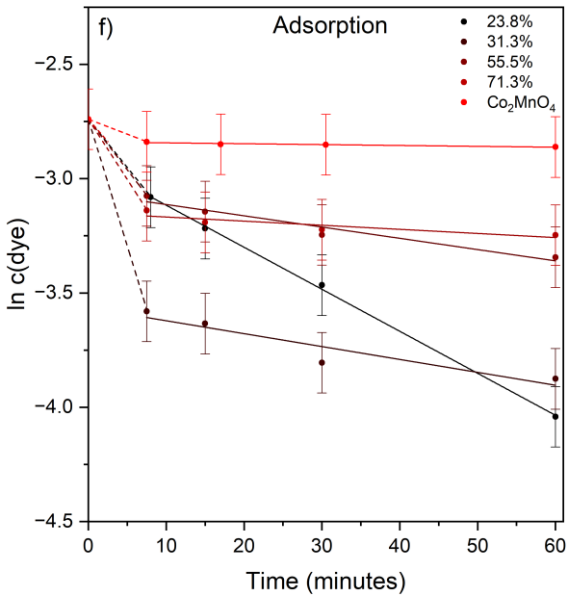
f)
Adsorption
23.8%
31.3%
55.5%
71.3%
Co2MnO4
ln c(dye)
Time (minutes)

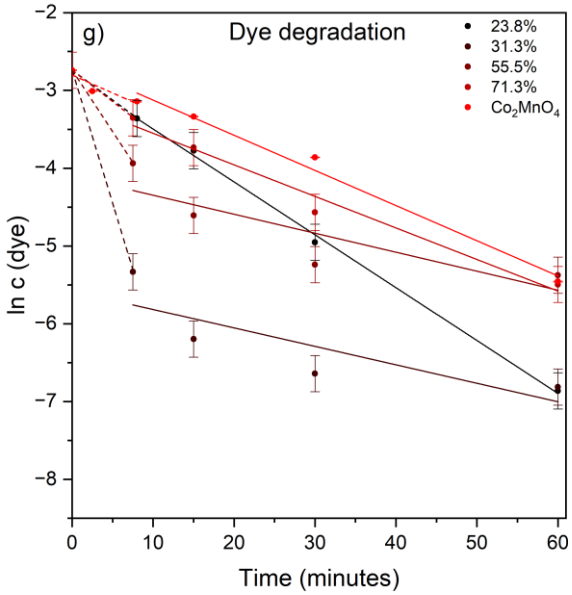

Supplementary figure 34 – Kinetic curves for Co_2MnO_4-oGNF composites of different catalyst loadings showing the relative dye concentrations versus time in adsorption and dye degradation experiments; **a:** 23.8% loading, **b:** 31.3% loading; **c:** 38.3% loading; **d:** 55.5% loading; **e:** 71.3% loading; **f:** Summary of ln c(dye) vs time curves for adsorption on all composites; **g:** Summary of ln c(dye) vs time curves for dye degradation on all composites.

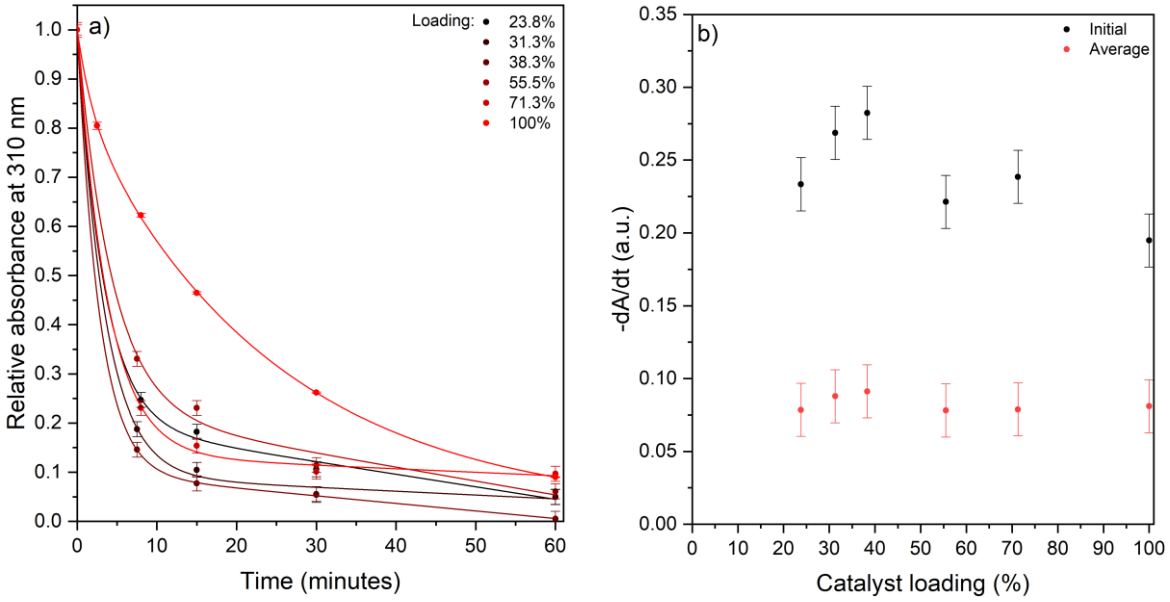

Supplementary figure 35 – Kinetic curves for Co_2MnO_4-oGNF composites; **a:** Relative absorbances at 310 nm; **b:** The rate of change in absorbance at 310 nm versus time, used as a proxy of reaction rate.

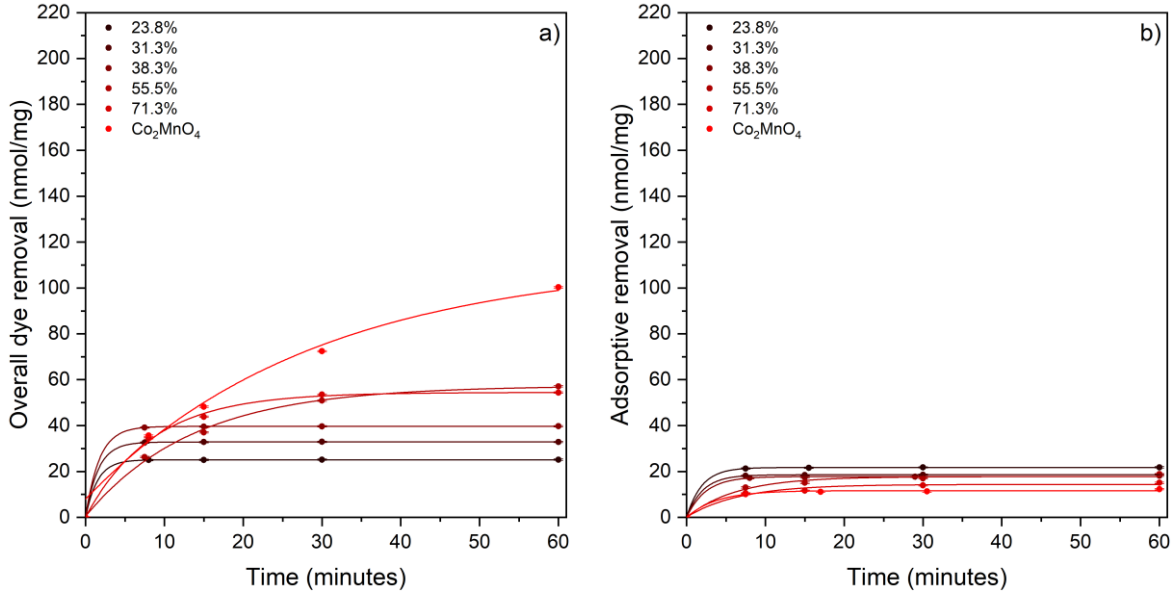

Supplementary figure 36 – Graphs showing overall (**a**) and adsorptive (**b**) dye removal versus time for Co_2MnO_4-oGNF composites and Co_2MnO_4.

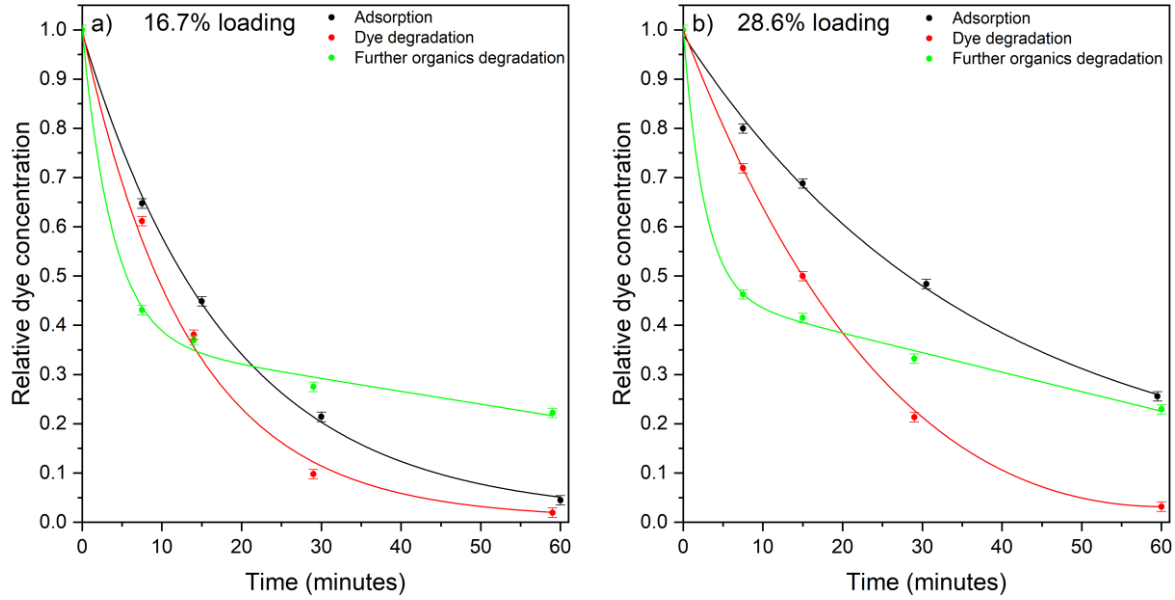

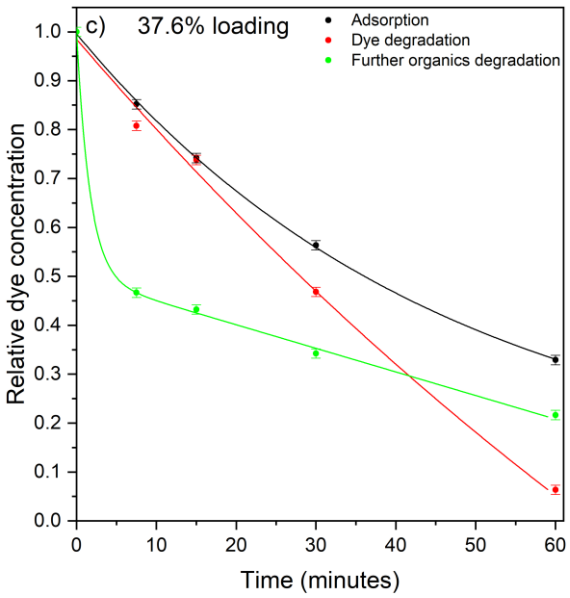
c) 37.6% loading
Adsorption
Dye degradation
Further organics degradation
Relative dye concentration
Time (minutes)

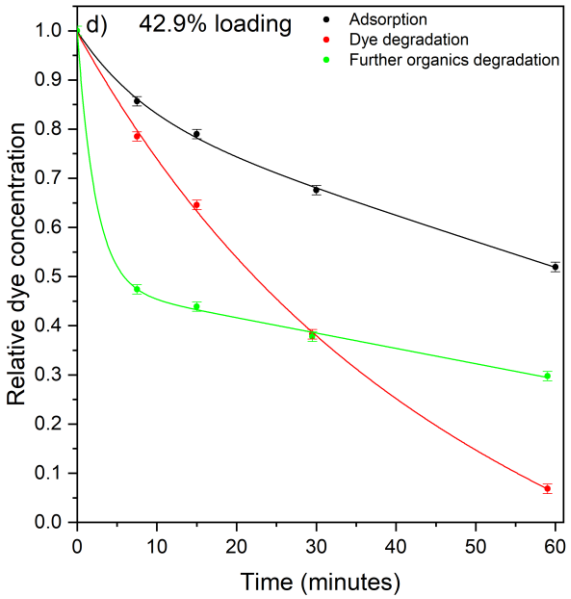
d) 42.9% loading
Adsorption
Dye degradation
Further organics degradation
Relative dye concentration
Time (minutes)

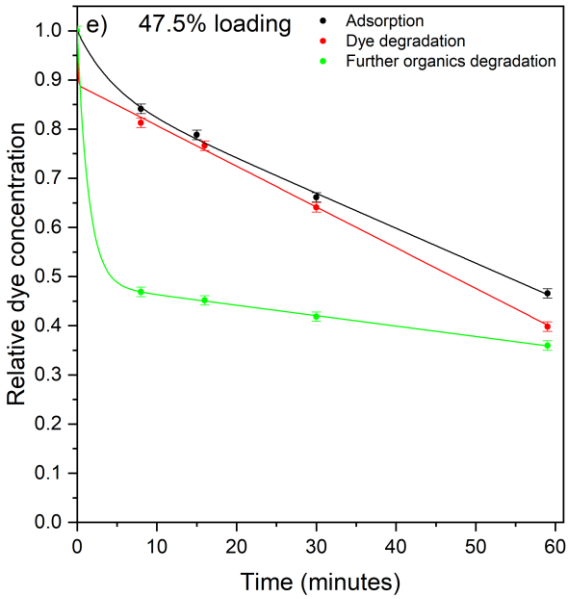
e) 47.5% loading
Adsorption
Dye degradation
Further organics degradation
Relative dye concentration
Time (minutes)

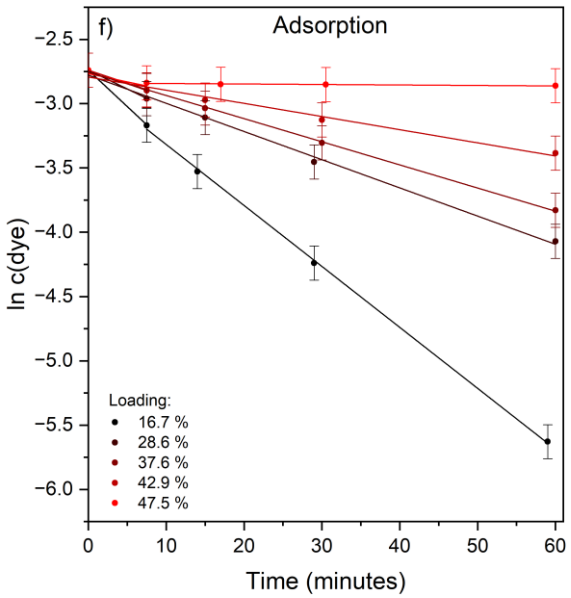
f) Adsorption
ln c(dye)
Loading:
16.7 %
28.6 %
37.6 %
42.9 %
47.5 %
Time (minutes)

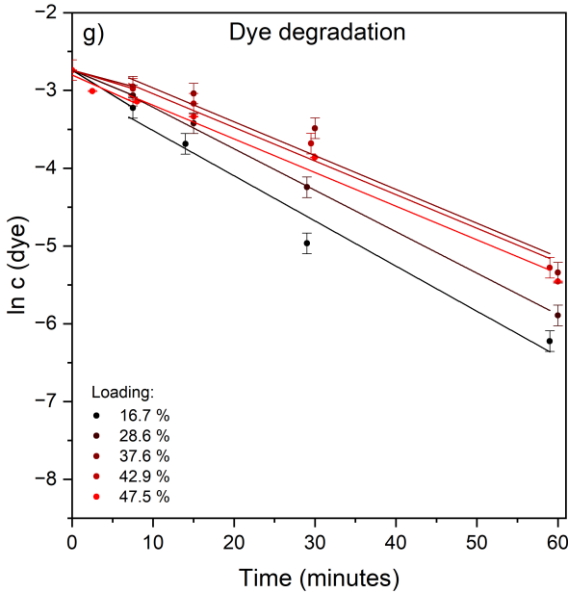
g) Dye degradation
ln c (dye)
Loading:
16.7 %
28.6 %
37.6 %
42.9 %
47.5 %
Time (minutes)

Supplementary figure 37 – Kinetic curves for Co_2MnO_4-CB composites of different catalyst loadings showing the relative dye concentrations versus time in adsorption and dye degradation experiments; **a:** 20% loading, **b:** 40% loading; **c:** 60% loading; **d:** 75% loading; **e:** 90% loading; **f:** Summary of ln c(dye) vs time curves for adsorption on all composites; **g:** Summary of ln c(dye) vs time curves for dye degradation on all composites.

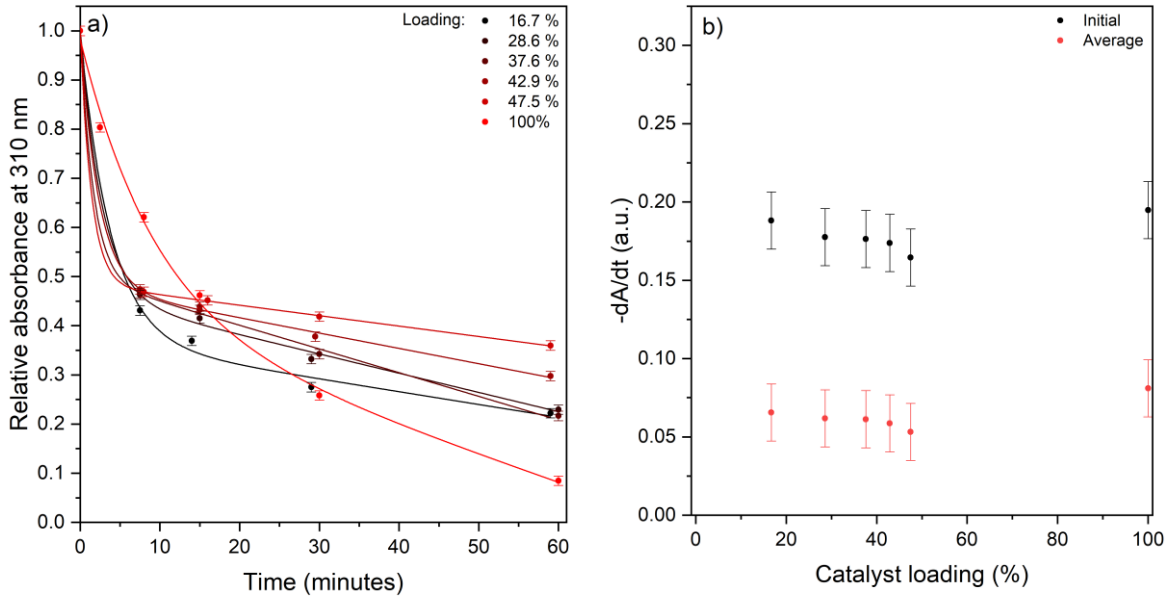

Supplementary figure 38 – Kinetic curves for Co_2MnO_4-CB composites; **a:** Relative absorbances at 310 nm; **b:** The rate of change in absorbance at 310 nm versus time, used as a proxy of reaction rate.

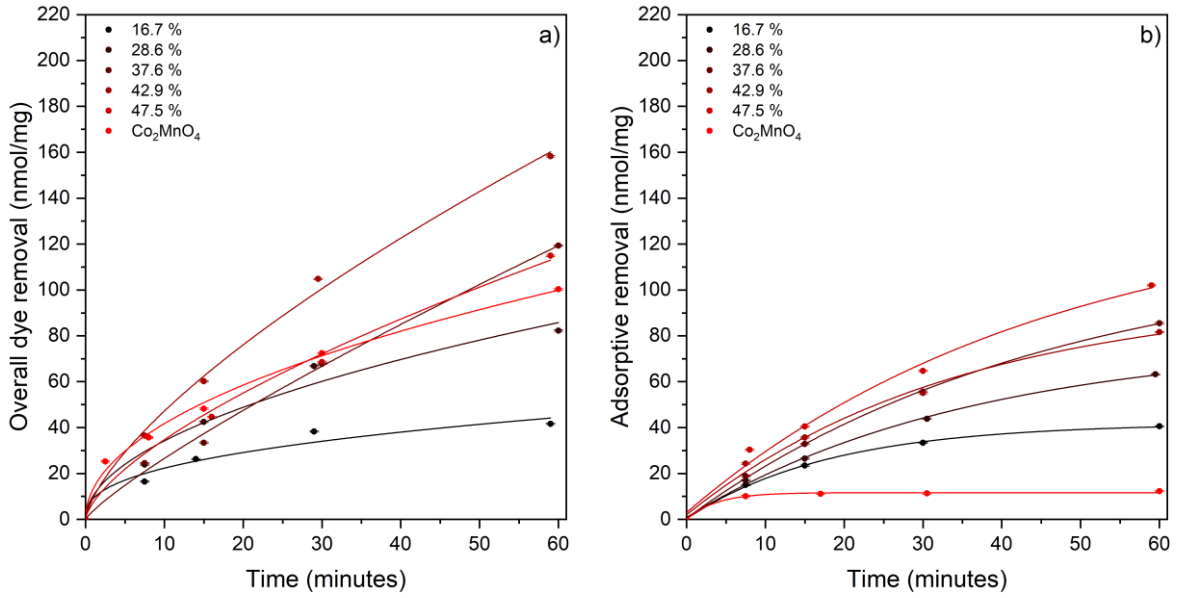

Supplementary figure 39 – Graphs showing overall (**a**) and adsorptive (**b**) dye removal versus time for Co_2MnO_4-CB composites and Co_2MnO_4.

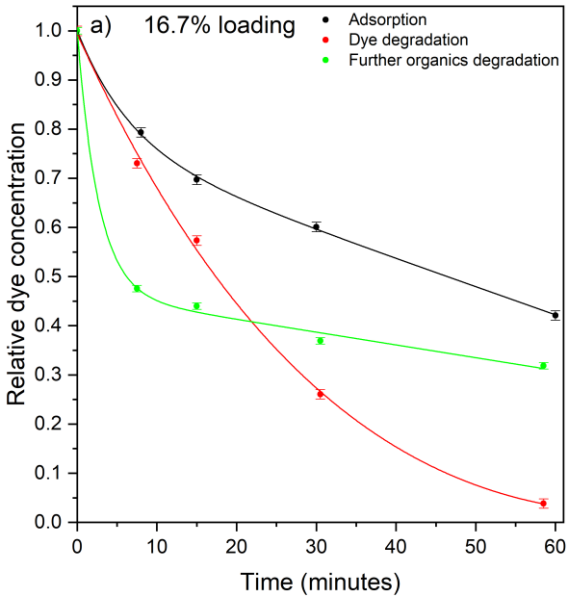
a)
16.7% loading
Adsorption
Dye degradation
Further organics degradation
Relative dye concentration
Time (minutes)

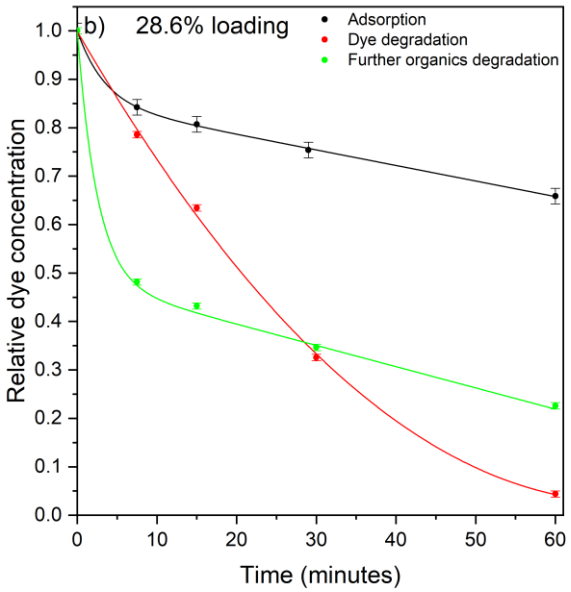
b)
28.6% loading
Adsorption
Dye degradation
Further organics degradation
Relative dye concentration
Time (minutes)

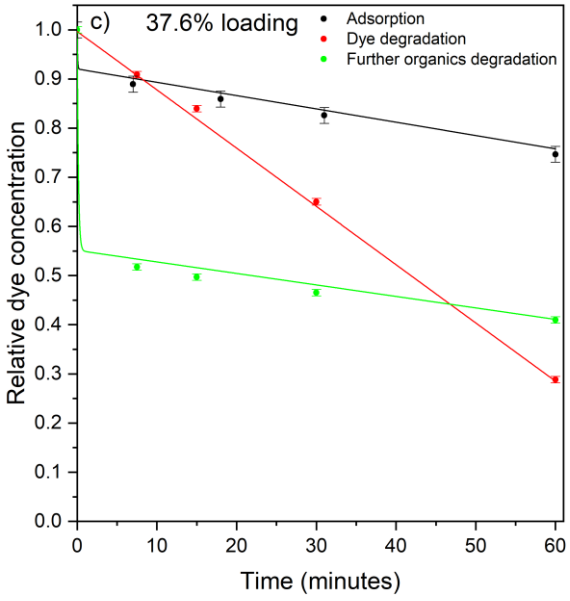
c)
37.6% loading
Adsorption
Dye degradation
Further organics degradation
Relative dye concentration
Time (minutes)

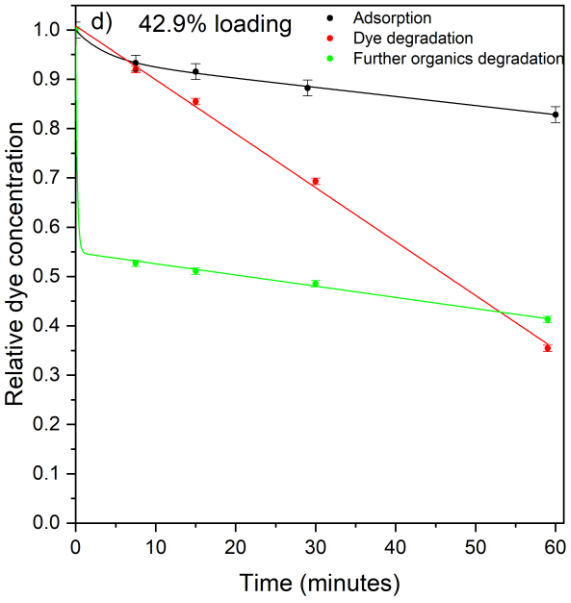
d)
42.9% loading
Adsorption
Dye degradation
Further organics degradation
Relative dye concentration
Time (minutes)

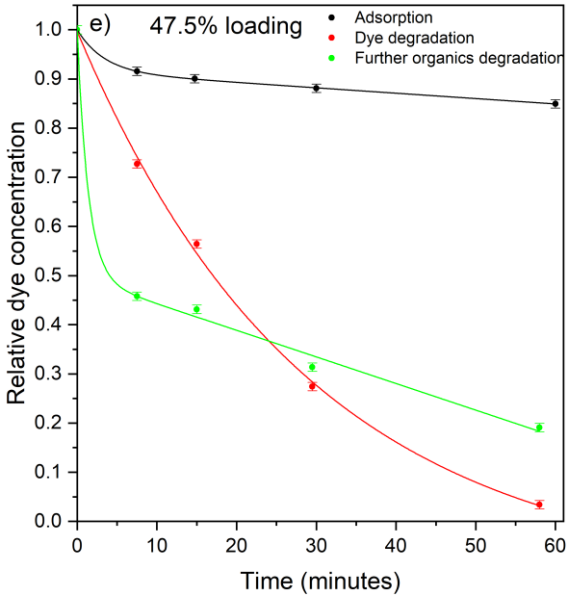
e)
47.5% loading
Adsorption
Dye degradation
Further organics degradation
Relative dye concentration
Time (minutes)

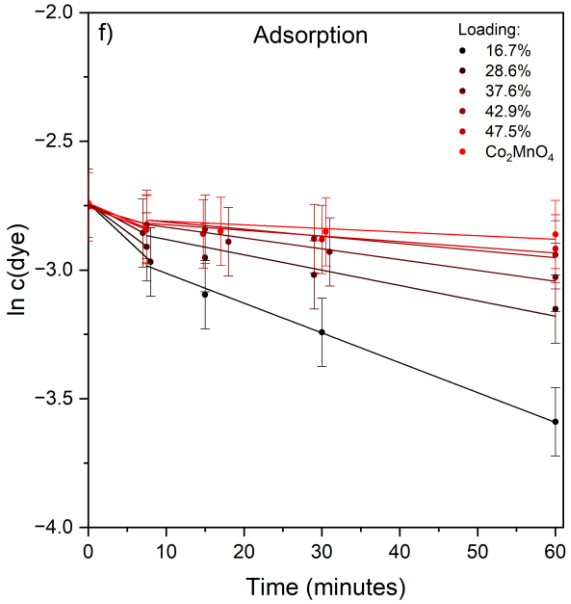
f)
Adsorption
Loading:
16.7%
28.6%
37.6%
42.9%
47.5%
Co2MnO4
ln c(dye)
Time (minutes)

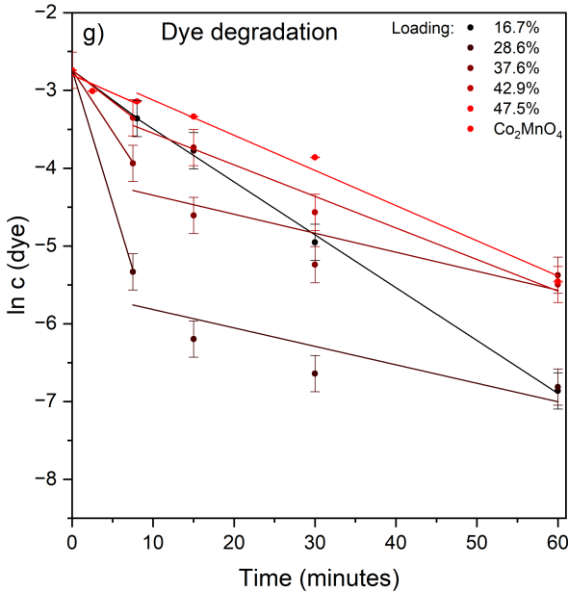

Supplementary figure 40 – Kinetic curves for Co_2MnO_4-oCB composites of different catalyst loadings showing the relative dye concentrations versus time in adsorption and dye degradation experiments; **a:** 20% loading, **b:** 40% loading; **c:** 60% loading; **d:** 75% loading; **e:** 90% loading.

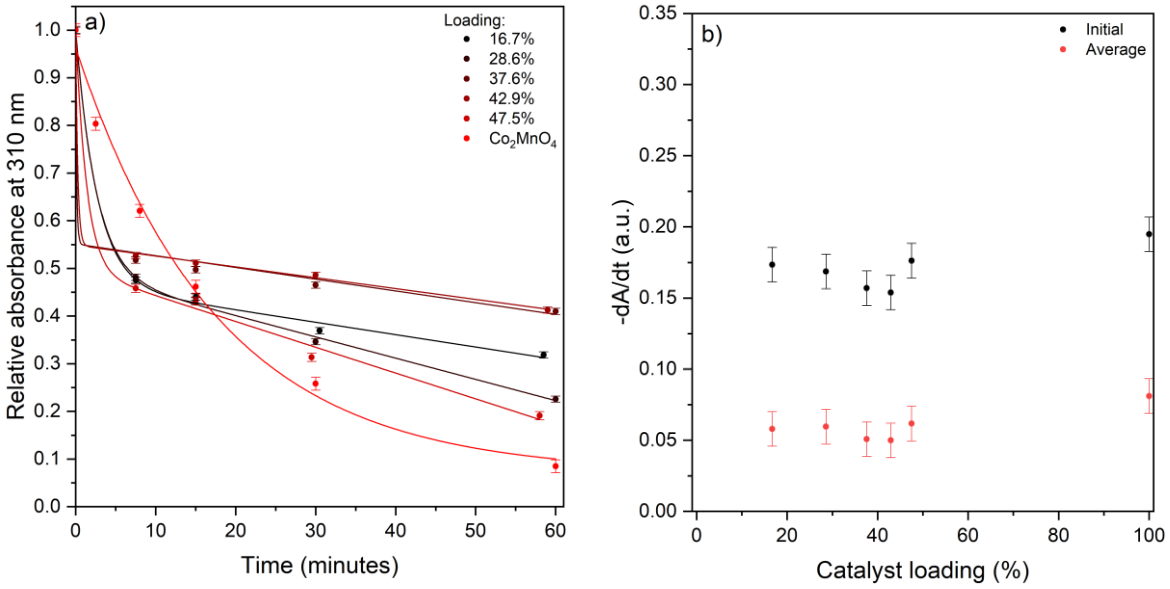

Supplementary figure 41 – Kinetic curves for Co_2MnO_4-oCB composites; **a:** Relative absorbances at 310 nm; **b:** The rate of change in absorbance at 310 nm versus time, used as a proxy of reaction rate.

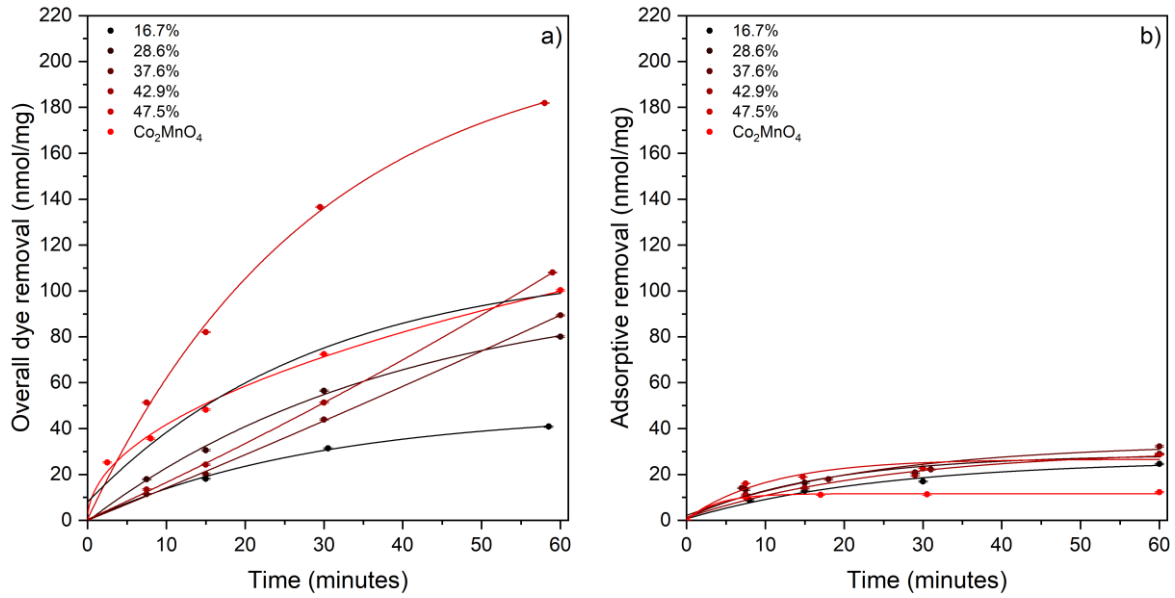

Supplementary figure 42 – Graphs showing overall (**a**) and adsorptive (**b**) dye removal versus time for Co_2MnO_4-oCB composites and Co_2MnO_4.

Supporting Information – Chapter 6

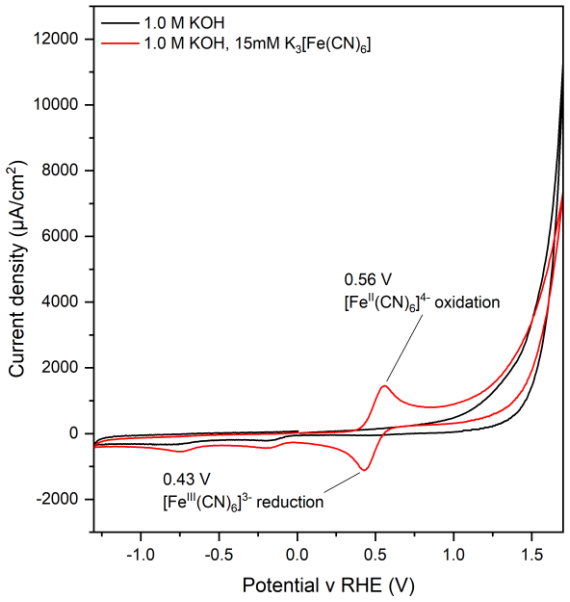

Supplementary figure 43 – Cyclic voltammograms of bare glassy carbon electrode.
Experimental conditions: WE: Glassy carbon, CE: graphite, RE: Ag/AgCl/3.5 M KCl; 1.0M KOH electrolyte.

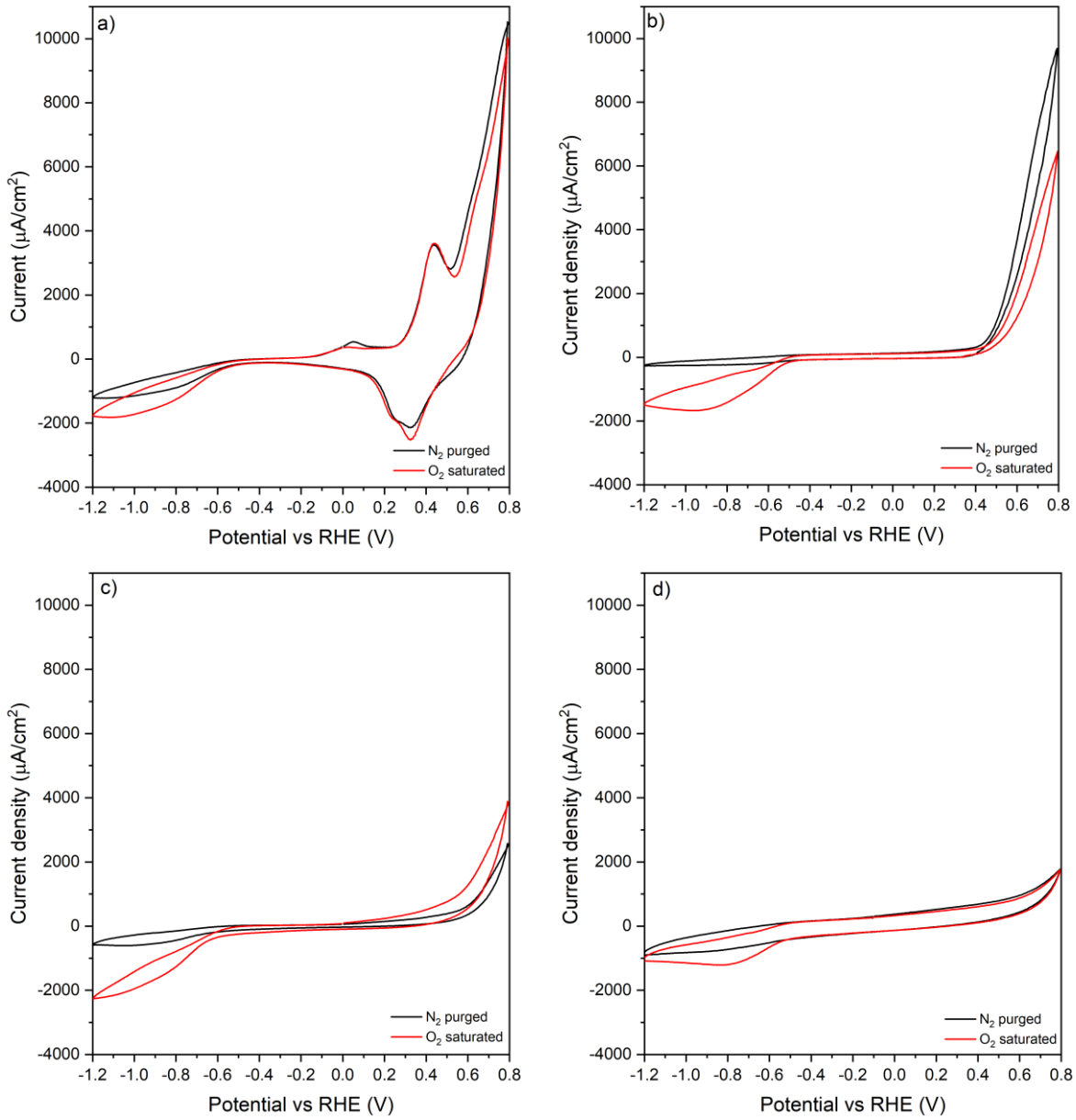

Supplementary figure 44 – Cyclic voltammograms of Co, Mn spinels; **a:** Co_3O_4, **b:** Co_2MnO_4, **c:** $CoMn_2O_4$, **d:** Mn_3O_4.
Experimental conditions: WE: Glassy carbon, CE: graphite, RE: Ag/AgCl/3.5 M KCl; 0.1 M KOH electrolyte.

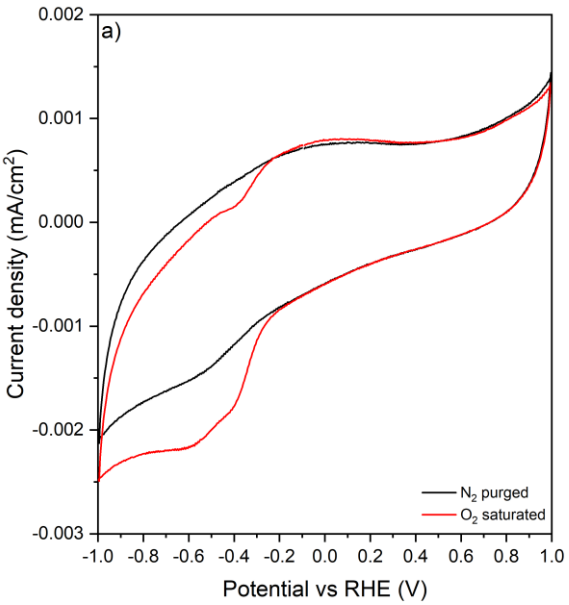

Supplementary figure 45 – Cyclic voltammograms of bare glassy carbon electrode.
Experimental conditions: WE: Glassy carbon, CE: graphite, RE: Ag/AgCl/3.5 M KCl; 0.1 M $NaNO_3$ electrolyte.

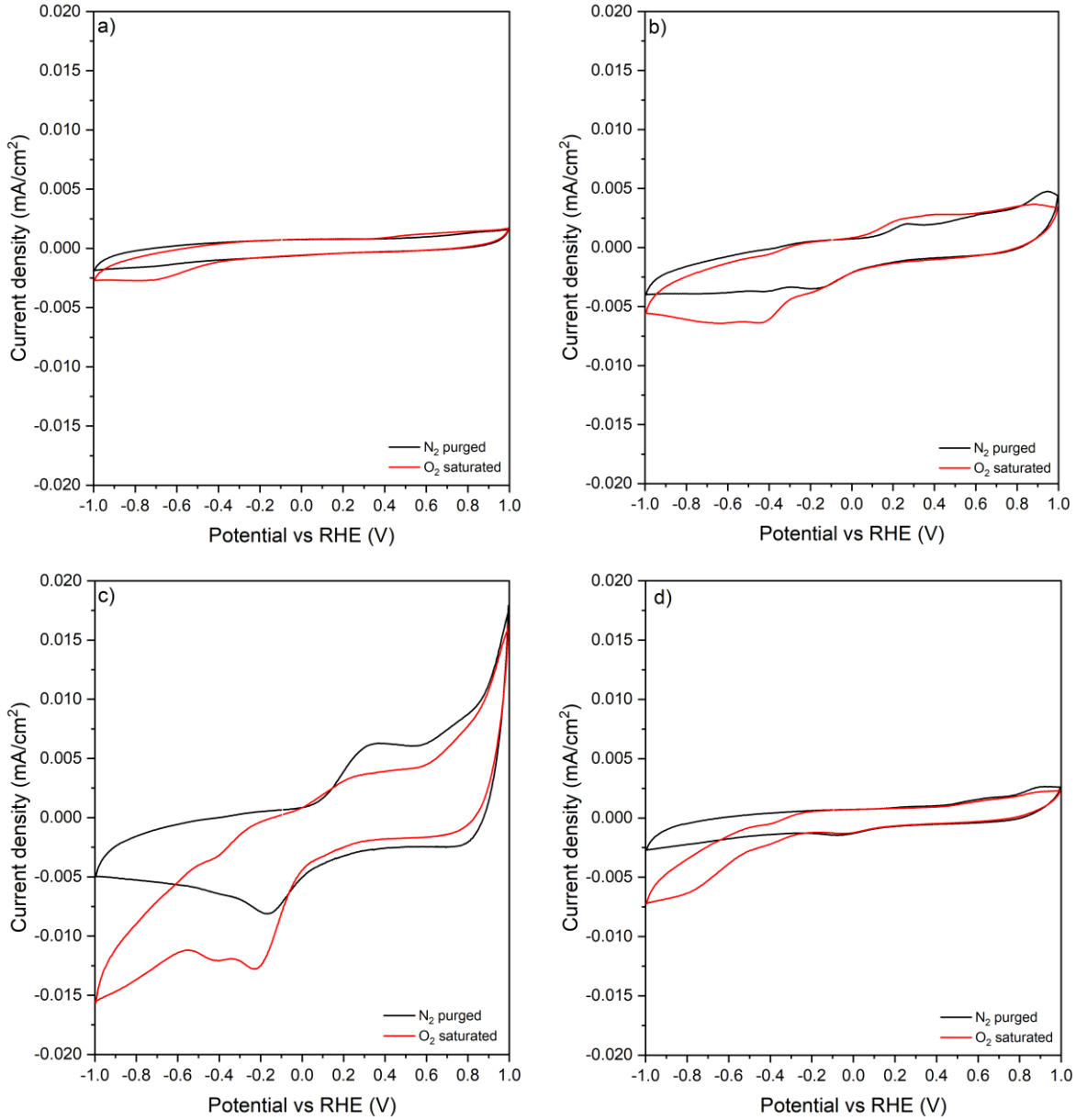

Supplementary figure 46 – Cyclic voltammograms of Co, Mn spinels; **a:** Co_3O_4, **b:** Co_2MnO_4, **c:** $CoMn_2O_4$, **d:** Mn_3O_4.
Experimental conditions: WE: Glassy carbon, CE: graphite, RE: Ag/AgCl/3.5 M KCl; 0.1 M $NaNO_3$ electrolyte.